Effects of Volcanic Eruption Source Parameters on Radiative Forcing and Sulfate Deposition

Lauren Rebecca Marshall

Submitted in accordance with the requirements for the degree of
Doctor of Philosophy

The University of Leeds
School of Earth and Environment

August 2018

The candidate confirms that the work submitted is her own, except where work which has formed part of jointly-authored publications has been included. The contribution of the candidate and the other authors to this work has been explicitly indicated below. The candidate confirms that appropriate credit has been given within the thesis where reference has been made to the work of others.

This thesis has been submitted in the alternative thesis-by-publication format so that the results are readily available and accessible, whilst facilitating publication during the PhD. The thesis comprises an introduction chapter, three publications as outlined below, and a discussion and conclusions chapter.

Chapter 2 of the thesis is the following publication:

Marshall, L., Schmidt, A., Toohey, M., Carslaw, K. S., Mann, G. W., Sigl, M., et al. 2018. Multi-model comparison of the volcanic sulfate deposition from the 1815 eruption of Mt. Tambora. ***Atmospheric Chemistry and Physics.*** **18(3), pp. 2307-2328.**

This study was designed by the candidate, AS and MT. The candidate set-up and ran the UM-UKCA model simulations with guidance from GWM and SD. The candidate processed the raw data from the other models, which were provided by co-authors. The candidate analysed all model output, prepared all figures and wrote the paper, with comments and suggestions from all co-authors. The original Tambora simulations were designed as part of a pre-study to the Model Intercomparison Project on the climatic response to Volcanic forcing (VolMIP) with initial results appearing in the following paper: Zanchettin, D., Khodri, M., Timmreck, C., Toohey, M., Schmidt, A., Gerber, E. P., et al. (including **Marshall, L.**) 2016. The Model Intercomparison Project on the climatic response to Volcanic forcing (VolMIP): experimental design and forcing input data for CMIP6. *Geoscientific Model Development*. **9**(8), pp. 2701-2719.

Chapter 3 of the thesis is the following manuscript, currently under review for the Journal of Geophysical Research-Atmospheres, which has received minor revisions:

Marshall, L., Johnson, J. S., Mann, G. W., Lee, L., Dhomse, S. S., Regayre, L., Yoshioka, M., Carslaw, K., and Schmidt, A. 2018. Exploring how eruption source parameters affect volcanic radiative forcing using statistical emulation. ***Journal of Geophysical Research-Atmospheres.***

This study was designed by the candidate, AS, KSC and GWM. The candidate set-up and ran the ensemble of simulations with guidance and assistance from MY, GWM and LR. The candidate built the statistical emulators and conducted the sensitivity analyses based on code written by JSJ and guidance from JSJ and LL. The candidate prepared all figures and wrote the manuscript with comments from all co-authors. The online tool provided as a supplement to this paper was initially designed and coded by the candidate, which was updated and significantly improved by Richard Rigby.

Chapter 4 is the following manuscript in preparation to be submitted to *Journal of Geophysical Research-Atmospheres:*

Marshall, L., Schmidt, A., Johnson, J. S., Mann, G. W., Lee, L., and Carslaw, K. S., in prep. Large uncertainty in volcanic radiative forcing derived from ice cores.

This study was designed by the candidate, AS and KS. The candidate ran the ensemble of simulations and analysed all model output. The candidate conducted the statistical emulation with guidance from JSJ and LL. The candidate wrote the manuscript with suggestions and comments from all co-authors.

Acknowledgements

Firstly, I would like to thank my supervisors, Anja Schmidt, Ken Carslaw and Graham Mann, who without their guidance, feedback and encouragement, this thesis would not have been possible. In particular, I'd like to express my gratitude to Anja for her endless inspiration, infectious enthusiasm, and for making me believe in myself. I feel privileged to have had such a great supervisory team and I would not be where I am today if not for your support and encouragement.

I would also like to express my thanks to Jill Johnson, Lindsay Lee and Leighton Regayre for helping me with all things emulator-related and patiently dealing with my endless stream of questions. I am also grateful to all co-authors on the publications presented in this thesis who have provided invaluable guidance and feedback, as well as many members of ICAS who have helped me with various things over the years – thank you! A special thank you to Richard Rigby for sorting out numerous IT panics and without whom this thesis would also not have been possible.

Thank you to the Leeds-York NERC DTP for funding this PhD and for the opportunity to present my research at a variety of conferences, including EGU, which resulted in my initial involvement with VolMIP. Thank you also to the Advanced Climate Dynamics Courses for a memorable summer school in Iceland, with a particular highlight of snowmobiling across Katla on the Mýrdalsjökull glacier that I will never forget!

For supporting and encouraging me over the last four years, I would like to thank my friends and family; in particular Mum, Dad, my Grandparents, Amy, Lydia, Rachel, Hannah, Charlotte and Ruth, and my fellow ICAS PhD cohort, Hana, Mike, Ilkka, and Ollie. Thank you also to the Monday night tennis group, Leeds University Symphonic Wind Orchestra and Mojo78 for providing a much-needed escape throughout my time here in Leeds.

Lastly, and by no means least I would like to express my thanks to Chris. I'm not sure what I would have done without you – thank you for everything!

Abstract

Explosive volcanic eruptions can inject sulfur dioxide (SO_2) into the stratosphere, which forms stratospheric sulfate aerosol that can significantly impact the climate. The radiative forcing of an eruption depends on several eruption source parameters: the mass of SO_2 emitted, the latitude and the emission height. However, the combined effects of these parameters are not well understood. Reconstructions of historic volcanic radiative forcing, which are essential for understanding the role of volcanism on climate variability, are derived from ice core sulfate records, but rely on relationships between ice sheet deposition, stratospheric aerosol burdens and radiative forcing from limited observations.

The aim of this thesis is to understand the impact of explosive volcanic eruptions on radiative forcing and volcanic sulfate deposition. The role of individual and combined eruption source parameters are comprehensively investigated using interactive stratospheric aerosol models, perturbed parameter ensembles and statistical emulation.

The results demonstrate that radiative forcing is primarily determined by the SO_2 emission magnitude, is stronger for tropical eruptions and has a greater dependency on the injection height if the eruption is tropical. The ice sheet deposition is relatively independent of the injection height. The results reveal complex combined effects of the eruption parameters and illustrate the importance of explicitly simulating aerosol microphysical processes to determine aerosol mass, size and lifetime.

A wide range of eruption-realisations is found that produce ice sheet deposition that is consistent with ice-core-derived estimates for historic eruptions in the last 2500 years. These eruptions have a range in time-integrated radiative forcing ($> \sim 300$ MJ m^{-2}) that is not considered in reconstructions. Sulfate deposition differs considerably between models for the 1815 eruption of Mt. Tambora. The results suggest there is a large uncertainty in radiative forcing derived from ice cores. Consequently, the efficacy of volcanic radiative forcing derived from previous reconstructions may be incorrect.

Contents

List of Tables

List of Figures

Abbreviations

ACCMIP	The **A**tmospheric **C**hemistry and **C**limate **M**odel **I**ntercomparison **P**roject
AOD	**A**erosol **O**ptical **D**epth
BDC	**B**rewer **D**obson **C**irculation
CCM	**C**omposition **C**limate **M**odel
CCN	**C**loud **C**ondensation **N**uclei
CCMI	**C**hemistry-**C**limate **M**odel **I**nitiative
CMIP5/6	**C**oupled **M**odel **I**ntercomparison **P**roject phase 5/6
DMS	**D**i**m**ethyl **S**ulfide
EVA	**E**asy **V**olcanic **A**erosol
GCM	**G**eneral **C**irculation **M**odel
GLOMAP	**GLO**bal **M**odel of **A**erosol **P**rocesses
GP	**G**aussian **P**rocess
HadGEM3	**Had**ley Centre **G**lobal **E**nvironment **M**odel version **3**
ICI	**I**ce **C**ore **I**ndex
ISA-MIP	**I**nteractive **S**tratospheric **A**erosol **M**odel **I**ntercomparison **P**roject
ITCZ	**I**nter **T**ropical **C**onvergence **Z**one
IVI	**I**ce Core **V**olcano **I**ndex
LW	**L**ong**w**ave
MSPs	**M**eteoric **S**moke **P**articles
NAO	**N**orth **A**tlantic **O**scillation
NH	**N**orthern **H**emisphere
OAT	**O**ne-**a**t-a-**t**ime
OCS	**C**arbonyl **S**ulfide
PMIP3/4	**P**aleoclimate **M**odelling **I**ntercomparison **P**roject phase 3/4
QBO	**Q**uasi **B**iennial **O**scillation
R_{eff}	Effective Radius
RF	**R**adiative **F**orcing
sAOD	**S**tratospheric **A**erosol **O**ptical **D**epth
SH	**S**outhern **H**emisphere

SO_2	Sulfur dioxide
SSA	**S**ingle-**S**cattering **A**lbedo
SSTs	**S**ea-**S**urface **T**emperatures
SW	**S**hort**w**ave
TOA	**T**op **o**f the **A**tmosphere
UM	**U**nified **M**odel
UKCA	**U**nited **K**ingdom **C**hemistry and **A**erosols
VolMIP	**M**odel **I**ntercomparison **P**roject on the climatic response to **Vol**canic forcing

Chapter 1 Introduction

1.1 Motivation

Explosive volcanic eruptions that inject sulfur dioxide (SO_2) into the stratosphere are significant drivers of natural climate variability (Hegerl et al., 2007; Myhre et al., 2013; Schurer et al., 2013; Sigl et al., 2015). SO_2 is oxidized to sulfuric acid vapour (H_2SO_4) that nucleates to form sulfate aerosol particles or condenses onto existing aerosol particles (e.g. Turco et al., 1979; Hamill et al., 1997). Sulfate aerosol particles scatter shortwave (SW) radiation and, to a lesser extent, absorb longwave (LW) radiation (Labitzke and McCormick, 1992) and therefore volcanic eruptions can significantly alter the Earth's radiative balance. The scattering of SW radiation leads to surface and tropospheric cooling, which is the net radiative effect following volcanic eruptions. Stratospheric sulfate aerosol can be transported globally and has a lifetime of several years before it is deposited to the surface, resulting in global negative radiative forcing for a number of years. The last eruption to occur in which significant SO_2 (10-20 Tg) was injected into the stratosphere was that of Mt. Pinatubo in 1991. This eruption led to approximately 0.4-0.5°C of surface cooling in 1992 (Dutton and Christy, 1992; McCormick et al., 1995).

The magnitude of aerosol scattering and absorption, and hence radiative forcing, is dependent on the aerosol particle size distribution (Lacis et al., 1992). The same mass of aerosol distributed into a large number of small particles has a greater scattering efficiency than when distributed into a small number of large particles. Larger aerosol particles also sediment more quickly out of the atmosphere (e.g. Pinto et al., 1989). In addition to the direct radiative effects, sulfate aerosol particles can also indirectly affect radiative forcing by modifying cloud albedo and lifetime (e.g. Jensen and Toon, 1992; Sassen, 1992; Schmidt et al., 2010; 2012; Gettelman et al., 2015). Additional indirect radiative effects can result from chemical and dynamical changes in stratospheric ozone caused by modification of stratospheric circulation and acceleration of heterogeneous chemistry on volcanically enhanced aerosol surface area (e.g. Tabazadeh et al., 2002; Tilmes et al., 2008; Dhomse et al., 2015). A

summary of the impact of volcanic eruptions on the Earth's radiative balance is presented in Figure 1.1.

Explosive eruptions can have many impacts on climate (Robock, 2000; Cole-Dai, 2010; Timmreck, 2012) as well as environmental and societal consequences such as crop failure, famine, plague and war (Puma et al., 2015; Toohey et al., 2016a; Nooren et al., 2017). Eruptions can reduce global precipitation due to the reduction of incoming SW radiation (Trenberth and Dai, 2007; Schneider et al., 2009; Fyfe et al., 2013; Iles and Hegerl, 2014), reduce the Asian and African summer monsoons due to preferential cooling of land (e.g. Man et al., 2014; Zambri et al., 2017) and can shift the position of the Inter Tropical Convergence Zone (ITCZ) if the volcanic sulfate aerosol is hemispherically asymmetric (Haywood et al., 2013; Iles and Hegerl, 2014; Baldini et al., 2015; Ridley et al., 2015). It has also been suggested that tropical stratospheric heating due to absorption of LW radiation can lead to winter warming in Europe by enhancing the meridional temperature gradient and causing a stronger polar vortex, which forces a positive North Atlantic Oscillation (NAO) phase (Robock, 2000; Fischer et al., 2007; Toohey et al., 2014; Bittner et al., 2016; Zambri and Robock, 2016). However, this mechanism remains uncertain (e.g. Stenchikov et al., 2002; Polvani et al., 2018).

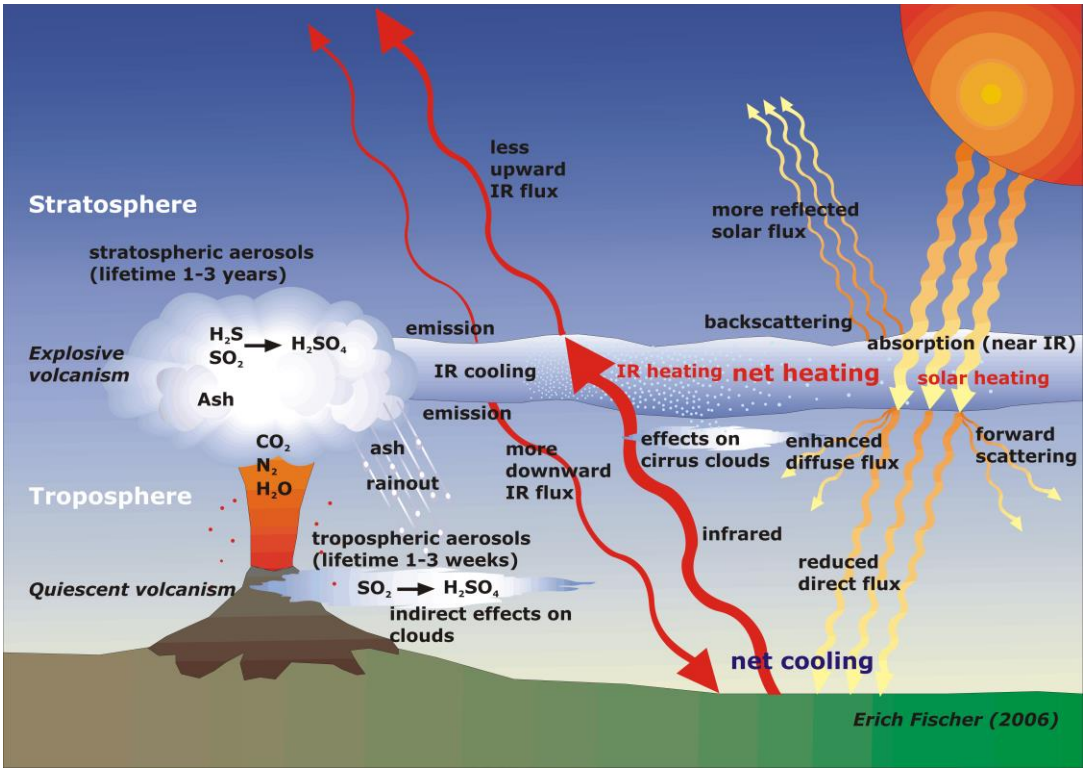

Figure 1.1: Impact of volcanic eruptions on Earth's radiative balance. Figure from Fischer (2006).

The climatic impact of an explosive eruption does not scale linearly with the mass of SO_2 emitted into the atmosphere (Rampino and Self, 1982; Pinto et al., 1989; Timmreck et al., 2010; English et al., 2013; Metzner et al., 2014). As the SO_2 emission magnitude increases, more H_2SO_4 vapour is produced and the high concentrations lead to increased H_2SO_4 vapour condensation rates and the growth of aerosol particles. Growth also occurs as particles coagulate, and the aerosol size distribution is shifted towards larger values (Pinto et al., 1989). The reduced radiative scattering efficiency of these particles and their enhanced sedimentation rates limits the climatic impact.

Hydroxyl radicals (OH) needed to oxidise the SO_2, can also become depleted after large SO_2 injections (Pinto et al., 1989; Bekki, 1995; Bekki et al., 1996), resulting in a slower conversion of SO_2 to sulfate aerosol. Climate model simulations without aerosol microphysics of the super-eruption of Toba ~74,000 years ago (Jones et al., 2005; Robock et al., 2009), which some studies estimate to have released more than 100 times the SO_2 that was emitted by 1991 Mt. Pinatubo (e.g. Rose and Chesner, 1990; Zielinski et al., 1996), predict surface cooling more than 3 times greater than that predicted from models with aerosol microphysics (Timmreck et al., 2010).

In addition to the SO_2 emission magnitude, there are other properties of an eruption, known as eruption source parameters, and factors related to when the eruption occurs, that can influence the magnitude of the climatic impact. These include the latitude and the injection height of the SO_2 emissions, the season of eruption (e.g. Toohey et al., 2011; Stevenson et al., 2017) and the phase of the Quasi Biennial Oscillation (QBO), which describes the direction of zonal wind in the tropical stratosphere (Baldwin et al., 2001). The latitude and the injection height at which the SO_2 is emitted can affect the transport, lifetime and size distribution of the sulfate aerosol that is formed (e.g. (Niemeier et al., 2011; Arfeuille et al., 2014). Sulfate aerosol in the tropical stratosphere can be transported to both hemispheres, with preferential transport to the winter hemisphere (e.g. Holton et al., 1995). This transport is also modulated by the QBO, as the stronger easterly phase restricts meridional transport of aerosol (Hitchman et al., 1994; Punge et al., 2009) as was observed after the 1991 eruption of Mt. Pinatubo (Trepte and Hitchman, 1992; Trepte et al., 1993). Most of the sulfate aerosol formed after high-latitude eruptions is confined within the hemisphere in which the SO_2 was emitted (e.g. Oman et al., 2005; Jones et al., 2017). Stratospheric heating following the absorption of LW radiation by the sulfate aerosol particles can

loft the aerosol to higher altitudes, increase the aerosol lifetime, and affect the cross-equatorial transport (Young et al., 1994; Timmreck et al., 1999; Niemeier et al., 2009; 2011; Aquila et al., 2012). Throughout this thesis, both the eruption properties and external factors are referred to as 'eruption source parameters'.

Although some studies have explored the influence of eruption source parameters (Section 1.3), they focus on a limited set of parameter values and there are limited studies that include interactive sulfur chemistry and aerosol microphysics. Consequently, the individual and combined effects of eruption source parameters on radiative forcing are not fully understood.

Stratospheric volcanic sulfate aerosol is eventually deposited to the surface and can be incorporated into polar ice. Ice core sulfate records provide a comprehensive record of volcanism with annual resolution and are used to reconstruct volcanic radiative forcing on millennial timescales (e.g. Gao et al., 2008; Crowley and Unterman, 2013; Toohey and Sigl, 2017). However, translating measured sulfate concentrations in Greenland and Antarctic ice cores to a global radiative forcing is highly uncertain, with assumptions needed to estimate the sulfate aerosol burden, and for the aerosol size, eruption latitude, injection height, and eruption season (Section 1.4). Because of uncertainties in the potential eruption source parameters and self-limiting radiative effects, there is significant uncertainty in the radiative forcing derived for historic eruptions that has not been assessed. Reconstructions of radiative forcing are essential for understanding the variability of past climate (e.g. Hegerl et al., 2007; Crowley et al., 2008; Sigl et al., 2015) therefore the uncertainty has implications for assessing the role of volcanism, especially in relation to other climate forcing agents such as solar radiation, greenhouse gases, anthropogenic aerosols and clouds (e.g. Hansen et al., 2005; Atwood et al., 2016).

The primary focus of this research is to disentangle and quantify the effects of eruption source parameters on radiative forcing and ice sheet sulfate deposition in order to understand the impact of past explosive volcanism and the potential impact of future eruptions. Similarly, understanding these relationships is also important to assess the impact of sulfate climate geoengineering, of which explosive volcanic eruptions are the natural analogue. By using a state-of-the-art interactive aerosol microphysics model, the chemical and physical evolution and radiative forcing of volcanically-enhanced stratospheric sulfate aerosol are investigated.

1.2 Stratospheric sulfate aerosol

The stratospheric aerosol layer or 'Junge layer' is a quasi-stationary layer between roughly 15 km and 25 km (Junge et al., 1961) that is composed mostly of aqueous sulfuric acid solution droplets (H_2SO_4-H_2O), commonly referred to as sulfate aerosol (Kremser et al., 2016). Under nonvolcanic conditions, the aerosol is maintained mainly by tropospheric emissions of sulfate precursor gases such as SO_2, carbonyl sulfide (OCS) and dimethyl sulfide (DMS) (SPARC, 2006; Kremser et al., 2016) that are transported into the stratosphere from the troposphere through the tropical tropopause layer. The aerosol layer is controlled by the large-scale stratospheric circulation, isentropic mixing (rapid mixing along lines of constant potential temperature), particle sedimentation and removal of particles at the bottom of the layer and evaporation of the particles at the top of the layer (SPARC, 2006). A comprehensive review of stratospheric aerosol has been conducted by Kremser et al. (2016).

1.2.1 Stratospheric transport

Strong zonal winds in the stratosphere result in aerosol circulating the globe in a matter of weeks (Bluth et al., 1992). The vertical and meridional transport of aerosol is controlled by the Brewer-Dobson Circulation (BDC), which is a large-scale residual circulation that includes upwelling at the tropics, poleward transport and descent at the poles (Holton et al., 1995; Butchart, 2014). It is a wave-driven circulation, arising due to momentum from breaking Rossby and gravity waves and is seasonally dependent with stronger transport towards the winter hemisphere, and strong descent over the winter polar vortex (Holton et al., 1995). The meridional transport includes two-way quasi-horizontal mixing in the midlatitudes via isentropic surfaces, in what is referred to as the 'surf zone', which is most pronounced in the winter hemisphere (Holton et al., 1995; Haynes and Shuckburgh, 2000).

Meridional mixing between the tropics and midlatitudes is restricted due to the presence of a subtropical transport barrier around 15 to 30° latitude and between roughly 21 and 30 km, known as the 'leaky tropical pipe' (Plumb, 1996; Neu and Plumb, 1999). The barrier leads to the formation of a tropical aerosol reservoir that builds up following tropical eruptions (Trepte and Hitchman, 1992). A further meridional transport barrier exists at the edge of the winter polar vortex (e.g. SPARC,

2006). These barriers arise from strong gradients in potential vorticity (e.g. Niemeier and Schmidt, 2017).

The strength and location of the subtropical barrier and meridional transport is strongly modulated by the phase of the QBO (e.g. Punge et al., 2009). During the easterly phase, the barrier is stronger, there is increased ascent within the tropical pipe, and meridional transport is weaker. In contrast, during the westerly phase the tropical pipe is widened and there is stronger transport to the poles (e.g. Hitchman et al., 1994).

The BDC is commonly split into faster shallow branches that exist below the tropical pipe in which transport occurs all year to both hemispheres, and a slower deeper branch that describes the stronger mass transport to the winter hemisphere (Plumb, 2002; Butchart, 2014). An overview of the stratospheric circulation is shown in Figure 1.2. In general the stratospheric circulation can be split into four regimes; the polar winter vortex, the surf zone, the tropical pipe and the summer hemisphere.

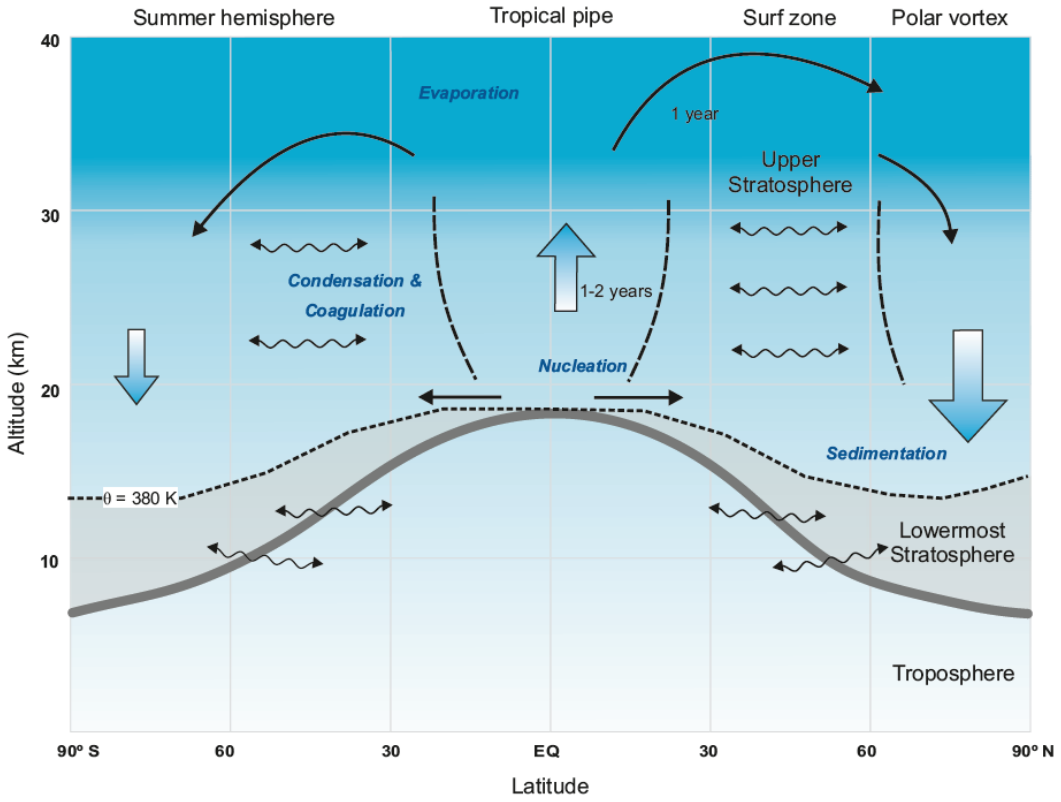

Figure 1.2: Latitude-altitude cross section for NH summer showing the zonal mean stratospheric circulation. The shaded area marks the lowermost stratosphere where isentropic surfaces span the tropopause. The dark grey line marks the tropopause. Wiggly arrows depict transport along isentropes. Arrows represent mean circulations and transport barriers are shown by dashed lines. Transport barriers in the tropics mark the edges of the 'leaky tropical pipe' (Plumb, 1996) and in the NH the edge of the polar vortex. Key microphysical processes are displayed in italics. Figure adapted from Holton et al. (1995) and Bönisch et al. (2011).

Exchange of material between the stratosphere and troposphere occurs via isentropic transport when isentropic surfaces intersect the tropopause, through cross-isentropic transport during ascent in the tropical pipe, and cross-isentropic transport during descent in the polar vortex. Stratosphere-troposphere exchange also occurs via tropopause folds in the extratropics that are intrusions of stratospheric air into the troposphere (e.g. Shapiro, 1980), which are considered to be the dominant removal process for stratospheric aerosol (SPARC, 2006).

The mean residual circulation is relatively slow compared to the isentropic mixing and aerosol reaching the stratosphere via the tropical pipe, which is subsequently transported globally, may reside in the stratosphere for years. Rapid isentropic mixing outside of the tropical pipe, tropospheric folds, and polar descent, results in a much shorter lifetime on the order of months for aerosol introduced into the stratospheric mid- to high-latitudes (e.g. Kremser et al., 2016).

1.2.2 Sulfur chemistry and aerosol microphysics

In the stratosphere SO_2 has a lifetime of several weeks (e.g. Bluth et al., 1992), with oxidation to H_2SO_4 occurring primarily by reaction with OH. Sulfur reactions included in the model used in this thesis are listed in Table A.2. New sulfate aerosol particles are formed by binary homogeneous nucleation in which H_2SO_4 and H_2O condense to form H_2SO_4-H_2O droplets. Binary homogeneous nucleation of new aerosol particles occurs when the vapours are supersaturated (exceeding the equilibrium vapour pressure) with respect to the solution droplet (Seinfeld and Pandis, 2016). H_2SO_4 vapour is also converted to liquid H_2SO_4 via condensation (heterogeneous nucleation) onto existing sulfate particles, and can also condense onto ions or meteoric smoke particles (Kremser et al., 2016).

The aerosol particles are in equilibrium with the water vapour and therefore grow and shrink by the uptake or evaporation of water depending on the temperature and relative humidity. In the lower stratosphere, the aerosol particles also grow by the condensation of H_2SO_4 because the partial pressure of H_2SO_4 exceeds its equilibrium vapour pressure over H_2SO_4-H_2O solution droplets. However, in the upper stratosphere above ~ 35 km where temperatures are higher and the H_2SO_4 and H_2O partial pressures are low, the H_2SO_4-H_2O droplets can evaporate completely (Carslaw et al., 1997; Hamill et al., 1997; SPARC, 2006). H_2SO_4 vapour can then nucleate and

re-condense during descent at high latitudes. Photolysis of H_2SO_4 vapour produces SO_2, which is transported via the BDC to the poles. In the absence of OH, a reservoir of SO_2 builds up in the polar winter, which is subsequently oxidized during polar spring, and results in new sulfate particle formation (Mills et al., 2005). Aerosol particles grow further by coagulation and eventually sediment out of the atmosphere.

Aerosol size and number concentrations can vary over several orders of magnitude and therefore an aerosol population is described using an aerosol size distribution (e.g. Seinfeld and Pandis, 2016). The size distribution is essential for understanding how the aerosol impacts radiation, chemistry, cloud properties and aerosol lifetime. Aerosols are typically split into several size categories, known as 'modes' that are best represented by log-normal distributions. These include a nucleation mode with particles less than ~0.01 µm in diameter, an Aitken mode with particles in the size range ~0.01 to ~0.1 µm, an accumulation mode from ~0.1 to ~2.5 µm and a coarse mode with particles greater than ~2.5 µm in diameter (Seinfeld and Pandis, 2016). A typical distribution of the size modes against the aerosol volume is shown in Figure 1.3. The size ranges in the aerosol model used in this thesis are listed in Table A.3.

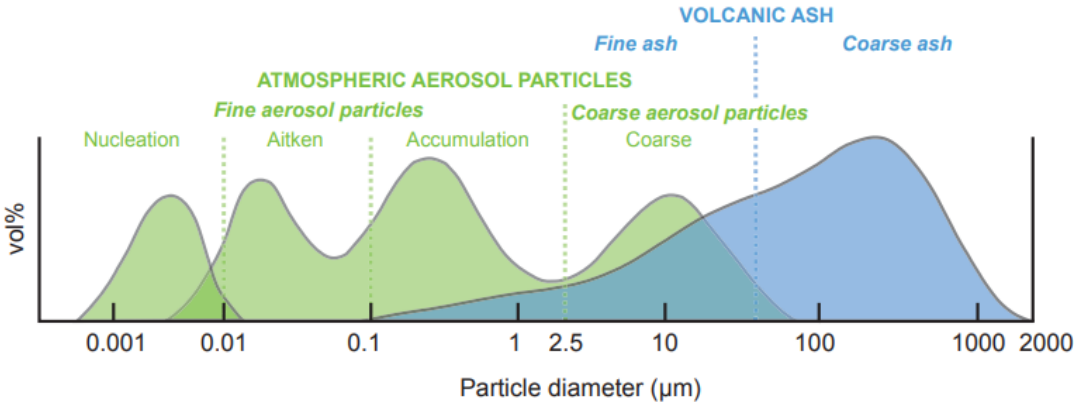

Figure 1.3: Aerosol size distribution of volcanic particles. Figure from Durant et al. (2010).

Nucleation of new sulfate aerosol particles increases the number concentration in the nucleation mode. Condensation of gaseous H_2SO_4 and water uptake leads to growth to Aitken sized particles. High concentrations of smaller particles favours coagulation and with continued condensation, particles grow to the accumulation size, the mode in which the majority of volcanic sulfate aerosol resides. Continued growth leads to coarse-mode aerosol, but these particles are most efficiently removed by gravitational

settling (sedimentation). Sedimentation complicates the transport of sulfate aerosol, acting in addition to the large-scale stratospheric circulation and meridional mixing. Similarly, upwelling following LW absorption also alters the transport of aerosol. Aerosol lifetime following large explosive eruptions is explored in Chapter 3.

Once in the troposphere, aerosols may be removed by dry deposition or wet deposition, either by nucleation scavenging or impaction scavenging. These processes are described in Appendix A.3 as part of the model description.

1.2.3 Radiative forcing

Scattering and absorption of radiation by aerosols assumed to be spherical can be calculated by Mie theory. The scattering and absorption are functions of the wavelength of incident radiation, particle size and the complex refractive index, which describes the particle optical properties (Seinfeld and Pandis, 2016). The sum of scattering and absorption is the extinction, which is the total attenuation of incident radiation. Properties used to diagnose the radiative effects of aerosol in addition to extinction include the single-scattering albedo (SSA), which is the ratio of scattering to the extinction, the asymmetry parameter, which describes whether more light is scattered in the forward or backward direction, and the aerosol optical depth (AOD), which is the vertical integral of extinction.

Extinction is most efficient per unit mass when particles are similar in size to the wavelength of incident radiation. Small volcanic aerosols in the nucleation and Aitken modes have a negligible scattering effect so must first grow to optically relevant sizes in the accumulation mode. For a given mass of sulfate aerosol, the SW radiative forcing is strongly dependent on the aerosol size distribution commonly described by the effective radius (R_{eff}). The R_{eff} is the area-weighted mean radius of an aerosol distribution (calculated as 3 times the total volume concentration divided by the total surface area concentration). The SW forcing (per unit mass) decreases as the R_{eff} increases from ~0.2 μm. In contrast, the LW forcing (per unit mass) is relatively independent of R_{eff} at radii relevant for volcanic aerosol (~0.2 to 2 μm) (Lacis, 2015). SW forcing by sulfate aerosol is therefore proportional to the aerosol surface area and LW forcing proportional to the aerosol mass. If R_{eff} is greater than ~2 μm, the LW forcing can exceed the SW forcing, resulting in surface warming (Lacis et al., 1992). The magnitude of stratospheric heating and subsequent aerosol lofting is also dependent on the vertical distribution of aerosol, since the heating depends on the

temperature of the stratosphere and whether the LW absorption (by either solar near infrared or terrestrial radiation) exceeds the local LW emission (Stenchikov et al., 1998; Robock, 2000; Lacis, 2015). The LW forcing also depends on the surface albedo and the presence of cloud below the aerosol layer (e.g. Stier et al., 2007).

1.3 Previous modelling studies of eruption source parameters

1.3.1 SO_2 emission magnitude

Several studies using models with size-resolved aerosol microphysics have demonstrated the self-limiting radiative effects of large SO_2 injections due to an increase in the aerosol particle size distribution (Pinto et al., 1989; Timmreck et al., 2009; 2010; English et al., 2013; Arfeuille et al., 2014; Metzner et al., 2014). However, studies are mostly based on tropical Pinatubo-like eruption scenarios and the non-linearity in radiative impacts with increasing SO_2 mass is model dependent. For example, English et al. (2013) showed that for an eruption 100 times that of 1991 Mt. Pinatubo, the global mean AOD (at 525 nm) was only 20 times higher. Conversely, also for an eruption ~100 times that of Pinatubo, Timmreck et al. (2010) simulated a larger peak global mean AOD (525 nm) of 4.0 compared to 2.5 in English et al. (2013). The two studies also found differences in the duration of the radiative effects. English et al. (2013) emitted slightly more SO_2 than Timmreck et al. (2010) (1000 Tg S vs. 850 Tg S) and included van der Waals forces in the model coagulation scheme, which results in larger particles. Timmreck et al. (2010) also included aerosol heating, which English et al. (2013) suggested could result in smaller R_{eff} and a larger AOD because the aerosol would be more quickly dispersed from the tropics following an increase in upwelling. A further difference in the two studies is the aerosol microphysics scheme used. Timmreck et al. (2010) used a modal scheme, with prescribed mode widths, whereas English et al. (2013) used a sectional bin scheme in which the aerosol is represented by discrete size bins. The representation of aerosol in either modal or sectional schemes can affect the evolution of the aerosol size distribution (Weisenstein et al., 2007; Kokkola et al., 2009; Mann et al., 2012), but the more sophisticated sectional schemes are more computationally expensive. Even so, modal schemes are capable of reproducing aerosol properties in agreement with sectional schemes (e.g. Mann et al., 2012) and which compare well to observations

including simulations following the 1991 eruption of Mt. Pinatubo (Niemeier et al., 2009; Toohey et al., 2011; Dhomse et al., 2014; Mills et al., 2016; 2017).

Metzner et al. (2014) simulated tropical eruptions with a large range of SO_2 emissions from ~0.5 Tg SO_2 to ~700 Tg SO_2 and found a linear relationship between emission and peak global mean AOD for SO_2 injections less than ~5 Tg SO_2, and a non-linear relationship for larger emissions that could be approximated by a 2/3 power scaling of aerosol mass. Volcanic forcing reconstructions that calculate visible AOD from estimated sulfate mass (Section 1.4) often use a 2/3 power scaling for large eruptions to account for a reduced scattering efficiency due to the formation of larger particles and lower number concentrations because of preferential condensation (over nucleation) and coagulation (e.g. Crowley and Unterman, 2013; Toohey and Sigl, 2017). Conceptually, this idealized relationship arises because visible AOD is proportional to the total cross-sectional area of the aerosol particles, whereas the aerosol mass is proportional to the volume of the particles (Arfeuille et al., 2014; Toohey et al., 2016b). However, the non-linear scaling is highly uncertain and is applied to large eruptions defined above some threshold, which varies between studies. For example Crowley and Unterman (2013) apply the power scaling for eruptions greater than 1991 Mt. Pinatubo (~10-20 Tg SO_2) but Toohey et al. (2016b) for eruptions greater than 1815 Mt. Tambora (~60 Tg SO_2).

1.3.2 Eruption latitude and injection height

The lifetime of stratospheric aerosol increases with distance from the tropopause and is longer for aerosol at the equator because it can be spread globally by the BDC (e.g. Robock, 2000). In the tropics, the injection height of the SO_2 emissions can affect the level of tropical confinement within the tropical pipe, whether it is transported by the upper or lower branches of the BDC, and subsequently the timing of cross-tropopause transport. Several studies have conducted sensitivity tests for specific tropical eruptions (e.g. 1815 Tambora and 1257 Samalas) and found higher altitude emissions resulted in stronger extratropical transport in the middle stratosphere (Arfeuille et al., 2014; Stoffel et al., 2015) and a stronger hemispheric asymmetry in aerosol burden due to the seasonally-varying BDC (Stoffel et al., 2015). Aquila et al. (2012) also demonstrated in simulations of a Pinatubo-like eruption that higher injection heights resulted in longer aerosol lifetime due to transport in the middle stratosphere, whereas injection into the lower stratosphere resulted in faster aerosol removal. Aquila et al.

(2012) also showed that the inclusion of radiatively-coupled aerosol was necessary to loft the aerosol to higher altitudes, which increased meridional mixing, although the amount of heating and whether subsequent lofting was significant to move the aerosol to the middle stratosphere was dependent on the mass of SO_2 emitted. Toohey et al. (2016a) also found that a higher injection height for eruptions at 42ºN (~24 km vs. ~16 km) resulted in a longer aerosol lifetime.

The importance of radiatively-coupled aerosol and the QBO on the level of tropical confinement of sulfate aerosol have been demonstrated in several geoengineering studies in which SO_2 is continuously emitted at the equator (Niemeier et al., 2011; Niemeier and Schmidt, 2017; Tilmes et al., 2017; Kleinschmitt et al., 2018; Visioni et al., 2018). These studies illustrate that the role of injection height is complicated by the level of tropical upwelling and tropical confinement and by subsequent particle growth, often with opposite effects. For example, higher injections into the tropical pipe led to a larger tropical burden due to increased tropical confinement and reduced meridional transport, and a larger global mean radiative forcing (e.g. Niemeier et al., 2011; Niemeier and Timmreck, 2015). However, particle growth can reduce the forcing compared to a lower altitude injection (e.g. Tilmes et al., 2017; Kleinschmitt et al., 2018). The impact of injection height depends on exactly where the aerosol forms in relation to the tropical pipe and whether upwelling leads to increased confinement or increased meridional transport in the upper branch of the BDC, with effects subsequently complicated by aerosol microphysics. Particle growth was not included by Aquila et al. (2012), although the microphysics surrounding a continuous injection with a constant supply of SO_2 or H_2SO_4 vapour differs compared to a single volcanic injection, for example by favouring nucleation (e.g. Niemeier et al., 2011).

Since aerosol is rapidly zonally homogenized in the stratosphere, the longitude of an eruption is not a factor in determining its climatic impact (Toohey et al., 2011). However, the latitudinal-dependent stratospheric dynamics (Figure 1.2) result in a strong dependency of aerosol transport and lifetime, and subsequently the amount of polar sulfate deposition, on the latitude of eruption. However, there have been limited studies that have quantified the change in radiative forcing and deposition following eruptions across a range in latitudes, with studies focusing either on tropical (Toohey et al., 2011; Aquila et al., 2012; Toohey et al., 2013; Stoffel et al., 2015) or high-latitude eruptions (Oman et al., 2005; 2006; Kravitz and Robock, 2011; Pausata et al., 2015) in isolation.

In a study of historical eruptions since 1600, Arfeuille et al. (2014) found that higher-latitude eruptions lead to smaller R_{eff} than tropical eruptions, which they suggested was because larger aerosol particles in the tropics were relatively longer lived due to upwelling, but they did not include aerosol radiative heating nor a QBO in their simulations.

Jones et al. (2017) investigated the change in aerosol distribution for a range of eruptions with latitudes between 60°S and 60°N and for injection heights of 11-15 km, 16-23 km and 23-28 km. Results demonstrated an increased hemispheric confinement and shorter lifetime of aerosol for the higher latitude eruptions, and greatest global spread and highest AOD for the highest altitude injections. However, the study is limited by the lack of size-resolved aerosol microphysics, such that changes to scattering and sedimentation efficiencies were not included.

Toohey et al. (2016a) examined the influence of eruption latitude on polar sulfate deposition in order to find possible candidate locations for two eruptions that occurred in 536 CE and 540 CE that matched sulfate deposition derived from ice cores (Section 1.4). They simulated a range of eruptions between 4ºS and 56ºN, with results suggesting that the 536 CE eruption could have been at a latitude of 46ºN or 56ºN (both latitudes produced similar radiative forcing) and the 540 CE eruption at a latitude near to 15ºN. This was the first study to comprehensively assess the impact of multiple eruption source parameters on sulfate deposition (the study also included perturbations to SO_2 emission, height and season), but is specific to these two eruption case studies with an otherwise limited range in latitude, height and emission magnitude scenarios. This study also lacked a QBO and although the model has been shown to simulate well the observed spatial patterns in sulfate deposition compared to ice core records for several major eruptions, the magnitude of the simulated sulfate deposition was roughly 5 times too large (Toohey et al., 2013; Sigl et al., 2014).

Toohey et al. (2016a) also demonstrated that extratropical eruptions can still lead to significant surface cooling comparable to that from tropical eruptions in contrast to Schneider et al. (2009) who suggested that extratropical eruptions have only a short lived climatic impact. Observational studies have also demonstrated that some SO_2 injected into the lower stratosphere at high-latitudes can be transported to the tropics where it can be spread globally (Kremser et al., 2016 and references therein). It remains an open question as to how high the latitude of an eruption could be and still

have a global climatic impact that rivals that from tropical eruptions given differences in injection height and the mass of SO_2 emitted.

1.3.3 Eruption season

The seasonal dependence of stratospheric dynamics (Section 1.2.1) strongly affects the cross-equatorial transport of stratospheric aerosol and the preferential transport towards the winter hemisphere has been demonstrated by several studies of tropical eruptions using General Circulation Models (GCMs) (Toohey et al., 2011; Aquila et al., 2012; Toohey et al., 2013; Stoffel et al., 2015; Stevenson et al., 2017) and parameterized transport models (e.g. Ammann et al., 2003; Gao et al., 2008).

In the high latitudes transport is modulated by the stratospheric winds (e.g. Timmreck and Graf, 2006), the strength of meridional mixing and the polar vortex (e.g. Holton et al., 1995), and the climatic impacts of eruptions have a strong sensitivity to season because of varying insolation (e.g. Kravitz and Robock, 2011). Photolysis is stronger in the summer resulting in higher OH concentrations and a faster conversion of SO_2 to H_2SO_4 vapour after summer eruptions (e.g. Schmidt et al., 2010). Kravitz and Robock (2011) demonstrated the role of seasonally-varying insolation on the radiative forcing of NH high-latitude eruptions with SO_2 emissions between 1.5 and 5 Tg, and found only summer eruptions of 5 Tg SO_2 led to detectable effects on surface temperature. Despite simulations having similar AOD perturbations between eruptions in March, June and August, June eruptions had larger peak SW radiative forcing. Both the AOD and radiative forcing following an eruption in December were very small compared to the other seasons. Kravitz and Robock (2011) also showed seasonally varying deposition rates with higher deposition in the midlatitude storm tracks during spring and summer and higher deposition near 30°N during the winter because of large-scale subsidence. However, this study used a fixed aerosol dry radius of 0.25 μm and hence changes in particle size and subsequent radiative effects were not included.

Toohey et al. (2011) investigated the radiative forcing of tropical eruptions with different emission magnitudes and eruption seasons using a global aerosol model and found the season to influence the aerosol size distribution as well as the aerosol transport. The smallest R_{eff} and largest radiative forcing occurred for a January eruption if the SO_2 injection was 17 Tg (comparable to 1991 Mt. Pinatubo), but for a July eruption if the mass of SO_2 emitted was 700 Tg (a near super-eruption). In both

cases, the smaller particles were found to coincide with aerosol mass being shifted to higher altitudes, either as a result of seasonal changes in tropical upwelling (in the 17 Tg case) or dynamically induced changes in zonal winds and tropical upwelling because of aerosol heating. The mechanism leading to smaller particles remains uncertain. This study demonstrates the combined effects of different parameters but was limited by the lack of a simulated QBO and a single injection height (~24 km), which may affect the reported sensitivities to season and SO_2 emission.

In a further study, Toohey et al. (2013) investigated the sensitivity of polar sulfate deposition to the eruption season (January vs. July eruptions) and SO_2 emission magnitude (8.5 Tg – 700 Tg) following tropical eruptions at 15ºN. Model results suggested that the sulfate deposition efficiency to the ice sheets (defined as the ratio of sulfate deposition flux to the maximum hemispheric stratospheric sulfate burden) was sensitive to season once the injection was greater than 17 Tg, with higher efficiencies on both ice sheets for July eruptions. These efficiencies are equivalent to the transfer functions used to estimate aerosol burdens from ice-core-derived sulfate deposition (Section 1.4). For Greenland, the higher efficiencies occurred in July because deposition was similar between the seasons but in January the NH burden was larger because of the BDC. In contrast, the SH burdens were relatively insensitive to the eruption month, but the deposition on Antarctica was higher for July eruptions. Aerosol heating led to strong dynamical anomalies and stronger polar vortices following the larger eruptions, which impeded transport to the high latitudes. Subsequently, deposition efficiencies were modulated by the magnitude of the dynamical anomalies combined with the decay of the sulfate aerosol, both of which were dependent on the magnitude of the SO_2 emission because of increases in particle size. Greenland deposition was also higher than Antarctica deposition and the relationship between the two increased nonlinearly with increasing SO_2 emission. The higher Greenland deposition was attributed to both the NH injection location and stronger NH meridional circulation, although Sigl et al. (2014) using the same model and simulation set-up, found that Antarctic sulfate deposition was not significantly different for eruptions located at 4ºS compared to the simulations at 15ºN.

Toohey et al. (2013) also found that the largest eruptions (>700 Tg) during NH winter resulted in Greenland deposition that was 5 times the Antarctic deposition. The results also showed that different eruption magnitudes in different seasons (170 Tg in July vs. 300 Tg in January) led to similar Antarctic deposition fluxes. Consequently, these

results highlight the uncertainties in translating measured ice core sulfate to atmospheric sulfate burdens given an unknown season of eruption and varying SO_2 emissions.

1.3.4 Summary and research gap

Despite several studies of the radiative effects of different explosive eruptions, there has been no systematic assessment of multiple eruption source parameters in one model. The radiative forcing of an eruption is dependent not only on each parameter, but also on their specific combination. Studies have investigated parameter effects in isolation and focused mainly on tropical 'Pinatubo-like' eruption scenarios, with a limited number of SO_2 emission magnitudes, injection heights and latitudes that have been investigated. Inter-model results are difficult to compare due to differences in the values of parameters perturbed and how SO_2 emissions are implemented in each model. For example, studies differ in the depth of the injection plume perturbed, ranging from single grid box injections (e.g. Toohey et al., 2016a), to plumes greater than 21 km in height (Stoffel et al., 2015). The inclusion of aerosol microphysical processes, highly-resolved stratospheric dynamics and radiatively-coupled aerosol in models is a necessity if the effects of these parameters are to be comprehensively investigated (e.g. Timmreck et al., 2018). However, not all studies have included size-resolved aerosol (Oman et al., 2006; Kravitz and Robock, 2011; Aquila et al., 2012; Jones et al., 2017), many lack a QBO (Toohey et al., 2011; English et al., 2013; Toohey et al., 2013; Arfeuille et al., 2014; Toohey et al., 2016a) or lack aerosol-induced radiative heating (English et al., 2013; Arfeuille et al., 2014; Dhomse et al., 2014).

1.4 Reconstructions of historic volcanic radiative forcing

Reconstructions of volcanic eruptions are needed as input datasets in GCMs, either as SO_2 emissions if the model is coupled to a sulfur chemistry and aerosol microphysics scheme, or as a prescribed dataset of spatially and temporally evolving stratospheric AOD (sAOD) or radiative forcing (Schmidt et al., 2011). Since aerosol microphysics schemes are computationally expensive, many models remain uncoupled when conducting long historic climate simulations.

SO_2 emissions, sulfate burdens and/or AOD can be derived from satellite retrievals (e.g. Carn et al., 2016) and ground-based optical measurements when available (Sato et al., 1993; Stothers, 1996; Stenchikov et al., 1998; Stothers, 2001; Thomason et al., 2018), although uncertainties exist because of limited spatial coverage of observations and saturation of the satellite sensors under high aerosol loading (e.g. Antuna et al., 2002; Arfeuille et al., 2013; Kremser et al., 2016). Information regarding the climatic impact of historical eruptions before the availability of modern instruments can be derived from temperature proxy reconstructions (e.g. Briffa et al., 1998; Esper et al., 2013; Sigl et al., 2015; Schneider et al., 2017), historical records (e.g. Ludlow et al., 2013; Sigl et al., 2015; Toohey et al., 2016a) and documented optical phenomena such as sunsets and the visibility of sunspots (Stothers, 1984). Early indices of past volcanism such as the Dust Veil Index by Lamb (1970) and Mitchell (1970) were based on these combined sources of information along with optical measurements when available. The mass of sulfur emitted by an eruption can also be estimated from petrological and geochemical studies of eruption deposits (e.g. Devine et al., 1984; Metzner et al., 2014; Vidal et al., 2016). However, these are limited datasets with large uncertainties and the most valuable source of information regarding historical volcanism comes from sulfate measured in ice cores (e.g. Hammer et al., 1980; Clausen and Hammer, 1988; Robock and Free, 1995; Zielinski, 1995; Robertson et al., 2001), which provide millennial records of volcanism with high temporal resolution due to annual layering (e.g. Sigl et al., 2015).

However, transfer functions are necessary to convert the sulfate deposited on ice sheets to stratospheric sulfate burdens and/or estimates of the sAOD and radiative forcing. These transfer functions are derived from observations of the relationship between the sulfate deposited on ice sheets and sulfur burden or sAOD following the 1991 eruption of Mt. Pinatubo (e.g. Gao et al., 2007; Crowley and Unterman, 2013),

from the relationship between radioactive material in the atmosphere and that deposited on the ice sheets following nuclear weapons testing in the 1950s and 1960s (e.g. Clausen and Hammer, 1988), and from climate model simulations (Gao et al., 2007). It is not known whether these transfer functions are robust, particularly for larger eruptions (e.g. Toohey et al., 2013, Section 1.3.3). Additionally, atmospheric variability can also impact the relationship between stratospheric loading and sulfate deposition (Toohey et al., 2013). Furthermore, ice core measurements are not evenly distributed over the ice sheets, and deposition varies spatially due to local accumulation rates, meteorology and snow drift, resulting in different estimates of ice sheet deposition depending on the ice cores used and how they are weighted to form a regional average or 'composite' (e.g. Cole-Dai et al., 1997; Zielinski et al., 1997; Cole-Dai et al., 2000; Gao et al., 2006; 2007; Stoffel et al., 2015).

It is also difficult to determine whether the sulfate deposited is from tropospheric aerosol, for example from local effusive eruptions, which will not have a large global climate impact compared to stratospheric-injecting eruptions, but could result in large deposition signals. Some attempts have been made to differentiate stratospheric sulfate from tropospheric sulfate based on isotopic anomalies (e.g. Baroni et al., 2007; 2008; Lanciki et al., 2012) but the applicability of this method has not been fully demonstrated and is subject to discussion.

Finally, there are uncertainties in the dating of ice cores, which affect the reconstructions and also the attribution of ice core signals to known eruptions, often used as volcanic 'tie points' for synchronization of multiple ice core records. For example, a large sulfate signal in the mid-15th century was originally assigned to an eruption in 1452/53 of Kuwae in Vanuatu (Gao et al., 2006) but was re-dated to 1458 following new high-resolution ice core records (Plummer et al., 2012; Sigl et al., 2013). Because of a lack of robust evidence such as the inclusion of identified tephra alongside the measured sulfate, this signal is not attributed to Kuwae and is considered unidentified by Toohey and Sigl (2017).

1.4.1 Identifying volcanic sulfur signals in ice cores

Measurements of sulfur, sulfate and total acidity in ice cores can be used to detect volcanic events. Acidity records are less reliable because acids other than sulfuric acid (e.g. nitric, hydrochloric and hydrofluoric acids) can contribute to the measurements and the acids can be reduced by bases (Gao et al., 2006). Volcanic sulfate must be

identified from ice core sulfate measurements that also include sulfate deposited from sea salt and biogenic and anthropogenic sources (e.g. Cole-Dai et al., 1997; Plummer et al., 2012). The sea-salt component is removed based on the measured sodium ion concentration and the ratio between $NaSO_4$ to NaCl in seawater (Robock and Free, 1995). The volcanic contribution to the remaining non-sea-salt total sulfate concentration is derived by using running means and medians (with large volcanic events already removed) and filtering to account for non-volcanic variations, and identifying sulfate peaks which are above background levels (e.g. Langway et al., 1995; Cole-Dai et al., 1997; Traufetter et al., 2004; Castellano et al., 2005; Ferris et al., 2011). Identifying the peaks can be subjective and different statistical detection thresholds are used, commonly based on either the standard deviation (e.g. Delmas et al., 1992; Cole-Dai et al., 1997) or median absolute deviation of the average sulfate concentrations (e.g. Gao et al., 2006; 2008; Sigl et al., 2014). The more conservative extraction criteria will be biased for medium to large events, but the less conservative criteria may identify false volcanic signals as a result of random variability in background concentrations, termed 'false positives' (e.g. Traufetter et al., 2004; Ferris et al., 2011).

Identified volcanic concentrations are integrated over the duration of the volcanic signal to obtain the total sulfate deposited for each eruption (e.g. Traufetter et al., 2004). Sulfate deposition fluxes are calculated from the identified volcanic sulfate concentrations by multiplying by the annual ice accumulation rate (e.g. Gao et al., 2006). Simultaneous spikes in Greenland and Antarctica ice core sulfate concentrations, termed bipolar deposition signals are commonly attributed to tropical eruptions with sulfate recorded only on one sheet attributed to extratropical eruptions (e.g. Crowley, 2000; Ammann et al., 2007; Gao et al., 2008; Toohey et al., 2016a).

1.4.2 Volcanic forcing reconstructions derived from ice cores

The two recommended forcing reconstructions for use in the Palaeoclimate Modelling Intercomparison Project Phase Three (PMIP3) Last Millennium simulations (Schmidt et al., 2011), which are the most commonly used reconstructions were the ice core-volcano index (IVI2) by Gao et al. (2008) and the ice core index (ICI) by Crowley et al. (2008), which is described by Crowley and Unterman (2013). An update to these reconstructions (eVolv2k), provided by Toohey and Sigl (2017) is recommended for

use in the PMIP4 transient simulations (Jungclaus et al., 2017). These forcing series are described below and are shown in Figure 1.4.

1.4.2.1 Gao et al. (2008)

The Gao et al. (2008) reconstruction is based on 54 ice core records from the Arctic and Antarctic and provides a time series of global and hemispheric total sulfate aerosol injections and sulfate aerosol mass as a function of latitude, altitude and month for the years 500-2000 CE. Individual ice core sulfate deposition records were averaged to create Greenland and Antarctic means. Ice cores were weighted to account for spatial variation in sulfate deposition based on the average ratio between individual ice core records and that of the ice sheet mean for 5 low-latitude eruptions (1809 Unknown, 1815 Mt. Tambora, 1883 Krakatau, 1963 Mt. Agung and 1991 Mt. Pinatubo).

Ice sheet deposition was converted to the total mass of stratospheric aerosol formed after each eruption using transfer functions derived by Gao et al. (2007). Two separate functions were derived, one for high-latitude and one for low-latitude eruptions, based on nuclear bomb tests, satellite observations of aerosol mass following the 1991 eruption of Mt. Pinatubo and climate model simulations of the 1783 Laki, 1815 Mt. Tambora, 1912 Mt. Katmai and 1991 Mt. Pinatubo eruptions.

The evolution of the sulfate mass was derived from a simple spatial-temporal transport parameterization scheme (Grieser and Schönwiese, 1999) that simulates transport between the tropics, extratropics and poles. Aerosol mass built up linearly during the first 4 months after an eruption and decreased exponentially with a global mean e-folding time of 12 months. Aerosols were assumed to have the same vertical distribution as observed after 1991 Mt. Pinatubo based on 11 lidar measurements (Antuna et al., 2002).

Stratospheric aerosol mass is commonly converted to mid-visible sAOD using a simple linear scaling such as dividing the mass by 150 Tg as suggested by Stothers (1984) but this does not consider changes to sulfate aerosol particle size (Pinto et al., 1989). sAOD can be scaled to radiative forcing by multiplying it by -20 W m^{-2} as suggested by Wigley et al. (2005), although the conversion factor between the two is uncertain, with previous estimates ranging from -21 W m^{-2} (Hansen et al., 2002) to -30 W m^{-2} (Lacis et al., 1992). A scaling of -25 W m^{-2} per unit of sAOD based on simulations of the 1991 Mt. Pinatubo eruption with the GISS climate model (Hansen et al., 2005) is used in the IPCC AR5 (Myhre et al., 2013). However, recent studies

with other climate models that account for aerosol-cloud interactions suggest that the total volcanic forcing per unit sAOD is roughly 30% smaller than reported by the IPCC AR5 (Gregory et al., 2016; Larson and Portmann, 2016). The relationship between sAOD and radiative forcing is also dependent on the latitude and season of an eruption (Andersson et al., 2015) and the sulfate aerosol particle size distribution (Lacis et al., 1992), which remains unknown for all large-magnitude eruptions other than 1991 Mt. Pinatubo.

1.4.2.2 Crowley and Unterman (2013)

The Crowley and Unterman (2013) or Crowley et al. (2008) reconstruction provides time series of sAOD at 550 nm and R_{eff} for four equal-area latitude bands at a time resolution of ten days over the years 800-2000 CE. It is based on 25 ice core sulfate records. In Greenland ice cores were averaged to create the Greenland composite, but in Antarctica the contributions from each ice core were area-weighted depending on snow accumulation rates.

Ice sheet composites were scaled to peak sAOD at 550 nm based on the relationship between ice sheet sulfate deposition following the Pinatubo and Hudson 1991 eruptions and satellite-observed sAOD from Sato et al. (1993). For eruptions of Pinatubo size and smaller this scaling is linear, but for larger eruptions a 2/3 power scaling is applied (Section 1.3.1).

The temporal evolution of sAOD for different latitude bands following low latitude eruptions is based on that observed after 1991 Mt. Pinatubo with linear increases in sAOD until the peak value followed by a plateau and exponential decay. The temporal evolution for mid to high latitude eruptions is based on the 1912 Novarupta eruption (Stothers, 1996). R_{eff} is estimated from the sAOD to a power of 1/3.

1.4.2.3 Toohey and Sigl (2017)

The eVolv2k reconstruction provided by Toohey and Sigl (2017) includes estimates of the magnitudes of major stratospheric SO_2 injections and monthly zonal mean sAOD timeseries from 500 BCE to 1900 CE. It is based on the most comprehensive array of highly temporally-resolved Antarctic ice cores (Sigl et al., 2014; 2015), revised transfer functions, and sAOD calculated using the Easy Volcanic Aerosol (EVA) forcing generator (Toohey et al., 2016b).

The ice core records include improvements in synchronization and dating (Sigl et al., 2014; 2015), which have resolved previous inconsistencies between volcanic aerosol burdens inferred from ice cores and cooling derived from dendrochronological climate reconstructions (Sigl et al., 2015). Ice core composites for Antarctica are based on between 8 and 17 ice cores that were weighted in the overall average using the spatial variability of deposition (Sigl et al., 2014). Three ice cores were used for the Greenland averages, which were given equal weight. The limited number of ice cores is a source of uncertainty, but individual records were found to be highly correlated with the composites suggesting that a small number of ice cores can represent the large-scale sulfate deposition.

Ice-core-derived composites are scaled to the stratospheric SO_2 injection as in Gao et al. (2007) except transfer functions are assumed to represent the relationship between deposited sulfate and sulfate mass in the stratosphere as opposed to sulfate aerosol as in Gao et al. (2007), which is assumed to contain 25% water by mass.

The EVA forcing generator creates spatio-temporal estimates of the optical properties (including extinction, SSA and asymmetry factor (Section 1.2.3)) of volcanic sulfate aerosol from an initial SO_2 injection. It is a parameterized three-box model of stratospheric transport, with transport and mixing based on sulfate aerosol observed after 1991 Mt. Pinatubo. Sulfate mass is scaled to sAOD and aerosol R_{eff} similar to Crowley and Unterman (2013), with a non-linear 2/3 power relationship between sulfate mass and sAOD for eruptions greater in magnitude than 1815 Mt. Tambora.

1.4.3 Summary and research gap

Ice core records of sulfate are an invaluable source of information regarding past volcanism, but considerable uncertainties remain in translating measured sulfate into stratospheric SO_2 injections, sulfate aerosol mass, sAOD and radiative forcing. The reconstructions are based on scaling the sulfate measured in ice cores, based on observed quantities after the 1991 eruption of Mt. Pinatubo. Although some attempts are made to account for changes to aerosol particle size for larger eruptions, these assumptions remain uncertain. The spatial and temporal evolution of aerosol is also based on either simple parameterized transport schemes and/or of that following the eruption of Mt. Pinatubo.

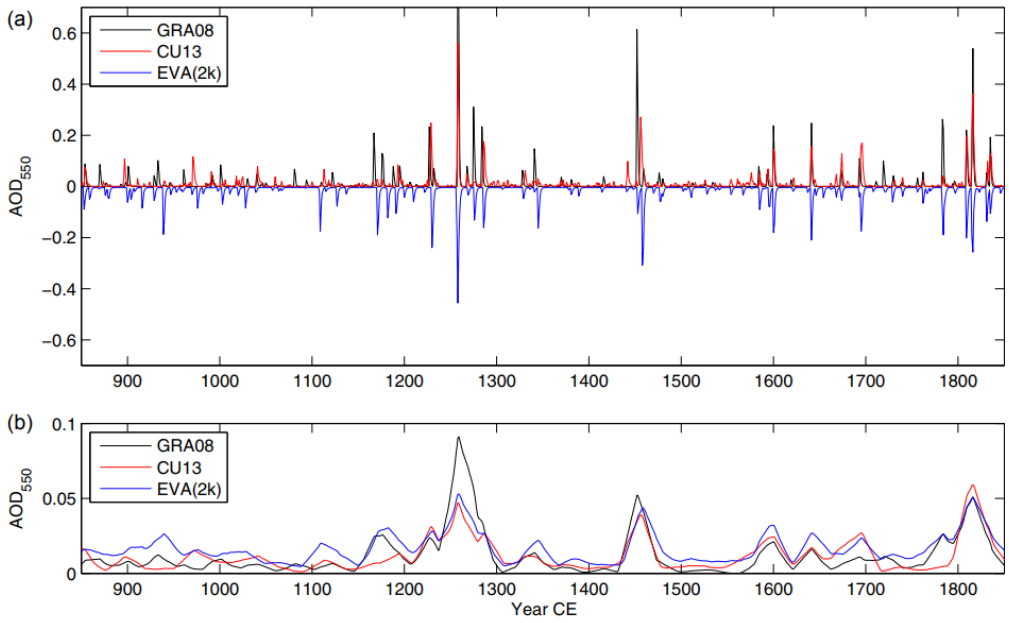

Figure 1.4: Reconstructions of global mean sAOD at 550 nm for years 850-1850 for annual means (a) and a smoothed time series for visualisation (using a 21-year wide triangular filter) (b). Reconstructions include GRA08 (Gao et al., 2008), CU13 (Crowley and Unterman, 2013) and EVA(2k) (Toohey and Sigl, 2017). Figure from Jungclaus et al. (2017).

The reconstructions are broadly in agreement (Figure 1.4) but there are important differences. These include the magnitude of forcing for the largest events (e.g. 1257 Samalas) because of different assumptions in the scaling parameterizations, and differences in the forcing surrounding the 1783-1784 Laki eruption depending on whether the sulfate signal is corrected to account for tropospheric as opposed to stratospheric aerosol (Crowley and Unterman, 2013). Further differences in the earlier parts of the reconstructions arise due to the ice core records used, the identification of events and the ice core age model (Sigl et al., 2015).

Climate model simulations using prescribed reconstructions overestimate the tropospheric cooling following large eruptions compared to tree-ring climate proxies (e.g. Brohan et al., 2012; Zanchettin et al., 2015; Wilson et al., 2016). Possible reasons for the discrepancy include underestimated volcanic cooling derived from tree-ring reconstructions (Anchukaitis et al., 2012; Stoffel et al., 2015; Wilson et al., 2016) and that the modelled forcing is too high (e.g. Marotzke and Forster, 2015), which in turn is related to the uncertainties in the reconstructions presented above, how the forcing is implemented in each model (e.g. as sAOD or radiative forcing and the spatial and temporal resolution) and the model climate sensitivity (e.g. Gregory et al., 2016).

Stoffel et al. (2015) demonstrated that the discrepancy between simulated cooling after the 1815 eruption of Mt. Tambora and that estimated from tree rings is reconciled when using a new temperature reconstruction based on tree-ring width and maximum latewood density, and simulations with a GCM coupled with size-resolved aerosol microphysics. Models with coupled aerosol microphysics modules are necessary to explicitly model stratospheric sulfate aerosol to account for both the self-limiting microphysical processes (Section 1.3.1) but also the influence of stratospheric circulation on the aerosol spatial distribution (Sections 1.3.2-3) (e.g. Toohey et al., 2011; Arfeuille et al., 2014; Stoffel et al., 2015). These models resolve the sulfate aerosol with altitude, which is necessary for simulating the location of stratospheric warming as well as the stratospheric transport (e.g. Arfeuille et al., 2014). The absence of vertically resolved forcing in most reconstructions is a limitation of these prescribed datasets.

However, even in coordinated simulations of the 1815 Mt. Tambora eruption using other climate models with size-resolving aerosol microphysics, simulated sAOD varied considerably (Zanchettin et al., 2016). These simulations are explored further in Chapter 2 with a focus on the sulfate deposition and the implications for reconstructing volcanic aerosol radiative forcing. Finally, microphysical simulations are limited by uncertain eruption source parameters used to initialize the eruptions. Results where eruption source parameters for historical eruptions are derived independently of transfer functions or any scaling between sulfate, sAOD and radiative forcing are presented in Chapter 4.

1.5 Aims and research questions

1.5.1 Summary of research rationale and thesis aims

Large-magnitude explosive volcanic eruptions are important drivers of natural climate variability (Section 1.1) but the evolution of volcanically-enhanced stratospheric sulfate aerosol and its radiative effects are complex (Section 1.2). To understand aerosol evolution and to simulate the radiative impact of eruptions, it is necessary to use GCMs coupled to interactive aerosol microphysics schemes. Eruption source parameters impact the atmospheric response but there has been no systematic study of the interaction of multiple eruption source parameters with an interactive stratospheric aerosol model (Section 1.3). As the SO_2 injection magnitude increases, the radiative forcing scales non-linearly (e.g. Pinto et al., 1989), but exactly how the forcing scales when other eruption source parameters are varied, is unknown. Reconstructions of volcanic radiative forcing derived from ice sheet sulfate deposition are based predominantly on the observed sulfate aerosol burden and sAOD following the 1991 eruption of Mt. Pinatubo (Section 1.4). It is unknown whether the radiative impacts of other historical eruptions evolved similarly to 1991 Mt. Pinatubo, and there have been limited modelling studies that have assessed sulfate deposition following different eruption-realisations. Reconstructions used to drive climate model simulations remain uncertain (e.g. Toohey and Sigl, 2017), and many volcanic sulfate signals in ice cores have not been attributed to specific eruptions (Sigl et al., 2015). Consequently, there is a large gap in our understanding of the effects of eruption source parameters on both radiative forcing and sulfate deposition following large-magnitude explosive eruptions, which this thesis aims to address.

Because interactive stratospheric aerosol models are computationally expensive, the number of simulations that can be run is limited. Therefore the research in this thesis also uses statistical emulation to facilitate a more comprehensive analysis of eruption source parameters. An emulator is a surrogate statistical model that can be used in place of the computationally expensive model. This approach has not been used in studies of volcanic eruptions and their radiative effects before. A detailed description is included in Section 1.6.2.

This thesis has two main aims and the following research questions:

1. **To assess the effect of eruption source parameters including the SO_2 emission, injection height and the eruption latitude and season, on sAOD and radiative forcing.**
    a) Can statistical emulation be used to investigate the sAOD and radiative forcing of large stratospheric-injecting eruptions and to explore the interacting effects of multiple eruption source parameters?
    b) How do individual and combined eruption source parameter perturbations affect the sAOD and radiative forcing of large stratospheric-injecting eruptions?
    c) Which eruption source parameter is more important in determining the radiative response?

2. **To examine the uncertainties in historic volcanic radiative forcing reconstructions based on volcanic sulfate deposited on polar ice sheets.**
    a) How well can models simulate the deposition of sulfate on the ice sheets following a large stratospheric-injecting eruption such as 1815 Mt. Tambora?
    b) How do variations in eruption source parameter values impact the sulfate deposited on polar ice sheets?
    c) How accurately can eruption source parameters be constrained from ice core sulfate records?
    d) How accurately can the radiative forcing of an eruption be constrained from ice core sulfate records?

1.5.2 Research novelty and publication roadmap

This thesis presents the first study to comprehensively investigate and quantify the atmospheric effects of different eruption source parameters, facilitated by a state-of-the-art interactive stratospheric aerosol model and statistical emulation (Section 1.6). Firstly, this thesis examines the sulfate deposition after the eruption of Mt. Tambora in 1815 simulated by four models with size-resolved aerosol schemes and compares to ice core measurements (Chapter 2, Marshall et al., 2018). Secondly, Chapter 3 explores the effects of eruption source parameters on radiative forcing using a perturbed parameter ensemble of hypothetical, yet realistic eruptions in which

different masses of SO_2 are injected into different parts of the stratosphere (Marshall et al., under review). This chapter uses the novel approach of building emulators that describe the covarying effects of the eruption source parameters so that several thousand samples of model output can be estimated. Finally, Chapter 4 examines ice sheet sulfate deposition in the ensemble of simulations and using emulators explores the relationship between ice sheet sulfate deposition, eruption source parameters and radiative forcing (Marshall et al., in prep). The mapping of each publication to the aims and research questions is presented in Figure 1.5.

Figure 1.5: Publication roadmap

1.6 Research approach

To conclude this chapter, the methods used in the three publications are outlined. Further specific details are included in each publication.

1.6.1 Interactive stratospheric aerosol modelling

The research presented in this thesis uses an interactive stratospheric aerosol model (UM-UKCA) composed of the Met Office's Hadley Centre Global Environment Model version 3 (HadGEM3), which is a configuration of the Unified Model (UM) (Davies et al., 2005; Walters et al., 2014), coupled with a whole-atmosphere chemistry scheme (Morgenstern et al., 2009; O'Connor et al., 2014) and the modal version of the GLObal Model of Aerosol Processes (GLOMAP-mode) (Mann et al., 2010). Chemistry and aerosols are specified by the UK Chemistry and Aerosol (UKCA) framework and are simulated online. The model configuration used here includes coupling between aerosol microphysics, atmospheric chemistry, radiation and dynamics. The QBO is internally generated.

GLOMAP-mode is a comprehensive aerosol microphysics model that simulates size-resolved aerosol mass and number concentrations in seven log-normal modes: four soluble modes (nucleation, Aitken, accumulation and coarse) and three insoluble modes (Aitken, accumulation and coarse). It includes the full lifecycle of aerosol comprising primary emissions, nucleation, condensation, coagulation, cloud processing, and wet and dry deposition. It also includes the evaporation of sulfate particles at high vapour pressures (Dhomse et al., 2014) often not included in studies (e.g. Aquila et al., 2012). GLOMAP-mode was developed as a less computationally expensive version of the sectional version, GLOMAP-bin (Spracklen et al., 2005a; 2005b) but is able to reproduce aerosol properties with good comparison to the bin scheme (Mann et al., 2012).

Radiative forcing is calculated as the difference between the top-of-the-atmosphere (TOA) outgoing all-sky net radiative flux (SW+LW) in a simulation with the volcanic perturbation and a control simulation without the volcanic perturbation. This includes the instantaneous radiative forcing arising from aerosols, and rapid adjustments such as changes to clouds, temperature and water vapour, and is therefore defined as an effective radiative forcing (Boucher et al., 2013) (sea-surface temperatures (SSTs) are prescribed). A detailed model description is included in Appendix A.

1.6.2 Gaussian process emulation

1.6.2.1 Overview

Interactive stratospheric aerosol models are computationally expensive, which limits the number of simulations that can be run. An emulator is a surrogate statistical model that can be used in place of the computationally expensive model to increase the number of available simulations. The emulator maps a model output response to a set of input parameters and is used to predict the model output for combinations of the input parameters that were not originally simulated by the model. Emulation is used in Chapters 3 and 4 of this thesis. The input parameters varied are the mass of SO_2 emitted by an eruption and the injection height and latitude of the emissions. The model outputs (e.g. radiative forcing) are each defined as functions of these input parameters, for example:

$$model\ output = f(SO_2\ emission, injection\ height, latitude) \quad (1.1)$$

The emulator is extremely fast to evaluate and can be sampled at thousands of parameter combinations in a matter of seconds. It is then possible to conduct statistical analysis, including variance-based sensitivity analysis, using the emulator predictions. The emulator facilitates analysis that is not feasible using the computationally expensive model alone.

1.6.2.2 Building a Gaussian process emulator

A Gaussian process (GP) is a probability distribution for a function defined by a mean function ($m(.)$) and a covariance function ($c(.,.)$):

$$f(.) \sim GP(m(.), c(.,.)) \quad (1.2)$$

A GP emulator represents the model response as a GP. The emulator is built by combining model output data with prior beliefs about how the model output varies in response to the input parameters. These prior beliefs include information on the form of the model output such as whether it has a constant mean, or a linear trend, or even a quadratic formula (specified by the mean function where hyperparameters specify the coefficients of the mean function), and how smoothly it varies (specified by the covariance function where hyperparameters specify the degree of smoothness in the

response). The hyperparameters of the prior distribution are estimated using information from a specially designed set of data points known as 'training runs', which are the model outputs for a set of simulations of the expensive model. This forms the posterior distribution, which is the emulator. It is a statistical approximation for the model output in that it provides a probability distribution for the function of the input parameters (Eq. 1.1) with a mean prediction that interpolates the model simulated data points and an associated variance measuring the uncertainty in this mean prediction (O'Hagan, 2006).

Figure 1.6 shows examples of GP emulation for a simple function involving one input parameter, x (O'Hagan, 2006). The scatter points show the model output of training runs for different values of x and the solid lines mark the emulator mean prediction. The dashed lines show the uncertainty around the emulator predictions. The emulator mean passes through the data points and is updated as more training runs are included (panels (a) – (c)). At the data points the emulator mean has zero uncertainty and the uncertainty increases away from the data points. As more data points are used to build the emulator, the prediction uncertainty also decreases. In panel (d) different hyperparameters have been used in the GP to represent a lower degree of smoothness of the model output. Consequently, the interpolation becomes less smooth and the uncertainty grows.

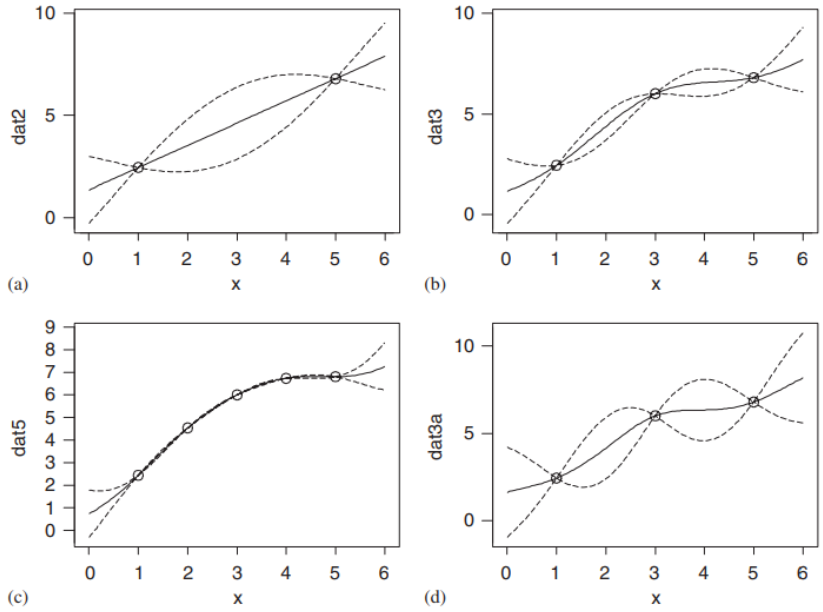

Figure 1.6: Examples of Gaussian process emulation for a simple function. Panels (a)-(c) show the how the emulator mean prediction varies as the number of training points is increased from 2 to 5. Panel (d) shows the emulator mean prediction based on 3 training points but with a different assumption on how smoothly the model output varies. Figure from O'Hagan (2006).

In this thesis, the emulators are built by assuming that the prior distribution has a linear mean function:

$$m(\boldsymbol{x}) = \beta_0 + \beta_1 x_1 + \beta_2 x_2 + \beta_3 x_3 \quad (1.3)$$

where the hyperparameter β_0 is a constant and the hyperparameters β_i are regression coefficients for each of the three input parameters, $x_1, x_2,$ and x_3 (SO_2 emission, injection height and latitude). These coefficients are estimated during the fitting of the emulator. The smoothness of the model output, which describes the degree of correlation between pairs of data points, is specified by the Matérn covariance function. It ensures that input values that are close together in parameter space have similar model outputs. The Matérn covariance function is chosen as it can deal with some departure from the smoothness assumption in the model output, which is likely the case for the model outputs considered in this thesis.

The hyperparameters of the mean and covariance functions are updated using maximum likelihood estimation of the training data to form a posterior GP. The updated mean function provides the estimation of the model output and the updated covariance function provides an estimate of the uncertainty on the predicted model output. Technical statistical details regarding the formation of GP emulators can be found in O'Hagan (1994) and the appendices of Lee et al. (2011) and Johnson et al. (2015). In this thesis the emulators are built using the R package DiceKriging and the function km() (Roustant et al., 2012; R Core Team, 2017).

Although in general the GP emulator is built so that the mean prediction passes through the data points with zero uncertainty, it is also possible to update the emulator fit so that it does not pass directly through the data points. This is useful when there is uncertainty in the model output for example if the model is stochastic. This is often the case of climate model output due to internal variability because changes in the initial conditions could lead to different model output given the same input parameters. An emulator fit that does not need to pass through the data points is achieved by specifying noise variance on each model output when building the emulator (e.g. Salter and Williamson, 2016). This approach is used in Chapter 4.

Once the emulator has been built, it must be validated to assess whether the emulator is a sufficiently good estimate of the actual model output. Validation is conducted by

using the emulator to predict the model output for a set of additional simulations of the expensive model and comparing the emulator predictions and their uncertainty with the actual output. The additional simulations are termed ‘validation runs’. Most of the model output must lie close to the emulator prediction and within the emulator prediction uncertainty bounds.

1.6.2.3 Design of the model simulations

The design of the training runs of the model is important to achieve the maximum amount of information about the model output on which the emulator is built, with a limited number of simulations. Typical experimental designs in which the sensitivity of model output to input parameters is tested often perturb single parameters in so called one-at-a-time (OAT) tests (e.g. Spracklen et al., 2005b), but this leaves much of a multidimensional parameter space unexplored (Saltelli and Annoni, 2010). OAT sampling is also inefficient if one of the input parameters has a weak effect in part of the parameter space as all other simulations which are lined up in this dimension provide no further information. A space-filling factorial analysis can be used where combinations of the parameters are perturbed, but the number of experiments rapidly increases per parameter dimension and, similarly, simulations can be wasted if they are lined up in a part of parameter space where there is a weak parameter effect. An example of these two designs is shown in Figure 1.7a. A better approach is to design simulations that are both space-filling but distributed randomly across the parameter space and an example is shown in Figure 1.7b. In Figure 1.7b each of the simulations has a different value of the three input parameters. It is possible to explore how parameters interact to effect model output and fewer simulations are required than in a factorial design. In this thesis simulations are designed using a ‘maximin’ Latin hypercube (McKay et al., 1979; Morris and Mitchell, 1995), which maximises the minimum distance between sample points in the parameter space. It is based on the Latin square, an example of which is the sudoku puzzle where no row or column can contain the same number (e.g. Lee et al., 2011; Xu et al., 2011).

The number of training runs necessary to represent a complex model is unknown, but a general rule of thumb is to use the number of parameters being explored multiplied by 10 (Loeppky et al., 2009). The number of additional validation runs is set to three times the number of parameters (Bastos and O’Hagan, 2009). In this thesis, two separate maximin Latin hypercubes are used to design the training and validation runs.

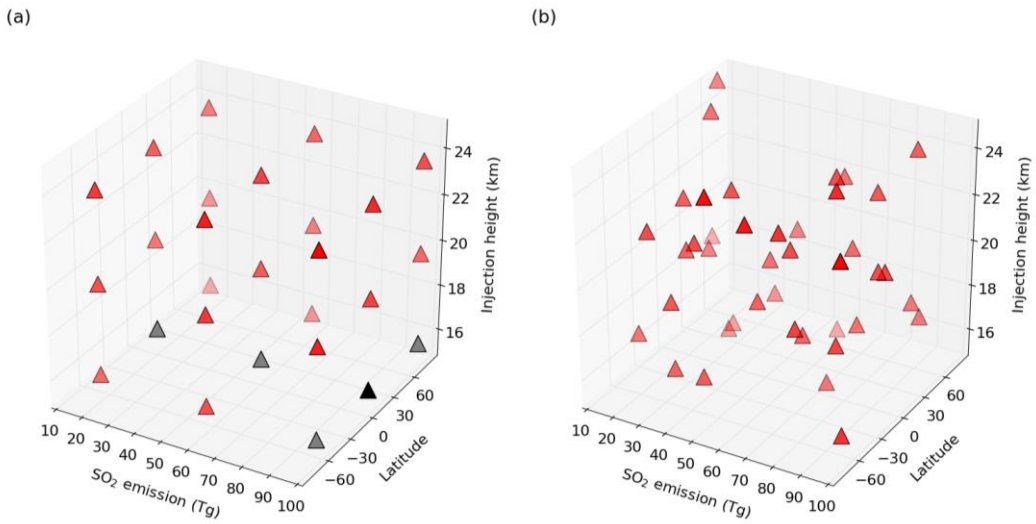

Figure 1.7: Sampling techniques in a factorial experimental design (a) versus Latin hypercube sampling (b). In (a) each triangle represents an experiment as part of a factorial design and the grey triangles show two example OAT tests, each of which is along one dimension departing from a single baseline (black triangle).

1.6.2.4 Sensitivity analyses

Variance-based sensitivity analysis decomposes the total variance in an output into contributions from individual inputs and sets of inputs. In this thesis it is used to evaluate the contributions that different eruption source parameters make to variance in a model output, such as radiative forcing.

The percentage contributions reported in Chapter 3 are calculated using the extended FAST (Fourier Amplitude Sensitivity Test) method (Saltelli et al., 1999), provided in the R package sensitivity (Pujol et al., 2017). The sensitivity analysis provides a main effect variance, which is the percentage of variance that an individual parameter contributes to the total variance, and a total variance which includes the main effect and additional variance due to its interactions with other parameters. The emulator is used to provide a large sample of model output on which the sensitivity analysis is conducted.

1.6.2.5 Emulator constraint

An important application of emulators is that they can be used to constrain the values and combinations of input parameters that result in a known measured value. This concept is known as ‘history matching’ (e.g. Craig et al., 1996; Williamson et al., 2013; 2015; Andrianakis et al., 2017) and is used in Chapter 4 to find combinations of eruption source parameters that produce ice sheet sulfate deposition consistent with ice-core-derived estimates.

References

Ammann, C.M., Joos, F., Schimel, D.S., Otto-Bliesner, B.L. and Tomas, R.A. 2007. Solar influence on climate during the past millennium: Results from transient simulations with the NCAR Climate System Model. *Proceedings of the National Academy of Sciences.* **104**(10), pp.3713–3718.

Ammann, C.M., Meehl, G.A., Washington, W.M. and Zender, C.S. 2003. A monthly and latitudinally varying volcanic forcing dataset in simulations of 20th century climate. *Geophysical Research Letters.* **30**(12), 1657.

Anchukaitis, K.J., Breitenmoser, P., Briffa, K.R., Buchwal, A., Buntgen, U., Cook, E.R., D'Arrigo, R.D., Esper, J., Evans, M.N., Frank, D., Grudd, H., Gunnarson, B.E., Hughes, M.K., Kirdyanov, A.V., Korner, C., Krusic, P.J., Luckman, B., Melvin, T.M., Salzer, M.W., Shashkin, A.V., Timmreck, C., Vaganov, E.A. and Wilson, R.J.S. 2012. Tree rings and volcanic cooling. *Nature Geoscience.* **5**(12), pp.836-837.

Andersson, S.M., Martinsson, B.G., Vernier, J.P., Friberg, J., Brenninkmeijer, C.A.M., Hermann, M., van Velthoven, P.F.J. and Zahn, A. 2015. Significant radiative impact of volcanic aerosol in the lowermost stratosphere. *Nature Communications.* **6**, 7692.

Andrianakis, I., Vernon, I., McCreesh, N., McKinley, T.J., Oakley, J.E., Nsubuga, R.N., Goldstein, M. and White, R.G. 2017. History matching of a complex epidemiological model of human immunodeficiency virus transmission by using variance emulation. *Journal of the Royal Statistical Society: Series C (Applied Statistics).* **66**(4), pp.717-740.

Antuna, J.C., Robock, A., Stenchikov, G.L., Thomason, L.W. and Barnes, J.E. 2002. Lidar validation of SAGE II aerosol measurements after the 1991 Mount Pinatubo eruption. *Journal of Geophysical Research-Atmospheres.* **107**(D14), 4194.

Aquila, V., Oman, L.D., Stolarski, R.S., Colarco, P.R. and Newman, P.A. 2012. Dispersion of the volcanic sulfate cloud from a Mount Pinatubo-like eruption. *Journal of Geophysical Research-Atmospheres.* **117**, D06216.

Arfeuille, F., Luo, B.P., Heckendorn, P., Weisenstein, D., Sheng, J.X., Rozanov, E., Schraner, M., Bronnimann, S., Thomason, L.W. and Peter, T. 2013. Modeling the stratospheric warming following the Mt. Pinatubo eruption: uncertainties in aerosol extinctions. *Atmospheric Chemistry and Physics.* **13**(22), pp.11221-11234.

Arfeuille, F., Weisenstein, D., Mack, H., Rozanov, E., Peter, T. and Bronnimann, S. 2014. Volcanic forcing for climate modeling: a new microphysics-based data set covering years 1600-present. *Climate of the Past.* **10**(1), pp.359-375.

Atwood, A.R., Wu, E., Frierson, D.M.W., Battisti, D.S. and Sachs, J.P. 2016. Quantifying Climate Forcings and Feedbacks over the Last Millennium in the CMIP5-PMIP3 Models. *Journal of Climate.* **29**(3), pp.1161-1178.

Baldini, J.U.L., Brown, R.J. and McElwaine, J.N. 2015. Was millennial scale climate change during the Last Glacial triggered by explosive volcanism? *Scientific Reports.* **5**, 17442.

Baldwin, M.P., Gray, L.J., Dunkerton, T.J., Hamilton, K., Haynes, P.H., Randel, W.J., Holton, J.R., Alexander, M.J., Hirota, I., Horinouchi, T., Jones, D.B.A., Kinnersley, J.S., Marquardt, C., Sato, K. and Takahashi, M. 2001. The quasi-biennial oscillation. *Reviews of Geophysics.* **39**(2), pp.179-229.

Baroni, M., Savarino, J., Cole-Dai, J.H., Rai, V.K. and Thiemens, M.H. 2008. Anomalous sulfur isotope compositions of volcanic sulfate over the last millennium in Antarctic ice cores. *Journal of Geophysical Research-Atmospheres.* **113**(D20), D20112.

Baroni, M., Thiemens, M.H., Delmas, R.J. and Savarino, J. 2007. Mass-independent sulfur isotopic compositions in stratospheric volcanic eruptions. *Science.* **315**(5808), pp.84-87.

Bastos, L.S. and O'Hagan, A. 2009. Diagnostics for Gaussian Process Emulators. *Technometrics.* **51**(4), pp.425-438.

Bekki, S. 1995. Oxidation of volcanic SO2: A sink for stratospheric OH and H2O. *Geophysical Research Letters.* **22**(8), pp.913-916.

Bekki, S., Pyle, J.A., Zhong, W., Toumi, R., Haigh, J.D. and Pyle, D.M. 1996. The role of microphysical and chemical processes in prolonging the climate forcing of the Toba Eruption. *Geophysical Research Letters.* **23**(19), pp.2669-2672.

Bittner, M., Timmreck, C., Schmidt, H., Toohey, M. and Kruger, K. 2016. The impact of wave-mean flow interaction on the Northern Hemisphere polar vortex after tropical volcanic eruptions. *Journal of Geophysical Research-Atmospheres.* **121**(10), pp.5281-5297.

Bluth, G.J.S., Doiron, S.D., Schnetzler, C.C., Krueger, A.J. and Walter, L.S. 1992. Global tracking of the SO2 clouds from the June, 1991 Mount Pinatubo eruptions. *Geophysical Research Letters.* **19**(2), pp.151-154.

Bönisch, H., Engel, A., Birner, T., Hoor, P., Tarasick, D.W. and Ray, E.A. 2011. On the structural changes in the Brewer-Dobson circulation after 2000. *Atmospheric Chemistry and Physics.* **11**(8), pp.3937-3948.

Boucher, O., Randall, D., Artaxo, P., Bretherton, C., Feingold, G., Forster, P.M., Kerminen, V.-M., Kondo, Y., Liao, H., Lohmann, U., Rasch, P., Satheesh, S.K., Sherwood, S., Stevens, B. and Zhan, X.Y. 2013. Clouds and Aerosols. In: Stocker, T.F., et al. eds. *Climate Change 2013: The Physical Science Basis. Contribution of Working Group I to the Fifth Assessment Report of the Intergovernmental Panel on Climate Change.* Cambridge, United Kingdom and New York, NY, USA.: Cambridge University Press.

Briffa, K.R., Jones, P.D., Schweingruber, F.H. and Osborn, T.J. 1998. Influence of volcanic eruptions on Northern Hemisphere summer temperature over the past 600 years. *Nature.* **393**(6684), pp.450-455.

Brohan, P., Allan, R., Freeman, E., Wheeler, D., Wilkinson, C. and Williamson, F. 2012. Constraining the temperature history of the past millennium using early instrumental observations. *Climate of the Past.* **8**(5), pp.1551-1563.

Butchart, N. 2014. The Brewer-Dobson circulation. *Reviews of Geophysics.* **52**(2), pp.157-184.

Carn, S.A., Clarisse, L. and Prata, A.J. 2016. Multi-decadal satellite measurements of global volcanic degassing. *Journal of Volcanology and Geothermal Research.* **311**, pp.99-134.

Carslaw, K.S., Peter, T. and Clegg, S.L. 1997. Modeling the composition of liquid stratospheric aerosols. *Reviews of Geophysics.* **35**(2), pp.125-154.

Castellano, E., Becagli, S., Hansson, M., Hutterli, M., Petit, J.R., Rampino, M.R., Severi, M., Steffensen, J.P., Traversi, R. and Udisti, R. 2005. Holocene volcanic history as recorded in the sulfate stratigraphy of the European Project for Ice Coring in Antarctica Dome C (EDC96) ice core. *Journal of Geophysical Research-Atmospheres.* **110**(D6), D06114.

Clausen, H.B. and Hammer, C.U. 1988. The Laki and Tambora eruptions as revealed in Greenland ice cores from 11 locations. *Annals of Glaciology.* **10**, pp.16-22.

Cole-Dai, J. 2010. Volcanoes and climate. *Wiley Interdisciplinary Reviews: Climate Change.* **1**(6), pp.824-839.

Cole-Dai, J.H., Mosley-Thompson, E., Wight, S.P. and Thompson, L.G. 2000. A 4100-year record of explosive volcanism from an East Antarctica ice core. *Journal of Geophysical Research-Atmospheres.* **105**(D19), pp.24431-24441.

Cole-Dai, J.H., MosleyThompson, E. and Thompson, L.G. 1997. Annually resolved southern hemisphere volcanic history from two Antarctic ice cores. *Journal of Geophysical Research-Atmospheres.* **102**(D14), pp.16761-16771.

Craig, P.S., Goldstein, M., Seheult, A.H. and Smith, J.A. 1996. Bayes linear strategies for matching hydrocarbon reservoir history. In: Bernado J. M., et al. eds. *Bayesian Statistics 5.* Oxford: Oxford Univ Press, pp.69-95.

Crowley, T. 2000. Causes of climate change over the past 1000 years. *Science.* **289**(5477), pp.270-277.

Crowley, T. and Unterman, M.B. 2013. Technical details concerning development of a 1200 yr proxy index for global volcanism. *Earth System Science Data.* **5**(1), pp.187-197.

Crowley, T., Zielinski, G., Vinther, B.M., Udisti, R., Kreutz, K., Cole-Dai, J. and Castellano, E. 2008. Volcanism and the little ice age. *PAGES Newsletter.* **16**, pp.22-23.

Davies, T., Cullen, M.J.P., Malcolm, A.J., Mawson, M.H., Staniforth, A., White, A.A. and Wood, N. 2005. A new dynamical core for the Met Office's global and regional modelling of the atmosphere. *Quarterly Journal of the Royal Meteorological Society.* **131**(608), pp.1759-1782.

Delmas, R.J., Kirchner, S., Palais, J.M. and Petit, J.-R. 1992. 1000 years of explosive volcanism recorded at the South Pole. *Tellus B.* **44**(4), pp.335-350.

Devine, J.D., Sigurdsson, H., Davis, A.N. and Self, S. 1984. Estimates of sulfur and chlorine yield to the atmosphere from volcanic eruptions and potential climatic effects. *Journal of Geophysical Research.* **89**(NB7), pp.6309-6325.

Dhomse, S.S., Chipperfield, M.P., Feng, W., Hossaini, R., Mann, G.W. and Santee, M.L. 2015. Revisiting the hemispheric asymmetry in midlatitude ozone changes following the Mount Pinatubo eruption: A 3-D model study. *Geophysical Research Letters.* **42**(8), pp.3038-3047.

Dhomse, S.S., Emmerson, K.M., Mann, G.W., Bellouin, N., Carslaw, K.S., Chipperfield, M.P., Hommel, R., Abraham, N.L., Telford, P., Braesicke, P., Dalvi, M., Johnson, C.E., O'Connor, F., Morgenstern, O., Pyle, J.A., Deshler, T., Zawodny, J.M. and Thomason, L.W. 2014. Aerosol microphysics simulations of the Mt. Pinatubo eruption with the UM-UKCA composition-climate model. *Atmospheric Chemistry and Physics.* **14**(20), pp.11221-11246.

Durant, A.J., Bonadonna, C. and Horwell, C.J. 2010. Atmospheric and Environmental Impacts of Volcanic Particulates. *Elements.* **6**(4), pp.235-240.

Dutton, E.G. and Christy, J.R. 1992. Solar radiative forcing at selected locations and evidence for global lower tropospheric cooling following the eruptions of El Chichón and Pinatubo. *Geophysical Research Letters.* **19**(23), pp.2313-2316.

English, J.M., Toon, O.B. and Mills, M.J. 2013. Microphysical simulations of large volcanic eruptions: Pinatubo and Toba. *Journal of Geophysical Research-Atmospheres.* **118**(4), pp.1880-1895.

Esper, J., Schneider, L., Krusic, P.J., Luterbacher, J., Buntgen, U., Timonen, M., Sirocko, F. and Zorita, E. 2013. European summer temperature response to

annually dated volcanic eruptions over the past nine centuries. *Bulletin of Volcanology.* **75**(7), 736.

Ferris, D.G., Cole-Dai, J., Reyes, A.R. and Budner, D.M. 2011. South Pole ice core record of explosive volcanic eruptions in the first and second millennia A.D. and evidence of a large eruption in the tropics around 535 A.D. *Journal of Geophysical Research: Atmospheres.* **116**(D17), D17308.

Fischer, E.M. 2006. Climate response to major volcanic eruptions. *PAGES Newsletter.* **13**(3), pp.8-9.

Fischer, E.M., Luterbacher, J., Zorita, E., Tett, S.F.B., Casty, C. and Wanner, H. 2007. European climate response to tropical volcanic eruptions over the last half millennium. *Geophysical Research Letters.* **34**(5), L05707.

Fyfe, J.C., von Salzen, K., Cole, J.N.S., Gillett, N.P. and Vernier, J.P. 2013. Surface response to stratospheric aerosol changes in a coupled atmosphere-ocean model. *Geophysical Research Letters.* **40**(3), pp.584-588.

Gao, C., Oman, L., Robock, A. and Stenchikov, G.L. 2007. Atmospheric volcanic loading derived from bipolar ice cores: Accounting for the spatial distribution of volcanic deposition. *Journal of Geophysical Research-Atmospheres.* **112**(D9), D09109.

Gao, C., Robock, A. and Ammann, C. 2008. Volcanic forcing of climate over the past 1500 years: An improved ice core-based index for climate models. *Journal of Geophysical Research-Atmospheres.* **113**(D23), D23111.

Gao, C., Robock, A., Self, S., Witter Jeffrey, B., Steffenson, J.P., Clausen Henrik, B., Siggaard-Andersen, M.-L., Johnsen, S., Mayewski Paul, A. and Ammann, C. 2006. The 1452 or 1453 A.D. Kuwae eruption signal derived from multiple ice core records: Greatest volcanic sulfate event of the past 700 years. *Journal of Geophysical Research: Atmospheres.* **111**(D12), D12107.

Gettelman, A., Schmidt, A. and Kristjansson, J.E. 2015. Icelandic volcanic emissions and climate. *Nature Geoscience.* **8**(4), pp.243-243.

Gregory, J.M., Andrews, T., Good, P., Mauritsen, T. and Forster, P.M. 2016. Small global-mean cooling due to volcanic radiative forcing. *Climate Dynamics.* **47**(12), pp.3979-3991.

Grieser, J. and Schönwiese, C.D. 1999. Parameterization of Spatio-temporal Patterns of Volcanic Aerosol Induced Stratospheric Optical Depth and its Climate Radiative Forcing. *Atmósfera.* **12**(2), pp.111-133.

Hamill, P., Jensen, E.J., Russell, P.B. and Bauman, J.J. 1997. The life cycle of stratospheric aerosol particles. *Bulletin of the American Meteorological Society.* **78**(7), pp.1395-1410.

Hammer, C.U., Clausen, H.B. and Dansgaard, W. 1980. Greenland ice sheet evidence of post-glacial volcanism and its climatic impact. *Nature.* **288**(5788), pp.230-235.

Hansen, J., Sato, M., Nazarenko, L., Ruedy, R., Lacis, A., Koch, D., Tegen, I., Hall, T., Shindell, D., Santer, B., Stone, P., Novakov, T., Thomason, L., Wang, R., Wang, Y., Jacob, D., Hollandsworth, S., Bishop, L., Logan, J., Thompson, A., Stolarski, R., Lean, J., Willson, R., Levitus, S., Antonov, J., Rayner, N., Parker, D. and Christy, J. 2002. Climate forcings in Goddard Institute for Space Studies SI2000 simulations. *Journal of Geophysical Research: Atmospheres.* **107**(D18), 4347.

Hansen, J., Sato, M., Ruedy, R., Nazarenko, L., Lacis, A., Schmidt, G.A., Russell, G., Aleinov, I., Bauer, M., Bauer, S., Bell, N., Cairns, B., Canuto, V., Chandler, M., Cheng, Y., Del Genio, A., Faluvegi, G., Fleming, E., Friend, A., Hall, T., Jackman, C., Kelley, M., Kiang, N., Koch, D., Lean, J., Lerner, J., Lo, K.,

Menon, S., Miller, R., Minnis, P., Novakov, T., Oinas, V., Perlwitz, J., Perlwitz, J., Rind, D., Romanou, A., Shindell, D., Stone, P., Sun, S., Tausnev, N., Thresher, D., Wielicki, B., Wong, T., Yao, M. and Zhang, S. 2005. Efficacy of climate forcings. *Journal of Geophysical Research-Atmospheres.* **110**(D18), D18104.

Haynes, P. and Shuckburgh, E. 2000. Effective diffusivity as a diagnostic of atmospheric transport: 1. Stratosphere. *Journal of Geophysical Research: Atmospheres.* **105**(D18), pp.22777-22794.

Haywood, J.M., Jones, A., Bellouin, N. and Stephenson, D. 2013. Asymmetric forcing from stratospheric aerosols impacts Sahelian rainfall. *Nature Climate Change.* **3**(7), pp.660-665.

Hegerl, G.C., Crowley, T.J., Allen, M., Hyde, W.T., Pollack, H.N., Smerdon, J. and Zorita, E. 2007. Detection of human influence on a new, validated 1500-year temperature reconstruction. *Journal of Climate.* **20**(4), pp.650-666.

Hitchman, M.H., McKay, M. and Trepte, C.R. 1994. A Climatology of Stratospheric Aerosol. *Journal of Geophysical Research-Atmospheres.* **99**(D10), pp.20689-20700.

Holton, J.R., Haynes, P.H., McIntyre, M.E., Douglass, A.R., Rood, R.B. and Pfister, L. 1995. Stratosphere-Troposphere Exchange. *Reviews of Geophysics.* **33**(4), pp.403-439.

Iles, C.E. and Hegerl, G.C. 2014. The global precipitation response to volcanic eruptions in the CMIP5 models. *Environmental Research Letters.* **9**(10), 104012.

Jensen, E.J. and Toon, O.B. 1992. The potential effects of volcanic aerosols on cirrus cloud microphysics. *Geophysical Research Letters.* **19**(17), pp.1759-1762.

Johnson, J.S., Cui, Z., Lee, L.A., Gosling, J.P., Blyth, A.M. and Carslaw, K.S. 2015. Evaluating uncertainty in convective cloud microphysics using statistical emulation. *Journal of Advances in Modeling Earth Systems.* **7**(1), pp.162-187.

Jones, A.C., Haywood, J.M., Dunstone, N., Emanuel, K., Hawcroft, M.K., Hodges, K.I. and Jones, A. 2017. Impacts of hemispheric solar geoengineering on tropical cyclone frequency. *Nature Communications.* **8**(1), 1382.

Jones, G.S., Gregory, J.M., Stott, P.A., Tett, S.F.B. and Thorpe, R.B. 2005. An AOGCM simulation of the climate response to a volcanic super-eruption. *Climate Dynamics.* **25**(7-8), pp.725-738.

Jungclaus, J.H., Bard, E., Baroni, M., Braconnot, P., Cao, J., Chini, L.P., Egorova, T., Evans, M., Gonzalez-Rouco, J.F., Goosse, H., Hurtt, G.C., Joos, F., Kaplan, J.O., Khodri, M., Goldewijk, K.K., Krivova, N., LeGrande, A.N., Lorenz, S.J., Luterbacher, J., Man, W.M., Maycock, A.C., Meinshausen, M., Moberg, A., Muscheler, R., Nehrbass-Ahles, C., Otto-Bliesner, B.I., Phipps, S.J., Pongratz, J., Rozanov, E., Schmidt, G.A., Schmidt, H., Schmutz, W., Schurer, A., Shapiro, A.I., Sigl, M., Smerdon, J.E., Solanki, S.K., Timmreck, C., Toohey, M., Usoskin, I.G., Wagner, S., Wu, C.J., Yeo, K.L., Zanchettin, D., Zhang, Q. and Zorita, E. 2017. The PMIP4 contribution to CMIP6-Part 3: The last millennium, scientific objective, and experimental design for the PMIP4 past1000 simulations. *Geoscientific Model Development.* **10**(11), pp.4005-4033.

Junge, C.E., Chagnon, C.W. and Manson, J.E. 1961. Stratospheric Aerosols. *Journal of Meteorology.* **18**(1), pp.81-108.

Kleinschmitt, C., Boucher, O. and Platt, U. 2018. Sensitivity of the radiative forcing by stratospheric sulfur geoengineering to the amount and strategy of the SO2

injection studied with the LMDZ-S3A model. *Atmospheric Chemistry and Physics.* **18**(4), pp.2769-2786.

Kokkola, H., Hommel, R., Kazil, J., Niemeier, U., Partanen, A.I., Feichter, J. and Timmreck, C. 2009. Aerosol microphysics modules in the framework of the ECHAM5 climate model - intercomparison under stratospheric conditions. *Geoscientific Model Development.* **2**(2), pp.97-112.

Kravitz, B. and Robock, A. 2011. Climate effects of high-latitude volcanic eruptions: Role of the time of year. *Journal of Geophysical Research-Atmospheres.* **116**, D01105.

Kremser, S., Thomason, L.W., von Hobe, M., Hermann, M., Deshler, T., Timmreck, C., Toohey, M., Stenke, A., Schwarz, J.P., Weigel, R., Fueglistaler, S., Prata, F.J., Vernier, J.P., Schlager, H., Barnes, J.E., Antuna-Marrero, J.C., Fairlie, D., Palm, M., Mahieu, E., Notholt, J., Rex, M., Bingen, C., Vanhellemont, F., Bourassa, A., Plane, J.M.C., Klocke, D., Carn, S.A., Clarisse, L., Trickl, T., Neely, R., James, A.D., Rieger, L., Wilson, J.C. and Meland, B. 2016. Stratospheric aerosol-Observations, processes, and impact on climate. *Reviews of Geophysics.* **54**(2), pp.278-335.

Labitzke, K. and McCormick, M.P. 1992. Stratospheric temperature increases due to Pinatubo aerosols. *Geophysical Research Letters.* **19**(2), pp.207-210.

Lacis, A. 2015. Volcanic aerosol radiative properties. *Past Global Changes Magazine.* **23**(2), pp.50-51.

Lacis, A., Hansen, J. and Sato, M. 1992. Climate forcing by stratospheric aerosols. *Geophysical Research Letters.* **19**(15), pp.1607-1610.

Lamb, H.H. 1970. Volcanic dust in the atmosphere; with a chronology and assessment of its meteorological significance. *Philosophical Transactions of the Royal Society of London.* **266**(1178), pp.425-533.

Lanciki, A., Cole-Dai, J., Thiemens, M.H. and Savarino, J. 2012. Sulfur isotope evidence of little or no stratospheric impact by the 1783 Laki volcanic eruption. *Geophysical Research Letters.* **39**(1), L01806.

Langway, C.C., Osada, K., Clausen, H.B., Hammer, C.U. and Shoji, H. 1995. A 10-century comparison of prominent bipolar volcanic events in ice cores. *Journal of Geophysical Research-Atmospheres.* **100**(D8), pp.16241-16247.

Larson, E.J.L. and Portmann, R.W. 2016. A Temporal Kernel Method to Compute Effective Radiative Forcing in CMIP5 Transient Simulations. *Journal of Climate.* **29**(4), pp.1497-1509.

Lee, L.A., Carslaw, K.S., Pringle, K.J., Mann, G.W. and Spracklen, D.V. 2011. Emulation of a complex global aerosol model to quantify sensitivity to uncertain parameters. *Atmospheric Chemistry and Physics.* **11**(23), pp.12253-12273.

Loeppky, J.L., Sacks, J. and Welch, W.J. 2009. Choosing the Sample Size of a Computer Experiment: A Practical Guide. *Technometrics.* **51**(4), pp.366-376.

Ludlow, F., Stine, A.R., Leahy, P., Murphy, E., Mayewski, P.A., Taylor, D., Killen, J., Baillie, M.G.L., Hennessy, M. and Kiely, G. 2013. Medieval Irish chronicles reveal persistent volcanic forcing of severe winter cold events, 431-1649 CE. *Environmental Research Letters.* **8**(2), 024035.

Man, W.M., Zhou, T.J. and Jungclaus, J.H. 2014. Effects of Large Volcanic Eruptions on Global Summer Climate and East Asian Monsoon Changes during the Last Millennium: Analysis of MPI-ESM Simulations. *Journal of Climate.* **27**(19), pp.7394-7409.

Mann, G.W., Carslaw, K.S., Ridley, D.A., Spracklen, D.V., Pringle, K.J., Merikanto, J., Korhonen, H., Schwarz, J.P., Lee, L.A., Manktelow, P.T., Woodhouse,

M.T., Schmidt, A., Breider, T.J., Emmerson, K.M., Reddington, C.L., Chipperfield, M.P. and Pickering, S.J. 2012. Intercomparison of modal and sectional aerosol microphysics representations within the same 3-D global chemical transport model. *Atmospheric Chemistry and Physics.* **12**(10), pp.4449-4476.

Mann, G.W., Carslaw, K.S., Spracklen, D.V., Ridley, D.A., Manktelow, P.T., Chipperfield, M.P., Pickering, S.J. and Johnson, C.E. 2010. Description and evaluation of GLOMAP-mode: a modal global aerosol microphysics model for the UKCA composition-climate model. *Geoscientific Model Development.* **3**(2), pp.519-551.

Marotzke, J. and Forster, P.M. 2015. Forcing, feedback and internal variability in global temperature trends. *Nature.* **517**, pp.565-570.

Marshall, L., Schmidt, A., Toohey, M., Carslaw, K.S., Mann, G.W., Sigl, M., Khodri, M., Timmreck, C., Zanchettin, D., Ball, W.T., Bekki, S., Brooke, J.S.A., Dhomse, S., Johnson, C., Lamarque, J.F., LeGrande, A.N., Mills, M.J., Niemeier, U., Pope, J.O., Poulain, V., Robock, A., Rozanov, E., Stenke, A., Sukhodolov, T., Tilmes, S., Tsigaridis, K. and Tummon, F. 2018. Multi-model comparison of the volcanic sulfate deposition from the 1815 eruption of Mt. Tambora. *Atmospheric Chemistry and Physics.* **18**(3), pp.2307-2328.

McCormick, M.P., Thomason, L.W. and Trepte, C.R. 1995. Atmospheric effects of the Mt Pinatubo eruption. *Nature.* **373**(6513), pp.399-404.

McKay, M.D., Beckman, R.J. and Conover, W.J. 1979. A Comparison of Three Methods for Selecting Values of Input Variables in the Analysis of Output from a Computer Code. *Technometrics.* **21**(2), pp.239-245.

Metzner, D., Kutterolf, S., Toohey, M., Timmreck, C., Niemeier, U., Freundt, A. and Kruger, K. 2014. Radiative forcing and climate impact resulting from SO2 injections based on a 200,000-year record of Plinian eruptions along the Central American Volcanic Arc. *International Journal of Earth Sciences.* **103**(7), pp.2063-2079.

Mills, M.J., Richter, J.H., Tilmes, S., Kravitz, B., MacMartin, D.G., Glanville, A.A., Tribbia, J.J., Lamarque, J.F., Vitt, F., Schmidt, A., Gettelman, A., Hannay, C., Bacmeister, J.T. and Kinnison, D.E. 2017. Radiative and Chemical Response to Interactive Stratospheric Sulfate Aerosols in Fully Coupled CESM1(WACCM). *Journal of Geophysical Research-Atmospheres.* **122**(23), pp.13061-13078.

Mills, M.J., Schmidt, A., Easter, R., Solomon, S., Kinnison, D.E., Ghan, S.J., Neely, R.R., Marsh, D.R., Conley, A., Bardeen, C.G. and Gettelman, A. 2016. Global volcanic aerosol properties derived from emissions, 1990-2014, using CESM1(WACCM). *Journal of Geophysical Research-Atmospheres.* **121**(5), pp.2332-2348.

Mills, M.J., Toon, O.B. and Thomas, G.E. 2005. Mesospheric sulfate aerosol layer. *Journal of Geophysical Research: Atmospheres.* **110**(D24), D24208.

Mitchell, J.M. 1970. A Preliminary Evaluation of Atmospheric Pollution as a Cause of the Global Temperature Fluctuation of the Past Century. In: Singer, S.F. ed. *Global Effects of Environmental Pollution.* Dordrecht: Springer Netherlands, pp.139-155.

Morgenstern, O., Braesicke, P., O'Connor, F.M., Bushell, A.C., Johnson, C.E., Osprey, S.M. and Pyle, J.A. 2009. Evaluation of the new UKCA climate-composition model - Part 1: The stratosphere. *Geoscientific Model Development.* **2**(1), pp.43-57.

Morris, M.D. and Mitchell, T.J. 1995. Exploratory designs for computational experiments. *Journal of Statistical Planning and Inference.* **43**(3), pp.381-402.

Myhre, G., Shindell, D., Bréon, F.-M., Collins, W., Fuglestvedt, J., Huang, J., Koch, D., Lamarque, J.-F., Lee, D., Mendoza, B., Nakajima, T., Robock, A., Stephens, G., Takemura, T. and Zhang, H. 2013. Anthropogenic and Natural Radiative Forcing. In: Stocker, T.F., et al. eds. *Climate Change 2013: The Physical Science Basis. Contribution of Working Group I to the Fifth Assessment Report of the Intergovernmental Panel on Climate Change.* Cambridge, United Kingdom and New York, NY, USA.: Cambridge University Press.

Neu, J.L. and Plumb, R.A. 1999. Age of air in a "leaky pipe" model of stratospheric transport. *Journal of Geophysical Research-Atmospheres.* **104**(D16), pp.19243-19255.

Niemeier, U. and Schmidt, H. 2017. Changing transport processes in the stratosphere by radiative heating of sulfate aerosols. *Atmospheric Chemistry and Physics.* **17**(24), pp.14871-14886.

Niemeier, U., Schmidt, H. and Timmreck, C. 2011. The dependency of geoengineered sulfate aerosol on the emission strategy. *Atmospheric Science Letters.* **12**(2), pp.189-194.

Niemeier, U. and Timmreck, C. 2015. What is the limit of climate engineering by stratospheric injection of SO2? *Atmospheric Chemistry and Physics.* **15**(16), pp.9129-9141.

Niemeier, U., Timmreck, C., Graf, H.F., Kinne, S., Rast, S. and Self, S. 2009. Initial fate of fine ash and sulfur from large volcanic eruptions. *Atmospheric Chemistry and Physics.* **9**(22), pp.9043-9057.

Nooren, K., Hoek, W.Z., van der Plicht, H., Sigl, M., van Bergen, M.J., Galop, D., Torrescano-Valle, N., Islebe, G., Huizinga, A., Winkels, T. and Middelkoop, H. 2017. Explosive eruption of El Chichón volcano (Mexico) disrupted 6th century Maya civilization and contributed to global cooling. *Geology.* **45**(2), pp.175-178.

O'Connor, F.M., Johnson, C.E., Morgenstern, O., Abraham, N.L., Braesicke, P., Dalvi, M., Folberth, G.A., Sanderson, M.G., Telford, P.J., Voulgarakis, A., Young, P.J., Zeng, G., Collins, W.J. and Pyle, J.A. 2014. Evaluation of the new UKCA climate-composition model - Part 2: The Troposphere. *Geoscientific Model Development.* **7**(1), pp.41-91.

O'Hagan, A. 1994. *Kendall's Advanced Theory of Statistics: Bayesian Inference.* London, U. K.: Edward Arnold.

O'Hagan, A. 2006. Bayesian analysis of computer code outputs: A tutorial. *Reliability Engineering & System Safety.* **91**(10-11), pp.1290-1300.

Oman, L., Robock, A., Stenchikov, G., Schmidt, G.A. and Ruedy, R. 2005. Climatic response to high-latitude volcanic eruptions. *Journal of Geophysical Research-Atmospheres.* **110**, D13103.

Oman, L., Robock, A., Stenchikov, G.L., Thordarson, T., Koch, D., Shindell, D.T. and Gao, C.C. 2006. Modeling the distribution of the volcanic aerosol cloud from the 1783-1784 Laki eruption. *Journal of Geophysical Research-Atmospheres.* **111**(D12), D12209.

Pausata, F.S.R., Chafik, L., Caballero, R. and Battisti, D.S. 2015. Impacts of high-latitude volcanic eruptions on ENSO and AMOC. *Proceedings of the National Academy of Sciences of the United States of America.* **112**(45), pp.13784-13788.

Pinto, J.P., Turco, R.P. and Toon, O.B. 1989. Self-limiting physical and chemical effects in volcanic eruption clouds. *Journal of Geophysical Research-Atmospheres.* **94**(D8), pp.11165-11174.

Plumb, R.A. 1996. A "tropical pipe" model of stratospheric transport. *Journal of Geophysical Research-Atmospheres.* **101**(D2), pp.3957-3972.

Plumb, R.A. 2002. Stratospheric transport. *Journal of the Meteorological Society of Japan.* **80**(4B), pp.793-809.

Plummer, C.T., Curran, M.A.J., van Ommen, T.D., Rasmussen, S.O., Moy, A.D., Vance, T.R., Clausen, H.B., Vinther, B.M. and Mayewski, P.A. 2012. An independently dated 2000-yr volcanic record from Law Dome, East Antarctica, including a new perspective on the dating of the 1450s CE eruption of Kuwae, Vanuatu. *Climate of the Past.* **8**(6), pp.1929-1940.

Polvani, L.M., Banerjee, A. and Schmidt, A. 2018. Northern Hemisphere continental winter warming following the 1991 Mt. Pinatubo eruption: Reconciling models and observations. *Atmospheric Chemistry Physics Discussions.* pp.1-25.

Pujol. G., Iooss, B., and Janon, A., 2017. *sensitivity: Global Sensitivity Analysis of Model Outputs. R package* (1.14.0). [Software] Available at https://CRAN.R-project.org/package=sensitivity

Puma, M.J., Chon, S. and Wada, Y. 2015. Exploring the potential impacts of historic volcanic eruptions on the contemporary global food system. *Past Global Changes Magazine.* **23**(2), pp.66-67.

Punge, H.J., Konopka, P., Giorgetta, M.A. and Muller, R. 2009. Effects of the quasi-biennial oscillation on low-latitude transport in the stratosphere derived from trajectory calculations. *Journal of Geophysical Research-Atmospheres.* **114**, D03102.

Rampino, M.R. and Self, S. 1982. Historic eruptions of Tambora (1815), Krakatau (1883), and Agung (1963), their stratospheric aerosols, and climatic impact. *Quaternary Research.* **18**(2), pp.127-143.

R Core Team. 2017. *R: A language and environment for statistical computing. R Foundation for Statistical Computing.* Vienna, Austria. Available at https://www.R-project.org/.

Ridley, H.E., Asmerom, Y., Baldini, J.U.L., Breitenbach, S.F.M., Aquino, V.V., Prufer, K.M., Culleton, B.J., Polyak, V., Lechleitner, F.A., Kennett, D.J., Zhang, M.H., Marwan, N., Macpherson, C.G., Baldini, L.M., Xiao, T.Y., Peterkin, J.L., Awe, J. and Haug, G.H. 2015. Aerosol forcing of the position of the intertropical convergence zone since AD 1550. *Nature Geoscience.* **8**(3), pp.195-200.

Robertson, A., Overpeck, J., Rind, D., Mosley-Thompson, E., Zielinski, G., Lean, J., Koch, D., Penner, J., Tegen, I. and Healy, R. 2001. Hypothesized climate forcing time series for the last 500 years. *Journal of Geophysical Research: Atmospheres.* **106**(D14), pp.14783-14803.

Robock, A. 2000. Volcanic eruptions and climate. *Reviews of Geophysics.* **38**(2), pp.191-219.

Robock, A., Ammann, C.M., Oman, L., Shindell, D., Levis, S. and Stenchikov, G. 2009. Did the Toba volcanic eruption of ~74 ka B.P. produce widespread glaciation? *Journal of Geophysical Research: Atmospheres.* **114**(D10), D10107.

Robock, A. and Free, M.P. 1995. Ice cores as an index of global volcanism from 1850 to the present. *Journal of Geophysical Research-Atmospheres.* **100**(D6), pp.11549-11567.

Rose, W.I. and Chesner, C.A. 1990. Worldwide dispersal of ash and gases from earth's largest known eruption: Toba, Sumatra, 75 ka. *Palaeogeography, Palaeoclimatology, Palaeoecology.* **89**(3), pp.269-275.

Roustant, O., Ginsbourger, D. and Deville, Y. 2012. DiceKriging, DiceOptim: Two R Packages for the Analysis of Computer Experiments by Kriging-Based Metamodeling and Optimization. *Journal of Statistical Software.* **51**(1), pp.1-55.

Saltelli, A. and Annoni, P. 2010. How to avoid a perfunctory sensitivity analysis. *Environmental Modelling & Software.* **25**(12), pp.1508-1517.

Saltelli, A., Tarantola, S. and Chan, K.P.S. 1999. A quantitative model-independent method for global sensitivity analysis of model output. *Technometrics.* **41**(1), pp.39-56.

Salter, J.M. and Williamson, D. 2016. A comparison of statistical emulation methodologies for multi-wave calibration of environmental models. *Environmetrics.* **27**(8), pp.507-523.

Sassen, K. 1992. Evidence for Liquid-Phase Cirrus Cloud Formation from Volcanic Aerosols: Climatic Implications. *Science.* **257**(5069), pp.516-519.

Sato, M., Hansen, J.E., McCormick, M.P. and Pollack, J.B. 1993. Stratospheric Aerosol Optical Depths, 1850-1990. *Journal of Geophysical Research-Atmospheres.* **98**(D12), pp.22987-22994.

Schmidt, A., Carslaw, K.S., Mann, G.W., Rap, A., Pringle, K.J., Spracklen, D.V., Wilson, M. and Forster, P.M. 2012. Importance of tropospheric volcanic aerosol for indirect radiative forcing of climate. *Atmospheric Chemistry and Physics.* **12**(16), pp.7321-7339.

Schmidt, A., Carslaw, K.S., Mann, G.W., Wilson, M., Breider, T.J., Pickering, S.J. and Thordarson, T. 2010. The impact of the 1783-1784 AD Laki eruption on global aerosol formation processes and cloud condensation nuclei. *Atmospheric Chemistry and Physics.* **10**(13), pp.6025-6041.

Schmidt, G.A., Jungclaus, J.H., Ammann, C.M., Bard, E., Braconnot, P., Crowley, T.J., Delaygue, G., Joos, F., Krivova, N.A., Muscheler, R., Otto-Bliesner, B.L., Pongratz, J., Shindell, D.T., Solanki, S.K., Steinhilber, F. and Vieira, L.E.A. 2011. Climate forcing reconstructions for use in PMIP simulations of the last millennium (v1.0). *Geoscientific Model Development.* **4**(1), pp.33-45.

Schneider, D.P., Ammann, C.M., Otto-Bliesner, B.L. and Kaufman, D.S. 2009. Climate response to large, high-latitude and low-latitude volcanic eruptions in the Community Climate System Model. *Journal of Geophysical Research-Atmospheres.* **114**, D15101.

Schneider, L., Smerdon, J.E., Pretis, F., Hartl-Meier, C. and Esper, J. 2017. A new archive of large volcanic events over the past millennium derived from reconstructed summer temperatures. *Environmental Research Letters.* **12**(9), 094005.

Schurer, A.P., Hegerl, G.C., Mann, M.E., Tett, S.F.B. and Phipps, S.J. 2013. Separating Forced from Chaotic Climate Variability over the Past Millennium. *Journal of Climate.* **26**(18), pp.6954-6973.

Seinfeld, J.H. and Pandis, S.N. 2016. *Atmosphere chemistry and physics: from air pollution to climate change.* Third ed. Hoboken, New Jersey: John Wiley & Sons, Inc.

Shapiro, M.A. 1980. Turbulent Mixing within Tropopause Folds as a Mechanism for the Exchange of Chemical Constituents between the Stratosphere and Troposphere. *Journal of the Atmospheric Sciences.* **37**(5), pp.994-1004.

Sigl, M., McConnell, J.R., Layman, L., Maselli, O., McGwire, K., Pasteris, D., Dahl-Jensen, D., Steffensen, J.P., Vinther, B., Edwards, R., Mulvaney, R. and Kipfstuhl, S. 2013. A new bipolar ice core record of volcanism from WAIS Divide and NEEM and implications for climate forcing of the last 2000 years. *Journal of Geophysical Research-Atmospheres.* **118**(3), pp.1151-1169.

Sigl, M., McConnell, J.R., Toohey, M., Curran, M., Das, S.B., Edwards, R., Isaksson, E., Kawamura, K., Kipfstuhl, S., Kruger, K., Layman, L., Maselli, O.J., Motizuki, Y., Motoyama, H., Pasteris, D.R. and Severi, M. 2014. Insights from Antarctica on volcanic forcing during the Common Era. *Nature Climate Change.* **4**(8), pp.693-697.

Sigl, M., Winstrup, M., McConnell, J.R., Welten, K.C., Plunkett, G., Ludlow, F., Buntgen, U., Caffee, M., Chellman, N., Dahl-Jensen, D., Fischer, H., Kipfstuhl, S., Kostick, C., Maselli, O.J., Mekhaldi, F., Mulvaney, R., Muscheler, R., Pasteris, D.R., Pilcher, J.R., Salzer, M., Schupbach, S., Steffensen, J.P., Vinther, B.M. and Woodruff, T.E. 2015. Timing and climate forcing of volcanic eruptions for the past 2,500 years. *Nature.* **523**(7562), pp.543–549.

SPARC. 2006. SPARC Assessment of Stratospheric Aerosol Properties (ASAP). Thomason, L., and Peter. T., eds., SPARC Report No. 4, WCRP-124, WMO/TD – No. 1295. Available at www.sparc-climate.org/publications/sparc-reports/.

Spracklen, D.V., Pringle, K.J., Carslaw, K.S., Chipperfield, M.P. and Mann, G.W. 2005a. A global off-line model of size-resolved aerosol microphysics: I. Model development and prediction of aerosol properties. *Atmospheric Chemistry and Physics.* **5**, pp.2227-2252.

Spracklen, D.V., Pringle, K.J., Carslaw, K.S., Chipperfield, M.P. and Mann, G.W. 2005b. A global off-line model of size-resolved aerosol microphysics: II. Identification of key uncertainties. *Atmospheric Chemistry and Physics.* **5**, pp.3233-3250.

Stenchikov, G., Robock, A., Ramaswamy, V., Schwarzkopf, M.D., Hamilton, K. and Ramachandran, S. 2002. Arctic Oscillation response to the 1991 Mount Pinatubo eruption: Effects of volcanic aerosols and ozone depletion. *Journal of Geophysical Research-Atmospheres.* **107**(D24), 4803.

Stenchikov, G.L., Kirchner, I., Robock, A., Graf, H.-F., Antuña, J.C., Grainger, R.G., Lambert, A. and Thomason, L. 1998. Radiative forcing from the 1991 Mount Pinatubo volcanic eruption. *Journal of Geophysical Research: Atmospheres.* **103**(D12), pp.13837-13857.

Stevenson, S., Fasullo, J.T., Otto-Bliesner, B.L., Tomas, R.A. and Gao, C.C. 2017. Role of eruption season in reconciling model and proxy responses to tropical volcanism. *Proceedings of the National Academy of Sciences of the United States of America.* **114**(8), pp.1822-1826.

Stier, P., Seinfeld, J.H., Kinne, S. and Boucher, O. 2007. Aerosol absorption and radiative forcing. *Atmospheric Chemistry and Physics.* **7**(19), pp.5237-5261.

Stoffel, M., Khodri, M., Corona, C., Guillet, S., Poulain, V., Bekki, S., Guiot, J., Luckman, B.H., Oppenheimer, C., Lebas, N., Beniston, M. and Masson-Delmotte, V. 2015. Estimates of volcanic-induced cooling in the Northern Hemisphere over the past 1,500 years. *Nature Geoscience.* **8**(10), pp.784-788.

Stothers, R.B. 1984. The Great Tambora Eruption in 1815 and Its Aftermath. *Science.* **224**(4654), pp.1191-1198.

Stothers, R.B. 1996. Major optical depth perturbations to the stratosphere from volcanic eruptions: Pyrheliometric period, 1881-1960. *Journal of Geophysical Research-Atmospheres.* **101**(D2), pp.3901-3920.

Stothers, R.B. 2001. Major optical depth perturbations to the stratosphere from volcanic eruptions: Stellar extinction period, 1961-1978. *Journal of Geophysical Research-Atmospheres.* **106**(D3), pp.2993-3003.

Tabazadeh, A., Drdla, K., Schoeberl, M.R., Hamill, P. and Toon, O.B. 2002. Arctic "ozone hole" in a cold volcanic stratosphere. *Proceedings of the National Academy of Sciences.* **99**(5), pp.2609-2612.

Thomason, L.W., Ernest, N., Millan, L., Rieger, L., Bourassa, A., Vernier, J.P., Manney, G., Luo, B.P., Arfeuille, F. and Peter, T. 2018. A global space-based stratospheric aerosol climatology: 1979-2016. *Earth System Science Data.* **10**(1), pp.469-492.

Tilmes, S., Muller, R., Salawitch, R.J., Schmidt, U., Webster, C.R., Oelhaf, H., Camy-Peyret, C.C. and Russell, J.M. 2008. Chemical ozone loss in the Arctic winter 1991-1992. *Atmospheric Chemistry and Physics.* **8**(7), pp.1897-1910.

Tilmes, S., Richter, J.H., Mills, M.J., Kravitz, B., MacMartin, D.G., Vitt, F., Tribbia, J.J. and Lamarque, J.F. 2017. Sensitivity of Aerosol Distribution and Climate Response to Stratospheric SO2 Injection Locations. *Journal of Geophysical Research-Atmospheres.* **122**(23), pp.12591-12615.

Timmreck, C. 2012. Modeling the climatic effects of large explosive volcanic eruptions. *Wiley Interdisciplinary Reviews-Climate Change.* **3**(6), pp.545-564.

Timmreck, C. and Graf, H.F. 2006. The initial dispersal and radiative forcing of a Northern Hemisphere mid-latitude super volcano: a model study. *Atmospheric Chemistry and Physics.* **6**, pp.35-49.

Timmreck, C., Graf, H.F. and Kirchner, I. 1999. A one and half year interactive MA/ECHAM4 simulation of Mount Pinatubo Aerosol. *Journal of Geophysical Research-Atmospheres.* **104**(D8), pp.9337-9359.

Timmreck, C., Graf, H.F., Lorenz, S.J., Niemeier, U., Zanchettin, D., Matei, D., Jungclaus, J.H. and Crowley, T.J. 2010. Aerosol size confines climate response to volcanic super-eruptions. *Geophysical Research Letters.* **37**, L24705.

Timmreck, C., Lorenz, S.J., Crowley, T.J., Kinne, S., Raddatz, T.J., Thomas, M.A. and Jungclaus, J.H. 2009. Limited temperature response to the very large AD 1258 volcanic eruption. *Geophysical Research Letters.* **36**, L21708.

Timmreck, C., Mann, G.W., Aquila, V., Hommel, R., Lee, L.A., Schmidt, A., Brühl, C., Carn, S., Chin, M., Dhomse, S.S., Diehl, T., English, J.M., Mills, M.J., Neely, R., Sheng, J., Toohey, M. and Weisenstein, D. 2018. The Interactive Stratospheric Aerosol Model Intercomparison Project (ISA-MIP): motivation and experimental design. *Geoscientific Model Development.* **11**(7), pp.2581-2608.

Toohey, M., Kruger, K., Bittner, M., Timmreck, C. and Schmidt, H. 2014. The impact of volcanic aerosol on the Northern Hemisphere stratospheric polar vortex: mechanisms and sensitivity to forcing structure. *Atmospheric Chemistry and Physics.* **14**(23), pp.13063-13079.

Toohey, M., Kruger, K., Niemeier, U. and Timmreck, C. 2011. The influence of eruption season on the global aerosol evolution and radiative impact of tropical volcanic eruptions. *Atmospheric Chemistry and Physics.* **11**(23), pp.12351-12367.

Toohey, M., Kruger, K., Sigl, M., Stordal, F. and Svensen, H. 2016a. Climatic and societal impacts of a volcanic double event at the dawn of the Middle Ages. *Climatic Change.* **136**(3-4), pp.401-412.

Toohey, M., Kruger, K. and Timmreck, C. 2013. Volcanic sulfate deposition to Greenland and Antarctica: A modeling sensitivity study. *Journal of Geophysical Research-Atmospheres.* **118**(10), pp.4788-4800.

Toohey, M. and Sigl, M. 2017. Volcanic stratospheric sulfur injections and aerosol optical depth from 500 BCE to 1900 CE. *Earth System Science Data.* **9**(2), pp.809-831.

Toohey, M., Stevens, B., Schmidt, H. and Timmreck, C. 2016b. Easy Volcanic Aerosol (EVA v1.0): an idealized forcing generator for climate simulations. *Geoscientific Model Development.* **9**(11), pp.4049-4070.

Traufetter, F., Oerter, H., Fischer, H., Weller, R. and Miller, H. 2004. Spatio-temporal variability in volcanic sulphate deposition over the past 2 kyr in snow pits and firn cores from Amundsenisen, Antarctica. *Journal of Glaciology.* **50**(168), pp.137-146.

Trenberth, K.E. and Dai, A. 2007. Effects of Mount Pinatubo volcanic eruption on the hydrological cycle as an analog of geoengineering. *Geophysical Research Letters.* **34**(15), L15702.

Trepte, C.R. and Hitchman, M.H. 1992. Tropical stratospheric circulation deduced from satellite aerosol data. *Nature.* **355**(6361), pp.626-628.

Trepte, C.R., Veiga, R.E. and McCormick, M.P. 1993. The poleward dispersal of Mount Pinatubo volcanic aerosol. *Journal of Geophysical Research-Atmospheres.* **98**(D10), pp.18563-18573.

Turco, R.P., Hamill, P., Toon, O.B., Whitten, R.C. and Kiang, C.S. 1979. A One-Dimensional Model Describing Aerosol Formation and Evolution in the Stratosphere: I. Physical Processes and Mathematical Analogs. *Journal of the Atmospheric Sciences.* **36**(4), pp.699-717.

Vidal, C.M., Metrich, N., Komorowski, J.C., Pratomo, I., Michel, A., Kartadinata, N., Robert, V. and Lavigne, F. 2016. The 1257 Samalas eruption (Lombok, Indonesia): the single greatest stratospheric gas release of the Common Era. *Scientific Reports.* **6**, 34868.

Visioni, D., Pitari, G., Tuccella, P. and Curci, G. 2018. Sulfur deposition changes under sulfate geoengineering conditions: quasi-biennial oscillation effects on the transport and lifetime of stratospheric aerosols. *Atmospheric Chemistry and Physics.* **18**(4), pp.2787-2808.

Walters, D.N., Williams, K.D., Boutle, I.A., Bushell, A.C., Edwards, J.M., Field, P.R., Lock, A.P., Morcrette, C.J., Stratton, R.A., Wilkinson, J.M., Willett, M.R., Bellouin, N., Bodas-Salcedo, A., Brooks, M.E., Copsey, D., Earnshaw, P.D., Hardiman, S.C., Harris, C.M., Levine, R.C., MacLachlan, C., Manners, J.C., Martin, G.M., Milton, S.F., Palmer, M.D., Roberts, M.J., Rodriguez, J.M., Tennant, W.J. and Vidale, P.L. 2014. The Met Office Unified Model Global Atmosphere 4.0 and JULES Global Land 4.0 configurations. *Geoscientific Model Development.* **7**(1), pp.361-386.

Weisenstein, D.K., Penner, J.E., Herzog, M. and Liu, X. 2007. Global 2-D intercomparison of sectional and modal aerosol modules. *Atmospheric Chemistry and Physics.* **7**(9), pp.2339-2355.

Wigley, T.M.L., Ammann, C.M., Santer, B.D. and Raper, S.C.B. 2005. Effect of climate sensitivity on the response to volcanic forcing. *Journal of Geophysical Research-Atmospheres.* **110**(D9), D09107.

Williamson, D., Blaker, A.T., Hampton, C. and Salter, J. 2015. Identifying and removing structural biases in climate models with history matching. *Climate Dynamics.* **45**(5-6), pp.1299-1324.

Williamson, D., Goldstein, M., Allison, L., Blaker, A., Challenor, P., Jackson, L. and Yamazaki, K. 2013. History matching for exploring and reducing climate model parameter space using observations and a large perturbed physics ensemble. *Climate Dynamics.* **41**(7-8), pp.1703-1729.

Wilson, R., Anchukaitis, K., Briffa, K.R., Buntgen, U., Cook, E., D'Arrigo, R., Davi, N., Esper, J., Frank, D., Gunnarson, B., Hegerl, G., Helama, S., Klesse, S., Krusic, P.J., Linderholm, H.W., Myglan, V., Osborn, T.J., Rydval, M., Schneider, L., Schurer, A., Wiles, G., Zhang, P. and Zorita, E. 2016. Last millennium northern hemisphere summer temperatures from tree rings: Part I: The long term context. *Quaternary Science Reviews.* **134**, pp.1-18.

Xu, X., Haaland, B. and Qian, P.Z.G. 2011. Sudoku-based space-filling designs. *Biometrika.* **98**(3), pp.711-720.

Young, R.E., Houben, H. and Toon, O.B. 1994. Radiatively forced dispersion of the Mt. Pinatubo volcanic cloud and induced temperature perturbations in the stratosphere during the first few months following the eruption. *Geophysical Research Letters.* **21**(5), pp.369-372.

Zambri, B., LeGrande, A.N., Robock, A. and Slawinska, J. 2017. Northern Hemisphere winter warming and summer monsoon reduction after volcanic eruptions over the last millennium. *Journal of Geophysical Research: Atmospheres.* **122**(15), pp.7971-7989.

Zambri, B. and Robock, A. 2016. Winter warming and summer monsoon reduction after volcanic eruptions in Coupled Model Intercomparison Project 5 (CMIP5) simulations. *Geophysical Research Letters.* **43**(20), pp.10,920-10,928.

Zanchettin, D., Khodri, M., Timmreck, C., Toohey, M., Schmidt, A., Gerber, E.P., Hegerl, G., Robock, A., Pausata, F.S.R., Ball, W.T., Bauer, S.E., Bekki, S., Dhomse, S.S., LeGrande, A.N., Mann, G.W., Marshall, L., Mills, M., Marchand, M., Niemeier, U., Poulain, V., Rozanov, E., Rubino, A., Stenke, A., Tsigaridis, K. and Tummon, F. 2016. The Model Intercomparison Project on the climatic response to Volcanic forcing (VolMIP): experimental design and forcing input data for CMIP6. *Geoscientific Model Development.* **9**(8), pp.2701-2719.

Zanchettin, D., Timmreck, C., Khodri, M., Robock, A., Rubino, A., Schmidt, A. and Toohey, M. 2015. A coordinated modeling assessment of the climate response to volcanic forcing. *PAGES Magazine* **23**(2), pp.54-55.

Zielinski, G.A. 1995. Stratospheric loading and optical depth estimates of explosive volcanism over the last 2100 years derived from the Greenland Ice Sheet Project 2 ice core. *Journal of Geophysical Research-Atmospheres.* **100**(D10), pp.20937-20955.

Zielinski, G.A., Mayewski, P.A., Meeker, L.D., Gronvold, K., Germani, M.S., Whitlow, S., Twickler, M.S. and Taylor, K. 1997. Volcanic aerosol records and tephrochronology of the Summit, Greenland, ice cores. *Journal of Geophysical Research-Oceans.* **102**(C12), pp.26625-26640.

Zielinski, G.A., Mayewski, P.A., Meeker, L.D., Whitlow, S., Twickler, M.S. and Taylor, K. 1996. Potential atmospheric impact of the Toba Mega-Eruption ~71,000 years ago. *Geophysical Research Letters.* **23**(8), pp.837-840.

Chapter 2 Multi-model comparison of the volcanic sulfate deposition from the 1815 eruption of Mt. Tambora

Lauren Marshall[1], Anja Schmidt[1,a] , Matthew Toohey[2,3] , Ken S. Carslaw[1] , Graham W. Mann[1,4], Michael Sigl[5], Myriam Khodri[6], Claudia Timmreck[3], Davide Zanchettin[7], William T. Ball[8,9], Slimane Bekki[10], James S. A. Brooke[11], Sandip Dhomse[1], Colin Johnson[12], Jean-Francois Lamarque[13], Allegra N. LeGrande[14,15], Michael J. Mills[13] , Ulrike Niemeier[3] , James O. Pope[16], Virginie Poulain[6], Alan Robock[17], Eugene Rozanov[8,9], Andrea Stenke[8], Timofei Sukhodolov[9], Simone Tilmes[13], Kostas Tsigaridis[15,14], and Fiona Tummon[8,b]

[1]*Institute for Climate and Atmospheric Science, School of Earth and Environment, University of Leeds, UK*

[2]*GEOMAR Helmholtz Centre for Ocean Research Kiel, Kiel, Germany*

[3]*Max Planck Institute for Meteorology, Hamburg, Germany*

[4]*National Centre for Atmospheric Science, University of Leeds, UK*

[5]*Laboratory of Environmental Chemistry, Paul Scherrer Institut, 5232 Villigen, Switzerland*

[6]*Laboratoire d'Océanographie et du Climat: Expérimentations et Approches Numériques, Sorbonne Universités, UPMC,*
IPSL, UMR CNRS/IRD/MNHN, 75005 Paris, France

[7]*Department of Environmental Sciences, Informatics and Statistics, University Ca' Foscari of Venice, Mestre, Italy*

[8]*Institute for Atmospheric and Climate Science, ETH Zurich, Zurich, Switzerland*
9PMOD/WRC, Davos, Switzerland

[10]*LATMOS-IPSL, UPMC/Paris-Sorbonne, UVSQ/Paris Saclay, CNRS/INSU, Paris, France*

[11]*School of Chemistry, University of Leeds, UK*

[12]*Met Office Hadley Centre, Exeter, UK*

[13]*Atmospheric Chemistry Observations and Modeling Laboratory, National Center for Atmospheric Research, Boulder, CO, USA*

[14]*NASA Goddard Institute for Space Studies, New York, NY, USA*

[15]*Center for Climate Systems Research, Columbia University, New York, NY, USA*

[16]*British Antarctic Survey, Cambridge, UK*

[17]*Department of Environmental Sciences, Rutgers University, New Brunswick, NJ, USA*

[a] *now at: Department of Chemistry, University of Cambridge, UK and Department of Geography, University of Cambridge, UK*

[b] *now at: Faculty of Biosciences, Fisheries, and Economics, UiT The Arctic University of Norway, Tromsø, Norway*

This chapter is an adaptation of the following publication where the reference style and the figure, table and section numbers have been updated for continuity throughout the thesis:

Marshall, L., Schmidt, A., Toohey, M., Carslaw, K. S., Mann, G. W., Sigl, M., et al. 2018. Multi-model comparison of the volcanic sulfate deposition from the 1815 eruption of Mt. Tambora. *Atmospheric Chemistry and Physics*, **18**(3), pp. 2307-2328.

The supplement to this paper is included in Appendix B.

Abstract

The eruption of Mt. Tambora in 1815 was the largest volcanic eruption of the past 500 years. The eruption had significant climatic impacts, leading to the 1816 "year without a summer", and remains a valuable event from which to understand the climatic effects of large stratospheric volcanic sulfur dioxide injections. The eruption also resulted in one of the strongest and most easily identifiable volcanic sulfate signals in polar ice cores, which are widely used to reconstruct the timing and atmospheric sulfate loading of past eruptions. As part of the Model Intercomparison Project on the climatic response to Volcanic forcing (VolMIP), five state-of-the-art global aerosol models simulated this eruption. We analyse both simulated background (no Tambora) and volcanic (with Tambora) sulfate deposition to polar regions and compare to ice core records. The models simulate overall similar patterns of background sulfate deposition, although there are differences in regional details and magnitude. However, the volcanic sulfate deposition varies considerably between the models with differences in timing, spatial pattern and magnitude. Mean simulated deposited sulfate

on Antarctica ranges from 19 to 264 kg km^{-2} and on Greenland from 31 to 194 kg km^{-2}, as compared to the mean ice-core-derived estimates of roughly 50 kg km^{-2} for both Greenland and Antarctica. The ratio of the hemispheric atmospheric sulfate aerosol burden after the eruption to the average ice sheet deposited sulfate varies between models by up to a factor of 15. Sources of this inter-model variability include differences in both the formation and the transport of sulfate aerosol. Our results suggest that deriving relationships between sulfate deposited on ice sheets and atmospheric sulfate burdens from model simulations may be associated with greater uncertainties than previously thought.

2.1 Introduction

Mt. Tambora in Indonesia (8.2° S, 118.0° E) erupted in April 1815 (e.g. Oppenheimer, 2003) and had a considerable impact on climate, leading to widespread tropical and Northern Hemisphere (NH) mean cooling of ~ 1 °C and a "year without a summer" in 1816 (e.g. Raible et al., 2016). Volcanic sulfate aerosol, produced from the oxidation of sulfur dioxide (SO_2) emitted into the atmosphere by volcanoes, is transported throughout the atmosphere and deposited to the surface by both wet and dry processes, and some is eventually incorporated into polar ice (e.g. Robock, 2000). Bipolar volcanic sulfate deposition signals are presumed to result from tropical eruptions, whereby sulfur entering the tropical stratosphere is converted to sulfate aerosol, which is transported globally by the Brewer–Dobson circulation (e.g. Trepte et al., 1993; Langway et al., 1995; Robock, 2000; Gao et al., 2007). Polar ice core deposition signals typically start around 0.5–1 year after a large tropical eruption and remain elevated for approximately 2–3 years (Robock and Free, 1995; Sigl et al., 2015). Throughout the last 2500 years, polar ice core records show over 200 sulfate spikes, which have been used to estimate the timing, evolution and magnitude of radiative forcing of climate caused by volcanic eruptions during this period (Sigl et al., 2015). The 1815 eruption of Mt. Tambora produced the sixth largest bipolar sulfate signal of the last 2500 years (Sigl et al., 2015).

Determining the stratospheric aerosol properties of the 1815 Mt. Tambora eruption such as spatial extent of the sulfate aerosol cloud, aerosol optical depth and aerosol size distribution bears substantial uncertainties, which ultimately affects the quantification of its climatic impacts using climate models. As part of the Model

Intercomparison Project on the climatic response to volcanic forcing (VolMIP) (Zanchettin et al., 2016), which is a Coupled Model Intercomparison Project Phase 6 (CMIP6) endorsed activity (Eyring et al., 2016), coordinated simulations of the 1815 eruption of Mt. Tambora were performed with five state-of-the-art global aerosol models. Our study, motivated by the uncertainty that remains in the climatic forcing from this eruption, investigates the sources of uncertainty in the sulfate deposition to polar regions in these simulations and discusses implications for reconstructions of historic volcanic forcing.

Previous reconstructions of volcanic sulfate aerosol properties used to force climate models scaled the average sulfate deposited on Antarctica and Greenland to the hemispheric atmospheric sulfate aerosol burden (e.g. Gao et al., 2007; Crowley and Unterman, 2013; Sigl et al., 2015). Scaling factors (ratios of the hemispheric sulfate aerosol burden to the sulfate deposited at the poles) were based on the ratio of these two quantities as observed after the eruption of Mt. Pinatubo in 1991 and from the estimated atmospheric burden and measured deposited radioactive material after nuclear bomb tests. Previous climate model simulations of the ratio between atmospheric sulfate burden and polar deposited sulfate were also used to derive the scaling factors (Gao et al., 2007; 2008). These scaling factors may not hold for larger eruptions where volcanic sulfate aerosol particles can grow larger, increasing their sedimentation rate (e.g. Pinto et al., 1989; Timmreck et al., 2009). Toohey et al. (2013) also found that differences in the dynamical response to large-magnitude eruptions changed the spatial distribution of the deposited sulfate. Furthermore, available ice core measurements are not evenly distributed over both ice caps, and large spatial variations in the sulfate deposition fluxes can exist between individual ice cores due to differences in local accumulation rates and sulfate redistribution by snow drift (Clausen and Hammer, 1988; Cole-Dai et al., 1997; Zielinski et al., 1997; Cole-Dai et al., 2000; Wolff et al., 2005; Gao et al., 2006; Gao et al., 2007). It is therefore important that a range of ice core records from different geographical regions is used to estimate the average volcanic sulfate deposited on each ice cap. Previous studies using only a few ice cores to reconstruct volcanic forcing histories may be biased (e.g. Zielinski, 1995; Zielinski et al., 1996; Crowley, 2000), although it has been demonstrated that deposition fluxes derived from single ice cores at high-accumulation sites are representative of total ice sheet deposition (Toohey and Sigl, 2017). Gao et al. (2007), who analysed 44 ice cores to investigate the spatial

distribution of volcanic sulfate deposition during the last millennium, found larger average deposited sulfate on Greenland (mean deposition of 59 kg km^{-2}, using 22 ice cores) than on Antarctica (mean deposition of 51 kg km^{-2}, 17 ice cores) for the eruption of Mt. Tambora. However, Sigl et al. (2015) found, using additional high-temporal-resolution ice core records in Antarctica (Sigl et al., 2014), average Antarctic deposited sulfate of 46 kg km^{-2} and a smaller average deposited sulfate on Greenland of 40 kg km^{-2}, with both averages smaller than the averages provided by Gao et al. (2007). Although in Sigl et al. (2015) the Antarctic average was derived with 17 ice core records, the Greenland average was calculated from only 2 ice cores (NEEM and NGRIP) compared to the 22 cores used for Greenland in Gao et al. (2007).

Previous modelling studies that have investigated the sulfate deposition from the 1815 eruption of Mt. Tambora have failed to reproduce the magnitude of the measured deposited sulfate on both ice caps compared to ice core records, although the models were able to capture the spatial pattern (Gao et al., 2007; Toohey et al., 2013). Gao et al. (2007) found the model-simulated mean deposited sulfate to be a factor of 2 greater than the ice-core-derived estimate, with average Antarctic deposited sulfate of 113 kg km^{-2} and smaller Greenland deposited sulfate of 78 kg km^{-2}. Toohey et al. (2013), in contrast, found higher deposition to Greenland and, although matching the spatial pattern of deposited sulfate on Antarctica remarkably well, found model-simulated mean deposited sulfate to be ∼4.7 times greater than inferred from ice cores. Differences between simulated and measured deposited sulfate could be caused by inaccuracies in the model representation of several physical processes such as the formation and transport of sulfate aerosol, sedimentation, cross-tropopause transport and deposition processes (e.g. Hamill et al., 1997; SPARC, 2006). Neither of the models used by Toohey et al. (2013) and Gao et al. (2007) included a representation of the quasi-biennial oscillation (QBO), which may significantly impact the initial aerosol dispersion (e.g. Trepte et al., 1993). Furthermore, uncertainties exist in the source parameters used for simulating the eruption in models such as the SO_2 emission magnitude and emission height.

In general, sulfate deposited on the polar ice caps is only a small fraction of the sulfate deposited globally (e.g. Toohey et al., 2013) and there remains uncertainty surrounding the partitioning of the 1815 Mt. Tambora volcanic sulfate aerosol between both hemispheres. Model results can aid in the interpretation of the ice core

estimates by allowing us to assess the relationship between the simulated atmospheric sulfate aerosol burdens and the simulated deposited sulfate.

In this paper we focus on the model-simulated sulfate deposition and the implications for reconstructions of historic volcanic forcing by analysing the deposited sulfate simulated by four global aerosol models and comparing to ice core records. Section 2.2 describes the model simulations and ice core records. In Section 2.3 we assess the sulfate deposition simulated under both background (no Tambora) (Section 2.3.1) and volcanically perturbed (with Tambora) conditions (Section 2.3.2) and compare the simulated deposited sulfate to ice core measurements. We investigate the relationship between hemispheric atmospheric sulfate burdens and mean ice sheet deposited sulfate in Section 2.3.3 and explore reasons for model differences in Section 2.4. Conclusions are presented in Section 2.5.

2.2 Models and ice core data

2.2.1 Model descriptions

Of the five models that took part in the coordinated simulations of the 1815 eruption of Mt. Tambora (Zanchettin et al., 2016), only four simulated the sulfate deposition and are therefore included in our study. Model details are listed in Table 2.1. In each model aerosol formation and growth is simulated through parameterizations of nucleation, condensation and coagulation. Three of the four models have modal aerosol schemes in that the aerosol particle size distribution is represented by several log-normal modes. SOCOL-AER has a sectional scheme where the aerosol particle size distribution is represented by 40 discrete size bins. The models simulate the transport of stratospheric aerosol through sedimentation and large-scale circulation by the Brewer–Dobson circulation. The QBO is simulated by all models except for MAECHAM5-HAM and is either internally generated (UM-UKCA) or nudged (CESM1(WACCM) and SOCOL-AER). In CESM1(WACCM), MAECHAM5-HAM and UM-UKCA dry deposition schemes are resistance-based and wet deposition is parameterized based on model precipitation and convective processes, with aerosol removal calculated via first-order loss processes representing in-cloud and below-cloud scavenging (Stier et al., 2005; Mann et al., 2010; Lamarque et al., 2012; Liu et al., 2012; Bellouin et al., 2013; Kipling et al., 2013). In SOCOL-AER dry deposition is calculated by multiplying concentrations in the lowest model level by fixed values

depending on surface cover. Wet deposition in SOCOL-AER is not related to the precipitation in the model and H_2SO_4 wet deposition is approximated based on H_2SO_4 lifetime (Sheng et al., 2015b). Apart from MAECHAM5-HAM, the models include interactive hydroxyl radical (OH) chemistry, allowing OH concentrations to evolve throughout the simulations (Section 2.4.1.1). Photolysis rates are not impacted by sulfate aerosol in any of the models.

All four models simulate the 1991 eruption of Mt. Pinatubo in reasonable agreement with observations of the sulfate burden, aerosol optical depth and stratospheric heating (Niemeier et al., 2009; Toohey et al., 2011; Dhomse et al., 2014; Sheng et al., 2015a; Mills et al., 2016), giving confidence in the models' overall abilities to accurately simulate the atmospheric and climatic effects of a large-magnitude eruption. However, the models vary in the details regarding the model–observation comparisons. For example, MAECHAM5-HAM (Niemeier et al., 2009) and SOCOL-AER (Sheng et al., 2015a) simulated a too-rapid aerosol decay and UM-UKCA (Dhomse et al., 2014) had a low bias in the model-simulated aerosol effective radius compared to observations. Possible reasons for these differences include omitted or underrepresented influences from meteoric particles, too large sedimentation and cross-tropopause transport and too-fast transport from tropics to high latitudes. Conversely, the models differ in the amount of emitted SO_2 required to achieve good comparisons to observations with the mass of SO_2 emitted by the four models ranging from 10 Tg for UM-UKCA (Dhomse et al., 2014) and CESM1(WACCM) (Mills et al., 2016, 2017) to 12–14 Tg for SOCOL-AER (Sheng et al., 2015a) to 17 Tg for MAECHAM5-HAM (Niemeier et al., 2009; Toohey et al., 2011). For this reason, the use of a common protocol in this study (Section 2.2.2) enables us to better attribute potential differences in the results to model processes rather than to the eruption source parameters.

Table 2.1: Description of models, adapted from Kremser et al. (2016). Modal vs. sectional aerosol size distributions are described in the text.

Model	Horizontal resolution	Model top, model levels	Aerosol size distribution	Stratospheric compounds	Het. chem.[a]	OH	Sulfur source species	QBO	Reference
CESM1(WACCM)	0.94° × 1.25°	4.5×10^{-6} hPa, 70 levels	Modal, 3 modes	Sulfate, PSC, organics	Y	Interactive	OCS (337 pptv), DMS, anthrop[b]. SO_2, volcanic[c] SO_2	Nudged	Mills et al. (2016, 2017)
MAECHAM5-HAM	2.8° × 2.8° (T42)	0.01 hPa, 39 levels	Modal, 7 modes	Sulfate	N	Prescribed	OCS (∼500 pptv), DMS	NA	Stier et al. (2005), Niemeier et al. (2009)
SOCOL-AER	2.8° × 2.8° (T42)	0.01 hPa, 39 levels	Sectional, 40 size bins	Sulfate, PSC	Y	Interactive	OCS (337 pptv), DMS, CS2, anthrop. SO_2, volcanic SO_2	Nudged	Sheng et al. (2015a)
UM-UKCA	1.25° × 1.875° (N96)	84 km, 85 levels	Modal, 7 modes	Sulfate, PSC, organics, meteoric dust	Y	Interactive	OCS (∼500 pptv), DMS, anthrop. SO_2, volcanic SO_2	Internally generated	Dhomse et al. (2014), Brooke et al. (2017)

[a] Heterogeneous chemistry. [b] Preindustrial anthropogenic SO_2. [c] Volcanic SO_2 indicates SO_2 from passively degassing volcanoes.

Table 2.2: Model parameters used for the Tambora simulations.

Parameter	Value in this study
SO_2 emission	60 Tg SO_2
Eruption length	24 h
Eruption date	1 Apr
Latitude	Equator[a]
QBO phase	Easterly
SO_2 injection height	22–26 km[b]

[a] SO_2 was emitted at 0° N in CESM1(WACCM), MAECHAM5-HAM and UM-UKCA and at 8° S in SOCOL-AER and at a longitude of 118° E. [b] The altitude distribution for the SO_2 emission varied slightly between the models: SOCOL-AER's SO_2 emission flux was between 22 and 26 km, increasing linearly with height from zero at 22 km to max at 24 km and then decreasing linearly to zero at 26 km. MAECHAM5-HAM injected at a single model level at 30 hPa (~ 24 km). UM-UKCA and CESM1(WACCM) used a uniform injection between 22 and 26 km but as the models are not on regular grids and their vertical resolutions differ, the distribution of the emission over the model grid boxes cannot be exactly the same. As a result, the injection profiles differed slightly between the models.

2.2.2 Experiment setup

The parameters used for the Mt. Tambora simulations are listed in Table 2.2. Each model simulated the eruption by emitting 60 Tg of SO_2 at the approximate location of Mt. Tambora between approximately 22 and 26 km (see details in Table 2.2 regarding the injection details for each model) and during the easterly QBO phase. This SO_2 emission estimate is based on both petrological and ice core estimates (Self et al., 2004; Gao et al., 2008), but there remains uncertainty regarding the amount of SO_2 emitted, which could range between ~ 30 and 80 Tg SO_2 (e.g. Stoffel et al., 2015). Nevertheless, 60 Tg SO_2 remains our best estimate. There is also uncertainty in the altitude of the emission and QBO phase due to the lack of observations. Therefore, the injection altitude and QBO phase were chosen to match those of the 1991 Mt. Pinatubo eruption based on satellite and lidar observations (McCormick and Veiga, 1992; Read et al., 1993; Herzog and Graf, 2010). The eruption was simulated by emitting the SO_2 over 24 h on 1 April.

In MAECHAM5-HAM, SOCOL-AER and UM-UKCA simulations were atmosphere-only with prescribed preindustrial sea surface temperatures. In CESM1(WACCM) the simulations were run in a preindustrial coupled atmosphere–ocean mode. Climatological preindustrial settings were used for greenhouse gas concentrations, tropospheric aerosols and ozone as defined by each modelling group. The simulations were run for ~ 5 years and included five ensemble members, except for CESM1(WACCM), which had three members only. The models include additional species and processes compared to earlier modelling studies of Mt.

Tambora (e.g. Gao et al., 2007; Toohey et al., 2013). UM-UKCA for example includes meteoric smoke particles (Brooke et al., 2017) and an internally generated QBO. Model output is in the form of monthly means.

2.2.3 Ice core data

The ice cores used in this analysis are provided in Tables B.1 and B.2 in the Supplement (Appendix B). The Antarctic ice cores are the most extensive array of annually resolved cores that have been used to reconstruct historic volcanic forcing (Sigl et al., 2014, 2015). Greenland ice core records have been compiled from several studies (Table B.1). Further ice core measurements of the natural background sulfate deposition fluxes were taken from Lamarque et al. (2013).

Sulfate deposition fluxes are derived from ice cores by multiplying measured sulfate concentrations by the annual ice accumulation rate. To derive the volcanic sulfate deposition flux contribution the natural sulfate background level (e.g. due to marine biogenic sulfur emissions) is calculated in each ice core (the non-volcanic contribution) and a threshold flux value is chosen, above which sulfate is assumed to be of volcanic origin. The ice-core-derived volcanic sulfate deposition flux is then calculated as the difference between a year with the volcanic contribution and the mean of the non-volcanic years, and the resulting reported volcanic sulfate deposition flux is the sum of the fluxes in these perturbed years (Ferris et al., 2011; Cole-Dai et al., 2013; Sigl et al., 2013). Our comparable model-simulated volcanic deposition flux is calculated as the sum of the sulfate deposition anomalies (perturbed run minus control run) over the duration of the simulations. For SOCOL-AER, which has a sectional aerosol scheme, diagnostics are available for the wet and dry components of the sulfate deposition. For modal models, each of these components is further split into the contribution from each aerosol size mode simulated in the models (e.g. nucleation, Aitken, accumulation, coarse). The sulfate deposition flux is calculated (comparable to the ice-core-derived values) as the sum of all of these wet and dry components with a composition of SO_4^{2-} only. In the following sections, we define "total deposition" as referring to the sum of wet and dry deposition fluxes. We define "volcanic sulfate deposition" to specify the total sulfate deposition flux anomaly due to the eruption of Mt. Tambora and use "cumulative deposited sulfate" to specify the time-integrated volcanic sulfate deposition fluxes.

To compare the model-simulated results with ice core values, we calculate two statistical metrics: the normalized mean bias (NMB) and correlation coefficient (r). NMB is defined by:

$$NMB = \frac{\sum_{i=1}^{N}(M_i - O_i)}{\sum_{i=1}^{N}(O_i)} \quad (1)$$

where O_i is the ice-core-derived sulfate deposition and M_i is the simulated sulfate deposition in the model grid box containing the ice core. N is the number of ice core records. For both NMB and r, each ice core is given equal weighting. We define a high correlation as $r > 0.7$ and low correlation as $r < 0.3$.

2.3 Results

2.3.1 Preindustrial background sulfate deposition

Figure 2.1 shows the average annual sulfate deposition fluxes in the preindustrial control simulations (no Tambora) for each model. Areas of high background sulfate deposition fluxes are found in close proximity to sulfur emission sources such as continuously degassing volcanoes (e.g. in South America and Indonesia) and along and near midlatitude storm tracks (30–60°) where aerosol is removed effectively by precipitation (except SOCOL-AER, where the deposition is not affected by precipitation). Continuously degassing volcanic emissions are not included in MAECHAM5-HAM. Sulfate deposition fluxes are higher over the oceans than over the land, mainly due to the emission of marine dimethyl sulfide (DMS). In general, Figure 2.1 shows that the models have similar background sulfate deposition patterns, with the global mean total (wet + dry) sulfate deposition flux ranging from 78 kg SO_4 km^{-2} yr^{-1} (CESM1(WACCM)) to 173 kg SO_4 km^{-2} yr^{-1} (UM-UKCA).

We find that the preindustrial background global mean atmospheric sulfate burdens are similar between CESM1(WACCM), MAECHAM5-HAM and SOCOL-AER but ~ 2–3 times larger in UM-UKCA (Figure B.1 in the Supplement). Sulfur source species included in each model are listed in Table 2.1. Although the models have similar background sulfate deposition patterns, the partitioning of wet and dry deposition fluxes differs markedly between the models (Figure 2.1, Table 2.3). MAECHAM5-HAM deposits very little sulfate by dry processes compared to the other models with annual global dry deposited sulfate a factor of ~ 40 less than the

global wet deposited sulfate. In SOCOL-AER, dry deposited sulfate is approximately half the magnitude of wet deposited sulfate.

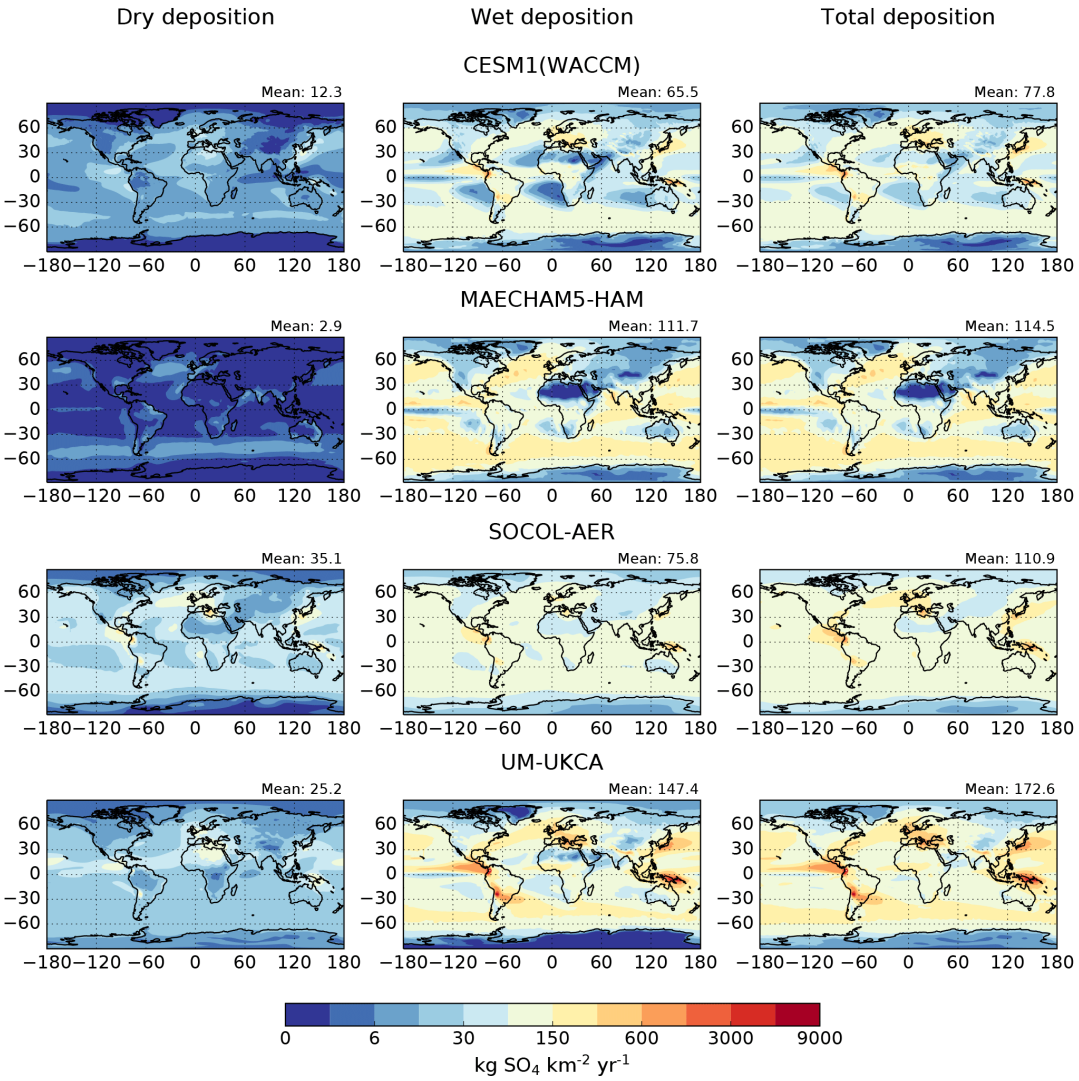

Figure 2.1: Preindustrial background annual dry, wet and total (wet + dry) sulfate deposition fluxes (kg SO_4 km^{-2} yr^{-1}) (left to right) for each model (top to bottom). The value shown in the top right-hand corner of each plot refers to the global mean sulfate deposition flux. Background fluxes are averages of the annual deposition from five control simulations each with 4 years of data for UM-UKCA, three controls each with 5 years of data for CESM1(WACCM) and one control with 5 years of data for MAECHAM5-HAM and SOCOL-AER.

Table 2.3: Annual global deposition fluxes of SO_2, SO_4 and SO_X (SO_2 + SO_4) for dry deposition, wet deposition and total dry + wet (Tg S yr^{-1}) in the preindustrial controls and in the ACCMIP multi-model mean (see text).

Model	Dry SO_2	Wet SO_2	Total SO_2	Dry SO_4	Wet SO_4	Total SO_4	Dry SO_X	Wet SO_X	Total SO_X
CESM1(WACCM)	5	11	16	2	11	13	7	22	29
MAECHAM5-HAM	2	2	4	0.5	19	19	3	21	24
SOCOL-AER	12	13	25	6	13	19	18	26	44
UM-UKCA	7	5	12	4	25	29	11	30	41
ACCMIP multi-model mean	–	–	–	–	–	–	11	23	34

The sulfate deposited on Antarctica and Greenland is a very small fraction (less than 1 %) of the sulfate deposited globally. In UM-UKCA the sulfate deposited on the polar ice sheets is dominated by dry deposition, which is supported by observations (Legrand and Mayewski, 1997), especially in the Antarctic interior (Wolff, 2012). In contrast, in MAECHAM5-HAM, SOCOL-AER and CESM1(WACCM) the sulfate deposited on the polar ice sheets is dominated by wet deposition, suggesting an issue with the deposition or precipitation representation. However, we find that the simulated total precipitation compares well between models both globally and over the poles (Figures B.2 and B.3) indicating the differences in wet and dry deposition partitioning are due to each model's deposition schemes.

The annual global deposition for both SO_2 and SO_4 is listed in Table 2.3 for each model. Included for reference is the equivalent preindustrial SO_X (SO_2 + SO_4) deposition from the multi-model mean of the Atmospheric Chemistry and Climate Model Intercomparison Project (ACCMIP) (Lamarque et al., 2013, their Table S4a). The ACCMIP simulations were set up as time-slice experiments and the multi-model mean listed is an average of seven models. UM-UKCA compares well to the ACCMIP multi-model mean for dry SO_X, but the wet SO_X is 7 Tg S yr^{-1} higher and the SO_4 deposition (29 Tg S yr^{-1}) is also much higher when compared to the other models (13–19 Tg S yr^{-1}). MAECHAM5-HAM has a similar total for wet SO_X compared to the ACCMIP multi-model mean, but dry deposition is a factor of 4 lower. CESM1(WACCM) has a similar total for wet SO_X deposition compared to the ACCMIP multi-model mean but total SO_X is 5 Tg S yr^{-1} lower. SOCOL-AER simulates the highest dry SO_X (18 Tg S yr^{-1}) and total SO_X (44 Tg S yr^{-1}) with total SO_X 10 Tg S yr^{-1} greater than the ACCMIP multi-model mean.

Following the analysis of Lamarque et al. (2013) we have taken the average sulfate deposition fluxes from 1850 to 1860 (a non-volcanic period) in several ice cores from Antarctica and Greenland and compared the ice core fluxes to the modelled polar

sulfate deposition fluxes in the control simulations (Figure 2.2). Ice core meta-data are included in the Supplement (Table B.2).

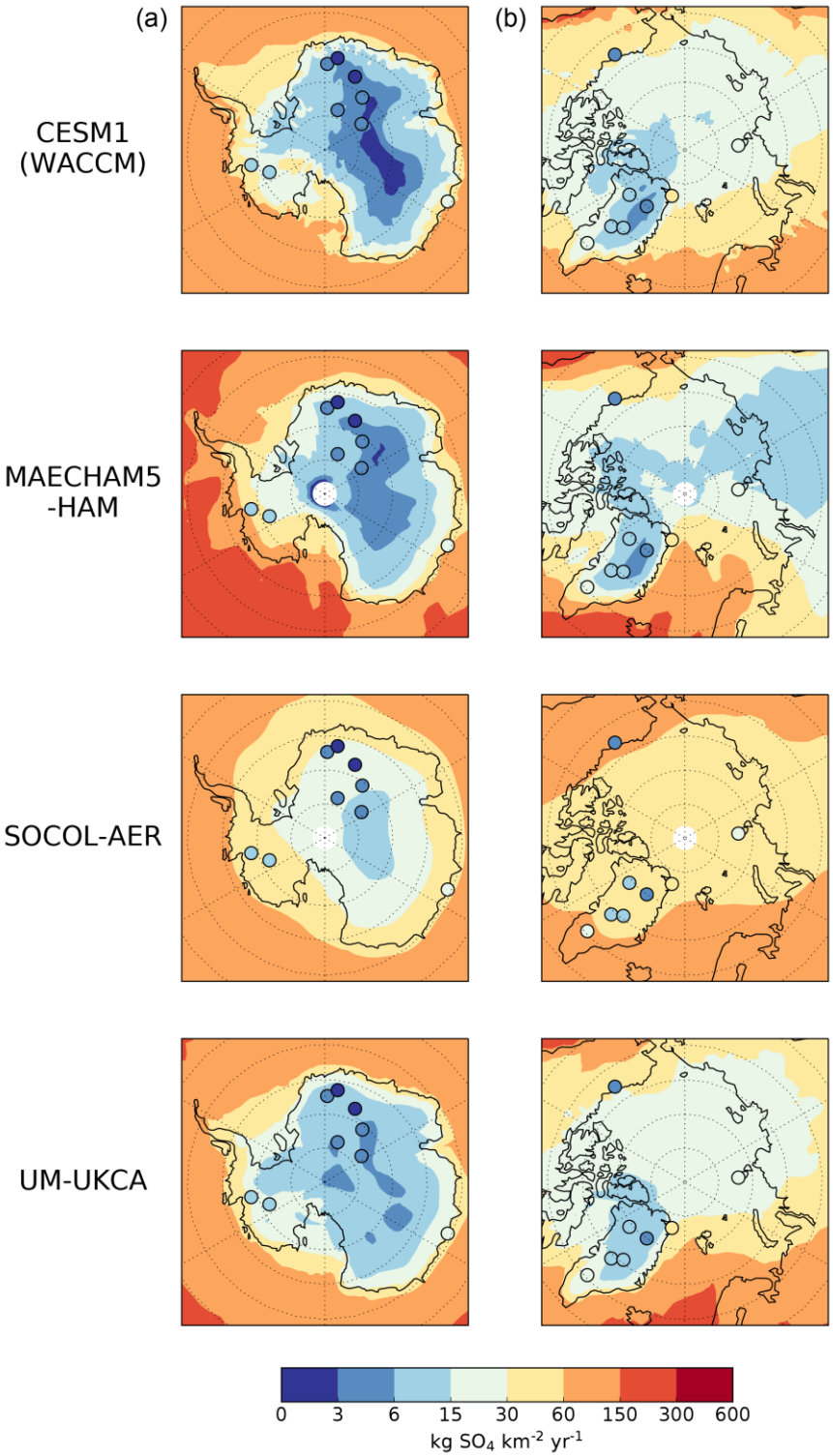

Figure 2.2: Total (wet + dry) sulfate deposition fluxes (kg SO_4 km^{-2} yr^{-1}) for Antarctica (a) and the Arctic (b) for the preindustrial background from the control simulations (shading) compared to preindustrial ice core sulfate fluxes (filled circles), averaged for 1850 to 1860.

Overall, CESM1(WACCM), MAECHAM5-HAM and UM-UKCA simulate similar background polar sulfate deposition patterns and magnitudes and compare well to preindustrial ice core sulfate fluxes. Scatter plots of the ice core fluxes vs. those simulated by each model are shown in Figure 2.3. SOCOL-AER simulates slightly higher deposition with reduced regional variability compared to the other models (Figure 2.2). However, compared to the ice cores, all models capture the lower sulfate deposition in the interior of Antarctica and higher sulfate deposition toward the coast. The models overestimate Antarctic deposition, particularly in West Antarctica. Antarctic NMB (Section 2.2.3, Eq. 1) ranges from 1.3 (UM-UKCA) to 3.9 (SOCOL-AER) but we find that the model-simulated Antarctic sulfate deposition and Antarctic ice core values are highly correlated for all models with r above 0.9 (Figure 2.3). Deposition over the Arctic is also well captured, with MAECHAM5-HAM and CESM1(WACCM) slightly underestimating the sulfate deposition fluxes, both with NMB of −0.1. UM-UKCA has a very small positive NMB of 0.01 but SOCOL-AER has the highest Arctic deposition with a NMB of 1.7. None of the models capture the low flux recorded in Alaska as also found by Lamarque et al. (2013).

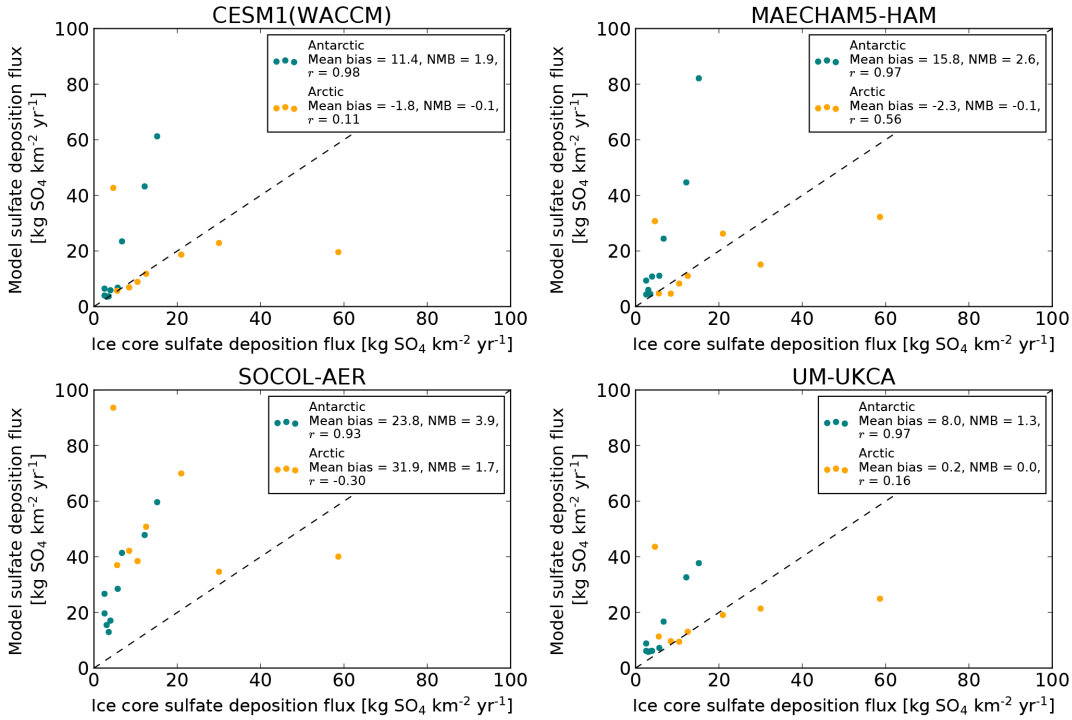

Figure 2.3: Scatter plots of preindustrial background ice core sulfate deposition fluxes vs. simulated preindustrial sulfate fluxes (kg SO_4 km^{-2} yr^{-1}) in the Antarctic (teal points) and in the Arctic (orange points) for each model. Simulated values represent the grid box value where each ice core is located. The dashed line marks the 1:1 line. Included in the legends are the mean bias, normalized mean bias (NMB) and the correlation coefficient (r) for the Antarctic and Arctic.

The background polar sulfate deposition flux is highly correlated with the simulated mean polar precipitation for CESM1(WACCM), MAECHAM5-HAM and UM-UKCA. Correlation coefficients in the Arctic (60–90°) are between 0.8 (MAECHAM5-HAM and UM-UKCA) and 0.9 (CESM1(WACCM)). The correlation coefficients are slightly higher in the Antarctic (−60° to −90°) with r = 0.9 for all models. In SOCOL-AER, the higher NMB between simulated polar sulfate deposition fluxes and ice core values is due to the more simplified deposition scheme in this model, which is not connected to the model's simulated precipitation. We find that the Antarctic precipitation in each model matches measured accumulation rates in ice cores (Figure B.3) and with a high correlation with r values of between 0.7 (SOCOL-AER, included for reference) to 0.9 (CESM1(WACCM), UM-UKCA). UM-UKCA and CESM1(WACCM) have very small NMB of ∼ 0.1. MAECHAM5-HAM has a slightly higher NMB of 0.6 and SOCOL-AER a NMB of 0.8. In the Arctic, the models also capture the precipitation reasonably well compared to the accumulation in the ice cores, with NMB of between 0.1 (UM-UKCA) and 0.5 (CESM1(WACCM)) but low correlation coefficients (r lies between 0.1 and 0.2 for all models). Thus, compared to the ice cores the models capture the magnitude and spatial pattern of the background polar precipitation. Overall, the magnitude of the deposited sulfate in CESM1(WACCM) and MAECHAM5-HAM, where deposition to the ice sheets is dominated by wet deposition, is expected to be driven by the snow accumulation rates across the ice sheets, which are well represented by all models (Figure B.3). In UM-UKCA, although the polar deposition is correlated with the polar precipitation, the ice sheet sulfate deposition mostly occurs by dry deposition. This is because this model deactivates nucleation scavenging when more than a threshold fraction of the cloud water is present as ice, greatly reducing the aerosol scavenging in polar regions. In SOCOL-AER, fewer regional details are captured since the deposition scheme is simpler and is not connected to precipitation, and therefore the deposition mostly reflects the tropospheric distribution of sulfate.

In summary the models simulate similar overall patterns of background sulfate deposition fluxes, although there are differences in the regional details and magnitude. The similarities and realistic deposition patterns amongst the models suggests that the background sulfate emissions, transport and deposition processes are reasonably parameterized. Although SOCOL-AER is less able to simulate regional details, its

simplified deposition scheme is still sufficient for the analysis of interhemispheric differences and the temporal evolution of deposition.

2.3.2 1815 Mt. Tambora eruption sulfate deposition

2.3.2.1 Global sulfate deposition

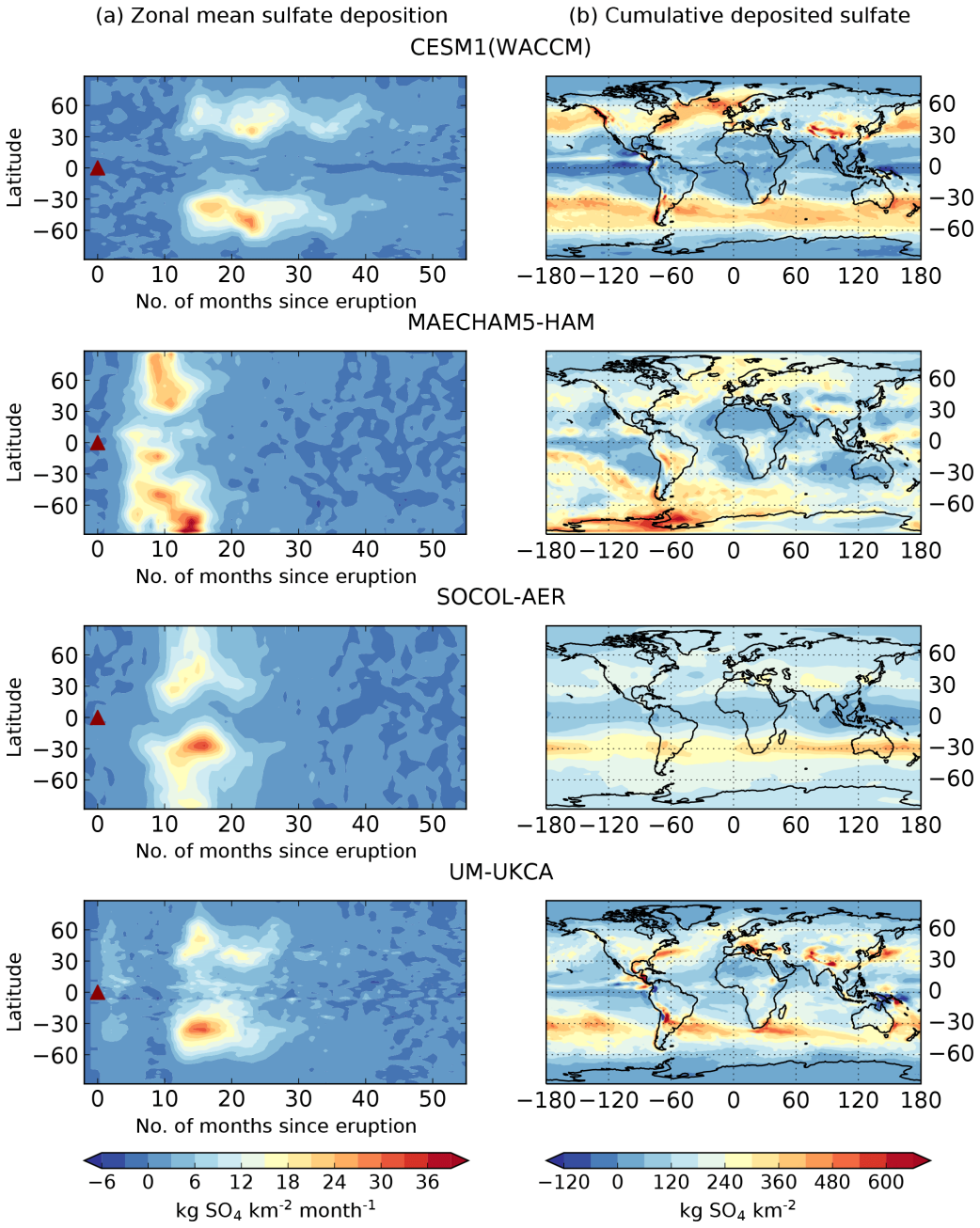

Figure 2.4: Zonal mean volcanic sulfate deposition (kg SO_4 km^{-2} $month^{-1}$) (a) and cumulative deposited sulfate (kg SO_4 km^{-2}) (b) for each model (ensemble mean). The red triangles mark the start of the eruption (1 April 1815). Volcanic sulfate deposition is calculated as the difference in total sulfate deposition (wet + dry) between the perturbed and control simulations and this anomaly is summed over the ~ 5 years of simulation to produce the cumulative sulfate deposition maps (right column).

Figure 2.4 shows the zonal mean monthly volcanic sulfate deposition (a) and cumulative deposited sulfate (b) simulated by each model and highlights inter-model differences in the timing and spatial distribution of the deposited sulfate. Deposition occurs rapidly in MAECHAM5-HAM with 35 % of the global deposition occurring in 1815 and the majority (60 %) occurring in 1816. SOCOL-AER simulates the sulfate deposition starting slightly later than in MAECHAM5-HAM, with the majority of the deposition (75 %) occurring in 1816. In contrast, only 9 % of deposition in UM-UKCA occurs in 1815, with 55 % in 1816 and 29 % in 1817. In CESM1(WACCM) the deposition occurs even later, with no deposition occurring in 1815. Instead, 32 % is deposited in 1816, 46 % in 1817 and 17 % in 1818. Deposition is longest in duration in CESM1(WACCM) and global sulfate deposition remains elevated at the end of the simulation (Figure 2.5). In MAECHAM5-HAM deposition returns to near background levels by ~ 30 months after the eruption and ~ 40 months for UM-UKCA and SOCOL-AER. We find individual ensemble members are similar for each model and the ensemble spread in the global volcanic sulfate deposition over time is small, as shown in Figure 2.5.

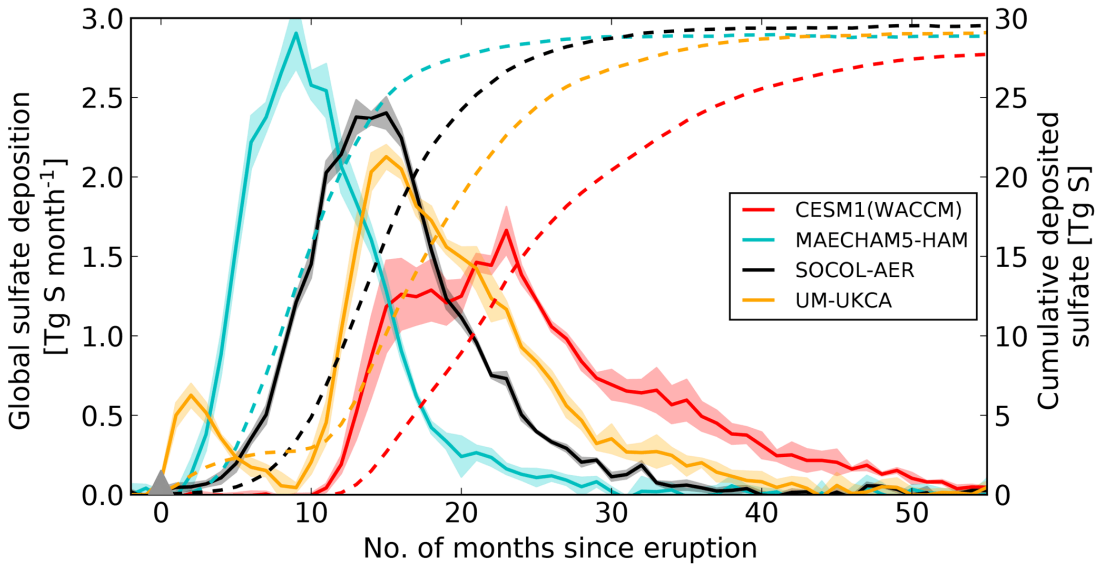

Figure 2.5: Global volcanic sulfate deposition (Tg S month^{-1}) (solid lines – left axis) and global cumulative deposited sulfate (Tg S) (dashed lines – right axis) for each model (colours). Ensemble mean is shown by the solid line; shading marks 1 SD. The grey triangle marks the start of the eruption (1 April 1815).

Table 2.4: Global cumulative deposited sulfate (Tg S) from dry and wet processes for each model (ensemble mean).

Model	Dry deposition	Wet deposition	Total deposition
CESM1(WACCM)	2.4	25.4	27.8
MAECHAM5-HAM	0.2	28.7	28.9
SOCOL-AER	1.0	28.5	29.5
UM-UKCA	3.7	25.4	29.1

In UM-UKCA and CESM1(WACCM) most of the volcanic sulfate is deposited at midlatitudes (30–60°). This contrasts with MAECHAM-HAM, where the deposition is globally more uniform, with greater deposition in the polar regions and high deposited sulfate exceeding 360 kg SO_4 km^{-2} over West Antarctica, which is completely absent in the other models. In SOCOL-AER, deposition is greatest in the Southern Hemisphere (SH) midlatitudes.

The models vary in the simulated relative contribution of wet deposition of sulfate and dry deposition of sulfate to the global cumulative deposited sulfate (Table 2.4), although the total deposition is always dominated by wet deposition, as was also the case with the background sulfate deposition (Figure 2.1, Table 2.3). Dry deposited sulfate in MAECHAM5-HAM is a factor of 15 lower than the dry deposited sulfate simulated by UM-UKCA and CESM1(WACCM). SOCOL-AER also simulates fairly low dry deposited sulfate (1.0 Tg S).

2.3.2.2 Ice sheet sulfate deposition

Although the models simulated similar preindustrial background (no Tambora) polar sulfate deposition (with the exception of SOCOL-AER) (Figure 2.2), the simulated polar volcanic sulfate deposition varies in time, space and magnitude between the models. Figure 2.6 shows the simulated cumulative deposited sulfate for each model compared to the cumulative deposited sulfate measured in ice cores from Greenland and Antarctica for the 1815 Mt. Tambora eruption.

In general, the ice cores from Antarctica show lower volcanic sulfate deposition in East Antarctica and higher deposition over the Antarctic Peninsula, with deposited sulfate ranging from 13 kg SO_4 km^{-2} (East Antarctica, core NUS07-7) to 133 kg SO_4 km^{-2} (Antarctic Peninsula, core Siple Station). In Greenland the ice core estimates range from 25 kg SO_4 km^{-2} (core B20) to 85 kg SO_4 km^{-2} (core D3).

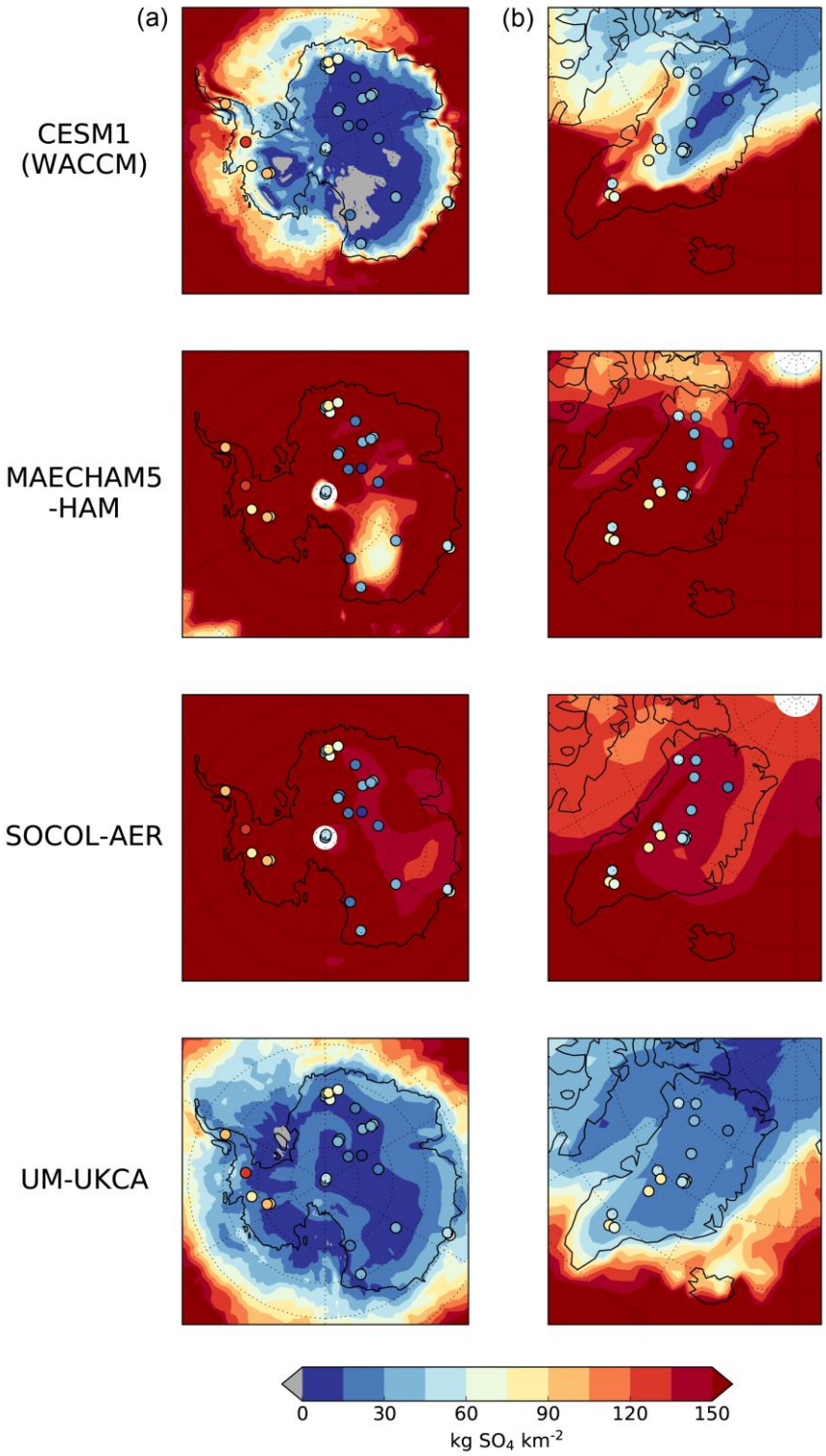

Figure 2.6: Cumulative deposited sulfate (kg SO_4 km^{-2}) integrated over the whole duration of model simulation (~ 5 years) on Antarctica (a) and Greenland (b) for each model (ensemble mean). Ice core cumulative deposited sulfate values are plotted as coloured circles. Ice cores from adjacent sites or in close proximity (Table B.1) have been slightly relocated to avoid cores completely overlapping. Scaled versions for MAECHAM5-HAM and SOCOL-AER are included in the Supplement (Figure B.4).

We find MAECHAM5-HAM and SOCOL-AER simulate too much deposited sulfate on Antarctica and Greenland compared to the ice cores records (also seen in Toohey et al., 2013), whereas UM-UKCA and CESM1(WACCM) simulate deposited sulfate much closer to the ice core values (Figure 2.6). For Antarctica the NMB are 3.9 for MAECHAM5-HAM, 2.0 for SOCOL-AER, −0.5 for CESM1(WACCM) and −0.7 for UM-UKCA. For Greenland the biases are slightly lower: 2.5 for MAECHAM5-HAM, 1.7 for SOCOL-AER, 0.03 for CESM1(WACCM) and −0.5 for UM-UKCA. However, although MAECHAM5-HAM is the model with the highest bias between the simulated cumulative deposited sulfate and ice core values, we find that the simulated Antarctic cumulative deposited sulfate in MAECHAM5-HAM is highly spatially correlated with the ice core values (r = 0.8) and Greenland deposition is moderately correlated (r = 0.6). Hence MAECHAM5-HAM captures the spatial pattern of the deposited sulfate, especially in Antarctica, with greater deposition on the Antarctic Peninsula and lower deposition in East Antarctica, but the magnitude of the deposition is ∼ 3.7 times too large. Figure 2.7 shows the ice core values vs. the model-simulated cumulative deposited sulfate. Correlation coefficients are less than ∼ 0.5 for all models except MAECHAM5-HAM, although these models have lower mean biases. A figure where the simulated deposition in MAECHAM5-HAM has been reduced by a factor of 3 to illustrate the well-captured spatial pattern of deposition is included in Figure B.4 (SOCOL-AER is also included in this figure). Both UM-UKCA and CESM1(WACCM), which are the higher-resolution models, simulate a strong gradient in deposition between the low deposition over land and high deposition over sea and, although they match the magnitude of the cumulative deposited sulfate more closely on the ice sheets than SOCOL-AER and MAECHAM5-HAM, they fail to produce the high values of cumulative deposited sulfate on the Antarctic Peninsula.

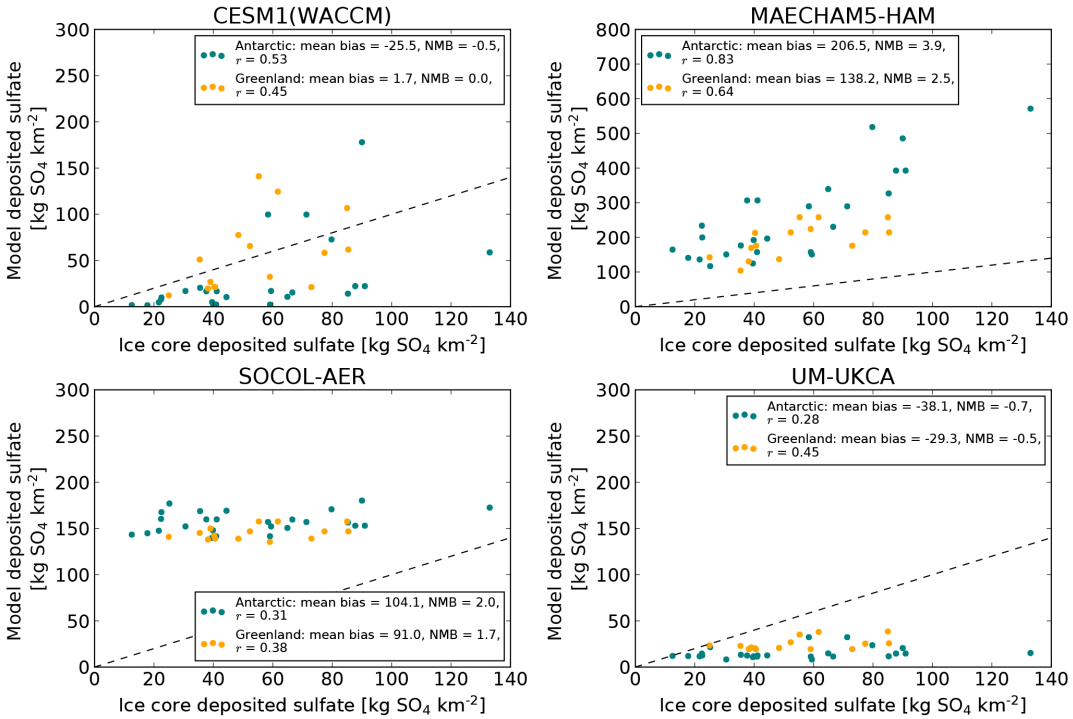

Figure 2.7: Scatter plots of cumulative deposited sulfate (kg SO_4 km^{-2}) due to the eruption of Mt. Tambora recorded in ice cores vs. that simulated by each model (ensemble mean) in Antarctica (teal points) and Greenland (orange points). Simulated values represent the grid box value where each ice core is located. The dashed line marks the 1:1 line. For each model and for Greenland and Antarctica the mean bias, normalized mean bias (NMB) and correlation coefficient (*r*) between the simulated deposited sulfate and ice core values are shown in the legend. There is an increased y-axis scale for MAECHAM5-HAM.

The polar deposition in UM-UKCA and CESM1(WACCM) more closely follows the models' precipitation field, with correlation coefficients between the polar (60–90°) precipitation (averaged over the 4 years after the eruption) and polar cumulative deposited sulfate (in the 4 years after the eruption) of 0.7 and 0.9, respectively. Polar correlation coefficients for MAECHAM5-HAM are 0.6 in the Arctic and 0.4 in the Antarctic. Figure 2.8 shows the zonal mean precipitation and zonal mean cumulative deposited sulfate in each model. The precipitation in the models is very similar, suggesting that the differences in model-simulated volcanic sulfate deposition arise from differences in the transport of the sulfate aerosol to the polar regions and/or the deposition schemes themselves. The ice sheet sulfate deposition in UM-UKCA remains dominated by dry deposition.

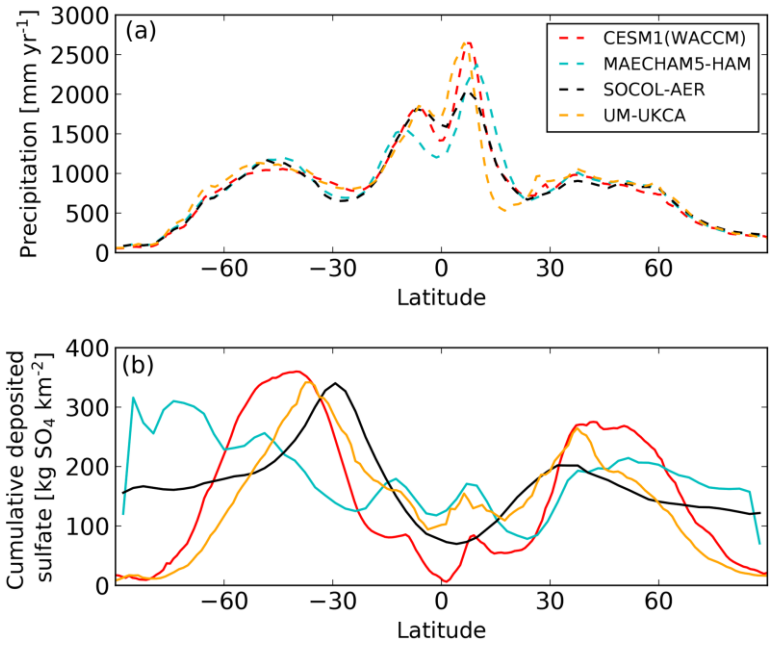

Figure 2.8: Zonal mean precipitation (mm yr^{-1}) averaged over the first 4 years after the eruption (a, dashed lines) and zonal mean cumulative deposited sulfate (kg SO_4 km^{-2}) in the first 4 years after the eruption (b, solid lines) for the ensemble mean in each model (colours).

Figure 2.9 shows for each model the simulated area-mean volcanic sulfate deposition to the Antarctic and Greenland ice sheets over time, compared to two of the highest resolved and most precisely dated ice cores (D4: McConnell et al., 2007; DIV2010: Sigl et al., 2014). We find that deposition to both ice sheets peaks first in MAECHAM5-HAM, followed by SOCOL-AER, then UM-UKCA and CESM1(WACCM). The main phase of deposition recorded in the two ice cores falls in time between that simulated by MAECHAM5-HAM and the other models. Compared to DIV2010 and D4, the deposition to the ice sheets in MAECHAM5-HAM is too quick, but too slow in CESM1(WACCM) and UM-UKCA, although the timing is still relatively well captured for all models. The onset and duration of deposition to the ice sheets simulated by SOCOL-AER is most comparable to the two ice cores, suggesting a good representation of the volcanic aerosol evolution, but simulated deposition is too large (see Figure 2.6). The timing of the ice sheet deposition is further explored in Section 2.3.3.

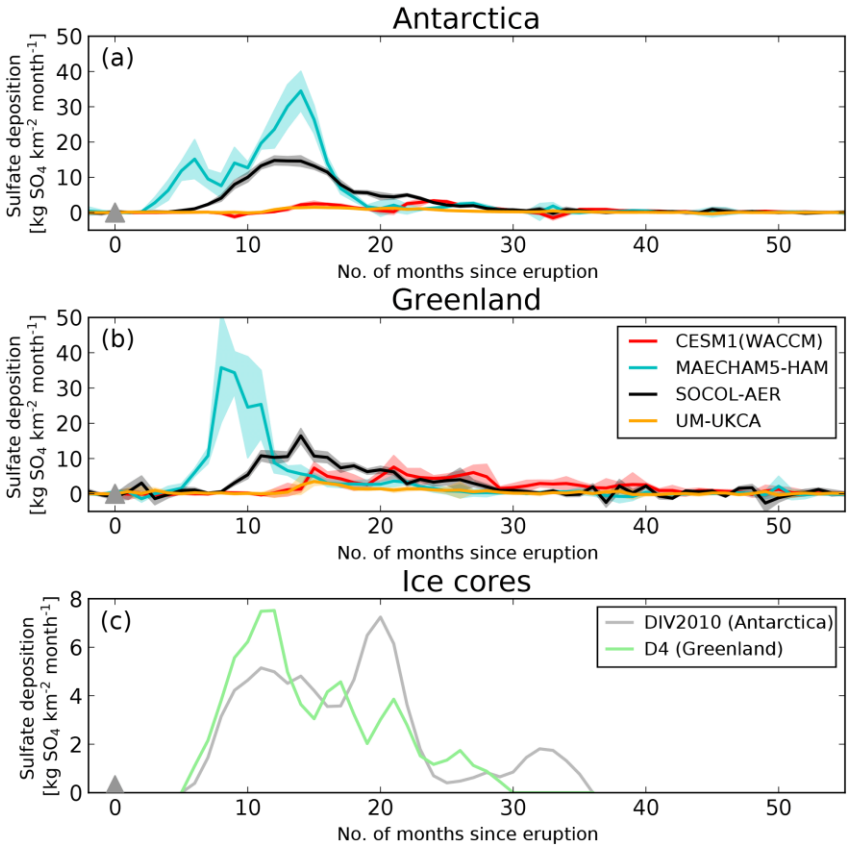

Figure 2.9: Simulated area-mean volcanic sulfate deposition (kg SO_4 km^{-2} $month^{-1}$) to the Antarctic ice sheet (a) and Greenland ice sheet (b) for each model (colours). Each ice sheet mean is defined by taking an area-weighted mean of the grid boxes in the appropriate regions once a land–sea mask has been applied. Solid lines mark the ensemble mean and shading is 1 SD. (c) Deposition fluxes from two monthly-resolved ice cores (DIV2010 from Antarctica and D4 from Greenland). The scale is reduced in (c). The grey triangles mark the start of the eruption (1 April 1815).

2.3.3 Ice sheet sulfate deposition and relationship to sulfate burdens

The temporal and spatial evolution of the volcanic sulfate deposition ultimately reflects the evolution of the atmospheric volcanic sulfate burdens. Figure 2.10 shows the zonal mean monthly mean and global monthly mean atmospheric volcanic sulfate burdens for each model. MAECHAM5-HAM has the fastest conversion of SO_2 to sulfate aerosol, with the global peak sulfate burden occurring only 4 months after the eruption (Figure 2.10b). This fast conversion is likely due to the lack of interactive OH in the model (Table 2.1), since OH does not become depleted by reaction with SO_2. In UM-UKCA and SOCOL-AER the peak global sulfate burden occurs 6–7 months after the eruption, but the global burden in SOCOL-AER decays more rapidly than in UM-UKCA. The global burden in CESM1(WACCM) peaks 12 months after

the eruption and remains elevated for another 3.5 years (until the end of the simulation) and hence deposition in CESM1(WACCM) is longer lived. The delay in full conversion of SO_2 to sulfate aerosol in these models is due to initial depletion of OH, which we explore further in Section 2.4.1.1. In all models there is stronger transport of the sulfate aerosol to the SH compared to the NH (Figure 2.10a) due to the Brewer–Dobson circulation, which is stronger in the winter hemisphere.

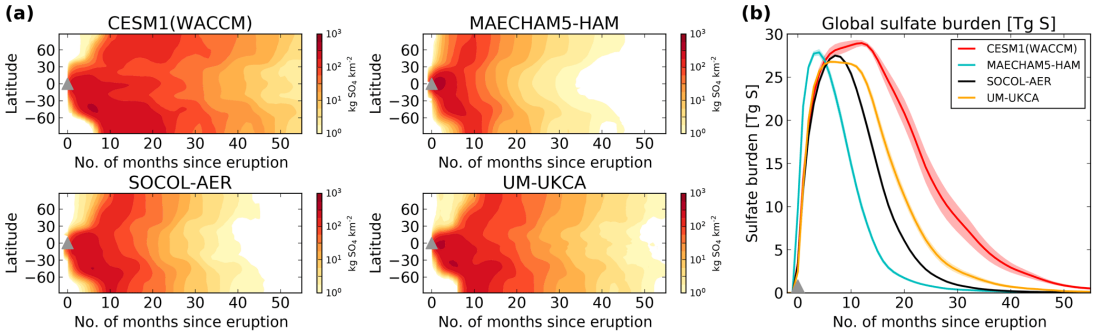

Figure 2.10: (a) Zonal mean atmospheric sulfate burdens in each model (kg SO_4 km^{-2}) (ensemble mean) and (b) global atmospheric sulfate burdens (Tg S) in each model (colours). Ensemble means are shown by the coloured lines; shadings mark 1 SD. Sulfate burdens are monthly mean anomalies. The grey triangles mark the start of the eruption (1 April 1815).

Table 2.5: Greenland and Antarctica ice sheet mean cumulative deposited sulfate and ratio (Antarctica deposition / Greenland deposition) and peak NH and SH sulfate burdens (total atmospheric column burden anomaly) and ratio (SH burden / NH burden) for each model (ensemble mean). Also included is the equivalent mean deposited sulfate on each ice sheet calculated from ice cores (Gao et al., 2007; Sigl et al., 2015).

Model	Mean Antarctica deposited sulfate ($kg\,SO_4\,km^{-2}$)	Mean Greenland deposited sulfate ($kg\,SO_4\,km^{-2}$)	Antarctica / Greenland deposition ratio	Peak SH sulfate burden ($Tg\,SO_4$)	Peak NH sulfate burden ($Tg\,SO_4$)	SH / NH burden ratio
CESM1(WACCM)	36	109	0.3	58	34	1.7
MAECHAM5-HAM	264	194	1.4	50	36	1.4
SOCOL-AER	163	148	1.1	56	32	1.8
UM-UKCA	19	31	0.6	56	29	1.9
Sigl et al. (2015)	46	40	1.2	–	–	–
Gao et al. (2007)	51	59	0.9	–	–	–

Here we consider the relationships between the NH sulfate burden vs. the SH sulfate burden, the cumulative sulfate deposited on Antarctica vs. Greenland and, most importantly, between the hemispheric sulfate burdens and the sulfate deposited on each ice sheet.

In all models the SH peak atmospheric sulfate burden is greater than the NH peak atmospheric sulfate burden (Table 2.5). Ratios between the SH and NH peak burdens are between 1.4 and 1.9. However, despite the larger SH burden, only MAECHAM5-HAM and SOCOL-AER simulate greater Antarctica mean deposited sulfate than in Greenland. CESM1(WACCM) has the smallest deposition ratio (0.3) with mean Greenland deposited sulfate of 109 kg SO_4 km^{-2} compared to 36 kg SO_4 km^{-2} in Antarctica. MAECHAM5-HAM and SOCOL-AER have the closest deposition ratio to that derived by Sigl et al. (2015), but with mean deposited sulfate ~ 4–6 times larger than the Sigl et al. (2015) estimates. Conversely, and as simulated in UM-UKCA and CESM1(WACCM), the mean deposited sulfate deduced by Gao et al. (2007) for the eruption of Mt. Tambora showed slightly more mean deposited sulfate on Greenland relative to Antarctica, with a ratio of 0.9, although this ratio is still much larger than in UM-UKCA and CESM1(WACCM). In contrast to MAECHAM5-HAM and SOCOL-AER, where the deposition ratio mirrors the hemispheric split of the sulfate aerosol burdens, deposition ratios for both UM-UKCA and CESM1(WACCM) are dissimilar to the ratio of the hemispheric peak burdens.

Figure 2.11 shows the simulated deposition to each ice sheet over time as in Figure 2.9, except we compare to the hemispheric sulfate burdens. In MAECHAM5-HAM the NH sulfate burden peaks only 2 months after the eruption and the SH burden peaks 4 months after the eruption. The ice sheet deposition follows suit with the majority of deposition to Greenland occurring 8 months after the eruption and peak deposition to Antarctica occurring 14 months after the eruption. However, in the other models the SH burden peaks before the NH burden. The SH burden is greatest between 5 and 7 months after the eruption in these models and the NH burden peaks between 10 and 12 months after the eruption. In contrast to MAECHAM5-HAM, there are no clear separate peaks between the deposition to each ice sheet. In SOCOL-AER both the majority of Greenland and Antarctic deposition occurs between 10 and 20 months after the eruption, which was found to compare well to the timing recorded in two ice cores (Figure 2.9). In UM-UKCA and CESM1(WACCM) the main phase of deposition is longer lived and occurs between 10 and 30 months after the eruption.

Overall, decay of the atmospheric sulfate burden and deposition to the ice sheets in MAECHAM5-HAM is rapid, occurring within the first 20 months after the eruption, suggesting a fast transport of sulfate aerosol to the poles. We find that in the first ~ 8 months after the eruption the sulfate burden in UM-UKCA and CESM1(WACCM) is restricted between ~ 60° S and ~ 40° N (Figure 2.10a), with strong gradients in sulfate burden across the SH polar vortex and NH subtropical edge, whereas more sulfate is transported to the poles in MAECHAM5-HAM and SOCOL-AER. Reasons for this are explored in Section 2.4.

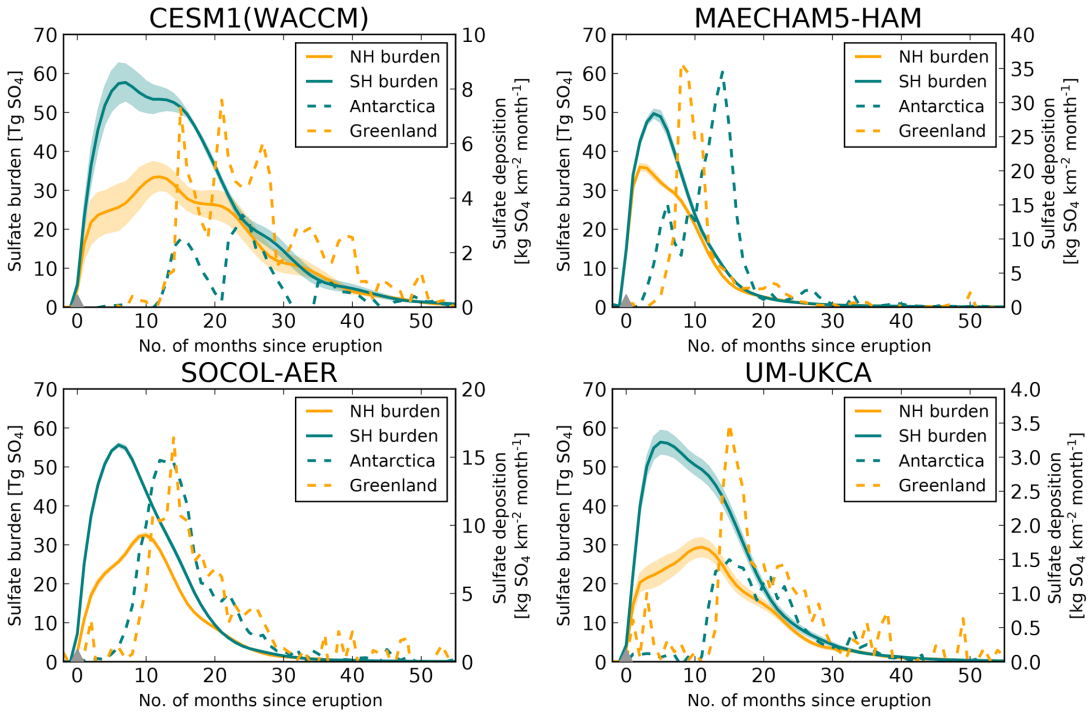

Figure 2.11: Hemispheric atmospheric sulfate burdens (Tg SO_4) (solid lines show the ensemble mean and shading is 1 SD) and area-mean ice sheet volcanic sulfate deposition as in Figure 2.9 (dashed lines) (kg SO_4 km^{-2} $month^{-1}$) for each model. The grey triangles mark the start of the eruption (1 April 1815). There are different scales on each secondary y axis for ice sheet deposition.

Table 2.6: Burden-to-deposition (BTD) factors ($\times 10^9$ km^2) between the hemispheric peak sulfate burden (Tg SO_4) (total atmospheric column burden anomaly) and the mean ice sheet cumulative deposited sulfate (kg SO_4 km^{-2}) for the four models and from Gao et al. (2007). The Gao et al. (2007) factors are interpreted as in Toohey and Sigl (2017) assuming the total burden is the mass of SO_4 not including the mass of water. Included are the values for the ensemble mean factor and the range from individual ensemble members.

	NH_BTD (10^9 km^2)		SH_BTD (10^9 km^2)	
Model	Ensemble mean	Ensemble range	Ensemble mean	Ensemble range
CESM1(WACCM)	0.31	0.29–0.34	1.63	1.44–1.96
MAECHAM5-HAM	0.19	0.14–0.24	0.19	0.17–0.20
SOCOL-AER	0.22	0.20–0.24	0.34	0.32–0.35
UM-UKCA	0.97	0.74–1.14	2.91	2.67–3.30
Multi-model mean	0.42	–	1.27	–
Gao et al. (2007)	1	–	1	–

Next, we calculate the ratio between the hemispheric peak atmospheric sulfate burdens (Tg SO_4) (representing the total amount of sulfate aerosol that has formed) and the average amount of sulfate deposited on each ice sheet (kg SO_4 km^{-2}) for each of the models. We refer to this ratio as the burden-to-deposition (BTD) factor, which is equivalent to the scaling factors derived by Gao et al. (2007) calculated from the observed relationship between the atmospheric burden and deposition of radioactive material after nuclear bomb tests. BTD factors are important for estimating the hemispheric atmospheric sulfate burden and subsequently estimating the forcing of historical volcanic eruptions based on ice core sulfate deposition records (Section 2.1). We calculate the BTD factors for both NH (NH_BTD) and SH (SH_BTD) (Table 2.6). BTD factors for MAECHAM5-HAM are the same for both the NH and SH, as in Gao et al. (2007), but a factor of 5 lower than Gao et al. (2007). CESM1(WACCM), SOCOL-AER and UM-UKCA simulate smaller NH_BTD than SH_BTD, but these factors are different in each model, with the NH_BTD ranging from 0.22×10^9 km^2 (SOCOL-AER) to 0.97×10^9 km^2 (UM-UKCA) and the SH_BTD from 0.34×10^9 km^2 (SOCOL-AER) to 2.91×10^9 km^2 (UM-UKCA). All models simulate a NH_BTD less than 1×10^9 km^2, but SH_BTD is less than 1×10^9 km^2 for only MAECHAM5-HAM and SOCOL-AER due to the much larger Antarctic deposition in these models compared to UM-UKCA and CESM1(WACCM). Overall, the NH_BTD factors differ by a factor of 5 between the models and SH_BTD by a factor of 15. The multi-model mean NH_BTD factor is 0.42×10^9 km^2 (~ 60 % smaller than in Gao et al., 2007) and multi-model mean SH_BTD factor is 1.27×10^9 km^2 (~ 30 % greater than

in Gao et al., 2007). We also find variability in the BTD factors across the individual ensemble members for each model arising due to internal variability, but ensemble spread is smaller than the inter-model spread.

We also test the sensitivity of the derived model BTD factors in Table 2.6 by taking polar deposition (60–90° N/S) as opposed to ice sheet deposition, given that both UM-UKCA and CESM1(WACCM) simulate strong gradients in cumulative deposited sulfate across the land–sea boundary (Figure 2.6). We find that the BTD factors remain similar for SOCOL-AER and MAECHAM5-HAM but are reduced by up to a factor of 3 in UM-UKCA due to the mean polar cumulative deposited sulfate being greater than the mean ice sheet cumulative deposited sulfate (Table B.3). In CESM1(WACCM) the SH_BTD is also reduced by a factor of 3, but the NH_BTD remains similar. Overall, the spread in the BTD factors between the models decreases and results in a reduction of the multi-model mean NH_BTD factor from 0.42×10^9 to 0.28×10^9 km^2 and the SH_BTD from 1.27×10^9 to 0.54×10^9 km^2.

2.4 Discussion

2.4.1 Differences in deposited sulfate

The spatial pattern and magnitude of deposited sulfate depends on the sources of atmospheric SO_2, the transport and mixing of the sulfate aerosol formed throughout the stratosphere and across the tropopause and wet and dry deposition processes (e.g. Hamill et al., 1997; Kremser et al., 2016). In the preindustrial background state (no Tambora) (Figure 2.1), all four models examined simulate similar patterns of sulfate deposition, with more sulfate deposited at the midlatitudes and in oceans and near SO_2 sources such as continuously degassing volcanoes. In the polar regions, the models also simulate similar sulfate deposition (with the exception of SOCOL-AER) with reasonable comparison to ice core records (Figure 2.2). This indicates that the models are realistically simulating aspects of the formation and transport of background sulfate aerosol and subsequent deposition processes.

However, under the volcanically perturbed conditions (with Tambora), the simulated volcanic sulfate deposition differs between all models, with differences in timing, spatial pattern and magnitude. Compared to ice core records of cumulative deposited sulfate for 1815 Mt. Tambora, MAECHAM5-HAM and SOCOL-AER simulate much higher deposition to polar ice sheets, which is ~ 3–5 times greater than the mean ice-

core-derived estimates by Gao et al. (2007) and Sigl et al. (2015). UM-UKCA and CESM1(WACCM) simulate deposition closer in magnitude to the ice core records although in UM-UKCA the sulfate deposited on both ice sheets is ~ 2 times too small compared to the mean ice-core-derived estimates. In CESM1(WACCM) the sulfate deposited on Antarctica is slightly too small but ~ 2 times greater in Greenland compared to the mean ice-core-derived estimates. Considering the models are more comparable in the background state it is likely that the inter-model differences in volcanic deposition are due to differences in the formation of the volcanic aerosol, the stratospheric transport of volcanic aerosol and stratosphere–troposphere exchange, since in the background state most of the deposited sulfate is of tropospheric origin. These processes are discussed in the following sections.

2.4.1.1 Volcanic sulfate formation and transport

The timing and duration of sulfate deposition mirrors that of the atmospheric sulfate burdens. In MAECHAM5-HAM the atmospheric sulfate burden peaks sooner and decays more quickly than in the other models, and ice sheet deposition occurs more rapidly (within the first 2 years after the eruption). The atmospheric sulfate burden in CESM1(WACCM) is still elevated 4 years after the eruption, and hence the deposition signal is also longer lived (Figure 2.5). MAECHAM5-HAM is the only model that has prescribed OH (Table 2.1). OH may become depleted in dense volcanic clouds by reaction with SO_2, affecting the rate of sulfate aerosol formation (Bekki, 1995). The background stratospheric OH concentrations are similar between the models (Figure B.5) but in SOCOL-AER, UM-UKCA and CESM1(WACCM), in the first 2 months after the eruption, stratospheric tropical OH becomes depleted, with ensemble mean peak reductions of between 15 and 33 % (Figure B.6). This reduces the rate of sulfate aerosol formation compared to MAECHAM5-HAM, where the SO_2 will be more rapidly oxidized, and explains the later peaks in sulfate burdens in these models.

The rapid decay of the sulfate burden in MAECHAM5-HAM also indicates that this model could have faster accumulation of particles and stronger sedimentation compared to the other models. Although beyond the scope of this paper a more detailed examination of the aerosol microphysical processes and the size of the aerosol particles, on which sedimentation is dependent, will facilitate a greater understanding of some of the model differences identified here.

The high biases in cumulative deposited sulfate in MAECHAM5-HAM and SOCOL-AER compared to ice cores may be caused by a high bias in poleward aerosol transport (e.g. Stenke et al., 2013; Toohey et al., 2013). MAECHAM5-HAM and SOCOL-AER also have the lowest resolution of the four models (Table 2.1), which may contribute to the high deposition bias since stratospheric circulation and cross-tropopause transport is better represented in higher-resolution models (e.g. Toohey et al., 2013). Gao et al. (2007), using the GISS ModelE, found that simulated deposited sulfate over the poles after the eruption of Mt. Tambora was a factor of 2 too large but that the spatial pattern of deposition recorded in ice cores was well captured. GISS ModelE had a much lower resolution than the models used here (4° × 5°) and a simplified scheme for stratospheric aerosol microphysics. SOCOL-AER and MAECHAM5-HAM have the same dynamical cores and therefore we expect transport to be similar in these models. Hence, the differences in simulated volcanic deposition between SOCOL-AER and MAECHAM5-HAM are likely due to aerosol growth and sedimentation, and the deposition schemes. In UM-UKCA and CESM1(WACCM) the poleward transport of volcanic aerosol may be too weak or midlatitude deposition too strong.

2.4.1.2 Dynamical effects

The direction and strength of the stratospheric winds impacts the transport of sulfate aerosol and hence where it is deposited. UM-UKCA, CESM1(WACCM) and SOCOL-AER have similarly defined QBOs with downward propagating easterly and westerly winds, with the eruption simulated in the easterly phase. MAECHAM5-HAM does not include a QBO and although stratospheric winds were easterly in the MAECHAM5-HAM simulations, we find that these winds are ~ 20 m s^{-1} weaker than the easterly phase winds in the other models (Figure B.7). This may contribute to the quicker transport and subsequent deposition to the poles in the MAECHAM5-HAM simulations.

In addition to midlatitude tropopause folds, a further location of cross-tropopause transport of sulfate aerosol is the polar winter vortex (e.g. SPARC, 2006; Kremser et al., 2016). The polar vortex inhibits poleward transport (e.g. Schoeberl and Hartmann, 1991), and it has been suggested that variations in the strength of the polar vortex may modulate volcanic aerosol transport and deposition to polar ice sheets (Toohey et al., 2013). We find that the strength of the background climatological winds differs

slightly across the models, with the strongest polar jets simulated in CESM1(WACCM) and the weakest in MAECHAM5-HAM (maximum zonal mean zonal winds are 52 m s^{-1} in CESM1(WACCM) and 32 m s^{-1} in MAECHAM5-HAM; Figure B.8). All models simulate a strengthening in the NH and SH polar zonal winds in the first year after the eruption; CESM1(WACCM) simulates the largest zonal mean anomalies and MAECHAM5-HAM the weakest. Figure 2.12 shows the zonal mean zonal wind averaged over the first year after the eruption in each model. Peak zonal mean SH polar zonal wind is 58 m s^{-1} in CESM1(WACCM), 46 m s^{-1} in SOCOL-AER, 45 m s^{-1} in UM-UKCA and 38 m s^{-1} in MAECHAM5-HAM. Inter-model differences in polar vortex strength may therefore contribute to differences in polar sulfate deposition. Following this hypothesis, the strong SH polar vortex simulated by CESM1(WACCM) may contribute to the lower deposited sulfate on Antarctica in this model and, likewise, the relatively weaker polar vortex in MAECHAM5-HAM may contribute to the greater deposited sulfate on Antarctica. In contrast, UM-UKCA simulates average polar vortex winds but the smallest deposited sulfate on Antarctica. Therefore, it appears to be a combination of factors that drive the inter-model differences in simulated polar volcanic sulfate deposition.

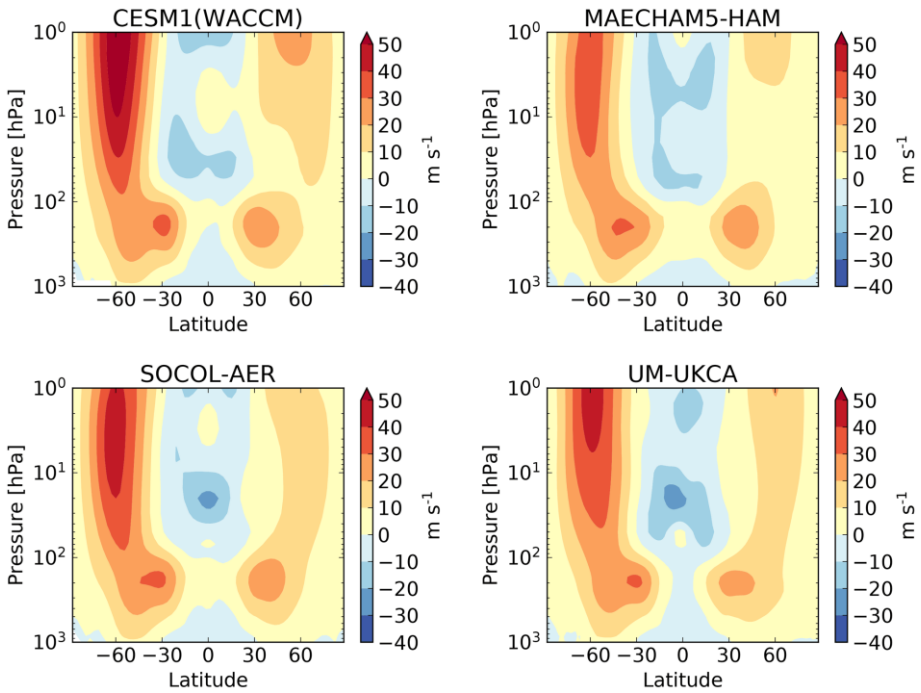

Figure 2.12: Zonal mean zonal wind (m s^{-1}) averaged over the first year after the eruption (April 1815–April 1816) in each model simulation (ensemble mean). Zonal wind is output on 36 pressure levels in UM-UKCA, 33 pressure levels in MAECHAM5- HAM and 32 pressure levels in SOCOL-AER. Zonal wind in CESM1(WACCM) is output on an atmosphere hybrid sigma-pressure coordinate and has been interpolated to the pressure levels used in UM-UKCA.

2.4.1.3 Deposition schemes

Differences in the deposition schemes contribute to the intermodel differences. The simplified scheme in SOCOL-AER results in deposition following more closely the atmospheric distribution of sulfate. The differences between wet and dry deposition simulated across the models are due to the individual deposition scheme parameterizations. The implication of these differences in dictating the resulting total sulfate deposition remains uncertain. However, since inter-model differences in volcanic sulfate deposition patterns appear unrelated to differences between climatological wet and dry deposition patterns, the proportion of wet vs. dry deposition is likely of secondary importance compared to differences between the models in aerosol transport processes including sedimentation and stratosphere–troposphere exchange. Smoother topography in the lower-resolution models will also influence the spatial pattern of deposition.

The realistic deposition of background sulfate suggests that the scavenging and deposition processes in the models are reasonably parameterized and thus that inter-model differences in the Tambora case are more likely due to differences in stratospheric transport and stratosphere–troposphere exchange as described above. However, due to the higher sulfate burdens in the perturbed case, differences in deposition due to the schemes may become more pronounced. Scavenging and deposition parameterizations are highly uncertain, and the chance that such parameterizations become unrealistic under the large sulfate aerosol loadings associated with a Tambora eruption cannot be discounted and should be explored in future work.

2.4.2 Implications for model differences in simulated sulfate deposition

Using just four global aerosol models, we find large differences in the mean deposited sulfate on the Antarctic and Greenland ice sheets. The multi-model mean BTD factors, which relate the atmospheric sulfate burdens to the deposition at the ice sheets, differ from the estimates by Gao et al. (2007) by ∼ 60 % in the NH and ∼ 30 % in the SH, although the Gao et al. (2007) estimates are within or close to the multi-model spread. We find that the multi-model spread in BTD factors is reduced when we take a polar cap average of deposition as opposed to the average ice sheet deposition because simulated deposition is more similar amongst the models when a greater area average is considered. Due to the large gradient between land and sea deposition simulated in

CESM1(WACCM) and UM-UKCA, mean polar deposition does not represent the mean ice sheet deposition and BTD factors are therefore sensitive to the areas chosen to represent the ice sheet deposition. This makes it difficult to estimate accurately the relationship between ice sheet deposition and sulfate aerosol loading in the models. We highlight this to emphasize caution when determining BTD factors in future modelling studies. Furthermore, although these simulations aimed to follow a common protocol, the injection setup did differ between models due to differences in the ways modelling groups interpret and simulate a volcanic injection (Table 2.2). This is a common problem in multi-model comparisons and makes it more difficult to isolate and attribute model differences.

We did not expect the models to be able to simulate the exact deposition at each ice core location given the large natural variability in local weather and snow patterns, which will be different in the models, uncertainties in estimating ice-core-derived volcanic sulfate deposition and in model inputs (e.g. magnitude and altitude of the volcanic sulfur emission), and, fundamentally, that in the real world there was only one realisation of weather. Regarding the model inputs, there are no direct observations of the injection altitude of SO_2 from the 1815 Mt. Tambora eruption, and often simulations are initiated with SO_2 injected at heights lower than the estimated injection altitude to account for self-lofting as the aerosol forms. Inter-model uncertainty is also initiated as soon as models convert the same input emission to their grids. Here, simulations followed a common protocol, but it may be that to better simulate the eruption of Mt. Tambora, sensitivity to injection height should be explored. Models may also contain inaccuracies due to uncertain physical representations and coarse resolution, and several ice core locations will be represented by the same model grid box. The differing resolutions between the models also means that the number of grid boxes and area that defines each ice sheet differs slightly between the models. Sulfate deposition fluxes have a large spatial variability due to differences in precipitation, the local synoptic conditions at the time of deposition and post-deposition movement through wind (Fisher et al., 1985; Robock and Free, 1995; Wolff et al., 2005). Deposition fluxes can vary by orders of magnitude, even between ice cores that are located close to each other. For example, in a very low-accumulation site in Antarctica (Dome C), Gautier et al. (2016) found that in five cores drilled 1 m apart, two cores missed the Tambora sulfate flux signal completely, which they attributed to snow drift and surface roughness. They reported

that the mean flux between these five cores is uncertain by ~ 30 %, highlighting the uncertainties in sulfate fluxes reported from single cores at such a low-accumulation site. This appears to be an extreme case, however, and the 1815 Mt. Tambora signal is clearly identifiable in all other Antarctic ice cores (Sigl et al., 2014).

Furthermore, the phase of the QBO at the time of the eruption is unknown, and here we have only used simulations where the SO_2 is emitted during the easterly phase. Toohey et al. (2013) also found that deposition to the poles varied as a function of SO_2 injection magnitude and season, and their simulations of a Tambora-like eruption showed greater deposition to Greenland than Antarctica. However, the volcanic eruptions in Toohey et al. (2013) were simulated in January and July, located at 15° N, which may explain the bias towards Greenland deposition. Further work is required on the influence of the QBO phase and injection height on the Antarctic and Greenland deposition efficiency.

Our multi-model mean NH_BTD factor is ~ 60 % lower than previously derived (Gao et al., 2007), which if used to estimate the NH atmospheric sulfate burden of other historic tropical eruptions from their mean Greenland deposited sulfate would result in lower burdens and likely less volcanic cooling. Model-simulated NH cooling following large-magnitude volcanic eruptions has been overestimated in the past (e.g. Stoffel et al., 2015; Zanchettin et al., 2016). However, our multi-model mean SH_BTD factor is ~ 30 % greater than Gao et al. (2007), which would result in a larger SH sulfate burden estimate. Applying our BTD factors (NH: 0.42; SH: 1.27) to the mean Greenland and Antarctic deposited sulfate from the 1257 Samalas eruption (90 and 73 kg km^{-2}, respectively; Sigl et al., 2015) results in a considerable hemispheric asymmetry in the estimated sulfate burdens. We calculate an SH burden that is ~ 2.5 times the NH burden, despite the eruption occurring in the tropics. This could result in further differences in aerosol optical depth and volcanic aerosol radiative forcing, and hemispheric asymmetry in atmospheric sulfate burdens has been shown to shift the Intertropical Convergence Zone, leading to precipitation anomalies (e.g. Haywood et al., 2013). However, this asymmetry seems unlikely, given that cooling in the SH after large tropical eruptions appears limited in proxy records (Neukom et al., 2014).

2.5 Conclusions

We have analysed the volcanic sulfate deposition in model simulations of the 1815 eruption of Mt. Tambora using four state-of-the-art global aerosol models (CESM1(WACCM), MAECHAM5-HAM, SOCOL-AER and UM-UKCA) and compared the simulated deposited sulfate to a comprehensive array of ice core records. We have also investigated the simulated sulfate deposition under preindustrial background conditions (without the eruption of Mt. Tambora). Although the models simulate relatively similar background sulfate deposition fluxes, the models differ substantially in their simulation of the Mt. Tambora volcanic sulfate deposition, with differences in the timing, spatial pattern and magnitude. CESM1(WACCM) and UM-UKCA simulate similar deposition patterns, with the majority of sulfate deposited at the midlatitude storm belts. On the ice sheets, UM-UKCA simulates too little deposited sulfate compared to mean ice-core-derived estimates (~ 2 times too small). In CESM1(WACCM) deposited sulfate on Antarctica is also slightly too small, but deposited sulfate on Greenland is ~ 2 times too large compared to the mean ice-core-derived estimate. In MAECHAM5-HAM and SOCOL-AER, the sulfate is deposited further across the globe and these models simulate ~ 3–5 times too much deposited sulfate on the ice sheets compared to mean ice-core-derived estimates. However, MAECHAM5-HAM is the only model to capture the spatial pattern of deposited sulfate compared to ice cores, especially in Antarctica.

Because the background deposition is more comparable between the models than in the perturbed case, differences in the volcanic sulfate deposition are likely due to differences in the formation of the volcanic aerosol, the stratospheric transport of volcanic aerosol and stratosphere–troposphere exchange. In addition, differences in deposition due to the deposition schemes may become more pronounced under the higher sulfate loading. We suggest that differences in model resolution, modelled stratospheric winds, aerosol microphysics and sedimentation and deposition schemes have all contributed to the range in model-simulated volcanic sulfate deposition.

We have calculated BTD factors between the mean deposited sulfate on each ice sheet and the corresponding hemispheric peak atmospheric sulfate burden for the Mt. Tambora simulations. The BTD factors differ by up to a factor of 15 between the models. The multi-model mean BTD factors also differ to BTD factors currently used

to deduce historical volcanic forcing (e.g. Gao et al., 2007, 2008; Sigl et al., 2015). Our range in derived BTD factors highlights uncertainties in the relationship between atmospheric sulfate burden and ice sheet deposited sulfate as simulated by models.

Given that GISS ModelE (Gao et al., 2007) did as good a job at simulating the deposited sulfate from this eruption as these newer, higher-resolution models, which also have more sophisticated treatments of gas-to-aerosol conversion, and the fact that the four models used here simulate very different sulfate deposition, it remains an open research question as to the optimal model configuration for this problem. A detailed analysis of the differences in sulfur chemistry and the aerosol formation and transport in each model will further aid in the interpretation of these results. Dedicated multi-model comparison projects with process-oriented comparisons, such as the Interactive Stratospheric Aerosol Modelling Intercomparison Project (ISA-MIP) (Timmreck et al., 2018), will be imperative to disentangling the reasons for model differences. Using idealized prescribed aerosol forcings such as Easy Volcanic Aerosol (Toohey et al., 2016) in future VolMIP experiments will also provide the opportunity to better understand model diversity. Simulations of other large-magnitude volcanic eruptions will also enable the calculation of additional multi-model BTD factors, which will aid in the calculation of historic volcanic forcing.

References

Bekki, S. 1995. Oxidation of volcanic SO2: A sink for stratospheric OH and H2O. *Geophysical Research Letters.* **22**(8), pp.913-916.

Bellouin, N., Mann, G.W., Woodhouse, M.T., Johnson, C., Carslaw, K.S. and Dalvi, M. 2013. Impact of the modal aerosol scheme GLOMAP-mode on aerosol forcing in the Hadley Centre Global Environmental Model. *Atmospheric Chemistry and Physics.* **13**(6), pp.3027-3044.

Brooke, J.S.A., Feng, W.H., Carrillo-Sanchez, J.D., Mann, G.W., James, A.D., Bardeen, C.G. and Plane, J.M.C. 2017. Meteoric Smoke Deposition in the Polar Regions: A Comparison of Measurements With Global Atmospheric Models. *Journal of Geophysical Research-Atmospheres.* **122**(20), pp.11112-11130.

Clausen, H.B. and Hammer, C.U. 1988. The Laki and Tambora eruptions as revealed in Greenland ice cores from 11 locations. *Annals of Glaciology.* **10**, pp.16-22.

Cole-Dai, J.H., Ferris, D.G., Lanciki, A.L., Savarino, J., Thiemens, M.H. and McConnell, J.R. 2013. Two likely stratospheric volcanic eruptions in the 1450s CE found in a bipolar, subannually dated 800 year ice core record. *Journal of Geophysical Research-Atmospheres.* **118**(14), pp.7459-7466.

Cole-Dai, J.H., Mosley-Thompson, E., Wight, S.P. and Thompson, L.G. 2000. A 4100-year record of explosive volcanism from an East Antarctica ice core. *Journal of Geophysical Research-Atmospheres.* **105**(D19), pp.24431-24441.

Cole-Dai, J.H., MosleyThompson, E. and Thompson, L.G. 1997. Annually resolved southern hemisphere volcanic history from two Antarctic ice cores. *Journal of Geophysical Research-Atmospheres.* **102**(D14), pp.16761-16771.

Crowley, T. 2000. Causes of climate change over the past 1000 years. *Science.* **289**(5477), pp.270-277.

Crowley, T. and Unterman, M.B. 2013. Technical details concerning development of a 1200 yr proxy index for global volcanism. *Earth System Science Data.* **5**(1), pp.187-197.

Dhomse, S.S., Emmerson, K.M., Mann, G.W., Bellouin, N., Carslaw, K.S., Chipperfield, M.P., Hommel, R., Abraham, N.L., Telford, P., Braesicke, P., Dalvi, M., Johnson, C.E., O'Connor, F., Morgenstern, O., Pyle, J.A., Deshler, T., Zawodny, J.M. and Thomason, L.W. 2014. Aerosol microphysics simulations of the Mt. Pinatubo eruption with the UM-UKCA composition-climate model. *Atmospheric Chemistry and Physics.* **14**(20), pp.11221-11246.

Eyring, V., Bony, S., Meehl, G.A., Senior, C.A., Stevens, B., Stouffer, R.J. and Taylor, K.E. 2016. Overview of the Coupled Model Intercomparison Project Phase 6 (CMIP6) experimental design and organization. *Geoscientific Model Development.* **9**(5), pp.1937-1958.

Ferris, D.G., Cole-Dai, J., Reyes, A.R. and Budner, D.M. 2011. South Pole ice core record of explosive volcanic eruptions in the first and second millennia A.D. and evidence of a large eruption in the tropics around 535 A.D. *Journal of Geophysical Research: Atmospheres.* **116**(D17), D17308.

Fisher, D.A., Reeh, N. and Clausen, H.B. 1985. Stratigraphic Noise in Time Series Derived from Ice Cores. *Annals of Glaciology.* **7**, pp.76-83.

Gao, C., Oman, L., Robock, A. and Stenchikov, G.L. 2007. Atmospheric volcanic loading derived from bipolar ice cores: Accounting for the spatial distribution

of volcanic deposition. *Journal of Geophysical Research-Atmospheres.* **112**(D9), D09109.

Gao, C., Robock, A. and Ammann, C. 2008. Volcanic forcing of climate over the past 1500 years: An improved ice core-based index for climate models. *Journal of Geophysical Research-Atmospheres.* **113**(D23), D23111.

Gao, C., Robock, A., Self, S., Witter Jeffrey, B., Steffenson, J.P., Clausen Henrik, B., Siggaard-Andersen, M.-L., Johnsen, S., Mayewski Paul, A. and Ammann, C. 2006. The 1452 or 1453 A.D. Kuwae eruption signal derived from multiple ice core records: Greatest volcanic sulfate event of the past 700 years. *Journal of Geophysical Research: Atmospheres.* **111**(D12), D12107.

Gautier, E., Savarino, J., Erbland, J., Lanciki, A. and Possenti, P. 2016. Variability of sulfate signal in ice core records based on five replicate cores. *Climate of the Past.* **12**(1), pp.103-113.

Hamill, P., Jensen, E.J., Russell, P.B. and Bauman, J.J. 1997. The life cycle of stratospheric aerosol particles. *Bulletin of the American Meteorological Society.* **78**(7), pp.1395-1410.

Haywood, J.M., Jones, A., Bellouin, N. and Stephenson, D. 2013. Asymmetric forcing from stratospheric aerosols impacts Sahelian rainfall. *Nature Climate Change.* **3**(7), pp.660-665.

Herzog, M. and Graf, H.F. 2010. Applying the three-dimensional model ATHAM to volcanic plumes: Dynamic of large co-ignimbrite eruptions and associated injection heights for volcanic gases. *Geophysical Research Letters.* **37**, L19807.

Kipling, Z., Stier, P., Schwarz, J.P., Perring, A.E., Spackman, J.R., Mann, G.W., Johnson, C.E. and Telford, P.J. 2013. Constraints on aerosol processes in climate models from vertically-resolved aircraft observations of black carbon. *Atmospheric Chemistry and Physics.* **13**(12), pp.5969-5986.

Kremser, S., Thomason, L.W., von Hobe, M., Hermann, M., Deshler, T., Timmreck, C., Toohey, M., Stenke, A., Schwarz, J.P., Weigel, R., Fueglistaler, S., Prata, F.J., Vernier, J.P., Schlager, H., Barnes, J.E., Antuna-Marrero, J.C., Fairlie, D., Palm, M., Mahieu, E., Notholt, J., Rex, M., Bingen, C., Vanhellemont, F., Bourassa, A., Plane, J.M.C., Klocke, D., Carn, S.A., Clarisse, L., Trickl, T., Neely, R., James, A.D., Rieger, L., Wilson, J.C. and Meland, B. 2016. Stratospheric aerosol-Observations, processes, and impact on climate. *Reviews of Geophysics.* **54**(2), pp.278-335.

Lamarque, J.F., Dentener, F., McConnell, J., Ro, C.U., Shaw, M., Vet, R., Bergmann, D., Cameron-Smith, P., Dalsoren, S., Doherty, R., Faluvegi, G., Ghan, S.J., Josse, B., Lee, Y.H., MacKenzie, I.A., Plummer, D., Shindell, D.T., Skeie, R.B., Stevenson, D.S., Strode, S., Zeng, G., Curran, M., Dahl-Jensen, D., Das, S., Fritzsche, D. and Nolan, M. 2013. Multi-model mean nitrogen and sulfur deposition from the Atmospheric Chemistry and Climate Model Intercomparison Project (ACCMIP): evaluation of historical and projected future changes. *Atmos. Chem. Phys.* **13**(16), pp.7997-8018.

Lamarque, J.F., Emmons, L.K., Hess, P.G., Kinnison, D.E., Tilmes, S., Vitt, F., Heald, C.L., Holland, E.A., Lauritzen, P.H., Neu, J., Orlando, J.J., Rasch, P.J. and Tyndall, G.K. 2012. CAM-chem: description and evaluation of interactive atmospheric chemistry in the Community Earth System Model. *Geoscientific Model Development.* **5**(2), pp.369-411.

Langway, C.C., Osada, K., Clausen, H.B., Hammer, C.U. and Shoji, H. 1995. A 10-century comparison of prominent bipolar volcanic events in ice cores. *Journal of Geophysical Research-Atmospheres.* **100**(D8), pp.16241-16247.

Legrand, M. and Mayewski, P. 1997. Glaciochemistry of polar ice cores: A review. *Reviews of Geophysics.* **35**(3), pp.219-243.

Liu, X., Easter, R.C., Ghan, S.J., Zaveri, R., Rasch, P., Shi, X., Lamarque, J.F., Gettelman, A., Morrison, H., Vitt, F., Conley, A., Park, S., Neale, R., Hannay, C., Ekman, A.M.L., Hess, P., Mahowald, N., Collins, W., Iacono, M.J., Bretherton, C.S., Flanner, M.G. and Mitchell, D. 2012. Toward a minimal representation of aerosols in climate models: description and evaluation in the Community Atmosphere Model CAM5. *Geoscientific Model Development.* **5**(3), pp.709-739.

Mann, G.W., Carslaw, K.S., Spracklen, D.V., Ridley, D.A., Manktelow, P.T., Chipperfield, M.P., Pickering, S.J. and Johnson, C.E. 2010. Description and evaluation of GLOMAP-mode: a modal global aerosol microphysics model for the UKCA composition-climate model. *Geoscientific Model Development.* **3**(2), pp.519-551.

McConnell, J.R., Edwards, R., Kok, G.L., Flanner, M.G., Zender, C.S., Saltzman, E.S., Banta, J.R., Pasteris, D.R., Carter, M.M. and Kahl, J.D.W. 2007. 20th-century industrial black carbon emissions altered arctic climate forcing. *Science.* **317**(5843), pp.1381-1384.

McCormick, M.P. and Veiga, R.E. 1992. SAGE II measurements of early Pinatubo aerosols. *Geophysical Research Letters.* **19**(2), pp.155-158.

Mills, M.J., Richter, J.H., Tilmes, S., Kravitz, B., MacMartin, D.G., Glanville, A.A., Tribbia, J.J., Lamarque, J.F., Vitt, F., Schmidt, A., Gettelman, A., Hannay, C., Bacmeister, J.T. and Kinnison, D.E. 2017. Radiative and Chemical Response to Interactive Stratospheric Sulfate Aerosols in Fully Coupled CESM1(WACCM). *Journal of Geophysical Research-Atmospheres.* **122**(23), pp.13061-13078.

Mills, M.J., Schmidt, A., Easter, R., Solomon, S., Kinnison, D.E., Ghan, S.J., Neely, R.R., Marsh, D.R., Conley, A., Bardeen, C.G. and Gettelman, A. 2016. Global volcanic aerosol properties derived from emissions, 1990-2014, using CESM1(WACCM). *Journal of Geophysical Research-Atmospheres.* **121**(5), pp.2332-2348.

Neukom, R., Gergis, J., Karoly, D.J., Wanner, H., Curran, M., Elbert, J., Gonzalez-Rouco, F., Linsley, B.K., Moy, A.D., Mundo, I., Raible, C.C., Steig, E.J., van Ommen, T., Vance, T., Villalba, R., Zinke, J. and Frank, D. 2014. Inter-hemispheric temperature variability over the past millennium. *Nature Climate Change.* **4**(5), pp.362-367.

Niemeier, U., Timmreck, C., Graf, H.F., Kinne, S., Rast, S. and Self, S. 2009. Initial fate of fine ash and sulfur from large volcanic eruptions. *Atmospheric Chemistry and Physics.* **9**(22), pp.9043-9057.

Oppenheimer, C. 2003. Climatic, environmental and human consequences of the largest known historic eruption: Tambora volcano (Indonesia) 1815. *Progress in Physical Geography.* **27**(2), pp.230-259.

Pinto, J.P., Turco, R.P. and Toon, O.B. 1989. Self-limiting physical and chemical effects in volcanic eruption clouds. *Journal of Geophysical Research-Atmospheres.* **94**(D8), pp.11165-11174.

Raible, C.C., Bronnimann, S., Auchmann, R., Brohan, P., Frolicher, T.L., Graf, H.F., Jones, P., Luterbacher, J., Muthers, S., Neukom, R., Robock, A., Self, S., Sudrajat, A., Timmreck, C. and Wegmann, M. 2016. Tambora 1815 as a test case for high impact volcanic eruptions: Earth system effects. *Wiley Interdisciplinary Reviews-Climate Change.* **7**(4), pp.569-589.

Read, W.G., Froidevaux, L. and Waters, J.W. 1993. Microwave limb sounder measurement of stratospheric SO2 from the Mt. Pinatubo Volcano. *Geophysical Research Letters.* **20**(12), pp.1299-1302.

Robock, A. 2000. Volcanic eruptions and climate. *Reviews of Geophysics.* **38**(2), pp.191-219.

Robock, A. and Free, M.P. 1995. Ice cores as an index of global volcanism from 1850 to the present. *Journal of Geophysical Research-Atmospheres.* **100**(D6), pp.11549-11567.

Schoeberl, M.R. and Hartmann, D.L. 1991. The dynamics of the stratospheric polar vortex and its relation to springtime ozone depletions. *Science.* **251**(4989), pp.46-52.

Self, S., Gertisser, R., Thordarson, T., Rampino, M.R. and Wolff, J.A. 2004. Magma volume, volatile emissions, and stratospheric aerosols from the 1815 eruption of Tambora. *Geophysical Research Letters.* **31**(20), L20608.

Sheng, J.X., Weisenstein, D.K., Luo, B.P., Rozanov, E., Arfeuille, F. and Peter, T. 2015a. A perturbed parameter model ensemble to investigate Mt. Pinatubo's 1991 initial sulfur mass emission. *Atmospheric Chemistry and Physics.* **15**(20), pp.11501-11512.

Sheng, J.X., Weisenstein, D.K., Luo, B.P., Rozanov, E., Stenke, A., Anet, J., Bingemer, H. and Peter, T. 2015b. Global atmospheric sulfur budget under volcanically quiescent conditions: Aerosol-chemistry-climate model predictions and validation. *Journal of Geophysical Research-Atmospheres.* **120**(1), pp.256-276.

Sigl, M., McConnell, J.R., Layman, L., Maselli, O., McGwire, K., Pasteris, D., Dahl-Jensen, D., Steffensen, J.P., Vinther, B., Edwards, R., Mulvaney, R. and Kipfstuhl, S. 2013. A new bipolar ice core record of volcanism from WAIS Divide and NEEM and implications for climate forcing of the last 2000 years. *Journal of Geophysical Research-Atmospheres.* **118**(3), pp.1151-1169.

Sigl, M., McConnell, J.R., Toohey, M., Curran, M., Das, S.B., Edwards, R., Isaksson, E., Kawamura, K., Kipfstuhl, S., Kruger, K., Layman, L., Maselli, O.J., Motizuki, Y., Motoyama, H., Pasteris, D.R. and Severi, M. 2014. Insights from Antarctica on volcanic forcing during the Common Era. *Nature Climate Change.* **4**(8), pp.693-697.

Sigl, M., Winstrup, M., McConnell, J.R., Welten, K.C., Plunkett, G., Ludlow, F., Buntgen, U., Caffee, M., Chellman, N., Dahl-Jensen, D., Fischer, H., Kipfstuhl, S., Kostick, C., Maselli, O.J., Mekhaldi, F., Mulvaney, R., Muscheler, R., Pasteris, D.R., Pilcher, J.R., Salzer, M., Schupbach, S., Steffensen, J.P., Vinther, B.M. and Woodruff, T.E. 2015. Timing and climate forcing of volcanic eruptions for the past 2,500 years. *Nature.* **523**(7562), pp.543–549.

SPARC. 2006. SPARC Assessment of Stratospheric Aerosol Properties (ASAP). L. Thomason and Th. Peter (Eds.), SPARC Report No. 4, WCRP-124, WMO/TD – No. 1295, available at www.sparc-climate.org/publications/sparc-reports/.

Stenke, A., Schraner, M., Rozanov, E., Egorova, T., Luo, B. and Peter, T. 2013. The SOCOL version 3.0 chemistry-climate model: description, evaluation, and implications from an advanced transport algorithm. *Geoscientific Model Development.* **6**(5), pp.1407-1427.

Stier, P., Feichter, J., Kinne, S., Kloster, S., Vignati, E., Wilson, J., Ganzeveld, L., Tegen, I., Werner, M., Balkanski, Y., Schulz, M., Boucher, O., Minikin, A. and Petzold, A. 2005. The aerosol-climate model ECHAM5-HAM. *Atmospheric Chemistry and Physics.* **5**, pp.1125-1156.

Stoffel, M., Khodri, M., Corona, C., Guillet, S., Poulain, V., Bekki, S., Guiot, J., Luckman, B.H., Oppenheimer, C., Lebas, N., Beniston, M. and Masson-Delmotte, V. 2015. Estimates of volcanic-induced cooling in the Northern Hemisphere over the past 1,500 years. *Nature Geoscience.* **8**(10), pp.784-788.

Timmreck, C., Lorenz, S.J., Crowley, T.J., Kinne, S., Raddatz, T.J., Thomas, M.A. and Jungclaus, J.H. 2009. Limited temperature response to the very large AD 1258 volcanic eruption. *Geophysical Research Letters.* **36**, L21708.

Timmreck, C., Mann, G.W., Aquila, V., Hommel, R., Lee, L.A., Schmidt, A., Brühl, C., Carn, S., Chin, M., Dhomse, S.S., Diehl, T., English, J.M., Mills, M.J., Neely, R., Sheng, J., Toohey, M. and Weisenstein, D. 2018. The Interactive Stratospheric Aerosol Model Intercomparison Project (ISA-MIP): motivation and experimental design. *Geoscientific Model Development.* **11**(7), pp.2581-2608.

Toohey, M., Kruger, K., Niemeier, U. and Timmreck, C. 2011. The influence of eruption season on the global aerosol evolution and radiative impact of tropical volcanic eruptions. *Atmospheric Chemistry and Physics.* **11**(23), pp.12351-12367.

Toohey, M., Kruger, K. and Timmreck, C. 2013. Volcanic sulfate deposition to Greenland and Antarctica: A modeling sensitivity study. *Journal of Geophysical Research-Atmospheres.* **118**(10), pp.4788-4800.

Toohey, M. and Sigl, M. 2017. Volcanic stratospheric sulfur injections and aerosol optical depth from 500 BCE to 1900 CE. *Earth System Science Data.* **9**(2), pp.809-831.

Toohey, M., Stevens, B., Schmidt, H. and Timmreck, C. 2016. Easy Volcanic Aerosol (EVA v1.0): an idealized forcing generator for climate simulations. *Geoscientific Model Development.* **9**(11), pp.4049-4070.

Trepte, C.R., Veiga, R.E. and McCormick, M.P. 1993. The poleward dispersal of Mount Pinatubo volcanic aerosol. *Journal of Geophysical Research-Atmospheres.* **98**(D10), pp.18563-18573.

Wolff, E.W. 2012. Chemical signals of past climate and environment from polar ice cores and firn air. *Chemical Society Reviews.* **41**(19), pp.6247-6258.

Wolff, E.W., Cook, E., Barnes, P.R.F. and Mulvaney, R. 2005. Signal variability in replicate ice cores. *Journal of Glaciology.* **51**(174), pp.462-468.

Zanchettin, D., Khodri, M., Timmreck, C., Toohey, M., Schmidt, A., Gerber, E.P., Hegerl, G., Robock, A., Pausata, F.S.R., Ball, W.T., Bauer, S.E., Bekki, S., Dhomse, S.S., LeGrande, A.N., Mann, G.W., Marshall, L., Mills, M., Marchand, M., Niemeier, U., Poulain, V., Rozanov, E., Rubino, A., Stenke, A., Tsigaridis, K. and Tummon, F. 2016. The Model Intercomparison Project on the climatic response to Volcanic forcing (VolMIP): experimental design and forcing input data for CMIP6. *Geoscientific Model Development.* **9**(8), pp.2701-2719.

Zielinski, G.A. 1995. Stratospheric loading and optical depth estimates of explosive volcanism over the last 2100 years derived from the Greenland Ice Sheet Project 2 ice core. *Journal of Geophysical Research-Atmospheres.* **100**(D10), pp.20937-20955.

Zielinski, G.A., Mayewski, P.A., Meeker, L.D., Gronvold, K., Germani, M.S., Whitlow, S., Twickler, M.S. and Taylor, K. 1997. Volcanic aerosol records and tephrochronology of the Summit, Greenland, ice cores. *Journal of Geophysical Research-Oceans.* **102**(C12), pp.26625-26640.

Zielinski, G.A., Mayewski, P.A., Meeker, L.D., Whitlow, S. and Twickler, M.S. 1996. A 110,000-yr record of explosive volcanism from the GISP2 (Greenland) ice core. *Quaternary Research.* **45**(2), pp.109-118.

Chapter 3 Exploring how eruption source parameters affect volcanic radiative forcing using statistical emulation

Lauren Marshall[1], Jill S. Johnson[1], Graham W. Mann[1,2], Lindsay Lee[1], Sandip S. Dhomse[1], Leighton Regayre[1], Masaru Yoshioka[1], Ken S. Carslaw[1] and Anja Schmidt[3,4]

[1]*School of Earth and Environment, University of Leeds, Leeds, LS2 9JT, UK*
[2]*National Centre for Atmospheric Science, University of Leeds, Leeds, LS2 9JT, UK*
[3]*Department of Chemistry, University of Cambridge, Lensfield Rd, Cambridge CB2 1EW, UK*
[4]*Department of Geography, University of Cambridge, Downing Place, Cambridge CB2 3EN, UK*

This chapter is an adaptation of the following publication submitted to *Journal of Geophysical Research: Atmospheres*, where the reference style and figure, table and section numbers have been updated for continuity throughout the thesis:

Marshall, L., Johnson, J. S., Mann, G. W., Lee, L., Dhomse, S. S., Regayre, L., Yoshioka, M., Carslaw, K., and Schmidt, A. 2018. Exploring how eruption source parameters affect volcanic radiative forcing using statistical emulation.

The supplement to this paper is included in Appendix C.

Key Points:

- We demonstrate the feasibility and value of using statistical emulation to quantify the radiative impact of volcanic eruptions
- Emulated response surfaces illustrate the dependencies of model output such as net radiative forcing on eruption source parameters
- Emulated response surfaces can also be used to constrain the eruption source parameters for a particular volcanic response

Abstract

The radiative forcing caused by a volcanic eruption is dependent on several eruption source parameters such as the mass of sulfur dioxide (SO_2) emitted, the eruption column height and the eruption latitude. General circulation models with prognostic aerosol and chemistry schemes can be used to investigate how each parameter influences the volcanic forcing. However, the range of multi-dimensional parameter space that can be explored is restricted because such simulations are computationally expensive. Here we use statistical emulation to explore the radiative impact of eruptions over a wide co-varying range of SO_2 emission magnitudes, injection heights and eruption latitudes based on only 30 simulations. We use the emulators to build response surfaces to visualize and predict the sulfate aerosol e-folding decay time, the stratospheric aerosol optical depth and net radiative forcing of thousands of different eruptions. We find that the volcanic stratospheric aerosol optical depth and net radiative forcing are primarily determined by the mass of SO_2 emitted, but eruption latitude is the most important parameter in determining the sulfate aerosol e-folding decay time. The response surfaces reveal joint effects of the eruption source parameters in influencing the net radiative forcing, such as a stronger influence of injection height for tropical eruptions than high-latitude eruptions. We also demonstrate how the emulated response surfaces can be used to find all combinations of eruption source parameters that produce a particular volcanic response, often revealing multiple solutions.

3.1 Introduction

Volcanic eruptions emit SO_2 into the atmosphere, which is oxidised and forms sulfate aerosol. Sulfate aerosol is very effective at scattering short-wave radiation, leading to surface cooling for a few years following a large-magnitude stratospheric volcanic eruption (e.g. Robock, 2000). The climatic effect of an eruption depends on several eruption source parameters, such as the mass of SO_2 emitted, the height of the SO_2 emissions, and the latitude of the volcano (e.g. Robock, 2000; Timmreck, 2012), as well as the season of eruption (e.g. Toohey et al., 2011) and the phase of the Quasi Biennial Oscillation (QBO) (e.g. Thomas et al., 2009). It is important to understand the potential climatic impact of an eruption in order to evaluate the effects of historical eruptions and to assess the possible effects of future eruptions.

Several modelling studies have investigated the influence of important eruption source parameters but for only a limited number of eruptions (e.g. Niemeier et al., 2009; Timmreck et al., 2010; Toohey et al., 2011; English et al., 2013; 2013; Dhomse et al., 2014; Metzner et al., 2014; Jones et al., 2017). These studies also focus on the effects of variations in individual parameter values, which leaves almost all of the multi-dimensional parameter space unexplored. This modelling approach therefore creates a major problem for model interpretation if the parameter variations have non-linear effects or if combinations of parameter perturbations have effects that cannot be predicted from the combined effects of individual parameters.

The effects of eruptions vary a lot across the range of possible source parameters. Studies investigating the influence of SO_2 emission magnitude have shown that the climatic impact becomes self-limiting as the mass of emitted SO_2 increases (e.g. Pinto et al., 1989; Timmreck et al., 2009; English et al., 2013; Metzner et al., 2014) due to the formation of larger sulfate aerosol particles, which have a smaller optical depth per unit mass than smaller particles and are quickly deposited to the surface (Pinto et al., 1989). Furthermore, in eruptions with large SO_2 emissions, hydroxyl radicals (OH) in the ambient atmosphere, needed to oxidize the SO_2, can become depleted (Pinto et al., 1989; Bekki, 1995). Eruptions in which the SO_2 is emitted higher into the stratosphere can have a greater climatic impact due to the residence time of stratospheric air increasing with distance from the tropopause and global transport if emitted at the equator (e.g. Robock, 2000). For stratosphere-injecting eruptions at high latitudes, aerosols are confined within the hemisphere and deposited to the surface more quickly (e.g. Oman et al., 2005; 2006; Kravitz and Robock, 2011). The effect of each of these parameters could be more or less important depending on the value of the other parameters, and a comprehensive and systematic investigation of such interactions, whilst accounting for changes to the aerosol particle size distribution, has not been conducted.

In this study, we use the approach of ‘designed experiments’ (Sacks et al., 1989) and model emulation (O'Hagan, 2006) to efficiently map out how the outputs of an interactive stratospheric aerosol model (UM-UKCA) vary across a three-dimensional parameter space. We do this by building surrogate statistical models (emulators) of several global model outputs (described in Section 3.2) based on a set of simulations of eruptions with different SO_2 emission magnitude, injection height and latitude. We do not investigate the influence of eruption season or QBO phase. The emulator maps

the relationship between the model output (such as radiative forcing) and the eruption source input parameters within an uncertainty (compared to the original model) that can be quantified. The emulator is very fast to evaluate and can be used to determine the impact of eruptions with parameter combinations that we did not explicitly simulate, in a matter of seconds. As such, we can analyse model output without further runs of the computationally expensive model. We analyse how diagnostics describing the atmospheric impact of an eruption (Section 3.2.4) vary with different SO_2 emission magnitudes, injection heights and latitudes and we are able, for the first time, to determine the effect of individual and combined parameter perturbations on the volcanic radiative forcing.

Section 3.2 describes the methods used in this study, including the experimental design of the UM-UKCA model simulations and details of the statistical emulation. In Section 3.3.1 we show results from the simulations and in Section 3.3.2 we present the results from the statistical emulators. We demonstrate the value of the emulators in Section 3.3.3 by investigating the atmospheric impact of the 1991 eruption of Mt. Pinatubo given a range in the estimated mass of SO_2 emitted and the injection height of the emissions. We also demonstrate how the emulators can be used to find combinations of eruption source parameters for any given value of the model output. A summary and conclusions are found in Section 3.4.

3.2 Methods

3.2.1 Model description

We use the interactive stratospheric aerosol model UM-UKCA, which consists of the UK Met Office Unified Model (UM) general circulation model coupled with the UK Chemistry and Aerosol scheme (UKCA). In this study UM-UKCA is based on the "Global Atmosphere 4" (GA4) configuration of the UM (Walters et al., 2014), but includes the GLOMAP-mode aerosol microphysics scheme (Mann et al., 2010; Bellouin et al., 2013), which simulates aerosol mass and number concentrations using 7 log-normal modes and UKCA whole-atmosphere chemistry, which combines the previous stratospheric (Morgenstern et al., 2009) and tropospheric (O'Connor et al., 2014) chemistry schemes. The model has a horizontal resolution of 1.875° by 1.25° with 85 vertical levels up to 85 km, resulting in well-resolved dynamics in the stratosphere and an internally generated QBO (e.g. Osprey et al., 2013). We

performed atmosphere-only free-running simulations with prescribed climatological sea-surface temperatures and sea-ice extent repeating at year 2000 conditions (Reynolds et al., 2007). Concentrations of greenhouse gases and ozone-depleting substances were also set at year 2000 levels.

The model set-up is based upon the UM-UKCA version described in Dhomse et al. (2014), which includes stratospheric-tropospheric aerosol and interactive sulfur chemistry (including interactive hydroxyl radical (OH) chemistry), and simulated well the variations in stratospheric aerosol properties prior to and following the 1991 eruption of Mt. Pinatubo compared to observations. The model treats the full lifecycle of stratospheric aerosol particles from initial injection of sulfur containing species, formation of gas-phase sulfuric acid following oxidation principally by OH, initial particle formation via binary homogeneous nucleation (Vehkämaki et al., 2002), and subsequent growth via condensation and coagulation. Aerosol particles are removed from the stratosphere by sedimentation and dynamical exchange of air to the troposphere, where they are eventually deposited by wet and dry deposition. For the model simulations here, aerosol radiative heating is included (Mann et al., 2015) and the interactive stratospheric aerosol capability has been further improved (Brooke et al., 2017) to allow sulfuric particles to form heterogeneously on transported meteoric smoke particle cores (MSP). The same model set-up has also been applied in pre-industrial conditions for the UM-UKCA 1815 Mt. Tambora simulations in Zanchettin et al. (2016) and Marshall et al. (2018).

In the chemistry scheme aerosol surface area is prescribed for the year 2000 (Thomason et al., 2008) and therefore the simulations do not account for the acceleration of heterogeneous chemistry on volcanically-enhanced aerosol and subsequent radiative effects from changes to stratospheric ozone. However, the chemical indirect effects from the eruptions arising from radiative-dynamically induced changes in stratospheric ozone, water vapour and changes in heterogeneous chemistry from modified polar stratospheric clouds, are resolved.

3.2.2 Choice of eruption source parameters and their values

We investigate the effects of three key eruption source parameters: SO_2 emission magnitude, injection height and latitude, which are known to influence the climatic impact of a volcanic eruption (Section 3.1). We choose to only perturb these three parameters for simplicity so that we can assess the feasibility of using statistical

emulation in studies of volcanic forcing. The range of values over which we perturb each eruption source parameter is listed in Table 3.1 and the rationales behind these ranges are described below.

Table 3.1: Eruption source parameters and range in values that are perturbed in this study.

Parameter	Parameter range
SO_2 emission magnitude	10–100 Tg SO_2
Injection height	15–25 km
Latitude	80°S–80°N

The SO_2 emission magnitude range of 10 Tg to 100 Tg is chosen to cover an order of magnitude in eruption emission strength. This range also spans the estimated emissions from large-magnitude historical volcanic eruptions, often used as test-cases to investigate the climatic effects of large sulfur injections, such as 1991 Mt. Pinatubo (~10-20 Tg SO_2, Timmreck et al., 2018 and references therein) and 1815 Mt. Tambora (~60 Tg SO_2, Zanchettin et al., 2016 and references therein). We vary the injection height over the range 15–25 km, with an injection depth of 3 km (i.e. injections from 15-18 km to 25-28 km), so most of the SO_2 will be injected into the stratosphere. Our latitude range is near-global to assess the full range of possible eruptions, omitting only the very highest latitudes at the edges of the model domain.

3.2.3 Simulation design

The eruptions were simulated using parameter combinations (i.e., SO_2 emission, injection height, and latitude) selected using the space-filling 'maximin' Latin hypercube design algorithm (Morris and Mitchell, 1995) resulting in excellent coverage of the three-dimensional parameter space (Figure 3.1). The 'maximin' algorithm maximizes the minimum distance between all pairs of points in three-dimensional space so that each simulation is as far away as possible in parameter space from other simulations. Based on previous model emulation studies (Lee et al., 2011; Johnson et al., 2015), and following the recommendation of Loeppky et al. (2009), we used 10 simulations per parameter in the design, resulting in a total of 30 simulations to construct our emulators. We refer to these simulations as 'training runs'. We also ran a further 11 simulations that are used to validate the emulator once

built, referred to as 'validation runs' (see Section 3.2.5 for further details on the emulation itself).

Figure 3.1 shows our simulation design with each triangle representing a model simulation. All eruptions are 24 hours in duration and are simulated on 1 July, during the easterly QBO phase, and at 160°E longitude where many real volcanoes exist, and eruptions are frequent (Global Volcanism Program, 2013). The longitude of an eruption is not important for determining the climatic impact (e.g. Toohey et al., 2011) since aerosol in the stratosphere is rapidly transported around the globe, but our simulations have the added benefit of covering realistic eruption locations. Each simulation was run for 38 months following the eruption and we analyse monthly mean model output. We also run a control simulation with no eruption to diagnose the volcanic anomalies.

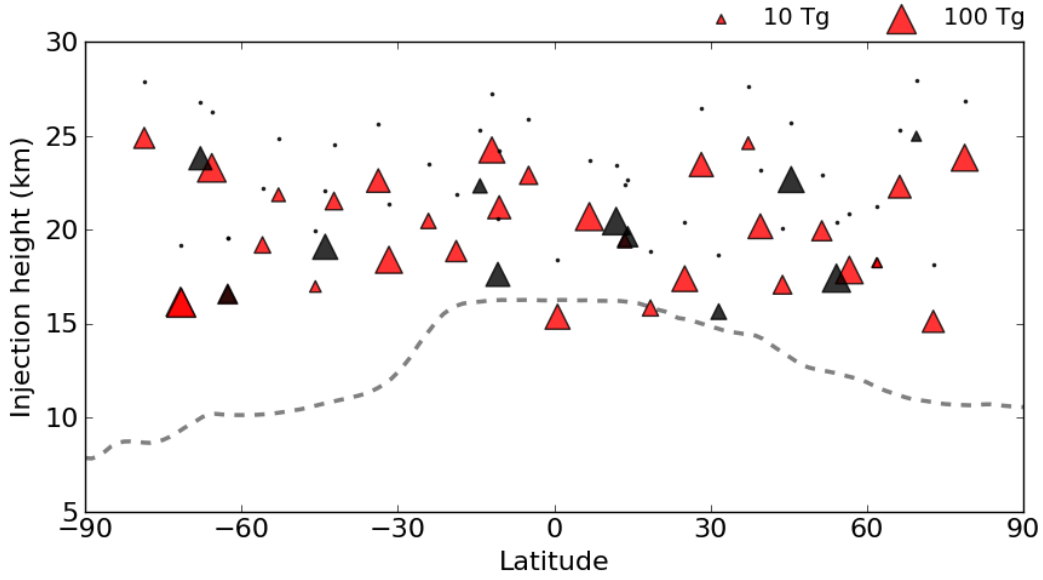

Figure 3.1: Volcanic eruptions simulated. Each triangle represents a model simulation that was conducted using UM-UKCA. The location of the triangle indicates the latitude and injection height of the SO_2 emission for each eruption. The injection height indicates the bottom of the emitted plume; emissions are distributed linearly between this value and 3 km higher, which is shown by the dots above each triangle. The size of the triangle represents the mass of SO_2 emitted. The simulations span SO_2 emissions between 10 Tg and 100 Tg, latitudes between 80°S and 80°N and injection heights with a column-bottom between 15 km and 25 km. Red triangles are training runs, which are the simulations used to build the statistical emulators. Black triangles are simulations which were used to validate the statistical emulators after they were built. There are two simulations (one training run and one validation run) at ~63°S and ~17 km which have SO_2 emissions of 35 Tg and 45 Tg and are not easily distinguished by the marker size scale. The dashed grey line shows the simulated July monthly mean zonal mean tropopause height.

3.2.4 Model outputs

We focus on three key model outputs that determine the magnitude and duration of the volcanic forcing: 1) the global volcanic sulfate burden e-folding decay time (in months), 2) the time-integrated global mean volcanic stratospheric aerosol optical depth (sAOD) at 550 nm (in months), and 3) the time-integrated global mean net radiative forcing (in MJ m^{-2}). The derivation of each output is outlined below.

The sulfate e-folding decay time is defined as the time it takes for the global volcanic sulfate burden (i.e. the sulfate mass anomaly compared to a quiescent background) to decay to 1/e of its peak value. This is a measure of the sulfate aerosol lifetime, which will determine the longevity of the volcanic radiative forcing. Volcanic sulfate aerosol does not decay with a constant e-folding timescale (e.g. SPARC, 2006), therefore we calculate an average e-folding time from the fit of a linear regression line to the natural logarithm of the global sulfate burden anomalies (e.g. Pitari et al., 2016). We fit the regression line from one month after the peak burden until the burden has decayed to below 10% of the peak burden. This calculation method accounts for different durations of the atmospheric volcanic perturbations between the different eruptions. We refer to this as the 'average global sulfate e-folding decay time' and an example of the derivation is included in the Appendix.

Integrated global mean sAOD is the sum of the monthly mean anomalies in global mean sAOD at 550 nm following each eruption, which is influenced by the number and size of sulfate aerosol particles. Integrated global mean net radiative forcing is the sum of the top-of-the-atmosphere outgoing global mean all-sky net radiative flux anomalies (shortwave (SW) + longwave (LW)). The anomalies are integrated over 38 months (until the end of the simulation). For all eruptions the anomalies have decayed to below 10% of the peak anomaly by the end of the simulation.

3.2.5 Emulation and sensitivity analysis

For each model output we construct a Gaussian process emulator that maps how the output depends on the input parameters over the three-dimensional parameter space. The emulator is a surrogate statistical representation of the UM-UKCA model. It is built by assuming that the model response is a Gaussian process and updating the parameters of this Gaussian process with the training data (Kennedy and O'Hagan, 2001; O'Hagan, 2006). An overview of this statistical methodology is given in Appendix A of Johnson et al. (2015) and Lee et al. (2011). The emulator is fast to

evaluate and can be used to predict the output quantity at any combination of the input parameters, enabling multi-dimensional response surfaces of output behaviour across parameter space to be generated.

Emulators have been used in several studies to analyse complex models in multiple scientific fields including tsunami modelling (Sarri et al., 2012), aerosol and cloud modelling (e.g. Carslaw et al., 2013; Lee et al., 2013; Hamilton et al., 2014; Regayre et al., 2014; Johnson et al., 2015; 2015) and galaxy formation (Vernon et al., 2010; Rodrigues et al., 2017). A recent study by Harvey et al. (2018) also successfully applied this approach to volcanic ash modelling of the 2010 Eyjafjallajökull eruption to understand the influence of eruption source parameters and internal model parameters on the simulated output.

Each emulator is constructed from the output of the training runs using the statistical software R (R Core Team, 2017) and the DiceKriging package (Roustant et al., 2012). We build separate emulators for the average global sulfate e-folding decay time, the integrated global mean sAOD, and the integrated global mean net radiative forcing (Section 3.2.4). The emulators are built assuming a linear mean function that includes all parameters and a Matérn covariance structure, which allows for slight variations in smoothness in the output response (Rasmussen and Williams, 2006). Further details regarding fitting the emulators using these assumptions can be found in Johnson et al. (2015). To validate the emulators, we use them to predict the model values at the parameter setting of each validation run and compare the prediction to the actual model output of these runs (Figure 3.2). For the integrated global mean sAOD, the model output lies within the 95% confidence bounds of the emulator prediction for the majority of the validation runs. For the integrated global mean net radiative forcing the emulator also performs well but is overly confident, with the emulator predictions having small confidence bounds that do not always cross the 1:1 line marking a perfect emulator prediction. We only take forward the emulator mean prediction for our analysis, which lies very close to the 1:1 line in all cases, so for our purposes it does not matter that the emulator is too confident at times. The average global sulfate e-folding decay time emulator validates less well. There is more variability in how closely the emulator can predict model output in this case, with three validation points that are over-estimated by the emulator, and for which the model output lies outside the 95% confidence bound of the emulator prediction. This emulator is less confident in its predictions overall (the 95% confidence bounds are larger). However, the e-

folding timescale evolves differently throughout the decay period for each of our simulated eruptions (very few of our eruptions simulated exhibit perfect exponential decay of the global sulfate aerosol burden). Hence the tightness of the fit of the regression line to the sulfate burden decay timeseries varies between simulated eruptions. Because this model output cannot perfectly describe the sulfate decay behaviour of all eruptions simulated, we expect greater uncertainty in the emulator representation for this output and conclude that this emulator fit is not unreasonable.

Using the validated emulators, we sample each output quantity at thousands of parameter combinations of the SO_2 emission magnitude, injection height and latitude that we did not explicitly simulate with UM-UKCA. By densely sampling the emulators across the parameter space defined by the ranges in Table 3.1, we can map response surfaces that show how each output responds to changes in the input parameters. We can also use statistical techniques such as variance-based sensitivity analysis (Saltelli et al., 2000) to quantify the sensitivity of each output to variation in individual parameters. This is achieved by implementing the extended FAST (Fourier Amplitude Sensitivity Test) approach of Saltelli et al. (1999) to decompose the total variance in the output quantity over the parameter space into individual and joint parameter contributions (Section 3.3.2.3) using the R package 'sensitivity' (Pujol et al., 2017).

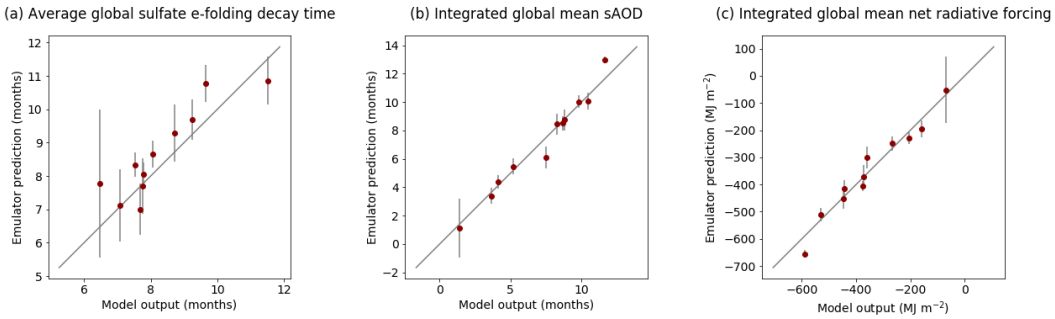

Figure 3.2: Validation of each emulator. For each model output (a-c), the value of the model output for the 11 validation runs is plotted against that predicted by the emulator (red circles). The vertical lines are 95% confidence bounds on the emulator predictions. The solid grey line marks the 1:1 line, indicating a perfect prediction by the emulator.

3.3 Results and discussion

3.3.1 Model output over the set of eruption simulations

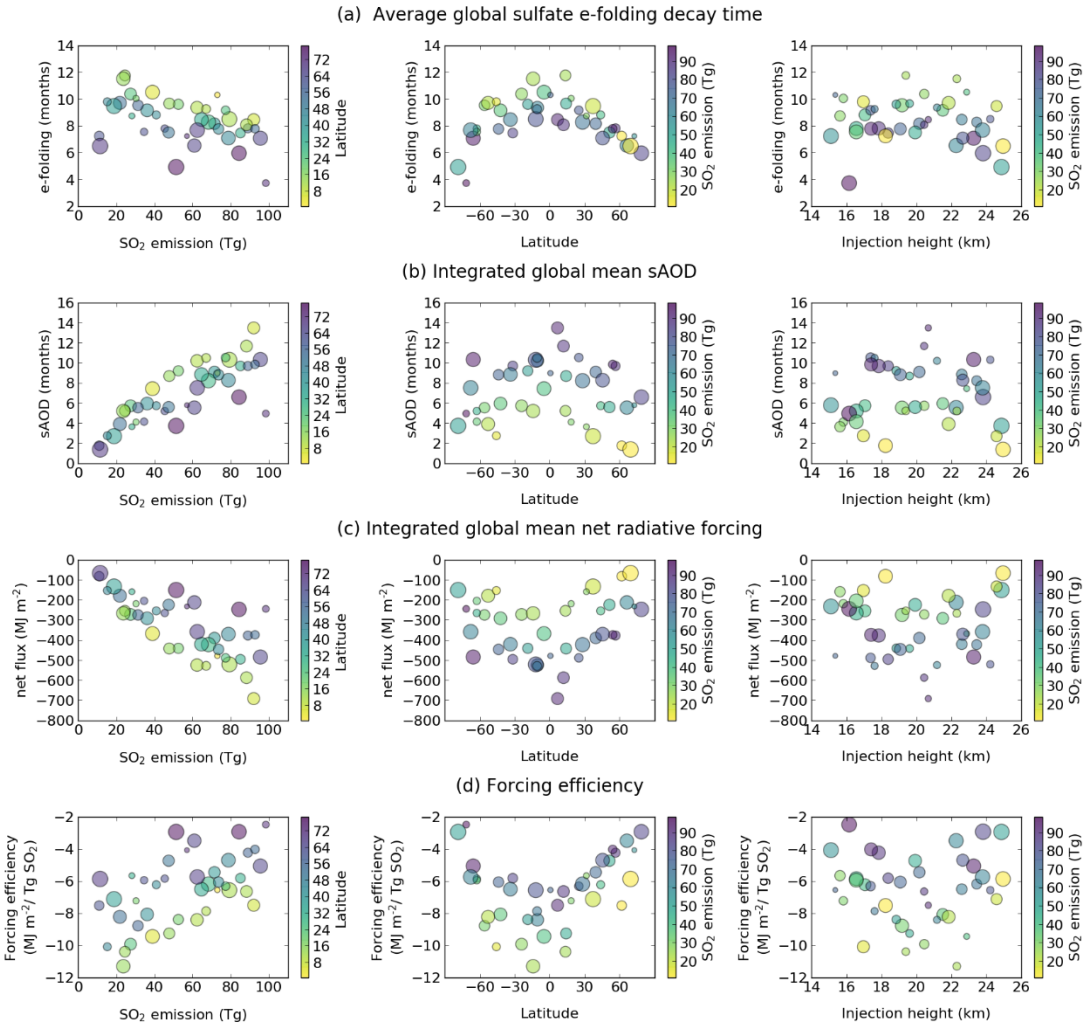

Figure 3.3: Model outputs versus the eruption source parameters for all 41 model simulations (training and validation). Each plotted point represents the output of one model simulation. For each output quantity (panels a - d), we show the output value vs. SO_2 emission (left), latitude (middle) and injection height (right). For the left hand plots the colour of the points indicates the latitude of the eruption in each simulation and the size indicates the injection height (the larger the point, the higher the injection height). For the plots in the middle, the colour represents the mass of SO_2 emitted and the size indicates the injection height. On the right, the colour indicates the mass of SO_2 emitted and the size represents the latitude of the eruption (smaller for low latitudes, larger for high latitudes).

Before emulating, we first examine the model output across the 41 simulations. Figure 3.3 shows the average global sulfate e-folding decay time, the integrated global mean sAOD anomalies, and the integrated global mean net radiative forcing. In addition, we also show the net radiative forcing efficiency calculated as the integrated net forcing divided by the mass of SO_2 emitted (MJ m^{-2}/Tg SO_2). Each of these output quantities is shown for each simulation plotted against the eruption source parameters.

3.3.1.1 Sulfate burden e-folding decay time

Figure 3.3a shows that the average global sulfate e-folding decay time is dependent on latitude with longer e-folding decay times for eruptions at low latitudes resulting from slower removal of the aerosol, and shorter e-folding decay times for eruptions at high latitudes resulting from faster removal of the aerosol. These differences are due principally to the stratospheric Brewer-Dobson circulation (BDC), which is characterized by upward motion at the tropics, poleward transport and downward motion at the poles (Holton et al., 1995; Butchart, 2014). The global sulfate e-folding decay times also decrease with increasing SO_2 emission magnitudes because of growth to larger particle sizes and increased gravitational sedimentation. The e-folding decay time generally increases as the injection height increases until the height of the SO_2 emission is ~20 km, although the response is weaker compared to that of the eruption latitude and SO_2 emission. The increase in decay time with injection height is a result of longer air residence time. However, for injection heights greater than ~20 km the e-folding decay time starts to decrease. The decrease in the average decay time (i.e. shorter aerosol lifetime) above ~20 km is contrary to the general increase in air residence time with height because it is complicated by aerosol microphysical processes (i.e. aerosol growth) and latitude-dependent circulation features and meridional transport barriers, such as the tropical pipe (Plumb, 1996). The average decay time reflects several phases of the aerosol evolution. For example, longer-lived volcanic sulfate aerosol particles have more time to grow by condensation and coagulation and therefore sediment more rapidly later during the aerosol decay, such that the average e-folding time decreases. We find that the ratio of the integrated global mean sAOD at 550 nm to the sAOD at 1020 nm, which is a proxy of particle size, decreases with increasing injection height, indicating larger particles are formed on average for eruptions with higher-altitude injections (not shown). Sedimentation rates are also higher with increasing altitude since the air

density is reduced. The influence of stratospheric dynamics and aerosol microphysics are explored in greater detail in Section 3.3.2.2.

By examining the colours of the points in the top left panel of Figure 3.3a we can begin to see joint dependencies between the SO_2 emission magnitude and latitude in influencing the e-folding time: for low latitude eruptions (yellow points) the reduction in the e-folding time with increasing SO_2 emission appears stronger than for high latitude eruptions (purple points). Overall the average sulfate aerosol e-folding decay time is strongly variable, ranging from 4 months to 12 months (Table 3.2).

Table 3.2: Model outputs considered and summary statistics across the 41 eruptions simulated. Included in parentheses are the eruption source parameter combinations of the simulation that resulted in the minimum and maximum for each model output. The injection height value represents the bottom of the 3-km-thick initial plume. Values have been rounded to the nearest integer.

Model output	Minimum	Maximum
(a) Average global sulfate e-folding decay time (months)	**4** (72°S, 98 Tg, 16 km)	**12** (14°N, 25 Tg, 19 km)
(b) Integrated global mean sAOD (months)	**1** (69°N, 11 Tg, 25 km)	**13** (7°N, 92 Tg, 21 km)
(c) Integrated global mean net radiative forcing (MJ m^{-2})	**-68** (69°N, 11 Tg, 25 km)	**-692** (7°N, 92 Tg, 21 km)
(d) Forcing efficiency (MJ m^{-2}/Tg SO_2)	**-2** (72°S, 98 Tg, 16 km)	**-11** (14°S, 24 Tg, 22 km)

3.3.1.2 Integrated global mean sAOD and net radiative forcing

Integrated global mean sAOD (Figure 3.3b) ranges from 1 to 13 months (Table 3.2) and has a strong dependency on the mass of SO_2 emitted with higher integrated sAOD for greater SO_2 emissions. This is due primarily to the formation of more sulfate aerosol mass. Integrated global mean sAOD is also greater for lower latitude eruptions and for eruptions with the altitude of the SO_2 emission near 20 km, likely reflecting the increase in aerosol lifetime and a decrease in scattering efficiency for higher-altitude injections following the formation of larger particles. As with the sulfate e-folding decay time (Figure 3.3a), there is greater variation in the integrated sAOD versus the injection height.

Integrated global mean net radiative forcing (Figure 3.3c) is also stronger for larger SO_2 emissions, low latitude eruptions and injection heights around ~20 km. The integrated net radiative forcing ranges from -68 MJ m^{-2} to -692 MJ m^{-2}. Like the

sulfate e-folding decay time, we can also begin to see some joint dependencies between the amount of SO_2 emitted and latitude in the increase in net radiative forcing. Net radiative forcing strengthens more rapidly (becomes more negative) with increasing SO_2 emission for low-latitude eruptions (yellow points) compared to high-latitude eruptions (purple points). Dependencies are explored in greater detail using the statistical emulators (Section 3.3.2).

The increase in net radiative forcing is not linear with increasing SO_2 emission. Figure 3.3d shows that the forcing efficiency weakens with increasing SO_2 emissions, in line with previous modelling studies of volcanic eruptions and sulfate geoengineering studies (e.g. Timmreck et al., 2010; English et al., 2013; Niemeier and Timmreck, 2015; Kleinschmitt et al., 2018). The weakening in forcing efficiency is predominantly due to a decrease in the SW efficiency as aerosol particles increase in size and become less effective at scattering SW radiation. The LW forcing efficiency is more constant for increasing SO_2 emission (Figure C.1). As a result, the net radiative forcing efficiency decreases (the forcing becomes less negative). The net forcing efficiency is higher for low-latitude eruptions because of an increase in the SW efficiency, but the LW efficiency also increases for low-latitude eruptions, which offsets some of the forcing by SW radiation. This increased forcing efficiency is due to increased insolation and outgoing radiation and likely the longer aerosol lifetime at low latitudes. Against injection height, the forcing efficiency is greatest for eruptions with emission altitudes near 20 km. The most effective eruption (per Tg of SO_2 mass emitted) occurs at a latitude of 14°S with 24 Tg SO_2 emitted between 22 and 25 km. The least effective eruption is at 72°S, with 98 Tg SO_2 emitted between 16 and 19 km (Table 3.2).

3.3.2 Multi-dimensional analysis using statistical emulation

3.3.2.1 Emulated response surfaces

We use the validated emulators (Figure 3.2) for each model output to predict the output at other parameter combinations that we have not explicitly simulated. Figure 3.4 shows example response surfaces that reveal the relationship between each model output and the value of latitude and the mass of SO_2 emitted, at a fixed injection height of 20 km. For visualisation purposes, injection height was fixed at its central value in the emulator as this parameter has the weakest relationship with each of the model outputs (Figure 3.3).

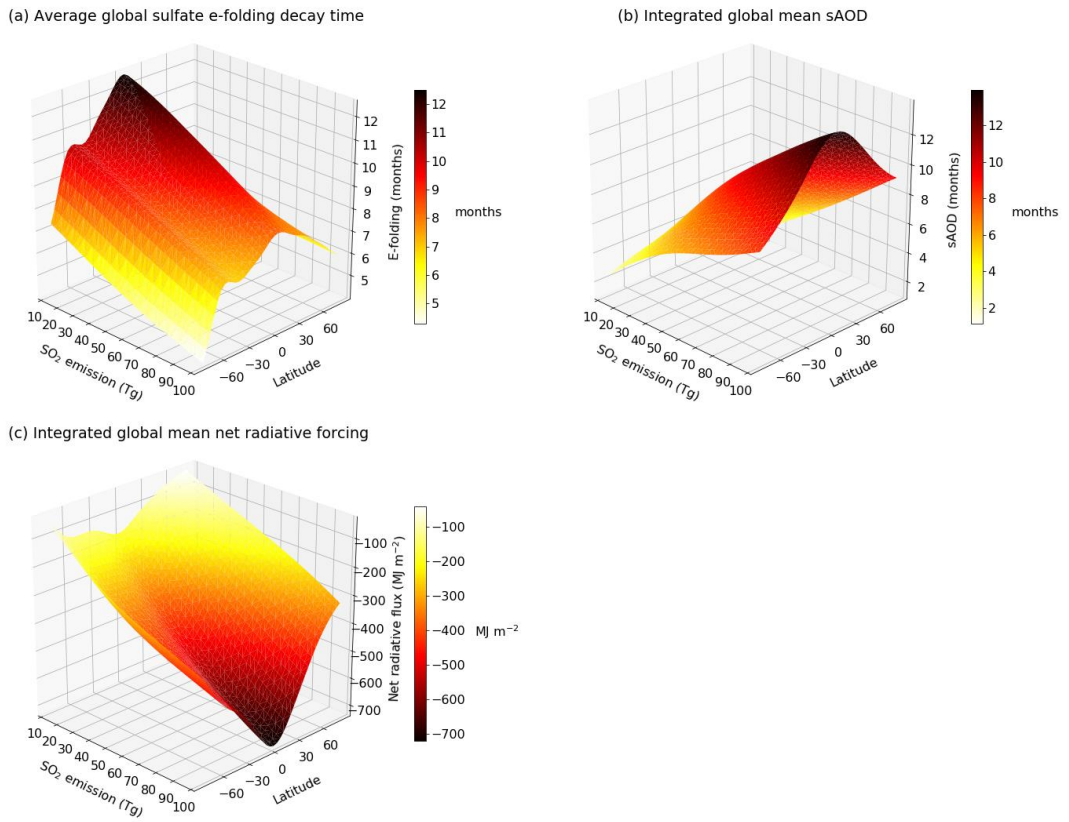

Figure 3.4: Emulated response surfaces for each model output (a-c) at a fixed injection height of 20 km. The surface shows the emulator's prediction of the model response (z axis) against the mass of SO_2 emitted (x axis) and latitude (y axes). The colour of the surface also indicates the value of the predicted model output. Each surface is plotted from 1600 combinations of latitude and SO_2 magnitude, which were determined over a grid of 40 equally spaced values of each varied parameter between the minimum and maximum parameter input values (Table 3.1).

The surfaces in Figure 3.4 further demonstrate the dependencies of the model outputs on the mass of SO_2 emitted by an eruption and its latitude. The average global sulfate e-folding decay time shows a stronger dependence on the value of latitude, with a sharp gradient observed in the response surface across the latitude dimension. The e-folding decay time is more than 12 months for eruptions at the equator that have less than ~24 Tg of SO_2 emitted. The surfaces for integrated global mean sAOD and integrated global mean net radiative forcing are more similar, with strong gradients across the SO_2 emission magnitude dimension especially for low latitude eruptions.

To explore the relationship between the model outputs and the latitude and SO_2 emission of an eruption for other injection heights, we also sample the emulated response surface at fixed injection heights of 16 km, 20 km and 24 km and show these surfaces in two-dimensions (Figure 3.5).

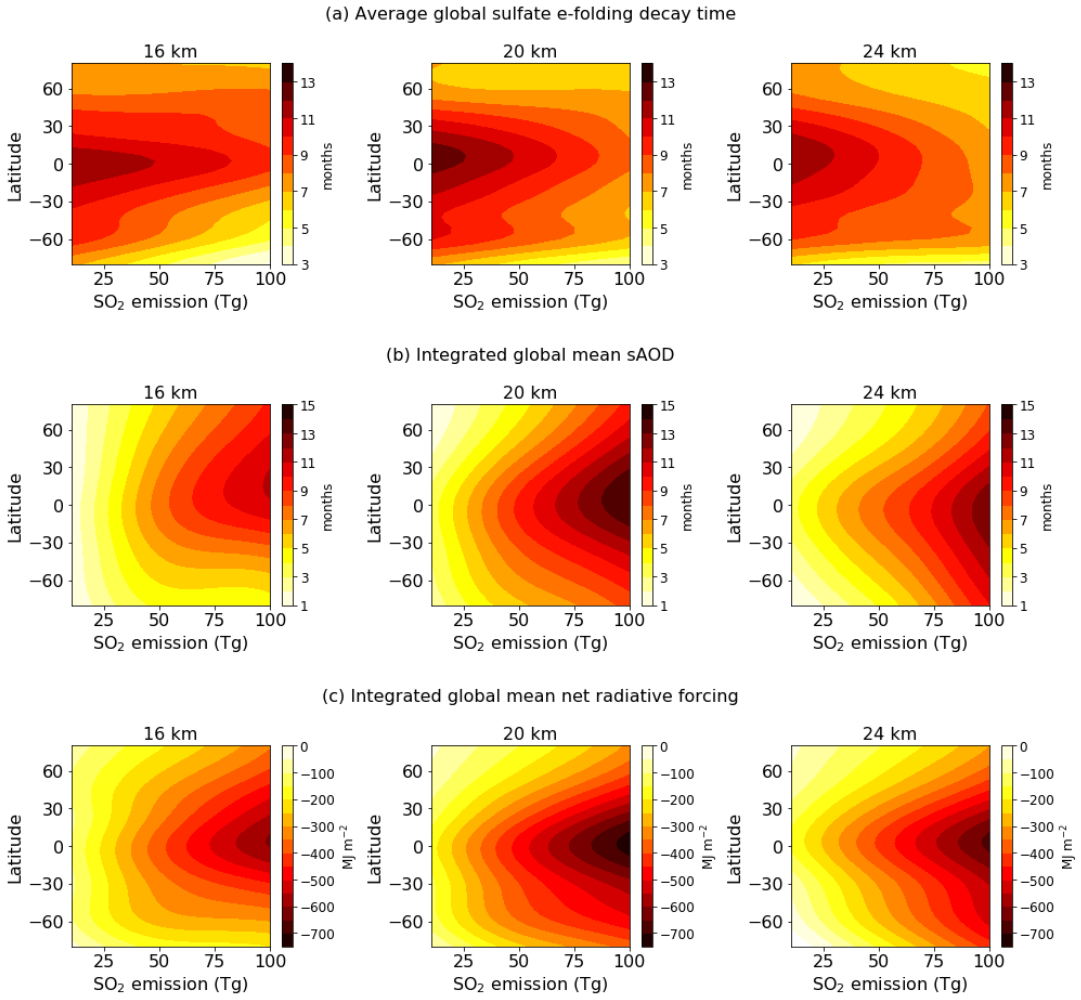

Figure 3.5: Emulated response surfaces at fixed injection heights for each model output. For each emulator (a–c), we sample at fixed injection heights of 16 km, 20 km (as in Figure 3.4) and 24 km. The resulting contour plots show the emulator prediction of each model output against SO_2 emission and latitude of the eruption at each of these injection heights.

Now we begin to see more clearly the influence of injection height on each model output because the response surfaces are not the same at each height. For example, for injections at 20 km, all model outputs reach greater values. The symmetry across latitude also changes with height; for example, at 16 km, integrated sAOD for SO_2 emissions greater than ~50 Tg is larger in the Northern Hemisphere (NH) than the Southern Hemisphere (SH). However, the surface is more symmetrical across latitude for injections at 20 km and 24 km.

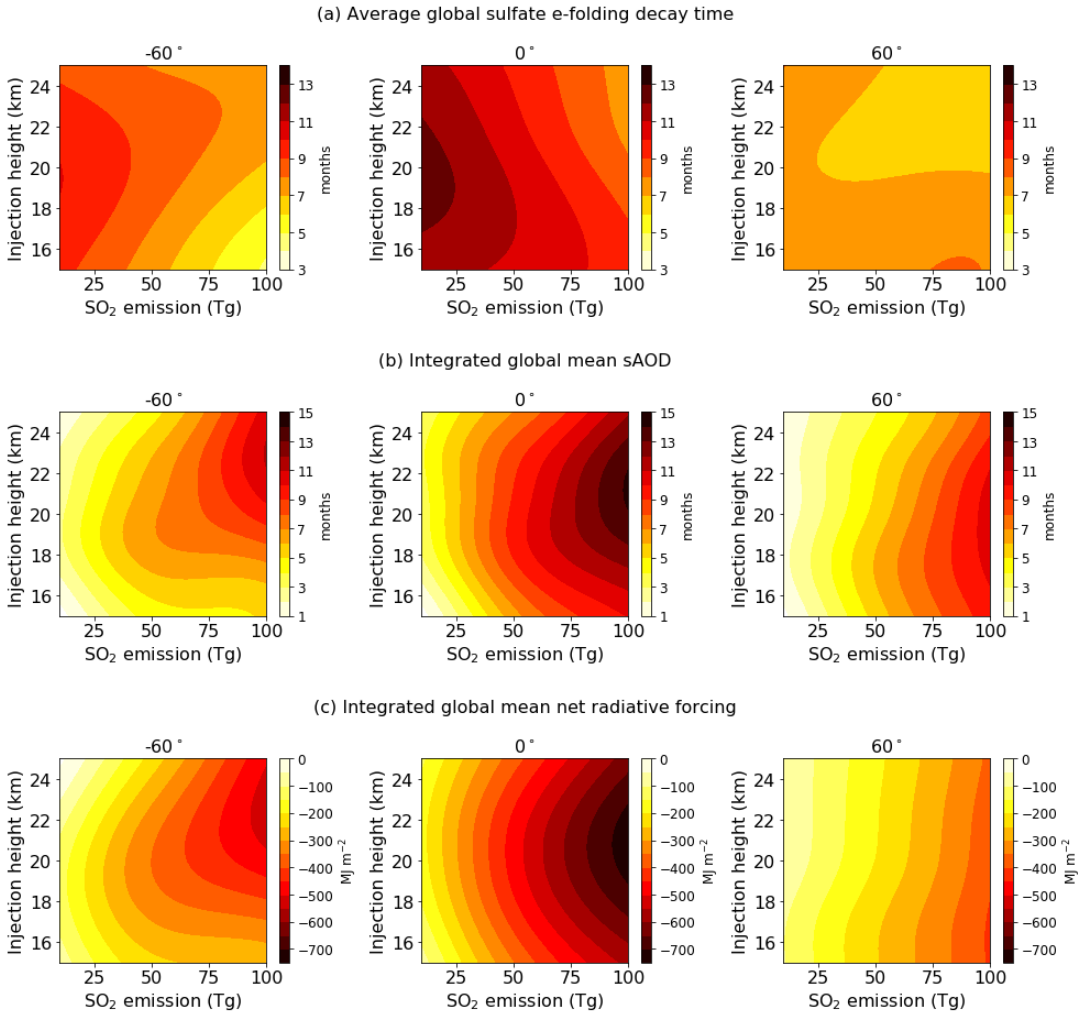

Figure 3.6: Emulated response surfaces at fixed latitude for each model output. For each emulator (a–c), we sample at fixed latitudes of 60°S, 0° and 60°N. The resulting contour plots show the emulator prediction of each model output against SO_2 emission and injection height of the emissions at each of these latitudes.

Figure 3.6 shows the emulated response surfaces plotted against the SO_2 emission and injection height at fixed latitudes of 60°S, 0°, and 60°N. At 60°S the integrated sAOD and radiative forcing are highest for eruptions that have injection heights above ~20 km and the highest emissions. However, for emissions less than ~50 Tg, the highest forcing occurs for eruptions with emission altitudes nearer 20 km. For eruptions at the equator, the largest integrated sAOD and radiative forcing occur for injection heights near 20 km for all SO_2 emissions. At 60°N, the model outputs are less sensitive to injection height than for eruptions at 60°S and 0° and are mainly dependent on the SO_2 emission. For the sulfate e-folding decay time, the surfaces are more variable and since this emulator validated the least well, we focus on the general patterns only. In general, the decay time decreases for larger SO_2 emissions and at 0° decreases for the high-altitude injections of low SO_2 emissions.

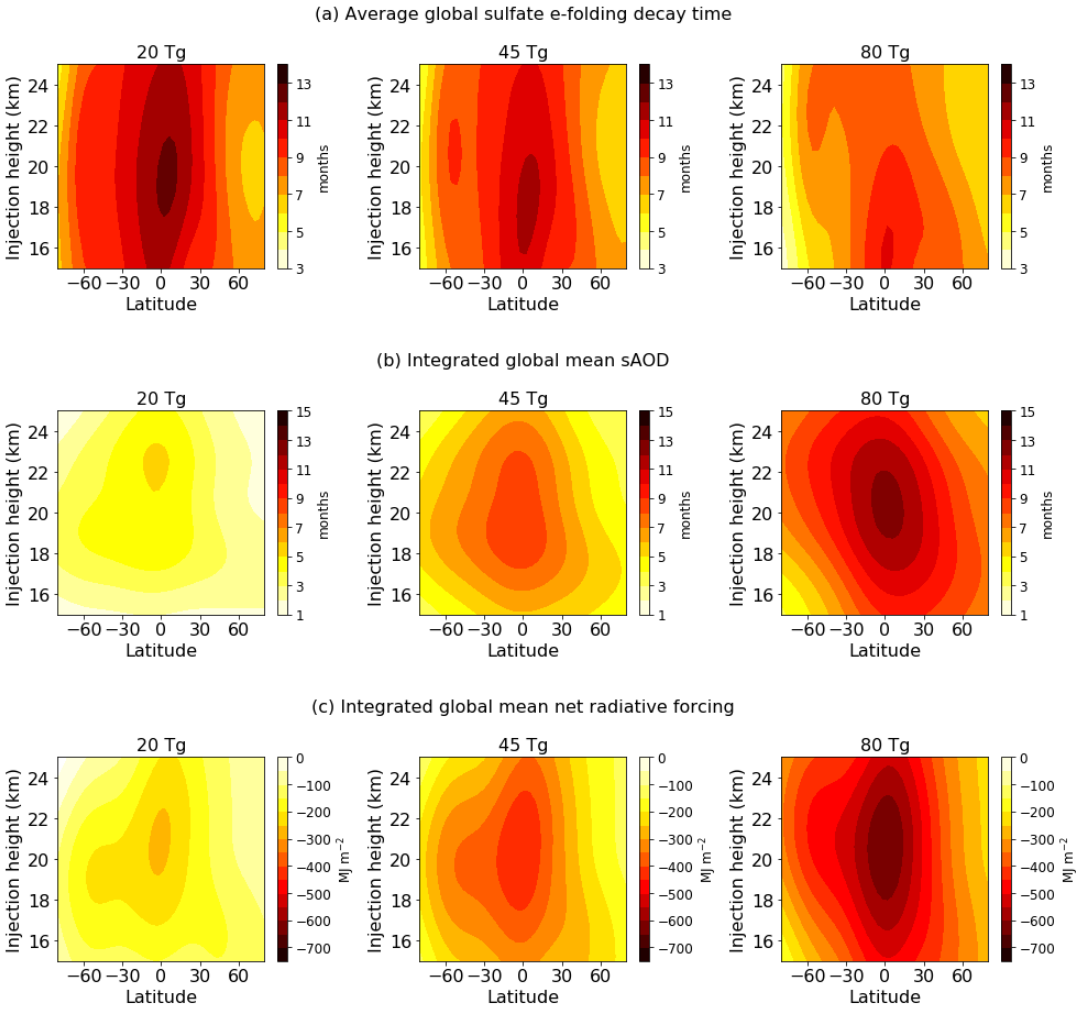

Figure 3.7: Emulated response surfaces at fixed SO_2 emissions for each model output. For each emulator (a–c), we sample at fixed SO_2 emissions of 20 Tg, 45 Tg and 80 Tg. The resulting contour plots show the emulator prediction of each model output against latitude and injection height of the emissions for each of these emission magnitudes.

Figure 3.7 shows the response surfaces at fixed SO_2 emissions of 20 Tg, 45 Tg and 80 Tg. Here we see the dependency that the model outputs have on latitude and injection height at these emission magnitudes. In general, these surfaces are more similar in shape, with peaks in each model output for eruptions at the equator and for injection heights at ~20 km. At higher latitudes, the model outputs are less dependent on the value of injection height. The surfaces are also not entirely symmetrical around the equator.

The surfaces also reveal that the same model outputs can be achieved for notably different combinations of parameter values. For example, the more circular contours in Figure 3.7b for an injection of 45 Tg (middle panel), show that an integrated sAOD

of 6–7 months can be caused by an eruption at 0° with the SO_2 injected at 25 km or an eruption at 60°S with the SO_2 injected at 19 km.

3.3.2.2 Mechanisms for the parameter dependencies

Figures 3.5-3.7 consolidate the patterns and responses revealed by the individual simulations (Figure 3.3) but allow us to explore the relationships at any point in parameter space, in which the dependencies of the output on the eruption source parameters change. The e-folding decay time of the sulfate aerosol is a function of the large-scale stratospheric BDC and sulfate particle sizes, which dictates the sedimentation rate. The integrated sAOD is a function of the mass of sulfate aerosol, its size distribution, and the sulfate e-folding decay time. The integrated net radiative forcing is dependent on the volcanic sAOD, but additionally the insolation, cloud cover and surface albedo. In general, the varying responses in Figures 3.5-3.7 can be explained by differences in the large-scale stratospheric circulation and in aerosol microphysical processes and are explored below.

Tropical eruptions

For tropical eruptions, the model outputs were more dependent on injection height than for eruptions in the high latitudes, with a turning point at roughly 20 km for the integrated global mean sAOD and net radiative forcing (e.g. Figure 3.7). In the tropics, sulfate aerosol transport is influenced by the stratospheric tropical pipe (Plumb, 1996), which extends from roughly 21 km to 28 km and restricts meridional transport from the tropics to the extratropics (Trepte and Hitchman, 1992). Consequently, sulfate aerosol builds up in the tropical reservoir after an eruption. However, in the lower stratosphere the rapid shallow branch of the BDC allows greater transport of the aerosol to high latitudes and with increasing altitude, the strength of the tropical barrier reduces (e.g. Holton et al., 1995), and smaller aerosol particles, which have not sedimented out can be transported to the extratropics in the upper branch of the BDC (e.g. Niemeier and Schmidt, 2017). Arfeuille et al. (2014) found that sulfate aerosol simulated after the eruption of Mt. Tambora had a shorter residence time in the tropics and stronger extratropical transport for a 27-29 km injection compared to a 23-25 km injection, which is comparable to the results presented here.

In addition to variations in the strength of subtropical transport barriers, the response to injection height in the tropics is also in part due to changes in sulfate aerosol particle size and sedimentation. The time-integrated and global nature of these outputs means

that several phases of the aerosol evolution are averaged and reflected in just one number. We suggest that in general there are two phases of the aerosol evolution. The first phase is a "growth phase" as the aerosol particles form and coagulate, in which aerosol removal mainly depends on the latitude of the eruption, rather than the SO_2 emission. The second "sedimentation phase" occurs after several months when particle growth has slowed and sedimentation becomes relatively more important. We suggest that longer air residence time and subsequent growth to larger particles for SO_2 injections above ~20 km increases the sedimentation rate and hence aerosol decay in the second phase of the aerosol evolution, causing a decrease in the integrated global mean sAOD and net radiative forcing. Radiative forcing is also weakened because larger particles are less effective at scattering SW radiation. Similar effects are also observed in geoengineering simulations of continuous sulfur emissions with increasing injection heights, such that the effects of a longer lifetime and larger particles cancel, and radiative forcing does not increase with higher altitude SO_2 injections (e.g. Niemeier and Schmidt, 2017; Tilmes et al., 2017; Kleinschmitt et al., 2018).

As the mass of SO_2 emitted is increased from 20 Tg to 45 Tg, the maximum values of the average global sulfate e-folding decay time, integrated sAOD and radiative forcing occur at decreasing injection heights (Figure 3.7), likely related to increased sedimentation as particles grow larger for the bigger SO_2 emissions. This is also seen in the average global sulfate e-folding decay time as the emission is increased from 45 Tg to 80 Tg, but this is not the case for the integrated sAOD and radiative forcing. The peak value in the average sulfate e-folding decay time also occurs for lower injection heights compared to the peak values in integrated sAOD and radiative forcing. The sulfate e-folding decay time reflects the loss of sulfate aerosol mass, but the sAOD is dependent on the aerosol surface area. As the particles grow and sediment, which decreases the average aerosol lifetime, the remaining particles are more optically efficient, hence the integrated sAOD remains higher. Increased upwelling due to aerosol-induced radiative heating may increase the tropical confinement and aerosol lifetime (e.g. Niemeier et al., 2009; Niemeier et al., 2011) when the strongest volcanic forcing occurs, despite a lower average e-folding decay time, which reflects all phases of the aerosol decay. For the higher altitude injections, enhanced lofting may also result in the aerosol moving to altitudes at which the tropical barrier is weaker, allowing it to spread meridionally (e.g. Young et al., 1994;

Aquila et al., 2012). Additionally, higher temperatures at high altitudes may reduce the amount of gaseous sulfuric acid that nucleates, and some of the formed aerosol may then evaporate, reducing the sulfate aerosol mass. Some of this vapour can also condense onto MSP, where it remains (in this version of UM-UKCA) and photolysis of sulfuric acid vapour will also produce SO_2. However, we find that the proportion of global sulfur that is in the form of gaseous sulfuric acid compared to sulfate aerosol is very small in all of the 41 simulations. The largest fraction of global sulfur accommodated onto MSP compared to the total sulfate aerosol plus gaseous sulfuric acid at any time in a simulation was 0.23. These effects are unlikely to significantly contribute to the response to injection height shown here.

Aerosol radiative heating can also modify the QBO (e.g. Aquila et al., 2012; Aquila et al., 2014; Niemeier and Schmidt, 2017; Kleinschmitt et al., 2018), which further modulates the tropical confinement and transport of sulfate aerosols out of the tropics (e.g. Trepte and Hitchman, 1992; Trepte et al., 1993; Punge et al., 2009). Although beyond the scope of the present study, such dynamical changes induced by the sulfate aerosol are likely contributing to the response in the model output as the SO_2 emission increases.

Mid- to high-latitude eruptions

Outside of the tropical pipe, the lifetime of sulfate aerosol is dependent on the large-scale meridional transport, isentropic mixing and transport to the troposphere via mid-latitude tropopause folds, sedimentation and large-scale subsidence, where it is eventually deposited by wet and dry deposition (e.g. Hamill et al., 1997). For mid- to high-latitude eruptions, the effect of injection height on the model outputs is less pronounced than those at low latitudes, as aerosol is not restricted by the tropical pipe and due to the much faster decay times of sulfate aerosol there is less time for the growth of particles to offset an otherwise increase in aerosol lifetime with increasing altitude.

Eruptions with middle injection heights (~18-22 km) in the SH have larger values of the model outputs than the equivalent eruptions in the NH (e.g. Figures 3.5 & 3.7), although this is not the case for all emission magnitudes and latitudes. Because our eruptions occurred in July, large-scale mixing, poleward transport and deposition are stronger in the winter SH at the time of the eruption (Holton et al., 1995). Insolation at the time of the eruption is greater in the NH, but in the majority of our simulations,

the peak aerosol burden occurs ~5-6 months after the eruption, consequently coinciding with the peak summer insolation if the eruption was in the SH and resulting in a larger radiative forcing. Climatologically, transport is stronger in the NH and therefore over the integrated time period NH eruptions may have a lesser impact as more of the aerosol plume is transported into the troposphere. Differences in the global model output between eruptions in each hemisphere are also related to other aspects of the stratospheric dynamics such as the position of the tropopause and the polar winter vortices. The tropopause is lower in the SH (Figure 3.1) such that the lowest injections in the NH will be closer to the tropopause where the aerosol is removed more effectively via isentropic transport and tropopause folds compared to the equivalent SH eruption. The polar winter vortices at ~60° inhibit transport of aerosol to the poles, but effectively remove aerosol that is within the vortex, and the vortex is stronger in the SH (Holton et al., 1995; Hamill et al., 1997).

In summary, the three outputs investigated are global and time-integrated values, whose end value is a result of processes that change in both time and space. The response surfaces shown here are the result of multiple interacting and compensating effects, such as the level of tropical confinement, particle growth and sedimentation and large-scale transport and mixing. The results highlight the necessity of using models with interactive aerosol microphysics in contrast to simpler mass-based aerosol schemes (with fixed size distribution) where increasing injection heights tends to result in larger forcing (e.g. Jones et al., 2017). These results illustrate the value of using statistical emulation to explore the entirety of the three-dimensional parameter space, where the dependencies of the model output on the eruption source parameters can change. An online tool allowing the user to explore the response surfaces for other fixed values has been provided, the link to which is included in the supporting information.

3.3.2.3 Average response of the model output

Figure 3.8 shows the average response of each model output to each eruption source parameter over the three-dimensional parameter space (a-c) and the percentage contribution that each parameter makes to the model output value (d), calculated from a variance-based sensitivity analysis (Section 3.2.5). The sensitivity analysis allows quantification of the features and trends seen in the initial scatter plots and response surfaces (Figures 3.3-3.7).

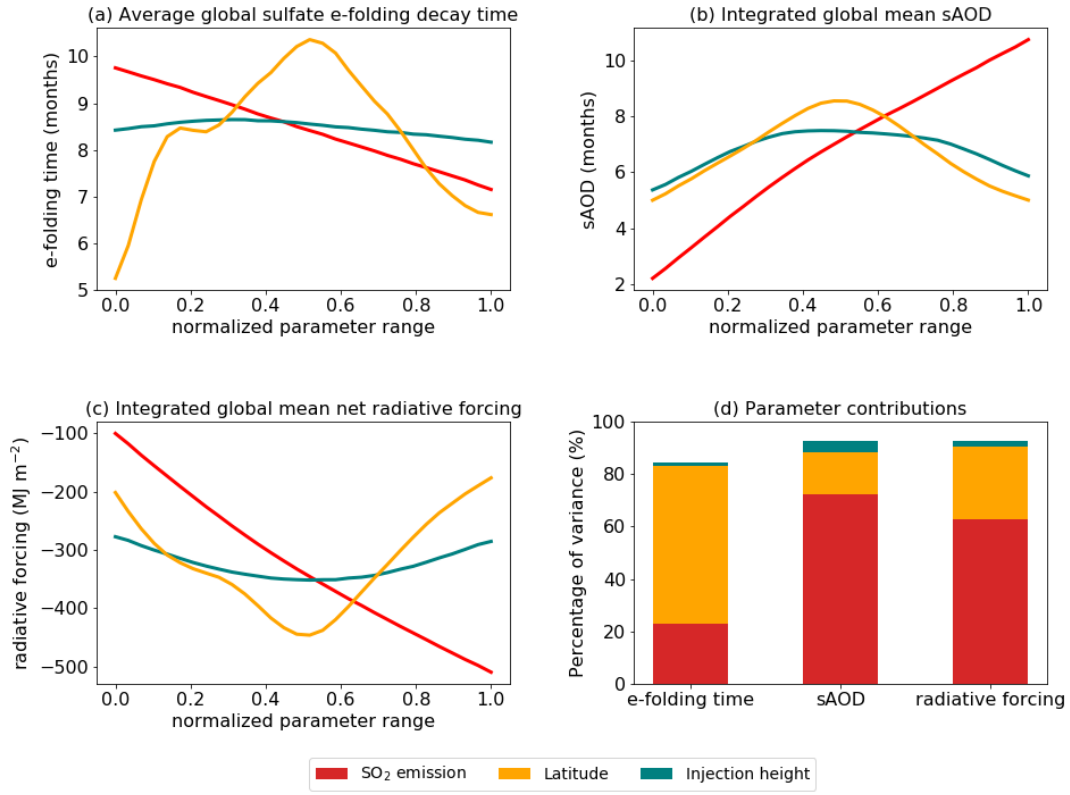

Figure 3.8: Sensitivity analysis results showing the average effects of the SO_2 emission magnitude (red), latitude (orange) and injection height (teal) on the value of each model output (a-c) and the percentage of variance in each model output explained by each eruption source parameter (d). The average responses are plotted against the normalized parameter range showing the effects from low to high SO_2 emissions (10 to 100 Tg), from high SH latitudes to high NH latitudes (80°S to 80°N) and from low injection heights to high injection heights (bottom of the plume from 15 to 25 km).

The red lines in Figure 3.8 show the response to SO_2 emission from low to high emissions, which results in a decrease in aerosol decay time, and an increase in integrated global mean sAOD and net radiative forcing. The response to injection height (teal) from low to high altitudes is seen most clearly for the integrated sAOD. The response to latitude (orange) from high southern latitudes to high northern latitudes is most dominant for the sulfate e-folding decay time. Interestingly the average response shows a ridge in the response to latitude in the mid-to-high latitudes in the SH, which is apparent for the sulfate e-folding decay time and net radiative forcing, but not for sAOD. The exact cause of the decrease in response remains uncertain but could be influenced by increased stratosphere-troposphere exchange in the jet stream regions and deposition of aerosol in the SH storm tracks for the sulfate e-folding decay time and due to seasonally varying insolation for the radiative forcing.

For all three model outputs, the injection height is relatively the least important parameter, contributing to less than 5% of the variance in each output. As a result, any change in the model outputs by changing the injection height is dwarfed by changes to the SO_2 emission magnitude and latitude. For the average global sulfate e-folding decay time, the SO_2 emission explains 23% of the variance and latitude explains 60%. However, for the integrated global mean sAOD, we see the opposite situation, where the SO_2 emission contributes more to the variance at 72% compared to 16% from the latitude. The integrated global mean net radiative forcing is sensitive to the parameters in a very similar way as we see for the integrated global mean sAOD, but with a slightly lower contribution from the SO_2 emission (63%) and a slightly higher contribution from latitude (28%). The contributions suggest that the decay rate of the sulfate aerosol is primarily dependent on the stratospheric circulation, but the integrated sAOD and radiative forcing depends primarily on the SO_2 emission, which dictates the amount of aerosol that can form. The slightly larger contribution from latitude for integrated radiative forcing compared to the integrated sAOD is likely due to the fact that although primarily a function of the sAOD, the radiative forcing is also dependent on the insolation and cloud cover, which vary as a function of latitude. The variance contributions do not total to 100% as the total variance is also explained by possible interaction effects (the combined effect of each parameter with the other parameters) and random noise. In general, this contribution is very small and likely noise related.

In the following section we explore some of the novel applications of the emulated surfaces.

3.3.3 Emulator applications

3.3.3.1 Emulator predictions for the 1991 eruption of Mt. Pinatubo

The emulators can be used to predict the atmospheric effects of historic eruptions that have eruption source parameters within our simulated ranges. There is substantial uncertainty in both the mass of SO_2 emitted and the injection height of emissions for historic eruptions due to a lack of direct observations. We can use the emulators to quantify the range of a model output that is consistent with the estimated uncertainty range of the eruption source parameters. As an example, Figure 3.9 shows the emulator response surfaces for parameter ranges relevant to the 1991 eruption of Mt. Pinatubo (latitude 15ºN). For one possible realisation of this eruption (the grey

triangle), with 14 Tg of SO_2 emitted between 21 km and 24 km, the emulator predicts an average global sulfate e-folding time of 12 months, integrated global mean sAOD of 3.6 months and integrated global mean net radiative forcing of -187 MJ m^{-2}. When we account for the uncertainties in the eruption source parameters (SO_2 emissions of 10-20 Tg and injection heights spanning 18-25 km; Timmreck et al., 2018 and references therein) we predict an average global sulfate e-folding decay time of ~11-12 months, an integrated global mean sAOD of ~2.7-4.6 months, and integrated global mean net radiative forcing of about -133 to -229 MJ m^{-2}.

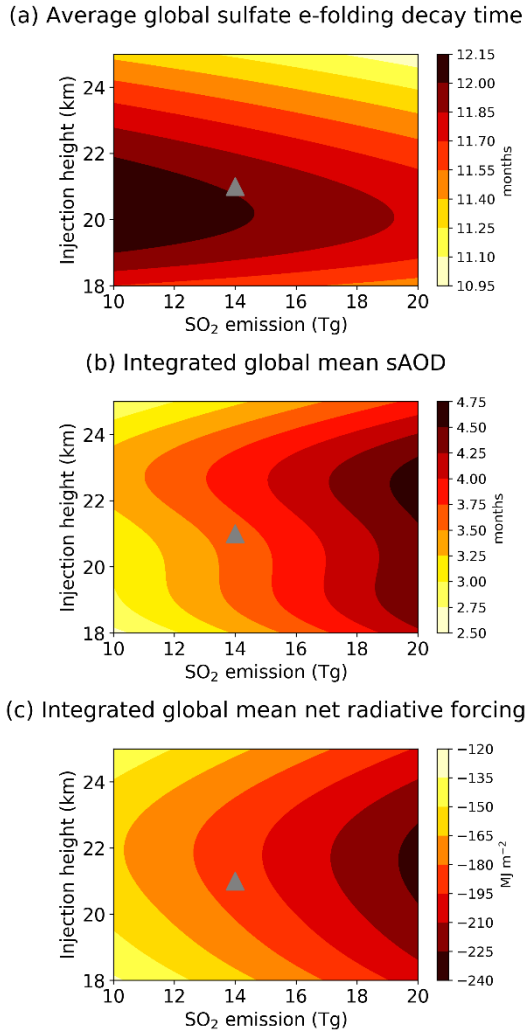

Figure 3.9: Emulated response surfaces at the latitude of Mt. Pinatubo for each model output (a–c). These surfaces show the predicted model outputs for possible combinations of the SO_2 emission and injection height estimated for the 1991 eruption of Mt. Pinatubo. We sample a grid of 10000 parameter combinations with the SO_2 emission ranging between 10 and 20 Tg (100 equally spaced values) and injection height between 18 and 25 km (100 equally spaced values representing the bottom of the plume) and latitude fixed at 15°N. The grey triangle marks one possible realisation of the 1991 eruption with an SO_2 emission of 14 Tg and injection height of 21 – 24 km (the triangle marks the bottom of the 3-km plume).

Our estimates of average global sulfate e-folding decay time, regardless of the combination of SO_2 emission and injection height are in good agreement with observations and previous model simulations, which report e-folding decay times of about 1 year (e.g. SPARC, 2006). The equivalent integrated global mean sAOD at 550 nm from the CMIP6 dataset (version 3) (Thomason et al., 2018) is ~2.5 months (we calculate post-Pinatubo sAOD anomalies by subtracting an estimate of the background sAOD using years 1999-2000) and is slightly less than the minimum value of ~2.7 months predicted by the emulator when emitting 10 Tg SO_2 between 18 km and 21 km.

We can also use the emulators "in reverse" to find the ranges of the eruption source parameters that are consistent with a particular volcanic response. For example, as seen in Figure 3.9b, there are other parts of the parameter space that can result in an integrated global mean sAOD close to 2.7 months. Toohey et al. (2011) calculated a four-year-integrated global mean volcanic AOD after the eruption of Mt. Pinatubo of ~3 months using a 17 Tg SO_2 emission, which is comparable to our results. The light-yellow region in Figure 3.9b shows the combinations of SO_2 emission and injection height that result in integrated sAOD < 3 months. The SO_2 emissions must be less than ~12 Tg, but the injection height can either be less than ~19.5 km or greater than ~24.5 km (given the assumed range in SO_2 emission and injection height). Of course, not all combinations of the constrained SO_2 emission and injection height will result in an integrated global mean sAOD less than 3; for example, if the mass of SO_2 emitted was 12 Tg, the injection height could not be 19.5 km.

To match the integrated sAOD value of ~2.5 from CMIP6 for the 1991 Mt. Pinatubo eruption, UM-UKCA requires SO_2 emissions nearer 10 Tg, with an injection column-bottom nearer 18 km (Figure 3.9b). The small mis-match between the CMIP6 value of integrated sAOD and the emulator prediction suggests that either the CMIP6 value is too low, UM-UKCA has overestimated the atmospheric perturbation, or the true SO_2 emission and injection height laid outside of our estimated ranges (10-20 Tg and 18-25 km). The UM-UKCA simulations were also idealized, with an assumed 3-km plume depth and were not nudged to 1991 meteorology, which has been shown to influence the initial plume dispersal (e.g. Jones et al., 2016). However, since the two estimates are very similar, and the estimated global sulfate e-folding decay time also agrees well with observations, the emulators do a very good job at capturing the

effects of the 1991 Mt. Pinatubo eruption, reflecting the validity of the emulators and the idealized UM-UKCA simulations.

Constraint of the eruption source parameters using the emulators is not limited to historic eruptions. They can be used to constrain the eruption source parameter combinations for any given value or range of values of the model outputs across the full three-dimensional parameter space (Section 3.3.3.2).

3.3.3.2 Parameter combinations that result in integrated sAOD > 10

We further demonstrate the value of the emulators by identifying parts of the eruption source parameter space that result in an integrated global mean sAOD greater than 10 months. An integrated value of 10 is roughly 3 times greater than that from the 1991 eruption of Mt. Pinatubo. We take a uniformly gridded sample of 1 million combinations covering the full three-dimensional parameter space (using 100 equally spaced values across each of the parameter ranges in Table 3.1) and evaluate the sAOD output at each combination using the emulator. We then retain only the parameter combinations that match our criterion of sAOD > 10. These resulting parameter combinations are plotted in Figure 3.10. The top row displays histograms of each individual constrained parameter and the bottom row shows the two-dimensional projections of the parameter space that remains on constraint. The colour indicates the density of parameter combinations in that part of remaining parameter space. A three-dimensional view can be obtained using the online tool.

Only eruptions in which more than ~56 Tg of SO_2 is emitted have the potential to produce an integrated global mean sAOD of at least 10 (Figure 3.10 a, d & f) as sufficient sulfate aerosol must be formed. This is approximately the magnitude of the mass of SO_2 emitted during the 1815 eruption of Mt. Tambora (Zanchettin et al., 2016). However, the injection height is not constrained and the column-bottom can be at any height between 15 km and 25 km (Figure 3.10 c, d & e). The volcano must be situated between ~80°S and ~67°N (Figure 3.10 b, e & f), with higher-latitude NH eruptions leading to too-rapid decay of the sulfate aerosol burden to sustain an sAOD > 10. The constrained space in Figure 3.10 enables the joint three-dimensional parameter space to be explored. For example, for emission magnitudes in the lower part of the range, the injection height must be nearer the middle of the range and the eruption must be near the equator. The eruption can only result in an integrated global mean sAOD > 10 with an injection height column-bottom of 24 km if the SO_2

emission is greater than ~75 Tg. In general, as the SO_2 emissions increase and as the eruption moves towards lower latitudes an integrated sAOD > 10 becomes more likely (i.e., there are more values of injection height that can be combined with these other two parameters to produce sAOD > 10). At the extremes of the injection height integrated sAOD > 10 is less likely. Figure 3.10 also reveals some interesting shapes in the surfaces. For example, Figure 3.10e is asymmetrical around the equator and the eruption can occur at higher southern latitudes with high injection heights, than in the NH. This is likely a seasonal response, given that our eruptions occur in July, but may also reflect differences in circulation strength and patterns between the two hemispheres, such as the polar winter vortex.

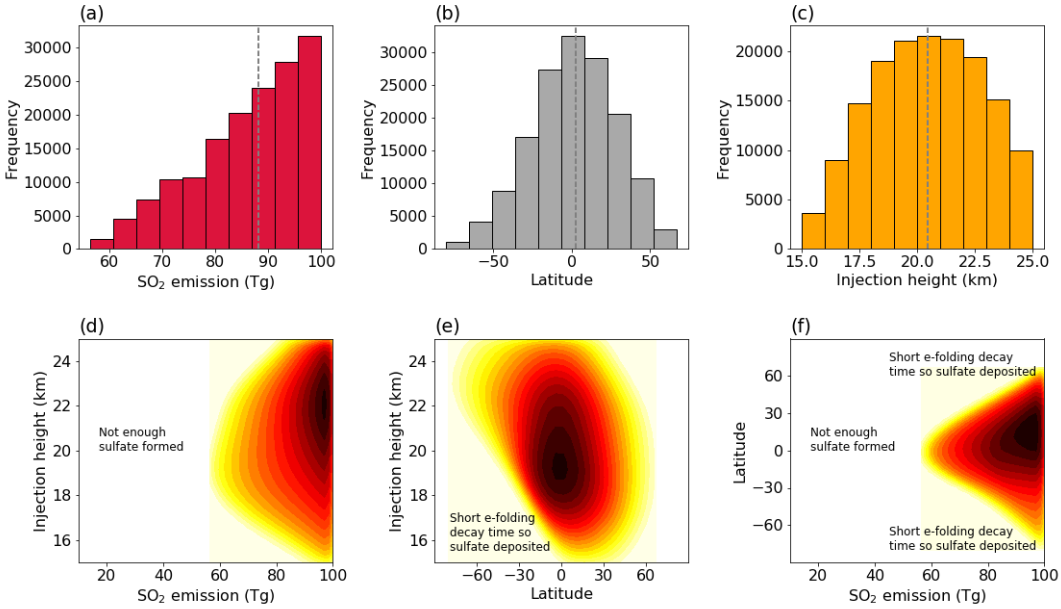

Figure 3.10: Parts of parameter space that result in an integrated global mean sAOD greater than 10 months. Panels (a) to (c) are histograms of the individual constrained parameter values using 10 bins and the dashed grey lines mark the median values. Panels (d) to (f) show the combinations of two parameters that remain after constraint and the colour indicates the density of parameter combinations (lighter = fewer points, darker = more points). Panels (d) to (f) are annotated in regions of the parameter space where the integrated global mean sAOD is not greater than 10 months with explanations of why the sAOD values are lower.

3.4 Summary and conclusions

We have investigated the influence of the mass of SO_2 emitted (between 10 Tg and 100 Tg), eruption latitude (between 80°S to 80°N) and injection height of the emissions (between 15 km and 25 km with an injection depth of 3-km) on the radiative forcing of a large-magnitude explosive eruption, using a state-of-the-art global climate model with interactive aerosol microphysics. We have focussed on three model outputs to understand the radiative impact: the global sulfate e-folding decay time, the time-integrated global mean sAOD and the time-integrated global mean net radiative forcing. In contrast to conventional climate model experimental designs in which parameters are perturbed in isolation, we simulated 41 eruptions each with different combinations of the three eruption source parameter values. Using Gaussian process emulators, we then predicted model output for parameter combinations that we did not explicitly simulate. We calculated the average response of each model output to each parameter and quantified the relative importance of each parameter.

Our results reveal that the e-folding decay time of the global sulfate aerosol burden depends primarily on the latitude of the eruption but the magnitude of the integrated global mean sAOD and net radiative forcing is most dependent on the mass of SO_2 emitted. In general, for successively larger SO_2 emissions and for eruptions closer to the equator, the magnitude of the net radiative forcing increases due to an increase in sulfate burden and a longer e-folding decay time of sulfate aerosol in the tropics. As the injection height of the SO_2 emissions increases from 15 km to ~20 km, the net radiative forcing increases, but above ~20 km the net radiative forcing decreases due to changes in aerosol decay rates and the scattering efficiency as particles grow and altitude-dependent transport to the extratropics. Compared to the mass of SO_2 emitted and eruption latitude, the injection height is in relative terms the least important parameter, contributing to less than 5% of the variance in each model output. Any change to the net radiative forcing by changing the injection height is dwarfed by any changes to the SO_2 emission magnitude and eruption latitude. Efforts to diagnose the global and time-integrated climatic impact of eruptions should therefore focus on determining the initial mass of SO_2 released rather than the injection altitude.

We have demonstrated that statistical emulation is a suitable and powerful tool for investigating the volcanic radiative forcing of past and future eruptions. Firstly, despite only running 41 model simulations, the emulated response surfaces allow us

to predict in a matter of seconds the global sulfate e-folding decay time, the time-integrated global mean sAOD and the time-integrated net radiative forcing of any eruption in the latitude range 80°S to 80°N, SO_2 emission between 10 Tg and 100 Tg and emission injection height between 15 km and 25 km (e.g. Figures 3.5-3.8). An online tool has been provided in which two-dimensional and three-dimensional emulated response surfaces for all combinations of eruption source parameters can be explored and constrained.

Secondly, the emulated surfaces expose relationships between the parameters and the model output across the whole parameter space, which in a conventional experimental design would have been difficult to see. For example, we find that the dependency of the net radiative forcing on injection height is more important for tropical eruptions, than for eruptions in the high latitudes (e.g. Figure 3.7). The emulated surfaces have revealed many compensating effects between stratospheric circulation, sedimentation and the scattering efficiency of particles in determining the net radiative forcing, which were not obvious from analysing the model output alone (Figure 3.3).

Thirdly, the emulators allow us to quantify the relationships between each parameter and the model output such that we can determine the relative importance of each and calculate the average effect of each parameter on the model output across the whole parameter space (Figure 3.8).

Finally, we have also shown that the emulators can be used to constrain the eruption source parameters for a given volcanic response (Figure 3.10), revealing multiple solutions.

The emulators are not limited to the three-dimensional space presented here nor to the three model outputs that we chose. For example, we have built 27-dimensional emulators to understand aerosol effective radiative forcing (Regayre et al., 2018), 11-dimensional emulators to understand deep-convective cloud behaviour (Johnson et al., 2015), and attempted to observationally constrain 28-dimensional emulators of tropospheric aerosol processes (Lee et al., 2016). In relation to volcano-climate studies, future work could explore the contributions of other eruption source parameters such as plume depth, eruption duration, season of eruption and QBO phase. These additional parameters could influence the importance of the three parameters presented here. However, the emulated surfaces still provide a first-order estimate of the effects of each of these parameters, which are still likely to be the most

important. Our simulations also started with the same meteorological conditions, and variations in meteorology could alter the initial plume evolution (e.g. Jones et al., 2016). However, since the stratospheric dynamics can be modified by aerosol radiative heating and the fact that we have analysed global and time-integrated output, the effect of initial conditions is likely second-order to that of the eruption source parameters. In simulations of the 1815 Mt. Tambora eruption we also found little variation amongst ensemble members with different initial conditions (Marshall et al., 2018). Other model outputs such as peak responses or regional impacts, which are likely to have larger extremes, could also be explored using this novel methodology.

Our results have highlighted the importance of aerosol microphysical processes such as sedimentation in determining the magnitude of the volcanic forcing, but model parameterizations of aerosol microphysical processes in volcanic clouds such as nucleation and sedimentation are also important causes of model uncertainties (e.g. English et al., 2013). Changes to particle coagulation schemes, for example with the inclusion of Van der Waals forces, have been shown to change aerosol distributions (e.g. English et al., 2013; Sukhodolov et al., 2018). Future ensembles in which the model process parameters are perturbed would allow quantification of the sensitivity of volcanic forcing to the model's aerosol microphysics (e.g. Lee et al., 2013; Johnson et al., 2015; Regayre et al., 2018).

Appendix: Derivation of the average global sulfate e-folding decay time

To determine the average global sulfate e-folding decay time we plot the natural logarithm of the monthly mean global sulfate burden anomalies from the peak burden and fit a linear regression line from one month after the peak burden to until the burden has fallen below 10% of the peak burden (Figure 3.11). Fitting from one month after the peak ensures that the sulfate burden is decaying, however the timing of the main phase of decay does differ between eruptions.

We calculate the average e-folding decay time by taking the fitted sulfate burden from the first and last values of the regression line:

$$efolding\ time = (t2 - t1)/\log(\frac{b1}{b2})$$

where b1 is the burden calculated from the first value of the regression line and b2 is the burden calculated from the last value of the line ($b = e^{burden}$). t2–t1 equals the time in months between the two burdens.

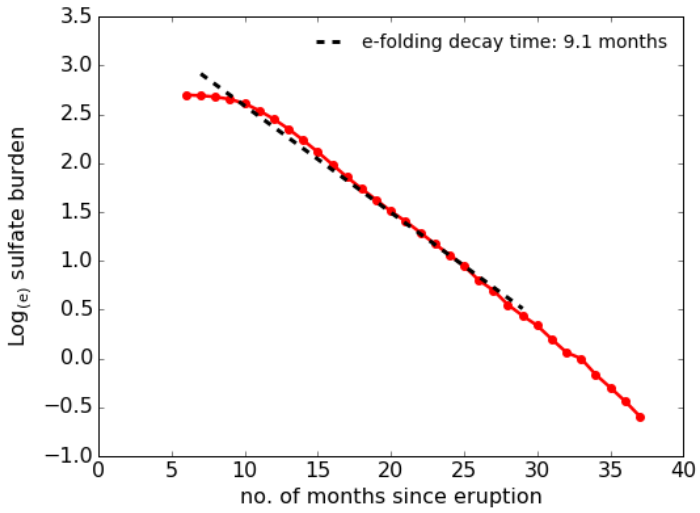

Figure 3.11: Global volcanic sulfate burden ($\log_{(e)}$ Tg S) for one example model simulation (red line and scatter points) from the maximum monthly mean burden and linear regression line (dashed line) fitted from one month after the peak burden up until the burden falls below 10% of the peak burden. The average e-folding decay time is calculated using the fitted regression line.

References

Aquila, V., Garfinkel, C.I., Newman, P.A., Oman, L.D. and Waugh, D.W. 2014. Modifications of the quasi-biennial oscillation by a geoengineering perturbation of the stratospheric aerosol layer. *Geophysical Research Letters.* **41**(5), pp.1738-1744.

Aquila, V., Oman, L.D., Stolarski, R.S., Colarco, P.R. and Newman, P.A. 2012. Dispersion of the volcanic sulfate cloud from a Mount Pinatubo-like eruption. *Journal of Geophysical Research-Atmospheres.* **117**, D06216.

Arfeuille, F., Weisenstein, D., Mack, H., Rozanov, E., Peter, T. and Bronnimann, S. 2014. Volcanic forcing for climate modeling: a new microphysics-based data set covering years 1600-present. *Climate of the Past.* **10**(1), pp.359-375.

Bekki, S. 1995. Oxidation of volcanic SO2: A sink for stratospheric OH and H2O. *Geophysical Research Letters.* **22**(8), pp.913-916.

Bellouin, N., Mann, G.W., Woodhouse, M.T., Johnson, C., Carslaw, K.S. and Dalvi, M. 2013. Impact of the modal aerosol scheme GLOMAP-mode on aerosol forcing in the Hadley Centre Global Environmental Model. *Atmospheric Chemistry and Physics.* **13**(6), pp.3027-3044.

Brooke, J.S.A., Feng, W.H., Carrillo-Sanchez, J.D., Mann, G.W., James, A.D., Bardeen, C.G. and Plane, J.M.C. 2017. Meteoric Smoke Deposition in the Polar Regions: A Comparison of Measurements With Global Atmospheric Models. *Journal of Geophysical Research-Atmospheres.* **122**(20), pp.11112-11130.

Butchart, N. 2014. The Brewer-Dobson circulation. *Reviews of Geophysics.* **52**(2), pp.157-184.

Carslaw, K.S., Lee, L.A., Reddington, C.L., Pringle, K.J., Rap, A., Forster, P.M., Mann, G.W., Spracklen, D.V., Woodhouse, M.T., Regayre, L.A. and Pierce, J.R. 2013. Large contribution of natural aerosols to uncertainty in indirect forcing. *Nature.* **503**(7474), pp.67-71.

Dhomse, S.S., Emmerson, K.M., Mann, G.W., Bellouin, N., Carslaw, K.S., Chipperfield, M.P., Hommel, R., Abraham, N.L., Telford, P., Braesicke, P., Dalvi, M., Johnson, C.E., O'Connor, F., Morgenstern, O., Pyle, J.A., Deshler, T., Zawodny, J.M. and Thomason, L.W. 2014. Aerosol microphysics simulations of the Mt. Pinatubo eruption with the UM-UKCA composition-climate model. *Atmospheric Chemistry and Physics.* **14**(20), pp.11221-11246.

English, J.M., Toon, O.B. and Mills, M.J. 2013. Microphysical simulations of large volcanic eruptions: Pinatubo and Toba. *Journal of Geophysical Research-Atmospheres.* **118**(4), pp.1880-1895.

Global Volcanism Program 2013. Volcanoes of the World, v. 4.2.2. Venzke, E ed. Smithsonian Institution.

Hamill, P., Jensen, E.J., Russell, P.B. and Bauman, J.J. 1997. The life cycle of stratospheric aerosol particles. *Bulletin of the American Meteorological Society.* **78**(7), pp.1395-1410.

Hamilton, D.S., Lee, L.A., Pringle, K.J., Reddington, C.L., Spracklen, D.V. and Carslaw, K.S. 2014. Occurrence of pristine aerosol environments on a polluted planet. *Proceedings of the National Academy of Sciences of the United States of America.* **111**(52), pp.18466-18471.

Harvey, N.J., Huntley, N., Dacre, H.F., Goldstein, M., Thomson, D. and Webster, H. 2018. Multi-level emulation of a volcanic ash transport and dispersion model to quantify sensitivity to uncertain parameters. *Natural Hazards and Earth System Sciences.* **18**(1), pp.41-63.

Holton, J.R., Haynes, P.H., McIntyre, M.E., Douglass, A.R., Rood, R.B. and Pfister, L. 1995. Stratosphere-Troposphere Exchange. *Reviews of Geophysics.* **33**(4), pp.403-439.

Johnson, J.S., Cui, Z., Lee, L.A., Gosling, J.P., Blyth, A.M. and Carslaw, K.S. 2015. Evaluating uncertainty in convective cloud microphysics using statistical emulation. *Journal of Advances in Modeling Earth Systems.* **7**(1), pp.162-187.

Jones, A.C., Haywood, J.M., Dunstone, N., Emanuel, K., Hawcroft, M.K., Hodges, K.I. and Jones, A. 2017. Impacts of hemispheric solar geoengineering on tropical cyclone frequency. *Nature Communications.* **8**(1), 1382.

Jones, A.C., Haywood, J.M., Jones, A. and Aquila, V. 2016. Sensitivity of volcanic aerosol dispersion to meteorological conditions: A Pinatubo case study. *Journal of Geophysical Research-Atmospheres.* **121**(12), pp.6892-6908.

Kennedy, M.C. and O'Hagan, A. 2001. Bayesian calibration of computer models. *Journal of the Royal Statistical Society: Series B (Statistical Methodology).* **63**(3), pp.425-464.

Kleinschmitt, C., Boucher, O. and Platt, U. 2018. Sensitivity of the radiative forcing by stratospheric sulfur geoengineering to the amount and strategy of the SO2 injection studied with the LMDZ-S3A model. *Atmospheric Chemistry and Physics.* **18**(4), pp.2769-2786.

Kravitz, B. and Robock, A. 2011. Climate effects of high-latitude volcanic eruptions: Role of the time of year. *Journal of Geophysical Research-Atmospheres.* **116**, D01105.

Lee, L.A., Carslaw, K.S., Pringle, K.J., Mann, G.W. and Spracklen, D.V. 2011. Emulation of a complex global aerosol model to quantify sensitivity to uncertain parameters. *Atmospheric Chemistry and Physics.* **11**(23), pp.12253-12273.

Lee, L.A., Pringle, K.J., Reddington, C.L., Mann, G.W., Stier, P., Spracklen, D.V., Pierce, J.R. and Carslaw, K.S. 2013. The magnitude and causes of uncertainty in global model simulations of cloud condensation nuclei. *Atmospheric Chemistry and Physics.* **13**(17), pp.8879-8914.

Lee, L.A., Reddington, C.L. and Carslaw, K.S. 2016. On the relationship between aerosol model uncertainty and radiative forcing uncertainty. *Proceedings of the National Academy of Sciences of the United States of America.* **113**(21), pp.5820-5827.

Loeppky, J.L., Sacks, J. and Welch, W.J. 2009. Choosing the Sample Size of a Computer Experiment: A Practical Guide. *Technometrics.* **51**(4), pp.366-376.

Mann, G.W., Carslaw, K.S., Spracklen, D.V., Ridley, D.A., Manktelow, P.T., Chipperfield, M.P., Pickering, S.J. and Johnson, C.E. 2010. Description and evaluation of GLOMAP-mode: a modal global aerosol microphysics model for the UKCA composition-climate model. *Geoscientific Model Development.* **3**(2), pp.519-551.

Mann, G.W., Dhomse, S., Deshler, T., Timmreck, C., Schmidt, A., Neely, R. and Thomason, L. 2015. Evolving particle size is the key to improved volcanic forcings. *Past Global Changes Magazine.* **23**(2), pp.52-53.

Marshall, L., Schmidt, A., Toohey, M., Carslaw, K.S., Mann, G.W., Sigl, M., Khodri, M., Timmreck, C., Zanchettin, D., Ball, W.T., Bekki, S., Brooke, J.S.A., Dhomse, S., Johnson, C., Lamarque, J.F., LeGrande, A.N., Mills, M.J., Niemeier, U., Pope, J.O., Poulain, V., Robock, A., Rozanov, E., Stenke, A., Sukhodolov, T., Tilmes, S., Tsigaridis, K. and Tummon, F. 2018. Multi-model comparison of the volcanic sulfate deposition from the 1815 eruption of Mt. Tambora. *Atmospheric Chemistry and Physics.* **18**(3), pp.2307-2328.

Metzner, D., Kutterolf, S., Toohey, M., Timmreck, C., Niemeier, U., Freundt, A. and Kruger, K. 2014. Radiative forcing and climate impact resulting from SO2 injections based on a 200,000-year record of Plinian eruptions along the Central American Volcanic Arc. *International Journal of Earth Sciences.* **103**(7), pp.2063-2079.

Morgenstern, O., Braesicke, P., O'Connor, F.M., Bushell, A.C., Johnson, C.E., Osprey, S.M. and Pyle, J.A. 2009. Evaluation of the new UKCA climate-composition model - Part 1: The stratosphere. *Geoscientific Model Development.* **2**(1), pp.43-57.

Morris, M.D. and Mitchell, T.J. 1995. Exploratory designs for computational experiments. *Journal of Statistical Planning and Inference.* **43**(3), pp.381-402.

Niemeier, U. and Schmidt, H. 2017. Changing transport processes in the stratosphere by radiative heating of sulfate aerosols. *Atmospheric Chemistry and Physics.* **17**(24), pp.14871-14886.

Niemeier, U., Schmidt, H. and Timmreck, C. 2011. The dependency of geoengineered sulfate aerosol on the emission strategy. *Atmospheric Science Letters.* **12**(2), pp.189-194.

Niemeier, U. and Timmreck, C. 2015. What is the limit of climate engineering by stratospheric injection of SO2? *Atmospheric Chemistry and Physics.* **15**(16), pp.9129-9141.

Niemeier, U., Timmreck, C., Graf, H.F., Kinne, S., Rast, S. and Self, S. 2009. Initial fate of fine ash and sulfur from large volcanic eruptions. *Atmospheric Chemistry and Physics.* **9**(22), pp.9043-9057.

O'Connor, F.M., Johnson, C.E., Morgenstern, O., Abraham, N.L., Braesicke, P., Dalvi, M., Folberth, G.A., Sanderson, M.G., Telford, P.J., Voulgarakis, A., Young, P.J., Zeng, G., Collins, W.J. and Pyle, J.A. 2014. Evaluation of the new UKCA climate-composition model - Part 2: The Troposphere. *Geoscientific Model Development.* **7**(1), pp.41-91.

O'Hagan, A. 2006. Bayesian analysis of computer code outputs: A tutorial. *Reliability Engineering & System Safety.* **91**(10-11), pp.1290-1300.

Oman, L., Robock, A., Stenchikov, G., Schmidt, G.A. and Ruedy, R. 2005. Climatic response to high-latitude volcanic eruptions. *Journal of Geophysical Research-Atmospheres.* **110**, D13103.

Oman, L., Robock, A., Stenchikov, G.L., Thordarson, T., Koch, D., Shindell, D.T. and Gao, C.C. 2006. Modeling the distribution of the volcanic aerosol cloud from the 1783-1784 Laki eruption. *Journal of Geophysical Research-Atmospheres.* **111**(D12), D12209.

Osprey, S.M., Gray, L.J., Hardiman, S.C., Butchart, N. and Hinton, T.J. 2013. Stratospheric Variability in Twentieth-Century CMIP5 Simulations of the Met Office Climate Model: High Top versus Low Top. *Journal of Climate.* **26**(5), pp.1595-1606.

Pinto, J.P., Turco, R.P. and Toon, O.B. 1989. Self-limiting physical and chemical effects in volcanic eruption clouds. *Journal of Geophysical Research-Atmospheres.* **94**(D8), pp.11165-11174.

Pitari, G., Di Genova, G., Mancini, E., Visioni, D., Gandolfi, I. and Cionni, I. 2016. Stratospheric Aerosols from Major Volcanic Eruptions: A Composition-Climate Model Study of the Aerosol Cloud Dispersal and e-folding Time. *Atmosphere.* **7**(6), 75.

Plumb, R.A. 1996. A "tropical pipe" model of stratospheric transport. *Journal of Geophysical Research-Atmospheres.* **101**(D2), pp.3957-3972.

Pujol. G., Iooss, B., and Janon, A., 2017. *sensitivity: Global Sensitivity Analysis of Model Outputs. R package* (1.14.0). [Software] Available at https://CRAN.R-project.org/package=sensitivity

Punge, H.J., Konopka, P., Giorgetta, M.A. and Muller, R. 2009. Effects of the quasi-biennial oscillation on low-latitude transport in the stratosphere derived from trajectory calculations. *Journal of Geophysical Research-Atmospheres.* **114**, D03102.

R Core Team. 2017. *R: A language and environment for statistical computing. R Foundation for Statistical Computing.* Vienna, Austria. Available at https://www.R-project.org/.

Rasmussen, C. E., and Williams, C. K. I. 2006. *Gaussian Processes for Machine Learning*. London, U. K.: MIT Press.

Regayre, L.A., Johnson, J.S., Yoshioka, M., Pringle, K.J., Sexton, D.M.H., Booth, B.B.B., Lee, L.A., Bellouin, N. and Carslaw, K.S. 2018. Aerosol and physical atmosphere model parameters are both important sources of uncertainty in aerosol ERF. *Atmospheric Chemistry and Physics.* **18**(13), pp.9975-10006.

Regayre, L.A., Pringle, K.J., Booth, B.B.B., Lee, L.A., Mann, G.W., Browse, J., Woodhouse, M.T., Rap, A., Reddington, C.L. and Carslaw, K.S. 2014. Uncertainty in the magnitude of aerosol-cloud radiative forcing over recent decades. *Geophysical Research Letters.* **41**(24), pp.9040-9049.

Regayre, L.A., Pringle, K.J., Lee, L.A., Rap, A., Browse, J., Mann, G.W., Reddington, C.L., Carslaw, K.S., Booth, B.B.B. and Woodhouse, M.T. 2015. The Climatic Importance of Uncertainties in Regional Aerosol-Cloud Radiative Forcings over Recent Decades. *Journal of Climate.* **28**(17), pp.6589-6607.

Reynolds, R.W., Smith, T.M., Liu, C., Chelton, D.B., Casey, K.S. and Schlax, M.G. 2007. Daily high-resolution-blended analyses for sea surface temperature. *Journal of Climate.* **20**(22), pp.5473-5496.

Robock, A. 2000. Volcanic eruptions and climate. *Reviews of Geophysics.* **38**(2), pp.191-219.

Rodrigues, L.F.S., Vernon, I. and Bower, R.G. 2017. Constraints on galaxy formation models from the galaxy stellar mass function and its evolution. *Monthly Notices of the Royal Astronomical Society.* **466**(2), pp.2418-2435.

Roustant, O., Ginsbourger, D. and Deville, Y. 2012. DiceKriging, DiceOptim: Two R Packages for the Analysis of Computer Experiments by Kriging-Based Metamodeling and Optimization. *Journal of Statistical Software.* **51**(1), pp.1-55.

Sacks, J., Welch, W.J., Mitchell, T.J. and Wynn, H.P. 1989. Design and Analysis of Computer Experiments. *Statistical Science.* **4**(4), pp.409-435.

Saltelli, A., K., C. and Scott, E.M. 2000. *Sensitivity Analysis.* N. Y.: John Wiley.

Saltelli, A., Tarantola, S. and Chan, K.P.S. 1999. A quantitative model-independent method for global sensitivity analysis of model output. *Technometrics.* **41**(1), pp.39-56.

Sarri, A., Guillas, S. and Dias, F. 2012. Statistical emulation of a tsunami model for sensitivity analysis and uncertainty quantification. *Natural Hazards and Earth System Sciences.* **12**(6), pp.2003-2018.

SPARC. 2006. SPARC Assessment of Stratospheric Aerosol Properties (ASAP). Thomason, L., and Peter. T., eds., SPARC Report No. 4, WCRP-124, WMO/TD – No. 1295. Available at www.sparc-climate.org/publications/sparc-reports/.

Sukhodolov, T., Sheng, J.X., Feinberg, A., Luo, B.P., Peter, T., Revell, L., Stenke, A., Weisenstein, D.K. and Rozanov, E. 2018. Stratospheric aerosol evolution after

Pinatubo simulated with a coupled size-resolved aerosol–chemistry–climate model, SOCOL-AERv1.0. *Geoscientific Model Development.* **11**(7), pp.2633-2647.

Thomas, M.A., Giorgetta, M.A., Timmreck, C., Graf, H.F. and Stenchikov, G. 2009. Simulation of the climate impact of Mt. Pinatubo eruption using ECHAM5-Part 2: Sensitivity to the phase of the QBO and ENSO. *Atmospheric Chemistry and Physics.* **9**(9), pp.3001-3009.

Thomason, L.W., Burton, S.P., Luo, B.P. and Peter, T. 2008. SAGE II measurements of stratospheric aerosol properties at non-volcanic levels. *Atmospheric Chemistry and Physics.* **8**(4), pp.983-995.

Thomason, L.W., Ernest, N., Millan, L., Rieger, L., Bourassa, A., Vernier, J.P., Manney, G., Luo, B.P., Arfeuille, F. and Peter, T. 2018. A global space-based stratospheric aerosol climatology: 1979-2016. *Earth System Science Data*. **10**(1), pp.469-492.

Tilmes, S., Richter, J.H., Mills, M.J., Kravitz, B., MacMartin, D.G., Vitt, F., Tribbia, J.J. and Lamarque, J.F. 2017. Sensitivity of Aerosol Distribution and Climate Response to Stratospheric SO2 Injection Locations. *Journal of Geophysical Research-Atmospheres.* **122**(23), pp.12591-12615.

Timmreck, C. 2012. Modeling the climatic effects of large explosive volcanic eruptions. *Wiley Interdisciplinary Reviews-Climate Change.* **3**(6), pp.545-564.

Timmreck, C., Graf, H.F., Lorenz, S.J., Niemeier, U., Zanchettin, D., Matei, D., Jungclaus, J.H. and Crowley, T.J. 2010. Aerosol size confines climate response to volcanic super-eruptions. *Geophysical Research Letters.* **37**, L24705.

Timmreck, C., Lorenz, S.J., Crowley, T.J., Kinne, S., Raddatz, T.J., Thomas, M.A. and Jungclaus, J.H. 2009. Limited temperature response to the very large AD 1258 volcanic eruption. *Geophysical Research Letters.* **36**, L21708.

Timmreck, C., Mann, G.W., Aquila, V., Hommel, R., Lee, L.A., Schmidt, A., Brühl, C., Carn, S., Chin, M., Dhomse, S.S., Diehl, T., English, J.M., Mills, M.J., Neely, R., Sheng, J., Toohey, M. and Weisenstein, D. 2018. The Interactive Stratospheric Aerosol Model Intercomparison Project (ISA-MIP): motivation and experimental design. *Geoscientific Model Development.* **11**(7), pp.2581-2608.

Toohey, M., Kruger, K., Niemeier, U. and Timmreck, C. 2011. The influence of eruption season on the global aerosol evolution and radiative impact of tropical volcanic eruptions. *Atmospheric Chemistry and Physics.* **11**(23), pp.12351-12367.

Toohey, M., Kruger, K. and Timmreck, C. 2013. Volcanic sulfate deposition to Greenland and Antarctica: A modeling sensitivity study. *Journal of Geophysical Research-Atmospheres.* **118**(10), pp.4788-4800.

Trepte, C.R. and Hitchman, M.H. 1992. Tropical stratospheric circulation deduced from satellite aerosol data. *Nature.* **355**(6361), pp.626-628.

Trepte, C.R., Veiga, R.E. and McCormick, M.P. 1993. The poleward dispersal of Mount Pinatubo volcanic aerosol. *Journal of Geophysical Research-Atmospheres.* **98**(D10), pp.18563-18573.

Vehkämaki, H., Kulmala, M., Napari, I., Lehtinen, K.E.J., Timmreck, C., Noppel, M. and Laaksonen, A. 2002. An improved parameterization for sulfuric acid-water nucleation rates for tropospheric and stratospheric conditions. *Journal of Geophysical Research-Atmospheres.* **107**(D22), 4622.

Vernon, I., Goldstein, M. and Bower, R.G. 2010. Galaxy Formation: a Bayesian Uncertainty Analysis. *Bayesian Analysis.* **5**(4), pp.619-669.

Walters, D.N., Williams, K.D., Boutle, I.A., Bushell, A.C., Edwards, J.M., Field, P.R., Lock, A.P., Morcrette, C.J., Stratton, R.A., Wilkinson, J.M., Willett, M.R., Bellouin, N., Bodas-Salcedo, A., Brooks, M.E., Copsey, D., Earnshaw, P.D., Hardiman, S.C., Harris, C.M., Levine, R.C., MacLachlan, C., Manners, J.C., Martin, G.M., Milton, S.F., Palmer, M.D., Roberts, M.J., Rodriguez, J.M., Tennant, W.J. and Vidale, P.L. 2014. The Met Office Unified Model Global Atmosphere 4.0 and JULES Global Land 4.0 configurations. *Geoscientific Model Development.* **7**(1), pp.361-386.

Young, R.E., Houben, H. and Toon, O.B. 1994. Radiatively forced dispersion of the Mt. Pinatubo volcanic cloud and induced temperature perturbations in the stratosphere during the first few months following the eruption. *Geophysical Research Letters.* **21**(5), pp.369-372.

Zanchettin, D., Khodri, M., Timmreck, C., Toohey, M., Schmidt, A., Gerber, E.P., Hegerl, G., Robock, A., Pausata, F.S.R., Ball, W.T., Bauer, S.E., Bekki, S., Dhomse, S.S., LeGrande, A.N., Mann, G.W., Marshall, L., Mills, M., Marchand, M., Niemeier, U., Poulain, V., Rozanov, E., Rubino, A., Stenke, A., Tsigaridis, K. and Tummon, F. 2016. The Model Intercomparison Project on the climatic response to Volcanic forcing (VolMIP): experimental design and forcing input data for CMIP6. *Geoscientific Model Development.* **9**(8), pp.2701-2719.

Chapter 4 Large uncertainty in volcanic radiative forcing derived from ice cores

Lauren Marshall[1], Anja Schmidt[2,3], Jill S. Johnson[1], Graham W. Mann[1,4], Lindsay Lee[1] and Ken S. Carslaw[1]

[1]*School of Earth and Environment, University of Leeds, Leeds, LS2 9JT, UK*

[2]*Department of Chemistry, University of Cambridge, Lensfield Rd, Cambridge CB2 1EW, UK*

[3]*Department of Geography, University of Cambridge, Downing Place, Cambridge CB2 3EN, UK*

[4]*National Centre for Atmospheric Science, University of Leeds, Leeds, LS2 9JT, UK*

This chapter is an adaptation of the following publication to be submitted to *Journal of Geophysical Research: Atmospheres*, where the reference style and figure, table and section numbers have been updated for continuity throughout the thesis:

Marshall, L., Schmidt, A., Johnson, J. S., Mann, G. W., Lee, L., and Carslaw, K., 2018. Large uncertainty in volcanic radiative forcing derived from ice cores.

The supplement to this paper is included in Appendix D.

Key Points:

- An aerosol microphysics model and statistical emulation are used to constrain eruption source parameters from ice sheet sulfate deposition
- Constrained combinations of eruption source parameters have a range in SO_2 emissions, latitude and radiative forcing dependent on season
- Volcanic aerosol radiative forcing ranges by more than ~300 MJ m^{-2} for eruptions consistent with the top 10 bipolar deposition signals

Abstract

Reconstructions of historic volcanic aerosol radiative forcing for pre-20th century eruptions are commonly based on sulfate aerosol burdens and stratospheric aerosol optical depth estimated from ice core sulfate records. The reconstructions rely on transfer functions that link volcanic sulfate deposited on ice sheets to the stratospheric sulfate burden, and hence radiative forcing, and are in part calculated from these quantities as observed after the 1991 eruption of Mt. Pinatubo. However, it is uncertain whether these functions hold for other large-magnitude eruptions. We use an ensemble of simulations of an interactive stratospheric aerosol microphysics model and statistical emulation to predict the ice sheet sulfate deposition and radiative forcing for thousands of possible eruptions with a range of sulfur dioxide emissions, injection heights, latitudes and seasons. We find that a wide range of eruption-realisations can produce ice sheet deposition consistent with measured values after historic eruptions, demonstrating that previously derived transfer functions are eruption-specific. For the top 10 bipolar deposition signals recorded in ice cores over the last 2500 years, the range in ~3-year integrated radiative forcing across each set of constrained eruption-realisations is greater than ~300 MJ m^{-2}, exceeding the magnitude of the time-integrated forcing following the 1991 Mt. Pinatubo eruption by about a factor of 2-3. As such, this uncertainty in historic volcanic aerosol radiative forcing could cause an uncertainty in global mean surface temperature response exceeding the 0.5°C following Pinatubo, which is not accounted for in historic climate model simulations.

4.1 Introduction

Explosive volcanic eruptions that inject large amounts of sulfur dioxide (SO_2) into the stratosphere are significant drivers of natural climate variability on multi-annual to decadal timescales (e.g. Myhre et al., 2013). Reconstructions of historic volcanic radiative forcing are therefore required to understand and attribute historic climate variability on millennial timescales (e.g. Hegerl et al., 2007; Crowley et al., 2008; Sigl et al., 2015) and are used as input to climate models for historical simulations (e.g. Schmidt et al., 2011; Jungclaus et al., 2017).

Despite their importance, reconstructions of volcanic radiative forcing are uncertain due to the lack of in-situ and remote sensing measurements for eruptions before 1963 Mt. Agung. When available, SO_2 emissions and stratospheric aerosol optical depth (sAOD) are derived from satellite retrievals (since ~1979) (e.g. Carn et al., 2016) and ground-based optical measurements (e.g. Sato et al., 1993; Stothers, 1996; 2001). Forcing datasets are otherwise constructed based on volcanic sulfate anomalies measured in ice cores, which are used to estimate the mass of sulfur injected into the stratosphere (Gao et al., 2008; Toohey and Sigl, 2017) or the sAOD (Crowley and Unterman, 2013). Alternatively, the injected mass of sulfur can be estimated from petrological and geochemical studies of eruption deposits (e.g. Devine et al., 1984; Scaillet, 2003; Self et al., 2004; Metzner et al., 2014; Vidal et al., 2016).

Sulfate measured in ice cores provides a record of volcanism with high temporal resolution over hundreds to thousands of years (e.g. Sigl et al., 2014; 2015). However, several assumptions must be made to translate measured volcanic sulfate in ice cores into stratospheric sulfate aerosol burdens, mid-visible sAOD and radiative forcing. Established methods include using transfer functions to estimate hemispheric stratospheric sulfate burdens (Gao et al., 2008; Sigl et al., 2015; Toohey and Sigl, 2017) or sAOD (Crowley and Unterman, 2013) from ice core composites. Transfer functions are derived from the measured ice core sulfate and observed stratospheric sulfate burden or sAOD following the 1991 eruption of Mt. Pinatubo, from estimates of radioactive material in the stratosphere and measured in ice cores following nuclear weapons testing in the 1950s and 1960s (e.g. Clausen and Hammer, 1988) and from climate model simulations (Gao et al., 2007).

There are several factors that may affect the relationship between ice sheet sulfate deposition and stratospheric sulfate burdens and sAOD. Consequently, it is unknown whether these transfer functions are applicable to eruptions other than 1991 Mt. Pinatubo. Polar sulfate deposition is modulated by the season (Gao et al., 2008; Toohey et al., 2013; Toohey et al., 2016a) and atmospheric variability (Robock and Free, 1995; Toohey et al., 2013). Toohey et al. (2013) found that transfer functions for tropical eruptions varied with both eruption season and the magnitude of injection because of differences in transport and dynamical responses, such as a stronger polar vortex that inhibited aerosol transport to the poles. Stratospheric SO_2 injections larger than Mt. Pinatubo may also lead to larger sulfate aerosol particles which have a lower

radiative forcing efficiency per unit mass (e.g. Pinto et al., 1989; Timmreck et al., 2010).

Further uncertainties also exist in converting estimated sulfate aerosol burdens into sAOD and radiative forcing. For the reconstruction of Gao et al. (2008), a linear scaling is applied between the sulfate aerosol mass and sAOD (Stothers, 1984). Other reconstructions scale ice sheet sulfate deposition to sAOD based on this relationship after 1991 Pinatubo but attempt to account for changes to particle sizes for larger eruptions by applying an idealized 2/3 power scaling (Crowley and Unterman 2013; Toohey and Sigl, 2017). sAOD is then converted to radiative forcing using further conversion factors based on climate model simulations of the 1991 eruption of Mt. Pinatubo (Hansen et al., 2005). However, the relationship between sAOD and radiative forcing is uncertain as it is dependent on the aerosol particle size distribution (Lacis et al., 1992) and the latitude and season of an eruption (Andersson et al., 2015). Derived values are also dependent on the model configuration and values used include -20 W m^{-2} (Wigley et al., 2005) and -25 W m^{-2} (Hansen et al., 2005; Myhre et al., 2013) per unit of sAOD. Models may also derive the radiative forcing internally by using the sAOD as the forcing or from individual SO_2 injections if the model is coupled to an aerosol microphysics scheme (Arfeuille et al., 2014).

The expected spatial and temporal evolution of the sulfate aerosol mass and sAOD is based on simple parameterized transport models and/or that following Mt. Pinatubo (Ammann et al., 2003; Gao et al., 2008; Crowley and Unterman, 2013). Toohey and Sigl (2017) derived sAOD from individual stratospheric SO_2 injections using the Easy Volcanic Aerosol (EVA) forcing generator (Toohey et al., 2016b). Many eruptions identified in ice core sulfate records are unattributed, and therefore the eruption season and latitude must be estimated or arbitrarily assigned. For season, unknown eruptions are assigned to either January (Crowley and Unterman, 2013; Toohey and Sigl, 2017) or April (Gao et al., 2008), which introduces further uncertainty because the season of eruption affects the transport of stratospheric sulfate aerosol and its deposition (Gao et al., 2008; Toohey et al., 2011; 2013). Eruptions are assumed to be tropical if simultaneous sulfate signals occur in both Antarctica and Greenland (bipolar deposition signals) and if the ratio between the sulfate deposited on each ice sheet is close to 1. Unipolar sulfate deposition signals are assumed to arise from extratropical eruptions (e.g. Gao et al., 2008; Sigl et al., 2015). Bipolar deposition signals may still be attributed to mid-latitude eruptions, which have polar deposition ratios that diverge

from 1 because more sulfate is deposited on the closer ice sheet (Toohey et al., 2016a). Conversely, Toohey et al. (2013) found that it was still possible for a tropical eruption to have considerable asymmetry in deposited sulfate on Antarctica versus that in Greenland, with an eruption of 700 Tg SO_2 during NH winter leading to Greenland deposition 5 times that of Antarctica deposition. As such, the ratio between Greenland and Antarctica deposition can vary for a given latitude of eruption, and for tropical eruptions the ratio may be considerably different from 1.

The difficulty with any reconstruction of radiative forcing is that it does not scale directly with the deposited sulfate. The forcing (integrated over time) depends on the global spread of the volcanic aerosol in the stratosphere, its lifetime, and the microphysical properties of the aerosol (size, mass and number). All of these depend on the emission strength, the altitude and latitude of emission and the eruption season (e.g. Marshall et al., under review). Consequently, for any observed ice core volcanic sulfate deposition there is potentially a very wide range of 'eruption-realisations' with a wide range of associated forcings.

Some attempts have been made to estimate the uncertainty in SO_2 emissions derived from ice core sulfate composites by considering uncertainties in the ice core composites themselves and in the transfer functions (e.g. Toohey and Sigl, 2017) but the possible range in radiative forcing has not been quantified. Previous sensitivity studies investigating the relationships between eruption source parameters and sulfate deposition in modelling studies have also been based on specific case-studies (e.g. Toohey et al., 2016a) or at single latitudes (Toohey et al., 2013).

Here, we use a state-of-the-art interactive stratospheric aerosol microphysics model to simulate a wide range of large-magnitude eruptions and use the results to build statistical emulators that describe how sulfate deposition and radiative forcing vary with eruption magnitude, latitude and injection height (e.g. Marshall et al., under review). The emulators enable us to predict the sulfate deposition and radiative forcing for thousands of eruptions that we did not simulate and subsequently, to investigate uncertainties in radiative forcing derived from ice core sulfate records. We examine the combinations of eruption source parameters that could lead to measured ice sheet deposited sulfate anomalies and estimate the associated range in radiative forcings. Consequently, we calculate the radiative forcing of eruptions from ice core sulfate records independently of transfer functions and conversion factors.

We describe the model setup and statistical emulation in Section 4.2 and examine the range in ice sheet sulfate deposition across our simulations in Section 4.3.1. In Section 4.3.2 we constrain the eruption source parameters for the top 10 bipolar deposition signals recorded in ice cores and examine the volcanic aerosol radiative forcing in Section 4.3.3. Implications for current reconstructions of historic volcanic aerosol forcing are discussed in Section 4.4.

4.2 Methods

4.2.1 Model description and experiment design

Simulations of volcanic eruptions were performed with the UM-UKCA interactive stratospheric aerosol microphysics model (Dhomse et al., 2014) as outlined in Marshall et al. (under review). The model has a horizontal resolution of 1.875° longitude by 1.25° latitude with 85 vertical levels up to 85 km and has an internally generated Quasi Biennial Oscillation (QBO) (e.g. Osprey et al., 2013). The simulations were atmosphere-only and free running, with year 2000 background conditions that included prescribed climatological sea surface temperatures and sea ice extent (Reynolds et al., 2007).

Aerosol processes were simulated using the GLOMAP-mode aerosol microphysics scheme (Mann et al., 2010), with aerosol mass and number concentrations simulated using 7 log-normal modes. GLOMAP-mode includes primary emissions, new particle formation, condensation, coagulation, cloud processing, sedimentation and dry and wet deposition. In the version used here UM-UKCA includes stratospheric and tropospheric chemistry (Morgenstern et al., 2009; O'Connor et al., 2014) and aerosols, and interactive sulfur chemistry as well as aerosol radiative heating, which has been shown to influence volcanic plume dispersion and subsequent radiative effects (Aquila et al., 2012; Mann et al., 2015).

Two ensembles of simulations were conducted, each containing 41 eruptions with different values of three eruption source parameters: the mass of SO_2 emitted, the eruption latitude and the emission injection height (as in Marshall et al., under review). SO_2 emissions ranged between 10 Tg and 100 Tg of SO_2, latitude ranged between 80°S and 80°N, and the bottom injection height varied between 15 km and 25 km, with a plume depth of 3 km. The values of the eruption source parameters for each ensemble simulation were defined by using a ‘maximin’ Latin hypercube design

(Figure D.1) to achieve good coverage of the three-dimensional parameter space (Morris and Mitchell, 1995; Lee et al., 2011; Marshall et al., under review). One ensemble was performed for eruptions on 1 January and the other on 1 July to examine the seasonal dependence of meridional stratospheric aerosol transport and sulfate deposition. Each eruption (simulation) was initialized by injecting the SO_2 into the grid boxes within the 3-km plume over 24 hours. Both ensembles were initialized during similar easterly QBO phases. Two control simulations were also conducted without any volcanic perturbation, initialized from the same point as each ensemble. The two control simulations together provided 9 years of background data. The ensemble simulations were run for 38 months post eruption, by which time the majority (at least 83%, mean = 93%) of the injected sulfur had been deposited as sulfate.

The simulated sulfate deposited in each month (kg SO_4 km^{-2}) was calculated by summing the dry and wet deposition flux components (kg SO_4 km^{-2} s^{-1}) for each aerosol mode and multiplying by the number of seconds in each month. The volcanic sulfate deposition was determined by subtracting the climatological monthly mean sulfate deposition derived from the 9 years of control simulation. These anomalies were integrated over the 38 months (~3 years) of each simulation to produce the total volcanic sulfate deposition. Time-integrated radiative forcing was similarly calculated by integrating the net (shortwave + longwave) top-of-the-atmosphere outgoing all-sky global-mean radiative flux anomalies over the 38 months of the simulation. Radiative flux anomalies were derived from a control simulation initialized at the same point as the volcanic simulations. We use the term RF to refer to the time-integrated global mean radiative forcing.

4.2.2 Statistical emulation

Statistical emulators are used as surrogate statistical representations of the UM-UKCA model, which can be evaluated in a fraction of the time compared to the simulations themselves. An emulator maps a model output (e.g. total sulfate deposited on Greenland) to the input parameters (here the SO_2 emission, latitude and injection height) and is used to predict that model output for any combination of the input parameters that was not explicitly simulated. By sampling from an emulator thousands of times, a multi-dimensional response surface of the model output can be generated across parameter space, based on only a small set of model simulations.

We build four Gaussian process emulators (O'Hagan, 2006; Lee et al., 2011; Johnson et al., 2015) of the simulated deposition: total sulfate deposited on Greenland for eruptions in January and July, and total sulfate deposited on Antarctica for eruptions in January and July. We build each emulator using R (R Core Team, 2017) and the DiceKriging package (Roustant et al., 2012). Following a Bayesian statistical approach, each model response is assumed a priori to follow a Gaussian process, which is then updated with the model output from 30 of the 41 ensemble members, known as 'training runs', to generate the Gaussian process emulator. The emulator provides a mean prediction of the model output along with an estimate of the variance in this prediction. The remaining 11 simulations of each ensemble are used to validate each emulator by comparing the emulator mean prediction with uncertainty for the parameter combinations of each simulation to the actual model output of each simulation.

The amount of sulfate deposited on the ice sheets for a given atmospheric burden is a result of a chain of several processes that includes the large-scale stratospheric transport of sulfate aerosol, stratosphere-troposphere exchange and deposition. These processes, especially the deposition, are variable due to stratospheric variability (e.g. because of the QBO) and tropospheric meteorological variability such that varying the initial conditions of our free-running simulations could lead to different ice sheet sulfate deposition fluxes. Here we do not run a meteorological ensemble for each training point in parameter space and cannot account for this internal variability in the conventional way. Instead, we account for the internal variability using an alternative method by adding a noise variance term when building the emulators (Roustant et al., 2012). The addition of the variance term allows the emulator to vary more smoothly such that the mean emulator prediction does not have to exactly pass through the model training data (e.g. Johnson et al., 2011; Andrianakis and Challenor, 2012; Williamson et al., 2015; Salter and Williamson, 2016). In this way, we can effectively characterize conventional ensemble member variability in the construction of the emulator with the emulator mean prediction reflecting a meteorological ensemble mean. The uncertainty on the emulator predictions accounts for the inherent emulator uncertainty and the additional noise term because of internal variability.

The variance is included by specifying an estimated variance on the model output of each training run during the construction of the emulator. We choose to add a homogeneous noise term to each emulator. We estimate that the calculated sulfate

deposition output has a standard deviation due to the internal variability of 10 kg SO_4 km^{-2} in Greenland and 2.5 kg SO_4 km^{-2} in Antarctica. These values were chosen based on prior knowledge of deposition in Antarctica and Greenland from previous modelling studies, from the deposition variability in previous UM-UKCA simulations, and whether the validation of the new emulator was improved compared to an emulator built without a noise term. For example Toohey and Sigl (2017) suggested relative standard deviations (RSD) of 16% in Greenland and 9% in Antarctica due to the meteorological state, based on ensembles of atmosphere-only simulations of eruptions with a range of SO_2 emission magnitudes from 8.5 Tg to 700 Tg (Toohey et al., 2013). Similarly, Gao et al. (2007) reported ~10-20% differences in sulfate deposition over Greenland and Antarctica amongst ensemble members following simulations of eruptions with SO_2 injections ranging from 5 Tg to 122 Tg. We found that across 5 meteorological ensemble members of simulations of UM-UKCA (also atmosphere-only) of the eruption of Mt. Tambora (Marshall et al., 2018), the standard deviation of the Greenland deposition was 6.2 kg SO_4 km^{-2} (RSD = 20%) and the standard deviation of Antarctica deposition was 1.6 kg SO_4 km^{-2} (RSD = 8%). Given that the simulation of Mt. Tambora was initialized with a 60 Tg injection at the equator, it is reasonable that an average noise variance term for our ensemble with emissions spanning 10 Tg to 100 Tg SO_2 and across both high and low latitudes, is higher. Regardless of the value of estimated noise, the overall shape and pattern of the emulated surfaces remains the same but emulator validation is improved using the given values. We found that higher estimates of this noise variance led to poorer emulator validation and response surfaces with reduced variation in model output versus the eruption source parameters.

We build two further Gaussian process emulators of the RF for each season (January and July). These emulators are built without noise because the radiative forcing signals have relatively low variability (they are not determined by tropospheric meteorology) and validation of the emulators was reasonable without an additional noise term (Marshall et al., under review).

Validation of the emulators we use is shown in Figures D.2 and D.3. The emulator predictions follow the 1:1 line in all cases, but Greenland deposition tends to be slightly underestimated by the emulator (Figure D.2). The 95% confidence bounds on the emulator predictions are larger for the deposition emulators (Figure D.2) compared to the RF emulators (Figure D.3) because the fit is more uncertain and

because of the additional noise term in the build. Overall, the emulators are reasonable surrogates of the UM-UKCA output. Emulated response surfaces of the model outputs were produced by sampling the predicted mean response of each emulator 1 million times over a three-dimensional grid generated with 100 values of each eruption source parameter (covering the range in values simulated for each parameter).

4.3 Results

4.3.1 UM-UKCA-simulated sulfate deposition

Figure 4.1 shows the time-integrated sulfate deposition anomalies (over 38 months) for the 82 UM-UKCA model simulations plotted against the SO_2 emission, latitude and injection height of each simulation. Deposition increases on each ice sheet as the SO_2 emission increases and for eruptions at high latitudes (i.e. closer to the ice sheets). Because the deposition is dependent on both these parameters, there are eruptions that are close to the ice sheets but have low deposition because the SO_2 emission was low and eruptions with high SO_2 emissions but low deposition because they are far away from the ice sheet (a three-dimensional view is shown in the supporting information (Figure D.4)). There does not appear to be an obvious relationship between the injection height and the deposition.

On average, we find that the deposition on Greenland is higher than on Antarctica, with a maximum of 148 kg SO_4 km^{-2} deposited for an eruption at 79ºN occurring in January, with a SO_2 emission of 84 Tg. The maximum simulated Antarctica deposition of 65 kg SO_4 km^{-2} occurs for a July eruption at 72ºS with a SO_2 emission of 98 Tg. Lower deposition on Antarctica compared to Greenland was also found by Toohey et al. (2013) for tropical eruptions, most likely because of stronger meridional transport in the NH and increased deposition because the NH is relatively more dynamically active than the SH. In the SH the stronger polar vortex will inhibit more of the polewards aerosol transport. Deposition on the ice sheets will also vary with SO_2 emission magnitude given an increase in sedimentation as particles grow larger such that they may be deposited before reaching the ice sheets and stronger polar vortices arising from aerosol-induced stratospheric heating (Toohey et al., 2013; 2014).

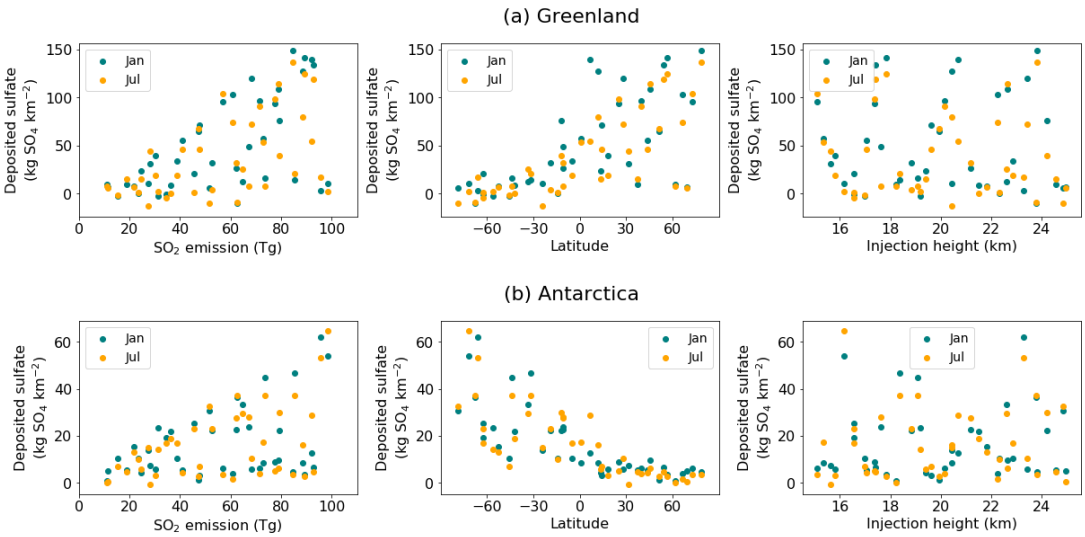

Figure 4.1: Time-integrated anomalous deposited sulfate on (a) Greenland and (b) Antarctica in each simulation versus the eruption source parameters (left = SO_2 emission, middle = latitude and right = injection height). Deposition from the January eruptions are shown in teal and in orange for the July eruptions. There are different scales on the y axes between (a) and (b). A three-dimensional view is shown in the supporting information (Figure D.4).

Deposition on Greenland is higher for tropical eruptions occurring in January (teal circles in Figure 4.1a) because more sulfate aerosol is transported to the Northern Hemisphere (NH) via the Brewer Dobson Circulation (BDC), which is stronger in the winter hemisphere. Similarly, both total Southern Hemisphere (SH) deposition (not shown) and deposition on Antarctica from tropical eruptions is greater if they occur in July (orange circles in Figure 4.1b) following the seasonal cycle of the BDC. For eruptions at latitudes greater than ~30°N/S we find that the total hemispheric deposition is similar between the seasons, but ice sheet deposition varies between seasons, but is not consistently larger in either one. Differences in the seasonal response for mid-to-high latitude eruptions could be dependent on the SO_2 emission magnitude and injection height but also seasonal variations in stratosphere-troposphere exchange and sulfate aerosol deposition rates for example in the mid-latitude storm tracks (e.g. Kravitz and Robock, 2011). Seasonal differences may also arise due to internal variability.

Figure 4.1 shows that there is some spread in the ice sheet sulfate deposition values around zero for eruptions located at high latitudes in the opposite hemisphere to the ice sheet. The time series of the sulfate deposition anomalies can be very noisy, and it is not certain that the anomalies are always due to the deposition of volcanic sulfate (Figure D.5). This is because the difference between the ice sheet sulfate deposition

in the volcanically-perturbed simulations and in the control climatology includes not only the volcanic sulfate deposition, but changes to the background tropospheric sulfate aerosol deposition because of changes to stratospheric dynamics and tropospheric meteorology induced by the eruption (i.e. the control and perturbed runs effectively behave like two meteorological ensemble members). Consequently, the amount of background tropospheric-originating sulfate aerosol can be very different in each perturbed simulation compared to the control climatology. For example, integrated deposition anomalies can even be negative because the climatological deposition is higher than in the perturbed simulation, which represents just one possible realisation of reality (an example is included in Figure D.5). Similarly, integrated anomalies can also be the same magnitude as possible volcanic signals if the background deposition in the perturbed run was higher than in the climatology. For example, an eruption simulated at 63ºS results in Greenland deposition of 21 kg SO_4 km^{-2}, unlikely to be of volcanic origin (Figure D.5) (i.e. a false positive) and which is similar in magnitude to the signal recorded in Greenland ice cores after the tropical eruption of Mt. Pinatubo in 1991 (Sigl et al., 2015). There is more anthropogenic sulfate in the NH, which may also add to the increased variability simulated in Greenland deposition. Ice sheet deposition signals from eruptions at latitudes of greater than ~30°N/S in the opposite hemisphere may therefore result from variability in the non-volcanic background deposition, although we do find that sulfate aerosol can be transported globally for eruptions at latitudes as high as 79° (not shown). The emergence of a signal showing an increase in deposition with increasing latitude occurs once the deposition is greater than ~20 kg SO_4 km^{-2} in Greenland and once it is greater than ~10 kg SO_4 km^{-2} in Antarctica.

Ice core records of sulfate deposition represent only one realisation of the possible deposited sulfate and although the variability in background sulfate deposition is less in the preindustrial atmosphere, our results (in a modern atmosphere) still demonstrate that the deposition is strongly influenced by tropospheric meteorological variability and that many eruption signals could be masked or even inflated by internal variability. Attempts are made to remove variable background deposition when detecting volcanic signals in ice core sulfate measurements, such as by filtering (e.g. Castellano et al., 2005; Gao et al., 2008; Ferris et al., 2011). However, these are still subjective, and volcanic events may be missing, under- or even over-predicted in volcanic forcing reconstructions (e.g. Gao et al., 2008; Sigl et al., 2015).

Next, we build statistical emulators of the deposition to each ice sheet for each season and from this point forward the emulator predictions are used in place of the UM-UKCA simulation output. The emulated response surfaces describe the trends and patterns seen across the UM-UKCA simulations (Figure 4.1) but enable us to see how the deposition varies continuously across the parameter values. However, Greenland deposition below ~20 kg SO_4 km^{-2} and Antarctica deposition below ~10 kg SO_4 km^{-2} may be produced by non-volcanic sulfate deposition as identified in Figure 4.1.

Emulated response surfaces showing the predicted deposition against the latitude and SO_2 emission of an eruption for three fixed injection heights are shown in Figure 4.2. The surfaces highlight further the dependency of deposition on the combination of the SO_2 and latitude. Sigl et al. (2014) suggested that Antarctica deposition following a tropical eruption was insignificantly different for eruptions at different latitudes (4ºS versus 15ºN). Our emulated surfaces show that this may be the case for smaller SO_2 emissions, but not necessarily for the largest emissions.

The majority of predicted deposition appears independent of injection height, but the response may be masked by the inherent noise in the deposition signals because injection height is the least important parameter in determining the magnitude of the deposited sulfate (Figure 4.1). In Figure 4.2c the curved response at high latitudes and high SO_2 emissions is likely due to the emulator fit, which struggles at the edge of the parameter space.

The difference between the emulated deposition in the two seasons (shown in Figure D.6) shows clearly that the deposition is higher on the ice sheet in the winter hemisphere if the eruption is tropical and these differences increase in magnitude as the SO_2 emission increases. For eruptions between ~30°S and ~60°S, Antarctica deposition is higher if they occur in January (summer) likely related to a weaker polar vortex, which otherwise inhibits the deposition following an eruption in July (winter), although the effect will depend on the time it takes for the aerosol to form and be transported to Antarctica and how strong the vortex is at this point.

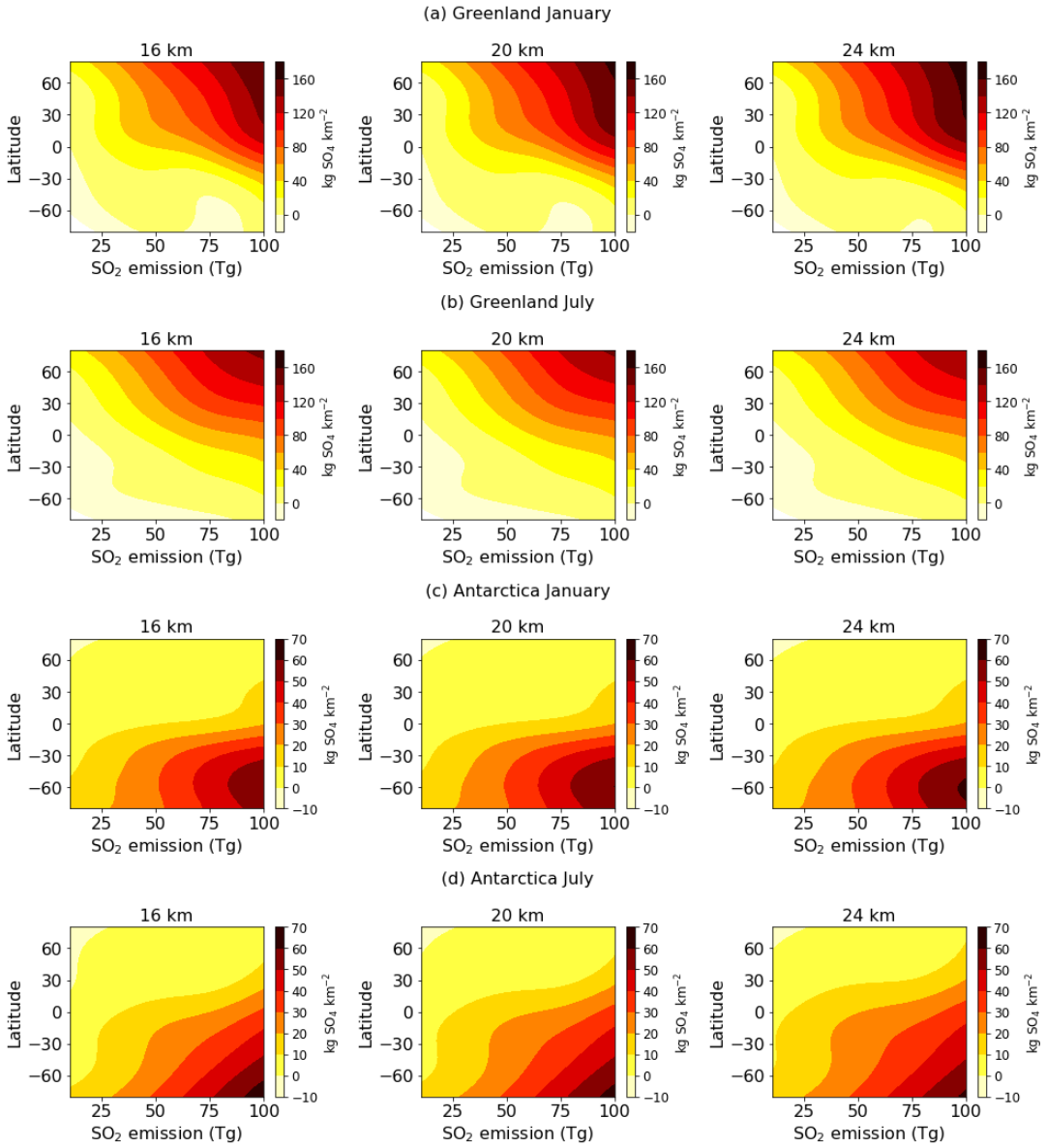

Figure 4.2: Emulated response surfaces at fixed injection heights for each of the deposition emulators: (a) Greenland deposition following a January eruption, (b) Greenland deposition following a July eruption, (c) Antarctica deposition following a January eruption and (d) Antarctica deposition following a July eruption. Each emulator is sampled at fixed injection heights of 16 km, 20 km and 24 km. The surfaces show the emulator mean prediction of the deposition against SO_2 emission and latitude of eruption at each of these heights. There are different colour scales for the Greenland and Antarctica deposition.

4.3.2 Constraining eruption source parameters

The validated emulators can be used to predict the sulfate deposited on each ice sheet for any combination of SO_2 emission, latitude and injection height within our parameter space, for eruptions occurring in either January or July. By using the emulated sulfate deposition "in reverse" we can find the combinations of eruption

source parameters that lead to deposition within a measured range. This is similar in concept to analysis by Toohey et al. (2016a) who constrained the likely parameters for the 536 CE and 540 CE unattributed eruptions by comparing the deposition in potential candidate simulations with measured ice sheet deposition, except they used the ratio of the ice sheet sulfate deposition as opposed to the absolute magnitude. To illustrate the constraint procedure in this study, we take the emulated deposition and constrain the source parameters of eruptions that lead to the ice sheet sulfate deposition derived from ice cores for the 1815 eruption of Mt. Tambora. Ice-core-derived deposited sulfate from the most recent comprehensive and high-resolution array of ice cores is 39.7±10.4 kg SO_4 km^{-2} in Greenland and 45.8±5.3 SO_4 km^{-2} in Antarctica (Table 4.1; Sigl et al., 2015).

Figures 4.3a and 4.3b show the three-dimensional constrained parameter space for each season using the ranges of ice sheet mean deposition on Greenland and Antarctica provided by Sigl et al. (2015). The uncertainties on the emulator predictions (that the emulator itself derives) are included during the constraint. These uncertainties increase with distance (in parameter space) from the training runs because there is less information on how the model output varies as a function of the input parameters. Here combinations of parameters are retained if the emulator mean prediction plus or minus one standard deviation (SD) falls within the range of the ice-core-derived sulfate deposition estimates. The colour in Figure 4.3 shows the emulated mean prediction of the RF for each eruption and is explored in Section 4.3.3.

For an eruption occurring in January, the predicted deposition falls within both the Greenland and Antarctica deposition constraints only if the SO_2 emission is greater than 73 Tg and the latitude of the eruption is between 20°S and 49°S. The injection height remains unconstrained. For an eruption in July, only eruptions with SO_2 emissions greater than 81 Tg and with a latitude between 4°S and 59°S can produce Greenland and Antarctica deposition that matches both ice sheet constraints. The high SH latitude eruptions may be returning combinations where the Greenland deposited sulfate is a result of non-volcanic sulfate. Constrained combinations that have latitudes greater than ~30°N/S and result in a bipolar deposition signal should be interpreted with caution given that it is plausible that the lower ice sheet deposition magnitudes in the opposite hemisphere are produced by noise (Figure 4.1, Figure D.5).

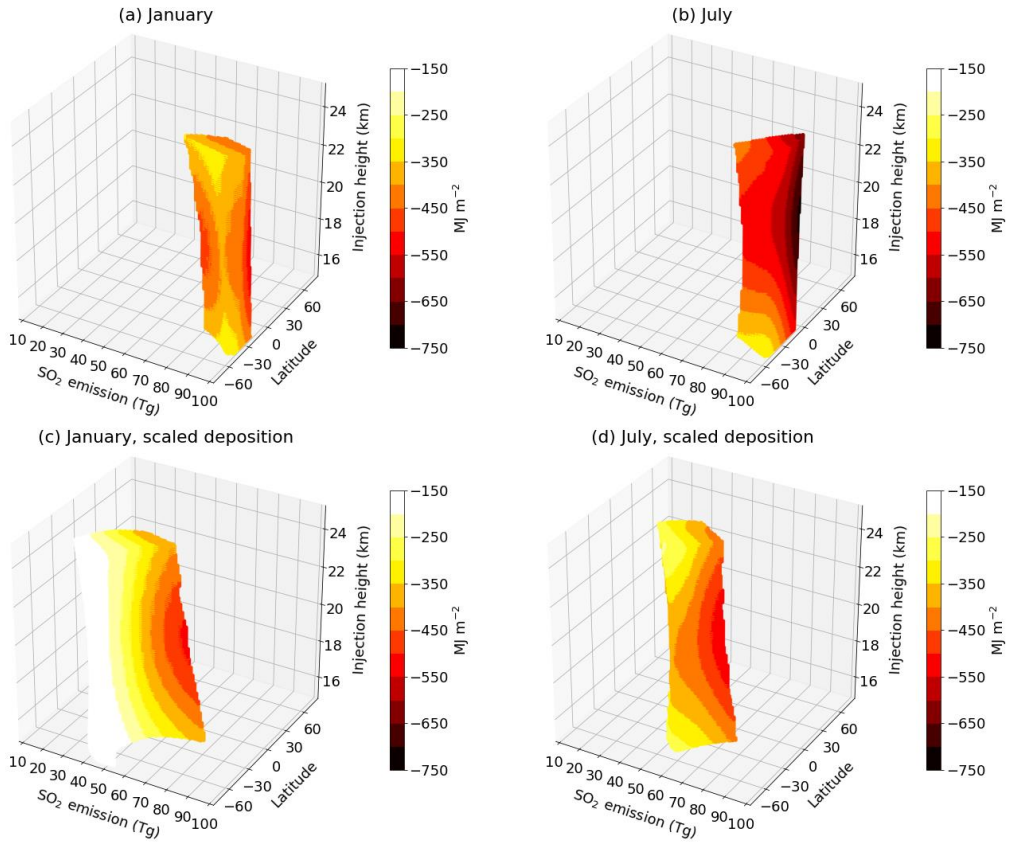

Figure 4.3: Constrained parameter space showing the combinations of SO_2 emission, latitude and injection height that result in the possible range of ice-core-derived sulfate deposition following 1815 Mt. Tambora from Sigl et al. (2015). (a) and (b) show the constrained space for January and July eruptions. (c) and (d) show the constrained space if the ice-core-derived estimates are divided by 2 for January and July eruptions, respectively. Parameter combinations are retained if the emulator mean prediction plus or minus 1 SD for both the Antarctica and Greenland deposition fall within the ice-core-derived constraints. The constrained space is made up of scatter points of the parameter combinations and the colour of each scatter point shows the emulator mean prediction of the RF for each of these eruptions (Section 4.3.3).

Only eruptions in July return matches of plausible eruption source parameter combinations that match the Mt. Tambora latitude of 8°S and the SO_2 emission of these combinations must be greater than 96 Tg. These combinations are also on the very edge of the latitude range retained. Because our SO_2 emissions are capped at 100 Tg, it may be that for an eruption at 8°S to produce the measured deposition, it is more likely that the emission needs to be much higher. We have also only built emulators for eruptions occurring on 1 January and 1 July, whereas Mt. Tambora erupted in April 1815. The predicted deposition is generally higher in Greenland for January eruptions, and higher in Antarctica for July eruptions (Figure 4.2) and deposition following an April eruption would also vary given seasonally varying stratospheric transport of sulfate aerosol and depositional processes (e.g. Gao et al., 2008).

Furthermore, previous simulations of the 1815 eruption of Mt. Tambora using UM-UKCA with 60 Tg SO_2 emitted at the equator between 22 and 26 km showed that sulfate deposited on the ice sheets was roughly half that derived from ice core estimates (Marshall et al., 2018). This indicates that either the SO_2 emission was too low, or a structural error exists within the model resulting in a low bias in deposition.

Figures 4.3c and 4.3d show the constrained parameter space when the ice-core-derived estimates are divided by 2 (to account for a potential bias in the model), although the scaled estimates are also more likely to be produced by noise. For eruptions in January the SO_2 emission now lies between 26 and 76 Tg and latitude between 11°S and 80°S. Any higher SO_2 emission leads to too-high deposition compared to the scaled ice core estimates. For eruptions in July, the SO_2 emission ranges between 35 and 75 Tg and latitude between 6°N and 53°S, covering the latitude of Mt. Tambora. This indicates that even if a structural bias does exist in UM-UKCA, there is still a range of eruption source parameter combinations that can lead to the same ice sheet deposited sulfate. The retained combinations also include the parameters used to simulate the eruption of Mt. Tambora in preindustrial conditions in Marshall et al. (2018).

4.3.3 Constraint of volcanic aerosol radiative forcing

Using emulators of the RF built for the January and July eruptions (Section 4.2.2), we examine the emulator mean predictions of RF for the combinations of eruption source parameters constrained from the top 10 bipolar deposition signals in the last 2500 years reported in Sigl et al. (2015). Of these 10 signals, only two have been confidently attributed to known eruptions (1815 Mt. Tambora, which is the 6th largest signal, and 1257 Samalas, which is the 2nd largest signal) (e.g. Toohey and Sigl, 2017). Because we do not know for certain that a structural bias exists in UM-UKCA, we do not scale the deposition constraints, which may otherwise add an additional bias. By including the emulator uncertainty (which also accounts for ensemble spread) and the uncertainty on the ice sheet composite observations, we provide a conservative estimate of the range in eruption source parameters and the RF. We aim to illustrate how a range of different eruption-realisations could be consistent with the same measured sulfate deposition signal. The constrained eruption source parameters and emulator-predicted RF for each of the deposition signals are listed in Table 4.1 and

shown in Figures D.8-D.9. Histograms of the constrained RF are presented in Figure 4.4.

We do not return any plausible eruption source parameter combinations for the 426 BCE and 1257 Samalas deposition (ice sheet deposition starts in 1258 CE), and very few combinations for the 1458 CE deposition. This suggests that the SO_2 emissions of these eruptions were greater than 100 Tg, consistent with previous estimates (e.g. Oppenheimer, 2003; Gao et al., 2007; Vidal et al., 2016; Toohey and Sigl, 2017). For the remaining deposition signals, we find many eruption-realisations are constrained, which have a large range in RF for both January and July eruptions. The largest range in RF for a single season is 410 MJ m^{-2} for the 1815 Mt. Tambora deposition constrained from July eruptions. The largest range in RF combined across both seasons is 424 MJ m^{-2} for the 574 CE deposition. The smallest range in RF across both seasons was -267 MJ m^{-2} for the 1458 CE eruption, but only because the eruption-realisations were capped at 100 Tg.

The uncertainty ranges of RF that we calculate (> ~300 MJ m^{-2} in all cases) are approximately 2 – 3 times the magnitude of RF predicted for the 1991 eruption of Mt. Pinatubo, which was between -133 MJ m^{-2} and -229 MJ m^{-2} (Marshall et al., under review). Therefore, the uncertainty in reconstructed RF can be related to the possibility that forcing reconstructions for individual events may be missing or including additional forcing of up to 3 times that from 1991 Mt. Pinatubo, which led to approximately 0.5°C of surface cooling (Dutton and Christy, 1992).

We find that the constrained RF differs between the eruptions in the different seasons (Figure 4.4) because different combinations of parameters are constrained that have different RF (e.g. Marshall et al., under review) but also because for the same combinations of parameters, RF can differ between seasons (Figure D.7). We find that the highest RF occurs for eruptions at the equator if they occur in July, but for tropical eruptions south of the equator if they occur in January (Figure D.7), likely because of seasonal variations in the position and strength of the tropical pipe (e.g. Holton et al., 1995; Seviour et al., 2012). We also find that mid-latitude eruptions have stronger RF if they occur in the winter because it takes up to 8 months for the peak aerosol burden to form (in the UM-UKCA simulations) and the highest aerosol burden subsequently coincides with peak summer insolation. A more detailed examination of the differences in RF between the seasons will be the focus of a future study.

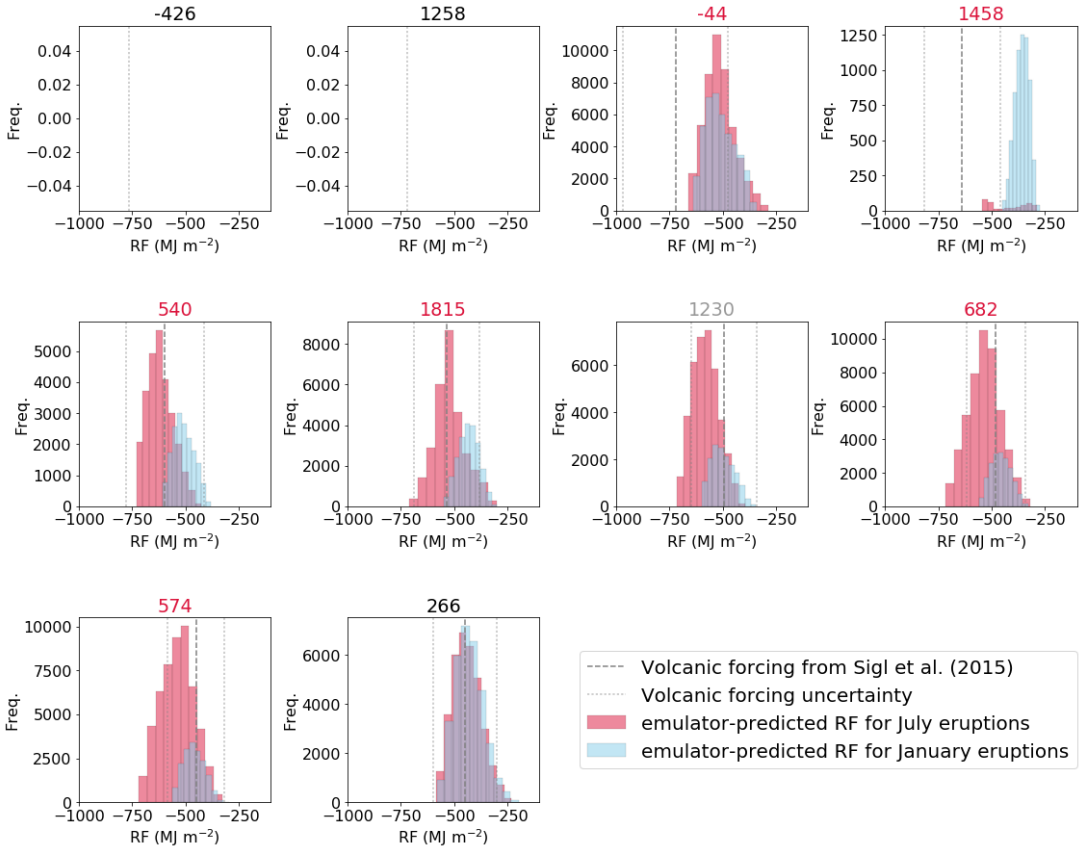

Figure 4.4: Histograms of the emulator-predicted RF (emulator mean) of constrained eruption source parameter combinations for the top 10 bipolar deposition signals in Sigl et al. (2015) (in rank order). The red distribution is the RF for July eruptions and the blue distribution is for January eruptions. Each histogram is plotted using 10 bins. The vertical grey dashed lines mark the annual-mean time-integrated global volcanic forcings derived by Sigl et al. (2015), which have been converted to roughly equivalent monthly-mean integrals by multiplying by 12 and the number of seconds in a 30-day month. The year (BCE/CE) of the onset of each deposition signal is shown at the top of each panel and colour-coded depending on whether the constrained space is capped at 100 Tg. The title is grey if only the July eruptions are capped at 100 Tg, red if both January and July eruptions are capped at 100 Tg and black if neither of the distributions are capped at 100 Tg.

Except for the 44 BCE and 266 CE deposition, the RF of the constrained July eruptions reaches larger values compared to the constrained January eruptions and more combinations are retained in total for the July eruptions (except 1458). Compared to the January constrained parameters, the July constrained parameters are either shifted towards the NH or expanded further into both hemispheres, reaching stronger values of RF near the equator. Tropical NH eruptions occurring in January would lead to higher Greenland deposition and lower Antarctic deposition because more aerosol is transported to the NH and deposition would fall outside of the ice sheet constraints. Several of the constrained January eruptions also have combinations

with lower SO_2 emissions than the July combinations. For the 1815 Mt. Tambora example (Figures 4.3a-b), RF ranges between -300 MJ m^{-2} and -550 MJ m^{-2} for a January eruption and between -300 MJ m^{-2} and -710 MJ m^{-2} for a July eruption. For the scaled deposition constraint, RF is much lower ranging from -113 MJ m^{-2} to -509 MJ m^{-2} for a January eruption and -244 MJ m^{-2} to -536 MJ m^{-2} for a July eruption, because the combinations of parameters that are retained have lower SO_2 emissions (Figures 4.3c-d).

The 44 BCE and 266 CE deposition have much more sulfate deposited on Greenland versus Antarctica (the ratio of mean Greenland to Antarctica deposition is 6.5 and 5.4, respectively) than the other eruptions (deposition ratios are less than 2.4). Consequently, the January constrained eruptions are in the tropics and the July constrained eruptions are shifted towards the NH mid-latitudes (especially for 44 BCE) with the closer proximity of these eruptions to Greenland balancing the reduction in poleward transport due to being in the summer hemisphere. The range in retained SO_2 emissions is also similar between seasons for both cases and therefore the similar RF distributions despite differences in latitude may be because of differences in RF related to the position and strength of the tropical pipe.

Our constrained parameter spaces are conservative as we also consider the uncertainty on the emulator mean predictions when constraining, which results in broader distributions than if this uncertainty were not included. Some of the lower deposition constraint values may also be low enough that the magnitude could be produced by non-volcanic sulfate. We find that some of the constrained latitudes are very high, for example for the 44 BCE deposition, July eruptions as high as 80°N are retained (Table 4.1, Figure D.9). The minimum Antarctica deposition constraint for 44 BCE is 11 kg SO_2 km^{-2}, and these combinations may therefore be false positives. Similarly, the minimum Antarctic deposition for the 266 CE signal is 10 kg SO_4 km^{-2} and some of the NH retained eruptions may also be erroneous. Bipolar deposition signals from extratropical eruptions are not implausible and Toohey et al. (2016a) showed that model-simulated extratropical eruptions at 56°N could have Greenland to Antarctica sulfate deposition ratios of 5:1. We find that sulfate aerosol can spread globally for eruptions at all latitudes (not shown), even if the amount reaching the poles is relatively small, as also found by Schmidt et al. (2010) following the 1783-1784 Laki eruption. It remains unclear as to how high a latitude could be and still result in a detectable (above natural variability) bipolar sulfate deposition signal.

Table 4.1: Constrained ranges in SO_2 emission (Tg SO_2), eruption latitude (°N) and RF (MJ m^{-2}) for the 10 largest bipolar ice-core-derived sulfate deposition signals in Greenland and Antarctica from Sigl et al. (2015) (in rank order). Year (BCE/CE) is the onset of the deposition signal. Also included is the Volcanic Stratospheric Sulfur Injection (VSSI) (plus or minus 1 standard deviation uncertainty) estimated by Toohey and Sigl (2017) (Tg of SO_2). For all cases the minimum and maximum retained injection heights were 15 km and 25 km. Grey shading marks signals that are unconstrained because they are outside of our parameter space. Although the latitude of 1815 Mt. Tambora is known, we keep the whole range in constrained parameters as an example for if the eruption had not been attributed.

	Ice sheet deposition (kg SO_4 km^{-2})		January eruptions						July eruptions						
Year	**Greenland**	**Antarctica**	**Lat max**	**Lat min**	**SO_2 min**	**SO_2 max**	**RF min**	**RF max**	**Lat max**	**Lat min**	**SO_2 min**	**SO_2 max**	**RF min**	**RF max**	**VSSI (Tg SO_2)**
-426	99.8±26.2	78.2±20.5													118.7± 35.9
1258	90.4±23.7	73.4±8.7													118.8±21.7
-44	100.6±26.4	15.4±4.0	44.4	-8.9	55.5	100.0	-341.6	-637.9	80.0	7.3	61.8	100.0	-286.2	-659.8	77.2±22.6
1458	39.0±10.2	63.6±7.4	-36.4	-65.5	88.2	100.0	-276.0	-452.0	-49.3	-60.6	98.2	100.0	-286.5	-543.4	66.0±9.6
540	61.2±16.0	34.4±4.0	-10.5	-28.3	69.1	100.0	-380.9	-606.9	17.0	-26.7	74.5	100.0	-424.4	-730.1	63.7±15.5
1815	39.7±10.4	45.8±5.3	-20.2	-49.3	72.7	100.0	-299.7	-550.1	-4.0	-59.0	80.9	100.0	-299.8	-710.0	56.2±9.0
1230	56.4±14.8	23.1±2.8	-4.0	-20.2	50.0	99.1	-344.4	-598.3	20.2	-17.0	52.7	100.0	-393.8	-716.1	47.6±10.5
682	38.4±10.1	38.7±4.6	-17.0	-39.6	62.7	100.0	-330.7	-557.6	-0.8	-50.9	70.0	100.0	-319.4	-718.1	54.4±9.3
574	38.3±10.0	34.1±4.1	-13.7	-34.7	51.8	100.0	-293.6	-563.0	0.8	-44.4	61.8	100.0	-328.0	-717.4	48.2±10.0
266	61.0±16.0	11.3±1.4	17.0	-8.9	34.5	86.4	-197.7	-581.0	36.4	2.4	39.1	90.0	-230.3	-584.2	43.7±11.4

For all 10 signals, the injection height across all retained combinations is not constrained. However, there are some combinations of SO_2 emission and latitude where injection height is marginally constrained. Figure D.8 shows that the January constrained space is often sloped, with lower emissions that have the highest injection heights. The lack of constrained injection heights suggests that the time-integrated deposition in general is not strongly dependent on the altitude of the emissions. Injection height is more likely to affect the timing of the ice sheet sulfate deposition rather than the total deposition.

Table 4.1 also includes the volcanic stratospheric sulfur injections (VSSI) estimated by Toohey and Sigl (2017) derived using hemispheric transfer functions between the ice sheet sulfate deposition and atmospheric sulfate burdens (Section 4.1). Toohey and Sigl (2017) also estimate the uncertainty in the VSSI due to random errors in the ice sheet sulfate deposition averages and in the transfer functions. Our independently derived SO_2 emission ranges reach much higher values than the VSSI, but the two ranges in general overlap for our lower estimates and the upper VSSI estimates, except for the 1458 CE and 1815 Mt. Tambora deposition where there are no comparable values. This suggests either that the mean transfer functions used by Toohey and Sigl (2017) do not hold for these eruptions and/or ice sheet deposition is too low in UM-UKCA (Marshall et al., 2018). For the 540 CE eruption, our constrained parameters include the latitude suggested by Toohey et al. (2016a) (15ºN) only if the eruption occurred in July, but do not include the emission (50 Tg).

Despite the range in constrained parameters including higher SO_2 emissions than previous studies (Gao et al., 2008; Toohey and Sigl, 2017), the emulator predictions of RF for these eruptions are generally consistent with the RF from Sigl et al. (2015), except for the 44 BCE and 1458 CE eruptions (Figure 4.4). The RF from Sigl et al. (2015) was derived by scaling the deposition to the global atmospheric burden using the scaling factors from Gao et al. (2008) and linearly scaling the burden to RF based on the relationship between the 1815 Mt. Tambora burden and RF derived from the Crowley and Unterman (2013) sAOD reconstruction (Schmidt et al., 2011). The comparison is reassuring but is likely a result of compensating errors. The Sigl et al. (2015) reconstruction does not directly consider particle size and linearly scales the burden to forcing, which may explain why our RF is similar for larger SO_2 emissions and less than the Sigl et al. (2015) estimates for the large 44 BCE and 1458 CE eruptions, because we include size-resolved aerosol microphysics. The RF uncertainty

provided by Sigl et al. (2015) included the uncertainty in the ice sheet composites and a 25% calibration uncertainty (Gao et al., 2008). The annual RF reported in Sigl et al. (2015) were also roughly converted to equivalent 38-month integrated monthly fluxes by multiplying by 12. If the ice sheet deposition is too low in UM-UKCA, constrained SO_2 emissions and RF would be lower (e.g. Figures 4.3c-d). We have also not considered the uncertainty on the emulator predictions of RF for each constrained set of parameters, which would provide an even larger range in RF for these eruptions.

4.4 Discussion and conclusions

We have constrained the eruption source parameters and RF of eruptions from the top 10 bipolar ice sheet sulfate deposition fluxes (Sigl et al., 2015), independently of transfer functions and scaling factors. Our results suggest that there are many different eruption-realisations that could be consistent with ice-core-derived sulfate deposition fluxes, with constrained SO_2 emissions ranging by up to 55 Tg (for the 266 CE deposition), latitude by up to 89° (for the 44 BCE deposition) and injection height by 10 km (all 10 deposition constraints). We find that RF ranges by up to 424 MJ m^{-2} (for the 574 CE deposition), representing an uncertainty in RF that is ~2-3 times the magnitude of the RF that occurred following the 1991 eruption of Mt. Pinatubo. The constrained eruptions have a range in RF because of differences in the eruption latitudes, SO_2 emissions and the season, which affect the amount of aerosol that is formed, the particle size distribution, the spatial distribution of the aerosol and its lifetime (e.g. Marshall et al., under review).

Our constrained SO_2 emissions are at the higher end of previous estimates, suggesting that the transfer functions used to link ice sheet deposition fluxes and atmospheric sulfate burdens do not hold for eruptions larger than 1991 Mt. Pinatubo (e.g. Toohey et al., 2013) or because of a structural bias in UM-UKCA. The ranges in SO_2 emissions are also consistent with modelling results by Toohey et al. (2013) who estimated an uncertainty of at least 25% in reconstructed sulfate aerosol burdens depending on whether a tropical eruption occurred in January or July. They demonstrated that ice sheet deposition could be similar for eruptions of very different magnitudes, although higher than the emissions perturbed in this study, with equivalent Antarctica deposition simulated for a 170 Tg SO_2 eruption in July and a 300 Tg SO_2 eruption in January. Although Toohey et al. (2013) only considered

eruptions at 15°N, they reported a plausible range of roughly 70 Tg in the SO_2 emission of a 1257 Samalas-like eruption. Our SO_2 emissions would also be larger if we had simulated eruptions with emissions greater than 100 Tg.

Deposition of sulfate on the ice sheets is strongly dependent on the meteorology (Robock and Free, 1995; Toohey et al., 2013; Sigl et al., 2014) and the long-range transport of non-volcanic aerosol, which may be altered following the eruption, and which makes it difficult to isolate volcanic signals even in model simulations (e.g. Figure D.5). We find that time-integrated sulfate deposition anomalies can be positive (above the climatological background) due to variations in tropospheric-originating sulfate (e.g. Cole-Dai et al., 2000; Ferris et al., 2011) and re-iterate previous conclusions that many volcanic signals will be missed, under-predicted or over-predicted because of variations due to internal variability.

It is possible that some of the constrained parameter combinations especially at high latitudes could be false positives because of the non-volcanic sulfate deposition variability. However, we also find that sulfate aerosol is transported globally even for high latitude eruptions and it is plausible that extratropical eruptions could lead to bipolar deposition signals. Volcanic forcing reconstructions that use transfer functions to translate measured deposition into atmospheric burdens assume that bipolar deposition signals can only be the result of tropical eruptions and apply tropical transfer functions (Gao et al., 2008; Sigl et al., 2015). Toohey and Sigl (2017) considered the possibility of extratropical eruptions resulting in bipolar signals, but only applied this scenario to the large 236 SH Taupo eruption. In the absence of an identified volcano, unknown eruptions are assigned tropical latitudes for bipolar sulfate deposition signals (e.g. 0°N in Toohey and Sigl (2017)) and extratropical latitudes for unipolar ice sheet signals (e.g. 45°N or S in Toohey and Sigl, 2017). It is also possible that unipolar signals could still result from tropical eruptions (Crowley and Unterman, 2013). Our results suggest that there are many more plausible latitudes that could lead to bipolar signals and more often than not these are south of the equator, especially if the eruption occurred in January.

We have used statistical emulation to comprehensively investigate the impact of different eruption source parameters on sulfate deposition and RF but there are several limitations that should be addressed in future work. We have accounted for internal variability during construction of the emulators by adding a noise variance term,

which negates the need for running conventional meteorological ensemble members and therefore reduces the computational cost of our experiment. However, there is uncertainty regarding the magnitude of internal variability and we have added only a homogeneous noise term to reflect the average variability in deposition across the whole parameter space and across both seasons. Future work should consider adding heterogeneous noise to better characterize the internal variability across the parameter space, which could improve the emulator fits and validation. We found that the Greenland deposition emulators, although valid for this study, were poorer fits than the Antarctica emulators and had a few validation points under the 1:1 line (Figure D.2). This may be because the emulator fit is characterizing well the ensemble mean and doesn't reflect the individual validation runs, which reflect one realisation of reality, or that some of the Greenland deposition is underestimated, which may alter the parameter space that we constrain. At present, it is impossible to characterize the uncertainty due to internal variability and due to the emulator uncertainty without additional sensitivity simulations.

We have also only investigated eruptions in two seasons and the deposition from eruptions at other times of the year will be influenced by seasonally-varying meridional and cross-tropopause transport and precipitation. Gao et al. (2008) found differences in polar deposition of around 10% across the four seasons and therefore parameter combinations and their RF constrained from ice sheet deposition for eruptions in other seasons could vary further than presented here. Furthermore, variations in the phase of the QBO, which were not considered in this study, could also impact the transport and deposition of sulfate (e.g. Trepte and Hitchman, 1992; Punge et al., 2009). Similarly, our simulations use prescribed SSTs and as such internal variability associated with ENSO is also not included. We have constrained preindustrial sulfate deposition signals from simulations conducted using a present-day atmosphere, where the background non-volcanic sulfate emissions are higher and large-scale atmospheric circulation is faster. However, we find that the emulators predict the deposition following 1815 Mt. Tambora in preindustrial UM-UKCA simulations (Marshall et al., 2018) and as such, the importance of the simulation set-up remains unknown.

Despite the caveats, our results illustrate that there is a range of different eruption-realisations that are consistent with ice-core-derived sulfate deposition, with implications for reconstructions of historic volcanic radiative forcing and historical

climate model simulations (e.g. Schmidt et al., 2011) that did not consider such uncertainty. For example, reconstructions could be under- or over-estimating the volcanic aerosol RF by an amount that exceeds the magnitude of RF after the 1991 eruption of Mt. Pinatubo. Given that our parameter space was capped at SO_2 emissions of 100 Tg, the RF ranges presented in Table 4.1, except for the 266 CE deposition, are underestimated. Uncertainties in the RF of this magnitude could alter the efficacy of volcanic RF compared to other forcing drivers of climate.

Ultimately, the conclusions of this study are based on one model and future studies with other models should consider this approach to assess the uncertainty in RF derived from ice cores and in disentangling the importance of each eruption source parameter on the total deposited sulfate. The constrained eruption-realisations are ultimately dependent on the accuracy of the ice-core-derived sulfate deposition constraints. Further work that reduces this ice sheet sulfate deposition uncertainty would be invaluable in reducing the number of constrained eruption-realisations.

References

Ammann, C.M., Meehl, G.A., Washington, W.M. and Zender, C.S. 2003. A monthly and latitudinally varying volcanic forcing dataset in simulations of 20th century climate. *Geophysical Research Letters.* **30**(12), 1657.

Andersson, S.M., Martinsson, B.G., Vernier, J.P., Friberg, J., Brenninkmeijer, C.A.M., Hermann, M., van Velthoven, P.F.J. and Zahn, A. 2015. Significant radiative impact of volcanic aerosol in the lowermost stratosphere. *Nature Communications.* **6**, 7692.

Andrianakis, I. and Challenor, P.G. 2012. The effect of the nugget on Gaussian process emulators of computer models. *Computational Statistics & Data Analysis.* **56**(12), pp.4215-4228.

Aquila, V., Oman, L.D., Stolarski, R.S., Colarco, P.R. and Newman, P.A. 2012. Dispersion of the volcanic sulfate cloud from a Mount Pinatubo-like eruption. *Journal of Geophysical Research-Atmospheres.* **117**, D06216.

Arfeuille, F., Weisenstein, D., Mack, H., Rozanov, E., Peter, T. and Bronnimann, S. 2014. Volcanic forcing for climate modeling: a new microphysics-based data set covering years 1600-present. *Climate of the Past.* **10**(1), pp.359-375.

Carn, S.A., Clarisse, L. and Prata, A.J. 2016. Multi-decadal satellite measurements of global volcanic degassing. *Journal of Volcanology and Geothermal Research.* **311**, pp.99-134.

Castellano, E., Becagli, S., Hansson, M., Hutterli, M., Petit, J.R., Rampino, M.R., Severi, M., Steffensen, J.P., Traversi, R. and Udisti, R. 2005. Holocene volcanic history as recorded in the sulfate stratigraphy of the European Project for Ice Coring in Antarctica Dome C (EDC96) ice core. *Journal of Geophysical Research-Atmospheres.* **110**(D6), D06114.

Clausen, H.B. and Hammer, C.U. 1988. The Laki and Tambora eruptions as revealed in Greenland ice cores from 11 locations. *Annals of Glaciology.* **10**, pp.16-22.

Cole-Dai, J.H., Mosley-Thompson, E., Wight, S.P. and Thompson, L.G. 2000. A 4100-year record of explosive volcanism from an East Antarctica ice core. *Journal of Geophysical Research-Atmospheres.* **105**(D19), pp.24431-24441.

Crowley, T. and Unterman, M.B. 2013. Technical details concerning development of a 1200 yr proxy index for global volcanism. *Earth System Science Data.* **5**(1), pp.187-197.

Crowley, T., Zielinski, G., Vinther, B.M., Udisti, R., Kreutz, K., Cole-Dai, J. and Castellano, E. 2008. Volcanism and the little ice age. *PAGES Newsletter.* **16**, pp.22-23.

Devine, J.D., Sigurdsson, H., Davis, A.N. and Self, S. 1984. Estimates of sulfur and chlorine yield to the atmosphere from volcanic eruptions and potential climatic effects. *Journal of Geophysical Research.* **89**(NB7), pp.6309-6325.

Dhomse, S.S., Emmerson, K.M., Mann, G.W., Bellouin, N., Carslaw, K.S., Chipperfield, M.P., Hommel, R., Abraham, N.L., Telford, P., Braesicke, P., Dalvi, M., Johnson, C.E., O'Connor, F., Morgenstern, O., Pyle, J.A., Deshler, T., Zawodny, J.M. and Thomason, L.W. 2014. Aerosol microphysics simulations of the Mt. Pinatubo eruption with the UM-UKCA composition-climate model. *Atmospheric Chemistry and Physics.* **14**(20), pp.11221-11246.

Dutton, E.G. and Christy, J.R. 1992. Solar radiative forcing at selected locations and evidence for global lower tropospheric cooling following the eruptions of El Chichón and Pinatubo. *Geophysical Research Letters.* **19**(23), pp.2313-2316.

Ferris, D.G., Cole-Dai, J., Reyes, A.R. and Budner, D.M. 2011. South Pole ice core record of explosive volcanic eruptions in the first and second millennia A.D. and evidence of a large eruption in the tropics around 535 A.D. *Journal of Geophysical Research: Atmospheres.* **116**(D17), D17308.

Gao, C., Oman, L., Robock, A. and Stenchikov, G.L. 2007. Atmospheric volcanic loading derived from bipolar ice cores: Accounting for the spatial distribution of volcanic deposition. *Journal of Geophysical Research-Atmospheres.* **112**(D9), D09109.

Gao, C., Robock, A. and Ammann, C. 2008. Volcanic forcing of climate over the past 1500 years: An improved ice core-based index for climate models. *Journal of Geophysical Research-Atmospheres.* **113**(D23), D23111.

Hansen, J., Sato, M., Ruedy, R., Nazarenko, L., Lacis, A., Schmidt, G.A., Russell, G., Aleinov, I., Bauer, M., Bauer, S., Bell, N., Cairns, B., Canuto, V., Chandler, M., Cheng, Y., Del Genio, A., Faluvegi, G., Fleming, E., Friend, A., Hall, T., Jackman, C., Kelley, M., Kiang, N., Koch, D., Lean, J., Lerner, J., Lo, K., Menon, S., Miller, R., Minnis, P., Novakov, T., Oinas, V., Perlwitz, J., Perlwitz, J., Rind, D., Romanou, A., Shindell, D., Stone, P., Sun, S., Tausnev, N., Thresher, D., Wielicki, B., Wong, T., Yao, M. and Zhang, S. 2005. Efficacy of climate forcings. *Journal of Geophysical Research-Atmospheres.* **110**(D18), D18104.

Hegerl, G.C., Crowley, T.J., Allen, M., Hyde, W.T., Pollack, H.N., Smerdon, J. and Zorita, E. 2007. Detection of human influence on a new, validated 1500-year temperature reconstruction. *Journal of Climate.* **20**(4), pp.650-666.

Holton, J.R., Haynes, P.H., McIntyre, M.E., Douglass, A.R., Rood, R.B. and Pfister, L. 1995. Stratosphere-Troposphere Exchange. *Reviews of Geophysics.* **33**(4), pp.403-439.

Johnson, J.S., Cui, Z., Lee, L.A., Gosling, J.P., Blyth, A.M. and Carslaw, K.S. 2015. Evaluating uncertainty in convective cloud microphysics using statistical emulation. *Journal of Advances in Modeling Earth Systems.* **7**(1), pp.162-187.

Johnson, J.S., Gosling, J.P. and Kennedy, M.C. 2011. Gaussian process emulation for second-order Monte Carlo simulations. *Journal of Statistical Planning and Inference.* **141**(5), pp.1838-1848.

Jungclaus, J.H., Bard, E., Baroni, M., Braconnot, P., Cao, J., Chini, L.P., Egorova, T., Evans, M., Gonzalez-Rouco, J.F., Goosse, H., Hurtt, G.C., Joos, F., Kaplan, J.O., Khodri, M., Goldewijk, K.K., Krivova, N., LeGrande, A.N., Lorenz, S.J., Luterbacher, J., Man, W.M., Maycock, A.C., Meinshausen, M., Moberg, A., Muscheler, R., Nehrbass-Ahles, C., Otto-Bliesner, B.I., Phipps, S.J., Pongratz, J., Rozanov, E., Schmidt, G.A., Schmidt, H., Schmutz, W., Schurer, A., Shapiro, A.I., Sigl, M., Smerdon, J.E., Solanki, S.K., Timmreck, C., Toohey, M., Usoskin, I.G., Wagner, S., Wu, C.J., Yeo, K.L., Zanchettin, D., Zhang, Q. and Zorita, E. 2017. The PMIP4 contribution to CMIP6-Part 3: The last millennium, scientific objective, and experimental design for the PMIP4 past1000 simulations. *Geoscientific Model Development.* **10**(11), pp.4005-4033.

Kravitz, B. and Robock, A. 2011. Climate effects of high-latitude volcanic eruptions: Role of the time of year. *Journal of Geophysical Research-Atmospheres.* **116**, D01105.

Lacis, A., Hansen, J. and Sato, M. 1992. Climate forcing by stratospheric aerosols. *Geophysical Research Letters.* **19**(15), pp.1607-1610.

Lee, L.A., Carslaw, K.S., Pringle, K.J., Mann, G.W. and Spracklen, D.V. 2011. Emulation of a complex global aerosol model to quantify sensitivity to

uncertain parameters. *Atmospheric Chemistry and Physics.* **11**(23), pp.12253-12273.

Mann, G.W., Carslaw, K.S., Spracklen, D.V., Ridley, D.A., Manktelow, P.T., Chipperfield, M.P., Pickering, S.J. and Johnson, C.E. 2010. Description and evaluation of GLOMAP-mode: a modal global aerosol microphysics model for the UKCA composition-climate model. *Geoscientific Model Development.* **3**(2), pp.519-551.

Mann, G.W., Dhomse, S., Deshler, T., Timmreck, C., Schmidt, A., Neely, R. and Thomason, L. 2015. Evolving particle size is the key to improved volcanic forcings. *Past Global Changes Magazine.* **23**(2), pp.52-53.

Marshall, L., Johnson, J.S., Mann, G.W., Lee, L.A., Dhomse, S.S., Regayre, L., Yoshioka, M., Carslaw, K.S., Rigby, R. and Schmidt, A. under review. Exploring how eruption source parameters affect volcanic radiative forcing using statistical emulation. *Journal of Geophysical Research-Atmospheres.*

Marshall, L., Schmidt, A., Toohey, M., Carslaw, K.S., Mann, G.W., Sigl, M., Khodri, M., Timmreck, C., Zanchettin, D., Ball, W.T., Bekki, S., Brooke, J.S.A., Dhomse, S., Johnson, C., Lamarque, J.F., LeGrande, A.N., Mills, M.J., Niemeier, U., Pope, J.O., Poulain, V., Robock, A., Rozanov, E., Stenke, A., Sukhodolov, T., Tilmes, S., Tsigaridis, K. and Tummon, F. 2018. Multi-model comparison of the volcanic sulfate deposition from the 1815 eruption of Mt. Tambora. *Atmospheric Chemistry and Physics.* **18**(3), pp.2307-2328.

Metzner, D., Kutterolf, S., Toohey, M., Timmreck, C., Niemeier, U., Freundt, A. and Kruger, K. 2014. Radiative forcing and climate impact resulting from SO2 injections based on a 200,000-year record of Plinian eruptions along the Central American Volcanic Arc. *International Journal of Earth Sciences.* **103**(7), pp.2063-2079.

Morgenstern, O., Braesicke, P., O'Connor, F.M., Bushell, A.C., Johnson, C.E., Osprey, S.M. and Pyle, J.A. 2009. Evaluation of the new UKCA climate-composition model - Part 1: The stratosphere. *Geoscientific Model Development.* **2**(1), pp.43-57.

Morris, M.D. and Mitchell, T.J. 1995. Exploratory designs for computational experiments. *Journal of Statistical Planning and Inference.* **43**(3), pp.381-402.

Myhre, G., Shindell, D., Bréon, F.-M., Collins, W., Fuglestvedt, J., Huang, J., Koch, D., Lamarque, J.-F., Lee, D., Mendoza, B., Nakajima, T., Robock, A., Stephens, G., Takemura, T. and Zhang, H. 2013. Anthropogenic and Natural Radiative Forcing. In: Stocker, T.F., et al. eds. *Climate Change 2013: The Physical Science Basis. Contribution of Working Group I to the Fifth Assessment Report of the Intergovernmental Panel on Climate Change.* Cambridge, United Kingdom and New York, NY, USA.: Cambridge University Press.

O'Connor, F.M., Johnson, C.E., Morgenstern, O., Abraham, N.L., Braesicke, P., Dalvi, M., Folberth, G.A., Sanderson, M.G., Telford, P.J., Voulgarakis, A., Young, P.J., Zeng, G., Collins, W.J. and Pyle, J.A. 2014. Evaluation of the new UKCA climate-composition model - Part 2: The Troposphere. *Geoscientific Model Development.* **7**(1), pp.41-91.

O'Hagan, A. 2006. Bayesian analysis of computer code outputs: A tutorial. *Reliability Engineering & System Safety.* **91**(10-11), pp.1290-1300.

Oppenheimer, C. 2003. Ice core and palaeoclimatic evidence for the timing and nature of the great mid-13th century volcanic eruption. *International Journal of Climatology.* **23**(4), pp.417-426.

Osprey, S.M., Gray, L.J., Hardiman, S.C., Butchart, N. and Hinton, T.J. 2013. Stratospheric Variability in Twentieth-Century CMIP5 Simulations of the Met Office Climate Model: High Top versus Low Top. *Journal of Climate.* **26**(5), pp.1595-1606.

Pinto, J.P., Turco, R.P. and Toon, O.B. 1989. Self-limiting physical and chemical effects in volcanic eruption clouds. *Journal of Geophysical Research-Atmospheres.* **94**(D8), pp.11165-11174.

Punge, H.J., Konopka, P., Giorgetta, M.A. and Muller, R. 2009. Effects of the quasi-biennial oscillation on low-latitude transport in the stratosphere derived from trajectory calculations. *Journal of Geophysical Research-Atmospheres.* **114**, D03102.

R Core Team. 2017. *R: A language and environment for statistical computing. R Foundation for Statistical Computing.* Vienna, Austria. Available at https://www.R-project.org/.

Reynolds, R.W., Smith, T.M., Liu, C., Chelton, D.B., Casey, K.S. and Schlax, M.G. 2007. Daily high-resolution-blended analyses for sea surface temperature. *Journal of Climate.* **20**(22), pp.5473-5496.

Robock, A. and Free, M.P. 1995. Ice cores as an index of global volcanism from 1850 to the present. *Journal of Geophysical Research-Atmospheres.* **100**(D6), pp.11549-11567.

Roustant, O., Ginsbourger, D. and Deville, Y. 2012. DiceKriging, DiceOptim: Two R Packages for the Analysis of Computer Experiments by Kriging-Based Metamodeling and Optimization. *Journal of Statistical Software.* **51**(1), pp.1-55.

Salter, J.M. and Williamson, D. 2016. A comparison of statistical emulation methodologies for multi-wave calibration of environmental models. *Environmetrics.* **27**(8), pp.507-523.

Sato, M., Hansen, J.E., McCormick, M.P. and Pollack, J.B. 1993. Stratospheric Aerosol Optical Depths, 1850-1990. *Journal of Geophysical Research-Atmospheres.* **98**(D12), pp.22987-22994.

Scaillet, B.J., Luhr, F., Carroll, M.R. . 2003. Petrological and volcanological constraints on volcanic sulfur emissions to the atmosphere. In: Robock, A. and Oppenheimer, C. eds. *Volcanism and the Earth's Atmosphere.* Washington D. C.: AGU, pp.11–40.

Schmidt, A., Carslaw, K.S., Mann, G.W., Wilson, M., Breider, T.J., Pickering, S.J. and Thordarson, T. 2010. The impact of the 1783-1784 AD Laki eruption on global aerosol formation processes and cloud condensation nuclei. *Atmospheric Chemistry and Physics.* **10**(13), pp.6025-6041.

Schmidt, G.A., Jungclaus, J.H., Ammann, C.M., Bard, E., Braconnot, P., Crowley, T.J., Delaygue, G., Joos, F., Krivova, N.A., Muscheler, R., Otto-Bliesner, B.L., Pongratz, J., Shindell, D.T., Solanki, S.K., Steinhilber, F. and Vieira, L.E.A. 2011. Climate forcing reconstructions for use in PMIP simulations of the last millennium (v1.0). *Geoscientific Model Development.* **4**(1), pp.33-45.

Self, S., Gertisser, R., Thordarson, T., Rampino, M.R. and Wolff, J.A. 2004. Magma volume, volatile emissions, and stratospheric aerosols from the 1815 eruption of Tambora. *Geophysical Research Letters.* **31**(20), L20608.

Seviour, W.J.M., Butchart, N. and Hardiman, S.C. 2012. The Brewer-Dobson circulation inferred from ERA-Interim. *Quarterly Journal of the Royal Meteorological Society.* **138**(665), pp.878-888.

Sigl, M., McConnell, J.R., Toohey, M., Curran, M., Das, S.B., Edwards, R., Isaksson, E., Kawamura, K., Kipfstuhl, S., Kruger, K., Layman, L., Maselli, O.J.,

Motizuki, Y., Motoyama, H., Pasteris, D.R. and Severi, M. 2014. Insights from Antarctica on volcanic forcing during the Common Era. *Nature Climate Change.* **4**(8), pp.693-697.

Sigl, M., Winstrup, M., McConnell, J.R., Welten, K.C., Plunkett, G., Ludlow, F., Buntgen, U., Caffee, M., Chellman, N., Dahl-Jensen, D., Fischer, H., Kipfstuhl, S., Kostick, C., Maselli, O.J., Mekhaldi, F., Mulvaney, R., Muscheler, R., Pasteris, D.R., Pilcher, J.R., Salzer, M., Schupbach, S., Steffensen, J.P., Vinther, B.M. and Woodruff, T.E. 2015. Timing and climate forcing of volcanic eruptions for the past 2,500 years. *Nature.* **523**(7562), pp.543–549.

Stothers, R.B. 1984. The Great Tambora Eruption in 1815 and Its Aftermath. *Science.* **224**(4654), pp.1191-1198.

Stothers, R.B. 1996. Major optical depth perturbations to the stratosphere from volcanic eruptions: Pyrheliometric period, 1881-1960. *Journal of Geophysical Research-Atmospheres.* **101**(D2), pp.3901-3920.

Stothers, R.B. 2001. Major optical depth perturbations to the stratosphere from volcanic eruptions: Stellar extinction period, 1961-1978. *Journal of Geophysical Research-Atmospheres.* **106**(D3), pp.2993-3003.

Timmreck, C., Graf, H.F., Lorenz, S.J., Niemeier, U., Zanchettin, D., Matei, D., Jungclaus, J.H. and Crowley, T.J. 2010. Aerosol size confines climate response to volcanic super-eruptions. *Geophysical Research Letters.* **37**, L24705.

Toohey, M., Kruger, K., Bittner, M., Timmreck, C. and Schmidt, H. 2014. The impact of volcanic aerosol on the Northern Hemisphere stratospheric polar vortex: mechanisms and sensitivity to forcing structure. *Atmospheric Chemistry and Physics.* **14**(23), pp.13063-13079.

Toohey, M., Kruger, K., Niemeier, U. and Timmreck, C. 2011. The influence of eruption season on the global aerosol evolution and radiative impact of tropical volcanic eruptions. *Atmospheric Chemistry and Physics.* **11**(23), pp.12351-12367.

Toohey, M., Kruger, K., Sigl, M., Stordal, F. and Svensen, H. 2016a. Climatic and societal impacts of a volcanic double event at the dawn of the Middle Ages. *Climatic Change.* **136**(3-4), pp.401-412.

Toohey, M., Kruger, K. and Timmreck, C. 2013. Volcanic sulfate deposition to Greenland and Antarctica: A modeling sensitivity study. *Journal of Geophysical Research-Atmospheres.* **118**(10), pp.4788-4800.

Toohey, M. and Sigl, M. 2017. Volcanic stratospheric sulfur injections and aerosol optical depth from 500 BCE to 1900 CE. *Earth System Science Data.* **9**(2), pp.809-831.

Toohey, M., Stevens, B., Schmidt, H. and Timmreck, C. 2016b. Easy Volcanic Aerosol (EVA v1.0): an idealized forcing generator for climate simulations. *Geoscientific Model Development.* **9**(11), pp.4049-4070.

Trepte, C.R. and Hitchman, M.H. 1992. Tropical stratospheric circulation deduced from satellite aerosol data. *Nature.* **355**(6361), pp.626-628.

Vidal, C.M., Metrich, N., Komorowski, J.C., Pratomo, I., Michel, A., Kartadinata, N., Robert, V. and Lavigne, F. 2016. The 1257 Samalas eruption (Lombok, Indonesia): the single greatest stratospheric gas release of the Common Era. *Scientific Reports.* **6**, 34868.

Wigley, T.M.L., Ammann, C.M., Santer, B.D. and Raper, S.C.B. 2005. Effect of climate sensitivity on the response to volcanic forcing. *Journal of Geophysical Research-Atmospheres.* **110**(D9), D09107.

Williamson, D., Blaker, A.T., Hampton, C. and Salter, J. 2015. Identifying and removing structural biases in climate models with history matching. *Climate Dynamics.* **45**(5-6), pp.1299-1324.

Chapter 5 Discussion and conclusions

The overall aim of this thesis was to understand the radiative forcing and sulfate deposition following large-magnitude explosive volcanic eruptions that affect the stratosphere. The research presented in this thesis, through three publications, has advanced knowledge of how different eruptions affect the Earth's radiative balance and of the relationship between volcanic sulfate deposited on polar ice sheets and the radiative forcing.

The research in this thesis has been facilitated by the use of state-of-the-art interactive stratospheric aerosol models and Gaussian process emulators used to replace the UM-UKCA model (Section 1.6.2). Paper 1 (Chapter 2) (Marshall et al., 2018) conducted the first multi-model comparison of sulfate deposition following an explosive eruption. In paper 2 (Chapter 3), the first comprehensive investigation of the role of different eruption source parameters on the time-integrated global mean sAOD and radiative forcing was conducted. Finally, paper 3 (Chapter 4) investigated the uncertainty in radiative forcing derived from ice sheet sulfate deposition. This paper is the first to consider the range of eruption-realisations that are consistent with measured sulfate deposition, and to calculate radiative forcing independently of transfer functions. In the following chapter, the three publications and their results are discussed in context of each other and in context of the aims and research questions outlined in Section 1.5. Identified future work and concluding remarks follow.

Unless otherwise stated, sAOD and radiative forcing refer to the time-integrated global mean diagnostics investigated within this thesis.

5.1 Summary of key results

The conclusions of this thesis across the three publications and in context of the aims and research questions outlined in Section 1.5 are:

1. **The separate and combined effects of eruption source parameters including the SO_2 emission, injection height, latitude and eruption season on ~3-year integrated global mean stratospheric Aerosol Optical Depth (sAOD) and ~3-year integrated global mean radiative forcing have been investigated using the UM-UKCA interactive stratospheric aerosol model and Gaussian process emulation.**
    a) Statistical emulation has been successfully used to explore the joint effects of eruption source parameters on sAOD and radiative forcing across a large range of SO_2 emission magnitudes (10 Tg to 100 Tg), latitudes (80ºS to 80ºN) and injection heights (15 km to 25 km). Statistical emulation facilitated an investigation of the whole co-varying parameter space, based on only 30 runs of UM-UKCA, and enabled the variance in model output to be quantified and attributed to the eruption source parameters (Section 3.3.2.3). The emulators were used to predict the sulfate e-folding decay time, sAOD and radiative forcing of eruptions within the parameter ranges and can be used to find the eruptions that lead to a particular volcanic response, often with a wide range of possible eruption-realisations. For example, an eruption leading to 3-year integrated sAOD 3 times that of 1991 Mt. Pinatubo could be situated between ~80°S and ~67°N, provided the SO_2 emission was greater than 56 Tg (Section 3.3.3.2).
    b) Chapter 3 quantified the separate and combined effects of eruption source parameters over wide parameter ranges, while previous modelling studies have investigated the effects of parameters in isolation and often focused on specific ‘Pinatubo-like’ case studies. As such, important interactions between parameters have been identified, which has not been possible in previous studies (e.g. Toohey et al., 2011; Aquila et al., 2012; English et al., 2013; Toohey et al., 2013). Chapter 3 showed that the sAOD and radiative forcing increase as the SO_2 emission increases, as the latitude decreases and on average across

the parameter space, as the injection height increases up to ~20 km. After ~20 km an increase in injection height acts to reduce the sAOD and radiative forcing, a result that is in contrast to previous studies (e.g. Jones et al., 2017) that do not account for aerosol growth (Section 3.3.2). The injection height has a stronger influence on the sAOD and radiative forcing for tropical eruptions compared to high-latitude eruptions because of sub-tropical transport barriers and a longer aerosol lifetime. The emulators describe the response to parameters over their continuous range and reveal larger radiative forcing for eruptions in the winter hemisphere (Sections 3.3.2 and 4.3.3, Figure D.7).

c) For eruptions occurring in July, the SO_2 emission is the most important parameter in determining the radiative response, contributing to 72% of the variance in sAOD and 63% of the variance in radiative forcing. In contrast, the latitude contributes the most (60%) to the variance in the sulfate e-folding decay time. Compared to the latitude and the SO_2 emission, the injection height is relatively the least important parameter, contributing to less than 5% of the variance in each model output (Section 3.3.2.3). This paper is the first to have quantified these contributions.

2. **Uncertainties in historic volcanic radiative forcing reconstructions based on volcanic sulfate deposited on polar ice sheets have been investigated using multiple models and perturbed parameter ensembles of a single model.**

   a) Simulated sulfate deposition following the 1815 eruption of Mt. Tambora differs considerably between four interactive stratospheric aerosol models (CESM1(WACCM), MAECHAM5-HAM, SOCOL-AER and UM-UKCA) (Chapter 2). Burden-to-deposition factors, relating ice sheet sulfate to atmospheric sulfate burdens ('transfer functions'), differ considerably between the models by up to a factor of 15 (Section 2.3.3). These results suggest uncertainty in the relationship between the two quantities in models and therefore in deriving atmospheric burdens from ice sheet deposition, which are used to estimate volcanic aerosol radiative forcing. Compared to ice

core composites for each ice sheet, simulated deposition was ~2 times too small in UM-UKCA, ~2 times too large in Greenland in CESM1(WACCM), and ~3-5 times too large on both ice sheets for MAECHAM5-HAM and SOCOL-AER (Section 2.3.3). Reasons for the model-observation discrepancies include:

i. Model deficiencies in the formation of volcanic aerosol related to oxidation of SO_2 by OH, the stratospheric transport related to the model resolution and simulation of the QBO, the stratosphere-troposphere exchange due to large-scale dynamics and aerosol sedimentation and limitations in the deposition parameterizations.

ii. Uncertainties in the ice core measurements due to spatial variability in sulfate deposition fluxes on ice sheets and difficulties in isolating volcanic signals from ice core sulfate records.

iii. Uncertainties in the eruption source parameters used to initialize the eruption such as the mass of SO_2 emitted (60 Tg), which will determine the amount of sulfate aerosol formed. Chapter 4 investigated this uncertainty directly by examining the range in eruption-realisations (in UM-UKCA only) that could be consistent with the sulfate deposition deduced from ice cores for the 1815 Mt. Tambora eruption, and found that in the UM-UKCA model the emission had to be more than 96 Tg SO_2.

b) Chapter 4 investigated the relationship between the eruption source parameters and the ice sheet sulfate deposition using two UM-UKCA perturbed parameter ensembles (for January and July eruptions) and statistical emulators built from the model output of these simulations. The time-integrated ice-sheet sulfate deposition anomalies are dependent on the SO_2 emission magnitude and the latitude of eruption (higher for larger SO_2 emissions and eruptions closer to the ice sheet), but relatively independent of the injection height. The deposition is also seasonally dependent, with stronger transport of aerosol to the winter hemisphere and consequently higher deposition on the winter

ice sheet following tropical eruptions. For eruptions at other latitudes, emulated response surfaces reveal variable responses related to seasonally-varying stratospheric transport and transport barriers such as the polar vortex (Section 4.3.1).

c) A wide range of eruption-realisations (i.e. eruptions with different SO_2 emissions, latitudes and either in January or July) led to ice sheet deposited sulfate consistent with ice-core-derived estimates for each of the top 10 bipolar sulfate deposition signals in the last 2500 years (Sigl et al., 2015). SO_2 emissions ranged by up to 55 Tg, latitude by up to 89° and injection height by 10 km (sections 4.3.2-4.3.3). Therefore, single eruption-realisations cannot be accurately identified from ice core sulfate records. Constrained SO_2 emissions are in general higher than previous estimates derived using transfer functions (Toohey and Sigl, 2017), however the discrepancy could also be related to a low-bias in the UM-UKCA deposition (~2 times too small, conclusion 2a), which warrants further investigation.

d) The ice-core-consistent eruption-realisations have a range in time-integrated global mean radiative forcing due to differences in their SO_2 emissions, latitudes and injection heights as demonstrated in Chapter 3. The range in ~3-year integrated radiative forcing across each set of constrained eruption realisations for the top 10 bipolar deposition signals is greater than ~300 MJ m^{-2}, exceeding the magnitude of the time-integrated forcing following the 1991 Mt. Pinatubo eruption (between -133 MJ m^{-2} and -229 MJ m^{-2}) (Section 4.3.3). Therefore, there is potentially a large uncertainty in the radiative forcing in previous reconstructions that do not consider the full range of consistent eruption-realisations and as such the results presented in this thesis suggest that radiative forcing cannot be accurately constrained from ice sheet records. As the relationship between sulfate burden and ice sheet deposition is also model dependent (conclusion 2a), ranges in radiative forcing constrained from ice sheet deposition in other models could be significantly different to those presented here, further illustrating the uncertainties in deriving volcanic aerosol radiative forcing from ice core sulfate records.

5.2 Research implications

5.2.1 Understanding the role of eruption source parameters

The evolution of volcanic sulfate aerosol and its radiative effects are complex (Section 1.2) and previous studies are limited because they do not include interactive sulfur chemistry (e.g. Toohey et al., 2011; 2013), interactive aerosol microphysical processes (e.g. Oman et al., 2006; Kravitz and Robock, 2011; Aquila et al., 2012; Jones et al., 2017), radiatively coupled aerosol (English et al., 2013; Arfeuille et al., 2014; Dhomse et al., 2014), or a QBO (Toohey et al., 2011; English et al., 2013; Toohey et al., 2013; Arfeuille et al., 2014; Toohey et al., 2016). UM-UKCA includes these processes and the research presented in this thesis offers substantial new information on how explosive eruptions affect radiative forcing and sulfate deposition. The results have illustrated the importance of co-variations in parameters (conclusion 1b), with differences in the radiative impact of eruptions dependent on the interacting and relative effects of the sulfate aerosol particle growth, large-scale transport, sedimentation and seasonally-varying insolation. Ultimately, this research has provided a better understanding of the forcing efficacy of volcanic SO_2.

Another key innovation in this thesis is the use of statistical emulators, which can be used to ask questions such as: What if the eruption of Mt. Pinatubo had injected 100 Tg of SO_2 into the stratosphere instead of 10 Tg or what if the eruption had been at a different latitude with a different injection height? The emulators negate the need for further computationally-expensive simulations and the answers to these questions can be obtained in a matter of seconds by using the online tool provided as a supplement to Chapter 3, available at: 'https://www.see.leeds.ac.uk/see-research/icas/volcanic_forcing_online_tool/'. This functionality could be used to estimate the magnitude of the forcing that could occur following a future eruption as soon as the initial eruption source parameters have been measured.

5.2.2 Uncertainties in volcanic aerosol radiative forcing

The large uncertainty in volcanic aerosol radiative forcing derived from ice core sulfate records demonstrated in both Chapters 2 and 4 has substantial implications for climate model simulations using previously derived reconstructions by Gao et al. (2008), Crowley and Unterman (2013) and Toohey and Sigl (2017) (Section 1.4). These reconstructions are derived using transfer functions based on limited

observations (from nuclear bomb tests and that following the 1991 eruption of Mt. Pinatubo) and limited model simulations (Gao et al., 2007). The results in Chapter 4 demonstrate that there is a much larger range in possible transfer functions given a range in eruption-realisations that are consistent with measured deposition than previously considered (e.g. Gao et al., 2008; Toohey and Sigl, 2017). Some of the range in eruption-realisations is also because the uncertainty on the ice core composites (Sigl et al., 2015) was included during constraint, which on the other hand, may mean that some of the transfer functions could be similar despite different SO_2 emissions. The constrained eruption-realisations in Chapter 4 also demonstrated that the ice sheet deposition was relatively independent of the height of the SO_2 emissions, but injection height had an important role in determining the radiative forcing especially for tropical eruptions (Chapter 3). The injection height is not considered in any of the current volcanic forcing timeseries. Models with aerosol microphysics schemes that use the reconstructed SO_2 emissions and derive their own radiative forcing have to assume an injection height (e.g. Arfeuille et al., 2014) but the results presented in this thesis illustrate that this will affect the radiative forcing. In Chapter 4, the radiative forcing was calculated interactively within UM-UKCA consistent with the aerosol mass and particle size distribution, in contrast to the scaling factors between aerosol mass, sAOD and radiative forcing described in Section 4.1. These relationships in the model could be explored in future work.

If the volcanic aerosol radiative forcing is incorrect in climate models, the efficacy of volcanic forcing and that of other forcing agents may be wrongly calculated (e.g. Atwood et al., 2016). The efficacy is important for understanding the role of explosive eruptions on climate variability compared to other forcing agents such as land use changes, greenhouse gas concentrations and solar radiation, ultimately with the aim of separating and attributing anthropogenic forcing and natural forcing. The wide range in possible radiative forcing discovered in Chapter 4 may also help to explain why simulated volcanic cooling is overestimated compared to tree-ring reconstructions because the modelled forcing may be too high (e.g. Wilson et al., 2016, Section 1.4.3).

The results in Chapter 4 also demonstrate the difficulties in identifying possible eruption locations (and other parameters) responsible for the unidentified eruptions deduced from volcanic sulfate anomalies in ice cores. If tephra is discovered that can be linked to specific volcanoes, which constrains the latitude, a smaller range in

plausible SO_2 emissions, heights and season, and consequently radiative forcing could be deduced from the emulators.

5.3 Limitations and recommendations for future work

5.3.1 An extended perturbed parameter ensemble

This research has demonstrated that statistical emulation is a powerful tool for investigating the effects of multiple eruption source parameter perturbations on the radiative forcing and sulfate deposition following explosive eruptions. However, the research presented in this thesis examined only a three-dimensional parameter space. There are many other factors in addition to the SO_2 emission, latitude and injection height that may influence the radiative forcing of an eruption and the sulfate deposition, such as the injection depth, which was fixed at 3 km in this study, and the phase of the QBO, which was easterly in all simulations. Spreading the emissions over a larger altitude range, and similarly over different durations (in all simulations the eruptions occurred over 24 hours) may alter the rate of SO_2 oxidation depending on the OH concentrations and the subsequent nucleation and condensation of sulfate aerosol particles, resulting in changes to the aerosol particle size distribution and the aerosol scattering efficiency (Section 1.2.3). The role of injection depth in comparison to the injection height remains to be assessed. Studies have demonstrated that the phase of the QBO modulates the meridional transport of tropical sulfate aerosol (Trepte and Hitchman, 1992; Punge et al., 2009; Thomas et al., 2009; Visioni et al., 2018) and affects the strength of the polar vortex (Holton and Tan, 1980). Perturbing these additional parameters may affect the importance of the three eruption source parameters presented in this study and that of the eruption season.

Chapter 4 found that in order to simulate polar sulfate deposition using UM-UKCA that was consistent with the largest ice-core-derived sulfate measurements in the past 2500 years (Sigl et al., 2015), eruptions had SO_2 emissions at the upper end of the perturbed parameter space, which were capped at 100 Tg. Extending the range of SO_2 emissions would enable the full range of eruption-realisations to be constrained. Similarly, extending the parameter space to cover SO_2 emissions that are less than 10 Tg but still climatically-relevant such as the eruptions of Mt. Agung (1963) and El Chichón (1982) that emitted ~5-10 Tg SO_2 (Timmreck et al., 2018 and references therein), would be an important extension to this work. The work presented in this

thesis focussed on eruptions that injected SO_2 directly into the stratosphere, but lower-altitude injections into the upper troposphere can still enhance the stratospheric sulfate aerosol layer following tropical upwelling, lofting and potentially transport via the Asian monsoon (e.g. Bourassa et al., 2012). Extending the injection height range to include upper-troposphere injections would likely result in an increase in the importance of injection height relative to the other parameters presented in Chapter 3 because of the contrasting lifetime of aerosol in the troposphere (shorter-lived) versus the stratosphere (longer-lived).

Future perturbed parameter ensembles could also consider meteorological ensembles to test the sensitivity of these results to initial conditions and to the assumptions made when attempting to account for this issue by adding noise variance to the emulator builds in Chapter 4. Although the global and integrated metrics are not expected to be strongly dependent on the meteorology, additional simulations would allow this variability to be quantified. Additional simulations could also be used to explore and assess the emulator fits, although this ultimately defeats the point of using emulation. For example, by identifying whether particular features (e.g. curves and wiggles) in the emulated surfaces such as between the deposition and forcing between the two seasons are real, and especially at the edge of parameter space where there are fewer training runs and the uncertainty in the emulator prediction grows. Emulator uncertainties could be further assessed in a more detailed statistical study that explores the sensitivity of the fits to assumptions used to build the emulators such as the covariance and mean functions and noise variance values.

5.3.2 Regional, peak and dynamical responses

There is a wealth of information available from the two ensembles of simulations that remains to be exploited. Chapter 3 focussed on global mean quantities for three model outputs; the average sulfate e-folding decay time and the 38-month time-integrated sAOD and radiative forcing. However, regional averages, peak responses and integrated metrics over different periods, will have different dependencies on the eruption source parameters.

Quantifying the aerosol radiative heating and dynamical responses such as a stronger polar vortex following tropical eruptions (e.g. Toohey et al., 2013; 2014; Bittner et al., 2016) could also aid in the interpretation of the parameter dependencies discovered in Chapter 3 and the variation in polar sulfate deposition in Chapter 4. In

geoengineering simulations of continuous SO_2 emissions, studies have also illustrated that radiative heating by tropical sulfate aerosol can weaken and even break down the QBO (Aquila et al., 2014; Niemeier and Schmidt, 2017; Kleinschmitt et al., 2018; Visioni et al., 2018). Whether a single explosive eruption could have a significant effect on the QBO remains to be determined.

5.3.3 Investigating the role of eruption season

The range of available simulations provides an exciting opportunity to investigate other processes between the eruptions such as the SO_2 oxidation rate and also the aerosol particle size distribution, which may be important for understanding the role of eruption season. Studies that have varied the eruption season have focussed on either high-latitude (e.g. Kravitz and Robock, 2011) or low-latitude eruptions (Toohey et al., 2011; Aquila et al., 2012; Toohey et al., 2013; Stoffel et al., 2015; Stevenson et al., 2017) (Section 1.3.3) and therefore the ensemble simulations lend themselves to a more comprehensive investigation.

The results presented in this thesis suggest that the seasonal response is complicated and dependent on the exact combinations of other eruption source parameters (Figure D.7). The results presented by Kravitz and Robock (2011) (stronger SW anomalies following NH summer eruptions) and Toohey et al. (2011) (stronger SW anomalies following a Pinatubo-sized tropical eruption in NH winter) are limited to these case-studies and may not be consistent with other values of SO_2 emissions, latitude and injection height, especially given changes to the aerosol particle size distribution, which was not considered by Kravitz and Robock (2011).

5.3.4 Coupled atmosphere-ocean simulations

The UM-UKCA simulations were run in an atmosphere-only mode and subsequently the climatic effects of eruptions such as changes to temperature and precipitation cannot be reliably diagnosed. An ensemble of fully-coupled atmosphere-ocean simulations using the UK Earth System Model (UKESM) would provide these additional climate impacts, which could also be used to constrain the eruption source parameters for historic eruptions from temperature and precipitation proxies, in addition to polar sulfate deposition constraints (Chapter 4). Additionally, fully-coupled simulations could be used to investigate the climatic impacts of a cluster of eruptions, which may cause sustained cooling (Miller et al., 2012; Lehner et al., 2013; McGregor et al., 2015) and to assess impacts on variability modes such as the NAO

and ENSO (e.g. Pausata et al., 2015; Swingedouw et al., 2017) and longer-term impacts following single eruptions. For example, Zanchettin et al. (2013) suggested that the thermal inertia of the ocean and ocean-atmosphere feedbacks can cause delayed responses beyond the initial radiative forcing; they find a positive NAO phase and winter warming over Europe one decade after a major tropical eruption. However, fully-coupled and interactive atmosphere-ocean simulations are more computationally-expensive, and simulations would need to be run for long integrations. Additionally, there would be increased variability associated with the initial conditions because of variability modes such as ENSO.

5.3.5 Assessing model uncertainties

Chapter 2 demonstrated that four interactive stratospheric aerosol models failed to produce the magnitude of sulfate deposition following the 1815 eruption of Mt. Tambora compared to ice-core-derived estimates. Whether this is because of incorrect eruption source parameters used to initialize the eruption (Chapter 4) or model limitations, remains to be determined. Although the Interactive Stratospheric Aerosol Modelling Intercomparison Project (ISA-MIP) (Timmreck et al., 2018) will provide further inter-model comparisons, only another major volcanic eruption that can be well observed with modern instruments will validate our understanding of aerosol microphysical processes and aerosol transport. Reducing the uncertainty on ice sheet sulfate deposition composites will also allow eruptions to be more tightly constrained.

Future work could also consider the injection of other gases in addition to SO_2 when simulating explosive eruptions such as H_2S, HCl and HF to assess the impact on atmospheric chemistry and stratospheric ozone concentrations, and also the co-injection of ash, which can scavenge SO_2 from the volcanic plume (e.g. Guo et al., 2004). In the UM-UKCA simulations the aerosol surface area is prescribed in the chemistry scheme and therefore heterogeneous chemistry is not accelerated following the eruptions, which for example would affect ozone concentrations. It is not expected that the lack of this process will cause significant differences in the resultant time-integrated and global model outputs assessed in this thesis, however, sensitivity studies in a future UM-UKCA version should investigate this assumption.

5.4 Concluding remarks

The results presented in this thesis have advanced knowledge of how volcanic radiative forcing and ice sheet sulfate deposition following a stratospheric eruption are dependent on the mass of SO_2 emitted, the injection height and the latitude, and most importantly, how they are dependent on the co-variations of these eruption source parameters. This thesis has also identified significant uncertainties in the radiative forcing of eruptions derived from sulfate measured in ice cores with implications for volcanic aerosol radiative forcing reconstructions. Ultimately, these results will aid in both assessing the impact of future eruptions and in understanding the radiative forcing of past eruptions. Finally, this research has demonstrated the feasibility and power of building statistical emulators to represent model output by describing the covarying effects of the eruption source parameters and increasing the amount of parameter space that can otherwise be explored.

References

Aquila, V., Garfinkel, C.I., Newman, P.A., Oman, L.D. and Waugh, D.W. 2014. Modifications of the quasi-biennial oscillation by a geoengineering perturbation of the stratospheric aerosol layer. *Geophysical Research Letters.* **41**(5), pp.1738-1744.

Aquila, V., Oman, L.D., Stolarski, R.S., Colarco, P.R. and Newman, P.A. 2012. Dispersion of the volcanic sulfate cloud from a Mount Pinatubo-like eruption. *Journal of Geophysical Research-Atmospheres.* **117**, D06216.

Arfeuille, F., Weisenstein, D., Mack, H., Rozanov, E., Peter, T. and Bronnimann, S. 2014. Volcanic forcing for climate modeling: a new microphysics-based data set covering years 1600-present. *Climate of the Past.* **10**(1), pp.359-375.

Atwood, A.R., Wu, E., Frierson, D.M.W., Battisti, D.S. and Sachs, J.P. 2016. Quantifying Climate Forcings and Feedbacks over the Last Millennium in the CMIP5-PMIP3 Models. *Journal of Climate.* **29**(3), pp.1161-1178.

Bittner, M., Timmreck, C., Schmidt, H., Toohey, M. and Kruger, K. 2016. The impact of wave-mean flow interaction on the Northern Hemisphere polar vortex after tropical volcanic eruptions. *Journal of Geophysical Research-Atmospheres.* **121**(10), pp.5281-5297.

Bourassa, A.E., Robock, A., Randel, W.J., Deshler, T., Rieger, L.A., Lloyd, N.D., Llewellyn, E.J. and Degenstein, D.A. 2012. Large Volcanic Aerosol Load in the Stratosphere Linked to Asian Monsoon Transport. *Science.* **337**(6090), pp.78-81.

Crowley, T. and Unterman, M.B. 2013. Technical details concerning development of a 1200 yr proxy index for global volcanism. *Earth System Science Data.* **5**(1), pp.187-197.

Dhomse, S.S., Emmerson, K.M., Mann, G.W., Bellouin, N., Carslaw, K.S., Chipperfield, M.P., Hommel, R., Abraham, N.L., Telford, P., Braesicke, P., Dalvi, M., Johnson, C.E., O'Connor, F., Morgenstern, O., Pyle, J.A., Deshler, T., Zawodny, J.M. and Thomason, L.W. 2014. Aerosol microphysics simulations of the Mt. Pinatubo eruption with the UM-UKCA composition-climate model. *Atmospheric Chemistry and Physics.* **14**(20), pp.11221-11246.

English, J.M., Toon, O.B. and Mills, M.J. 2013. Microphysical simulations of large volcanic eruptions: Pinatubo and Toba. *Journal of Geophysical Research-Atmospheres.* **118**(4), pp.1880-1895.

Gao, C., Oman, L., Robock, A. and Stenchikov, G.L. 2007. Atmospheric volcanic loading derived from bipolar ice cores: Accounting for the spatial distribution of volcanic deposition. *Journal of Geophysical Research-Atmospheres.* **112**(D9), D09109.

Gao, C., Robock, A. and Ammann, C. 2008. Volcanic forcing of climate over the past 1500 years: An improved ice core-based index for climate models. *Journal of Geophysical Research-Atmospheres.* **113**(D23), D23111.

Guo, S., Rose, W.I., Bluth, G.J.S. and Watson, I.M. 2004. Particles in the great Pinatubo volcanic cloud of June 1991: The role of ice. *Geochemistry Geophysics Geosystems.* **5**, Q05003.

Holton, J.R. and Tan, H.C. 1980. The Influence of the Equatorial Quasi-Biennial Oscillation on the Global Circulation at 50 mb. *Journal of the Atmospheric Sciences.* **37**(10), pp.2200-2208.

Jones, A.C., Haywood, J.M., Dunstone, N., Emanuel, K., Hawcroft, M.K., Hodges, K.I. and Jones, A. 2017. Impacts of hemispheric solar geoengineering on tropical cyclone frequency. *Nature Communications.* **8**(1), 1382.

Kleinschmitt, C., Boucher, O. and Platt, U. 2018. Sensitivity of the radiative forcing by stratospheric sulfur geoengineering to the amount and strategy of the SO2 injection studied with the LMDZ-S3A model. *Atmospheric Chemistry and Physics.* **18**(4), pp.2769-2786.

Kravitz, B. and Robock, A. 2011. Climate effects of high-latitude volcanic eruptions: Role of the time of year. *Journal of Geophysical Research-Atmospheres.* **116**, D01105.

Lehner, F., Born, A., Raible, C.C. and Stocker, T.F. 2013. Amplified Inception of European Little Ice Age by Sea Ice-Ocean-Atmosphere Feedbacks. *Journal of Climate.* **26**(19), pp.7586-7602.

Marshall, L., Schmidt, A., Toohey, M., Carslaw, K.S., Mann, G.W., Sigl, M., Khodri, M., Timmreck, C., Zanchettin, D., Ball, W.T., Bekki, S., Brooke, J.S.A., Dhomse, S., Johnson, C., Lamarque, J.F., LeGrande, A.N., Mills, M.J., Niemeier, U., Pope, J.O., Poulain, V., Robock, A., Rozanov, E., Stenke, A., Sukhodolov, T., Tilmes, S., Tsigaridis, K. and Tummon, F. 2018. Multi-model comparison of the volcanic sulfate deposition from the 1815 eruption of Mt. Tambora. *Atmospheric Chemistry and Physics.* **18**(3), pp.2307-2328.

McGregor, H.V., Evans, M.N., Goosse, H., Leduc, G., Martrat, B., Addison, J.A., Mortyn, P.G., Oppo, D.W., Seidenkrantz, M.S., Sicre, M.A., Phipps, S.J., Selvaraj, K., Thirumalai, K., Filipsson, H.L. and Ersek, V. 2015. Robust global ocean cooling trend for the pre-industrial Common Era. *Nature Geoscience.* **8**(9), pp.671-678.

Miller, G.H., Geirsdottir, A., Zhong, Y.F., Larsen, D.J., Otto-Bliesner, B.L., Holland, M.M., Bailey, D.A., Refsnider, K.A., Lehman, S.J., Southon, J.R., Anderson, C., Bjornsson, H. and Thordarson, T. 2012. Abrupt onset of the Little Ice Age triggered by volcanism and sustained by sea-ice/ocean feedbacks. *Geophysical Research Letters.* **39**, L02708.

Niemeier, U. and Schmidt, H. 2017. Changing transport processes in the stratosphere by radiative heating of sulfate aerosols. *Atmospheric Chemistry and Physics.* **17**(24), pp.14871-14886.

Oman, L., Robock, A., Stenchikov, G.L., Thordarson, T., Koch, D., Shindell, D.T. and Gao, C.C. 2006. Modeling the distribution of the volcanic aerosol cloud from the 1783-1784 Laki eruption. *Journal of Geophysical Research-Atmospheres.* **111**(D12), D12209.

Pausata, F.S.R., Chafik, L., Caballero, R. and Battisti, D.S. 2015. Impacts of high-latitude volcanic eruptions on ENSO and AMOC. *Proceedings of the National Academy of Sciences of the United States of America.* **112**(45), pp.13784-13788.

Punge, H.J., Konopka, P., Giorgetta, M.A. and Muller, R. 2009. Effects of the quasi-biennial oscillation on low-latitude transport in the stratosphere derived from trajectory calculations. *Journal of Geophysical Research-Atmospheres.* **114**, D03102.

Sigl, M., Winstrup, M., McConnell, J.R., Welten, K.C., Plunkett, G., Ludlow, F., Buntgen, U., Caffee, M., Chellman, N., Dahl-Jensen, D., Fischer, H., Kipfstuhl, S., Kostick, C., Maselli, O.J., Mekhaldi, F., Mulvaney, R., Muscheler, R., Pasteris, D.R., Pilcher, J.R., Salzer, M., Schupbach, S., Steffensen, J.P., Vinther, B.M. and Woodruff, T.E. 2015. Timing and climate

forcing of volcanic eruptions for the past 2,500 years. *Nature.* **523**(7562), pp.543–549.

Stevenson, S., Fasullo, J.T., Otto-Bliesner, B.L., Tomas, R.A. and Gao, C.C. 2017. Role of eruption season in reconciling model and proxy responses to tropical volcanism. *Proceedings of the National Academy of Sciences of the United States of America.* **114**(8), pp.1822-1826.

Stoffel, M., Khodri, M., Corona, C., Guillet, S., Poulain, V., Bekki, S., Guiot, J., Luckman, B.H., Oppenheimer, C., Lebas, N., Beniston, M. and Masson-Delmotte, V. 2015. Estimates of volcanic-induced cooling in the Northern Hemisphere over the past 1,500 years. *Nature Geoscience.* **8**(10), pp.784-788.

Swingedouw, D., Mignot, J., Ortega, P., Khodri, M., Menegoz, M., Cassou, C. and Hanquiez, V. 2017. Impact of explosive volcanic eruptions on the main climate variability modes. *Global and Planetary Change.* **150**, pp.24-45.

Thomas, M.A., Giorgetta, M.A., Timmreck, C., Graf, H.F. and Stenchikov, G. 2009. Simulation of the climate impact of Mt. Pinatubo eruption using ECHAM5-Part 2: Sensitivity to the phase of the QBO and ENSO. *Atmospheric Chemistry and Physics.* **9**(9), pp.3001-3009.

Timmreck, C., Mann, G.W., Aquila, V., Hommel, R., Lee, L.A., Schmidt, A., Brühl, C., Carn, S., Chin, M., Dhomse, S.S., Diehl, T., English, J.M., Mills, M.J., Neely, R., Sheng, J., Toohey, M. and Weisenstein, D. 2018. The Interactive Stratospheric Aerosol Model Intercomparison Project (ISA-MIP): motivation and experimental design. *Geoscientific Model Development.* **11**(7), pp.2581-2608.

Toohey, M., Kruger, K., Bittner, M., Timmreck, C. and Schmidt, H. 2014. The impact of volcanic aerosol on the Northern Hemisphere stratospheric polar vortex: mechanisms and sensitivity to forcing structure. *Atmospheric Chemistry and Physics.* **14**(23), pp.13063-13079.

Toohey, M., Kruger, K., Niemeier, U. and Timmreck, C. 2011. The influence of eruption season on the global aerosol evolution and radiative impact of tropical volcanic eruptions. *Atmospheric Chemistry and Physics.* **11**(23), pp.12351-12367.

Toohey, M., Kruger, K., Sigl, M., Stordal, F. and Svensen, H. 2016. Climatic and societal impacts of a volcanic double event at the dawn of the Middle Ages. *Climatic Change.* **136**(3-4), pp.401-412.

Toohey, M., Kruger, K. and Timmreck, C. 2013. Volcanic sulfate deposition to Greenland and Antarctica: A modeling sensitivity study. *Journal of Geophysical Research-Atmospheres.* **118**(10), pp.4788-4800.

Toohey, M. and Sigl, M. 2017. Volcanic stratospheric sulfur injections and aerosol optical depth from 500 BCE to 1900 CE. *Earth System Science Data.* **9**(2), pp.809-831.

Trepte, C.R. and Hitchman, M.H. 1992. Tropical stratospheric circulation deduced from satellite aerosol data. *Nature.* **355**(6361), pp.626-628.

Visioni, D., Pitari, G., Tuccella, P. and Curci, G. 2018. Sulfur deposition changes under sulfate geoengineering conditions: quasi-biennial oscillation effects on the transport and lifetime of stratospheric aerosols. *Atmospheric Chemistry and Physics.* **18**(4), pp.2787-2808.

Wilson, R., Anchukaitis, K., Briffa, K.R., Buntgen, U., Cook, E., D'Arrigo, R., Davi, N., Esper, J., Frank, D., Gunnarson, B., Hegerl, G., Helama, S., Klesse, S., Krusic, P.J., Linderholm, H.W., Myglan, V., Osborn, T.J., Rydval, M., Schneider, L., Schurer, A., Wiles, G., Zhang, P. and Zorita, E. 2016. Last

millennium northern hemisphere summer temperatures from tree rings: Part I: The long term context. *Quaternary Science Reviews.* **134**, pp.1-18.

Zanchettin, D., Timmreck, C., Bothe, O., Lorenz, S.J., Hegerl, G., Graf, H.F., Luterbacher, J. and Jungclaus, J.H. 2013. Delayed winter warming: A robust decadal response to strong tropical volcanic eruptions? *Geophysical Research Letters.* **40**(1), pp.204-209.

Appendix A Model description and evaluation

A.1 Model overview

The version of UM-UKCA used in this thesis is an atmosphere-only configuration of the HadGEM3 climate model based on the Global Atmosphere 4.0 configuration (Walters et al., 2014), but extended to include whole-atmosphere chemistry and GLOMAP-mode aerosol microphysics (Mann et al., 2010).

The dynamical core is described in Davies et al. (2005) and uses both semi-Lagrangian and semi-implicit methods to solve the atmospheric equations of motion. Sub-grid scale processes such as convection are parameterized (Walters et al., 2014). The model is used at N96 resolution with 1.875° longitude by 1.25° latitude, which is approximately 135 km at mid-latitudes. There are 85 vertical levels up to 85 km specified using terrain-following hybrid height coordinates. Orographic and non-orographic gravity wave drag is parameterized (Scaife et al., 2002; Webster et al., 2003) and the model internally generates the QBO (Morgenstern et al., 2009; Osprey et al., 2013).

In this thesis a preindustrial and present day configuration of the model are used. Both versions are timeslice runs with SSTs, sea-ice and emissions fixed at either preindustrial conditions (~1850) or the year 2000. In the present day version (Chapters 3 and 4) SSTs and sea-ice are set to 2000 conditions representing the average from 1995 to 2005 (Reynolds et al., 2007). Greenhouse gases (GHGs) and ozone depleting substances (ODS) are set to year 2000 conditions as specified by the Chemistry-Climate Model Initiative (CCMI) transient reference simulations (Eyring et al., 2013). Other emissions including anthropogenic SO_2 emissions are also year 2000 values as specified by the UKCA vn8.4 release job (Abraham, 2017).

In the preindustrial timeslice (Chapter 2) climatological SSTs and sea-ice are from a 40-year mean (1861-1900) of a preindustrial control run using HadGEM2-CC. Chemistry inputs are 1860 values taken from the CCMI data (Eyring et al., 2013) and aerosol forcing are 1850 values as specified for CMIP5 (Lamarque et al., 2010).

In both preindustrial and present day runs SO_2 emissions from degassing volcanoes are from Andres and Kasgnoc (1998) and OCS is prescribed as a boundary condition

of ~500 pptv. DMS emissions are calculated in the model using the concentration in seawater from Kettle and Andreae (2000) and an air-sea exchange scheme from Liss and Merlivat (1986). Both timeslice configurations also prescribe the stratospheric surface area density for heterogeneous chemistry for the year 2000 (Thomason et al., 2008).

In contrast to standard UKCA configurations, several parameters in the model have been updated following expert-elicited best estimates. These include emission scaling factors, for example the volcanic degassing SO_2 emissions are scaled by a factor of 1.45. The updated parameters are listed in Table A.1.

Table A.1: Updated parameters in the model. Table modified after Regayre et al. (2014).

Parameter	Value
Ageing – number of soluble monolayers required for an aerosol to become soluble	3.00
pH of cloud drops ($[H^+]$)	1.26×10^{-6}
Biomass burning emission flux scale factor	1.80
Biofuel emission flux scale factor	1.40
BC and OC from fossil fuel emitted aerosol diameter (nm)	58.00
BC and OC from biomass burning emitted aerosol diameter (nm)	198.00
BC and OC from biofuel emitted aerosol diameter (nm)	242.00
Fraction of SO_2 emitted as particulate SO_4	4.77×10^{-4}
Mode diameter of new sub-grid sulfate particles (nm)	18.00
Sea spray mass flux scale	1.30
Volcanic SO_2 emission flux scale factor	1.45
Biogenic monoterpene production of SOA scale factor	2.60
DMS emission flux scale factor	1.38
Hygroscopicity parameter κ for organic aerosols	0.23
Standard deviation of shallow-cloud updraft velocity	0.40
Dust emission flux scale factor	1.50
The fraction of the cloud covered area where rain forms	0.30
Threshold of cloud ice water fraction for scavenging	0.10

A fraction of 4.77×10^{-4} of the SO_2 emissions are emitted as particulate sulfate (Table A.1) representing sulfate that forms at a sub-grid level. These primary sulfate emissions are handled by GLOMAP-mode (Section A.3).

A.2 Chemistry scheme

Atmospheric chemistry is specified using the Chemistry of the Stratosphere and Troposphere (CheST) scheme with additional aerosol chemistry for use with

GLOMAP-mode. CheST combines previous stratosphere (Morgenstern et al., 2009) and troposphere (O'Connor et al., 2014) schemes. Together with the aerosol chemistry there are 86 species, which are involved in approximately 300 reactions.

Species included in the stratospheric aerosol chemistry scheme are DMS (dimethyl sulfide), SO_2, H_2SO_4, OCS (carbonyl sulfide) and SO_3 (sulfur trioxide). Sulfur chemistry reactions included are shown in Table A.2. The background stratospheric aerosol layer in the model is maintained by the precursor gas species SO_2 and OCS.

Table A.2: Sulfur chemistry reactions involved in simulating stratospheric aerosol. Table modified after Dhomse et al. (2014).

Reaction	Reference
$DMS + O(^3P) \rightarrow SO_2$	Weisenstein et al. (1997); Sander et al. (2006)
$DMS + OH \rightarrow SO_2 + CH_3O_2 + HCHO$	Weisenstein et al. (1997)
$DMS + OH \rightarrow SO_2 + CH_3O_2$	Weisenstein et al. (1997)
$DMS + NO_3 \rightarrow SO_2 + HNO_3 + CH_3O_2 + HCHO$	Weisenstein et al. (1997)
$OCS + O(^3P) \rightarrow CO + SO_2$	Weisenstein et al. (1997); Sander et al. (2006)
$OCS + OH \rightarrow CO_2 + SO_2$	Weisenstein et al. (1997); Sander et al. (2006)
$SO_2 + OH + M \rightarrow SO_3 + HO_2 + M$	Weisenstein et al. (1997)
$SO_2 + O_3 \rightarrow SO_3$	Weisenstein et al. (1997); Sander et al. (2006)
$SO_3 + H_2O \rightarrow H_2SO_4 + H_2O$	Sander et al. (2006)
$SO_2 + H_2O_2 \xrightarrow{aq.} SO_4$	Kreidenweis et al. (2003)
$OCS + h\nu \rightarrow CO + SO_2$	Weisenstein et al. (1997)
$H_2SO_4 + h\nu \rightarrow SO_3 + OH$	Weisenstein et al. (1997)
$SO_3 + h\nu \rightarrow SO_2 + O(^3P)$	Weisenstein et al. (1997)

Photolysis is included online using the FAST-JX photolysis scheme (Neu et al., 2007; Telford et al., 2013). Photolysis of H_2SO_4 is simplified and specified based on the measured cross-sections for HCl (Dhomse et al., 2014) and for wavelengths between 177 and 290 nm. It therefore does not consider photolysis of H_2SO_4 by visible light. Additionally aerosol does not impact the photolysis rates.

Gas-phase species are deposited by dry and wet deposition which is described in O'Connor et al. (2014). Dry deposition occurs throughout the boundary layer with rates calculated using a resistance-based approach (Wesely, 1989). Wet deposition is parameterized as first order loss rates dependent on the simulated precipitation (convective and large-scale) and the species' solubility.

A.3 Aerosol microphysics

GLOMAP-mode is a comprehensive aerosol microphysics model that simulates aerosol mass and number using seven log-normal modes that have multiple internally-mixed components. A detailed description is provided by Mann et al. (2010) with additional modifications for use in the stratosphere outlined in Dhomse et al. (2014). Here, important processes are outlined with a focus on the simulation of stratospheric sulfate aerosol.

The components included are sulfate, black carbon, organic carbon, dust and sea-salt. There are four soluble and three insoluble modes represented by fixed geometric standard deviations but varying size ranges (Table A.3).

GLOMAP-mode includes the formation of new sulfate aerosol particles (H_2SO_4-H_2O) by binary homogeneous nucleation using the parameterization provided by Vehkämaki et al. (2002). In this model version, new sulfate aerosol particles are also formed heterogeneously by condensation of gaseous H_2SO_4 onto meteoric smoke particle cores (Brooke et al., 2017). The model accounts for hygroscopic growth of the particles, which in the stratosphere is calculated following Carslaw et al. (1995), and at 225 K and 101 hPa the sulfate aerosols have a composition of approximately 75% H_2SO_4 and 25% H_2O. Sulfate aerosol can also be formed via in-cloud oxidation of SO_2 (Table A.2), which adds sulfate mass directly to the soluble accumulation and coarse modes (Mann et al., 2010). However, the most important pathway for forming sulfate aerosol in the stratosphere following volcanic eruptions is the oxidation of SO_2 by OH to form H_2SO_4 vapour.

Aerosol particles grow by water uptake, condensation of H_2SO_4 vapour onto the particle surface and by particles coagulating. If the geometric mean radius of the aerosol mode exceeds its specified size range, fractions of the mode number and mass concentrations are transferred to the next largest mode as in Mann et al. (2010). Particles in insoluble modes can also be transferred to the equivalent soluble mode following condensation and/or coagulation with smaller soluble particles in a process known as ageing. In this version ageing between the accumulation insoluble and accumulation soluble modes has been deactivated so that the sulfate particles with meteoric smoke particle cores can be tracked using the accumulation insoluble mode (Brooke et al., 2017). Similarly, mode-merging between the accumulation and coarse soluble modes is also deactivated as in Dhomse et al. (2014) so that aerosol in the

accumulation soluble mode can continue to grow outside of the specified size range following volcanic eruptions. This technique was found to lead to a better simulation of aerosol size distributions compared to sectional aerosol schemes and observations following the 1991 eruption of Mt. Pinatubo (Kokkola et al., 2009; Niemeier et al., 2009).

Condensation or evaporation of H_2SO_4 vapour occurs depending on the vapour pressure of H_2SO_4 (which is calculated online following Kulmala and Laaksonen (1990)) and the gas phase partial pressure. Further details can be found in Dhomse et al. (2014).

Table A.3: Aerosol configuration of GLOMAP-mode used in this thesis. Components are sulfate (SU), black carbon (BC), organic carbon (OC), sea salt (SS) and dust (DU). *r* is the geometric mean radius (nm) and the mode width is the geometric standard deviation of each mode. Table modified after Mann et al. (2010) and Mann et al. (2012).

Mode name	Size range (nm)	Composition	Mode width
Nucleation soluble	$r < 5$	SU, OC	1.59
Aitken soluble	$5 < r < 50$	SU, BC, OC	1.59
Aitken insoluble	$5 < r < 50$	BC, OC	1.59
Accumulation soluble	$50 < r < 500$	SU, BC, OC, SS	1.4
Accumulation insoluble	$50 < r < 500$	DU, SU*	1.59
Coarse soluble	$r > 500$	SU, BC, OC, SS, DU	2.0
Coarse insoluble	$r > 500$	DU	2.0

*in the standard configuration of GLOMAP-mode the accumulation insoluble mode is composed of dust only and the accumulation soluble mode contains dust.

Aerosols sediment throughout the atmosphere and are removed by dry and wet deposition. Dry deposition is dependent on particle size, particle density, the land surface type (e.g. water, grassland, forest) and the wind, specifically the surface friction velocity. It is parameterized based on the gravitational settling (i.e. sedimentation) velocity of each aerosol mode, which is dependent on particle density and size, and the aerodynamical and surface resistances (Slinn, 1982). The aerodynamical resistance depends on the stability of the boundary layer, the surface roughness length and the surface friction velocity. The surface resistance is a function of the surface friction velocity and collection efficiencies for Brownian diffusion, impaction and interception, which are also dependent on particle size (Zhang et al., 2001).

Deposition of aerosol by precipitation occurs in GLOMAP-mode by nucleation (in-cloud) scavenging and impaction (below-cloud) scavenging and for both large-scale

and convective precipitation. Nucleation scavenging occurs when aerosol particles act as cloud condensation nuclei (CCN) and form cloud droplets (activation) and eventually rain. Activation is simplified in the scavenging schemes compared to the UKCA activation scheme (described in Section A.4). For nucleation scavenging by large-scale precipitation, soluble particles with a wet radius greater than 103 nm are assumed dissolved and can be wet deposited, based on the precipitation rate (e.g. Spracklen et al., 2005). For nucleation scavenging by convective precipitation all soluble aerosol mass in the accumulation and coarse modes and 50% of the Aitken mode are assumed to be dissolved and are removed based on the convective precipitation rate (Kipling et al., 2013). Impaction scavenging is based on prescribed size-dependent collision efficiencies for aerosols and raindrops (Slinn, 1984).

A.4 Radiation scheme

The UM uses the Edwards-Slingo radiation scheme (Edwards and Slingo, 1996), which parameterizes radiation transfer using six SW and nine LW wavebands, split into downward and upward fluxes. To allow aerosols to interact with radiation, an additional code module 'UKCA_RADAER' is included that couples GLOMAP-mode to the radiation scheme. Aerosol optical properties required in the radiation scheme include scattering and absorption coefficients and the asymmetry parameter, which are calculated by Mie theory. Mie scattering calculations are too computationally expensive to conduct during runtime and therefore look-up tables of pre-computed values are used to derive the optical properties. These are calculated from the particle radius, radiation wavelength and the complex refractive index, which is dependent on the composition of the aerosol mode including water in the soluble modes. The optical properties are integrated over the size distribution and each waveband to be used by the radiation scheme (Bellouin et al., 2013).

Both the 1st and 2nd aerosol indirect effects on radiation through altering cloud albedo and lifetime are included. Aerosol activation is parameterized following Abdul-Razzak and Ghan (2000) according to Köhler theory, which considers aerosol size and composition and water vapour supersaturation, which depends on the parameterized cloud updraft velocity. The activated particles are used to diagnose the Cloud Droplet Number Concentration (CDNC) used in the calculation of cloud droplet effective radius needed in the radiation scheme. The CDNC is used in the

large-scale precipitation scheme to determine the rate at which cloud droplets are converted to raindrops and hence the cloud lifetime.

The radiation calculations use the aerosol optical properties and cloud droplet effective radius in addition to other key factors such as the mean solar zenith angle, surface emissivity and albedo, and topography (e.g. Walters et al., 2014). Radiative fluxes in both all-sky and clear-sky (without clouds) conditions are diagnosed.

A.5 Model evaluation

The interactive stratospheric aerosol capability of UM-UKCA was previously validated by Dhomse et al. (2014), who showed good comparisons between simulated and observed extinction and particle size distributions following the 1991 eruption of Mt. Pinatubo. The model configuration used in this thesis is an updated version of UM-UKCA used in Dhomse et al. (2014) that includes radiatively-coupled aerosol, shown to improve comparisons to observations (Mann et al., 2015), and meteoric smoke particles (MSP), the implementation of which is outlined in Brooke et al. (2017).

MSPs act as a sink for gaseous sulfuric acid (Section A.3) and their addition in the model has reduced a previous high bias in gaseous sulfuric acid (Dhomse et al., 2014) and reduced the upper troposphere-lower stratosphere sulfate burden in background conditions by more than a factor of 4. The stratospheric sulfate burden in the pre-industrial and present day control simulations used in this thesis are 78 Gg S and 93 Gg S, respectively. These burdens are roughly consistent with a satellite-derived present day estimate of 112.5 Gg S from the Stratospheric Aerosol and Gas Experiment II instrument (SAGE II) (Arfeuille et al., 2013; Sheng et al., 2015). However, the burdens are much lower than the most recently derived estimate of 164 Gg S from the CMIP6 stratospheric aerosol record (Thomason et al., 2018). Reasons for the lower burden in comparison to the CMIP6 record include uncertainties in the observations or a too-high MSP flux especially given that sulfuric acid cannot evaporate from the MSP cores in this model version. However, extinction profiles in comparison to SAGE II are in reasonable agreement, although lower than the model used in Dhomse et al. (2014) (not shown). An analysis of the effects of MSP on the quiescent stratospheric sulfate aerosol is in preparation (Mann et al., in prep).

References

Abdul-Razzak, H. and Ghan, S.J. 2000. A parameterization of aerosol activation 2. Multiple aerosol types. *Journal of Geophysical Research-Atmospheres.* **105**(D5), pp.6837-6844.

Abraham, N.L. 2017. *Release Job RJ4.0.* [Online]. Available from: http://www.ukca.ac.uk/wiki/index.php/Release_Job_RJ4.0

Andres, R.J. and Kasgnoc, A.D. 1998. A time-averaged inventory of subaerial volcanic sulfur emissions. *Journal of Geophysical Research-Atmospheres.* **103**(D19), pp.25251-25261.

Arfeuille, F., Luo, B.P., Heckendorn, P., Weisenstein, D., Sheng, J.X., Rozanov, E., Schraner, M., Bronnimann, S., Thomason, L.W. and Peter, T. 2013. Modeling the stratospheric warming following the Mt. Pinatubo eruption: uncertainties in aerosol extinctions. *Atmospheric Chemistry and Physics.* **13**(22), pp.11221-11234.

Bellouin, N., Mann, G.W., Woodhouse, M.T., Johnson, C., Carslaw, K.S. and Dalvi, M. 2013. Impact of the modal aerosol scheme GLOMAP-mode on aerosol forcing in the Hadley Centre Global Environmental Model. *Atmospheric Chemistry and Physics.* **13**(6), pp.3027-3044.

Brooke, J.S.A., Feng, W.H., Carrillo-Sanchez, J.D., Mann, G.W., James, A.D., Bardeen, C.G. and Plane, J.M.C. 2017. Meteoric Smoke Deposition in the Polar Regions: A Comparison of Measurements With Global Atmospheric Models. *Journal of Geophysical Research-Atmospheres.* **122**(20), pp.11112-11130.

Carslaw, K.S., Luo, B. and Peter, T. 1995. An analytic expression for the composition of aqueous HNO3-H2SO4 stratospheric aerosols including gas phase removal of HNO3. *Geophysical Research Letters.* **22**(14), pp.1877-1880.

Davies, T., Cullen, M.J.P., Malcolm, A.J., Mawson, M.H., Staniforth, A., White, A.A. and Wood, N. 2005. A new dynamical core for the Met Office's global and regional modelling of the atmosphere. *Quarterly Journal of the Royal Meteorological Society.* **131**(608), pp.1759-1782.

Dhomse, S.S., Emmerson, K.M., Mann, G.W., Bellouin, N., Carslaw, K.S., Chipperfield, M.P., Hommel, R., Abraham, N.L., Telford, P., Braesicke, P., Dalvi, M., Johnson, C.E., O'Connor, F., Morgenstern, O., Pyle, J.A., Deshler, T., Zawodny, J.M. and Thomason, L.W. 2014. Aerosol microphysics simulations of the Mt. Pinatubo eruption with the UM-UKCA composition-climate model. *Atmospheric Chemistry and Physics.* **14**(20), pp.11221-11246.

Edwards, J.M. and Slingo, A. 1996. Studies with a flexible new radiation code .1. Choosing a configuration for a large-scale model. *Quarterly Journal of the Royal Meteorological Society.* **122**(531), pp.689-719.

Eyring, V., Lamarque, J.-F., Hess, P., Arfeuille, F., Bowman, K., Chipperfield, M., Duncan, B., Fiore, A., Gettelman, A., Giorgetta, M.A., Granier, C., Hegglin, M., Kinnison, D., Kunze, M., Langematz, U., Luo, B., Martin, R., Matthes, K., Newman, P.A., Peter, T., Robock, A., Ryerson, T., Saiz-Lopez, A., Salawitch, R., Schultz, M., Shepherd, T.G., Shindell, D., Staehelin, J., Tegtmeier, S., Thomason, L., Tilmes, S., Vernier, J.-P., Waugh, D.W. and Young, P.J. 2013. Overview of IGAC/SPARC Chemistry-Climate Model Initiative (CCMI) Community Simulations in Support of Upcoming Ozone and Climate Assessments. *SPARC Newsletter No. 40.* pp.48-66.

Kettle, A.J. and Andreae, M.O. 2000. Flux of dimethylsulfide from the oceans: A comparison of updated data seas and flux models. *Journal of Geophysical Research-Atmospheres.* **105**(D22), pp.26793-26808.

Kipling, Z., Stier, P., Schwarz, J.P., Perring, A.E., Spackman, J.R., Mann, G.W., Johnson, C.E. and Telford, P.J. 2013. Constraints on aerosol processes in climate models from vertically-resolved aircraft observations of black carbon. *Atmospheric Chemistry and Physics.* **13**(12), pp.5969-5986.

Kokkola, H., Hommel, R., Kazil, J., Niemeier, U., Partanen, A.I., Feichter, J. and Timmreck, C. 2009. Aerosol microphysics modules in the framework of the ECHAM5 climate model - intercomparison under stratospheric conditions. *Geoscientific Model Development.* **2**(2), pp.97-112.

Kreidenweis, S.M., Walcek, C.J., Feingold, G., Gong, W., Jacobson, M.Z., Kim, C.-H., Liu, X., Penner, J.E., Nenes, A. and Seinfeld, J.H. 2003. Modification of aerosol mass and size distribution due to aqueous-phase SO2 oxidation in clouds: Comparisons of several models. *Journal of Geophysical Research: Atmospheres.* **108**(D7), 4213.

Kulmala, M. and Laaksonen, A. 1990. Binary nucleation of water–sulfuric acid system: Comparison of classical theories with different H2SO4 saturation vapor pressures. *Journal of Chemical Physics.* **93**(1), pp.696-701.

Lamarque, J.F., Bond, T.C., Eyring, V., Granier, C., Heil, A., Klimont, Z., Lee, D., Liousse, C., Mieville, A., Owen, B., Schultz, M.G., Shindell, D., Smith, S.J., Stehfest, E., Van Aardenne, J., Cooper, O.R., Kainuma, M., Mahowald, N., McConnell, J.R., Naik, V., Riahi, K. and van Vuuren, D.P. 2010. Historical (1850-2000) gridded anthropogenic and biomass burning emissions of reactive gases and aerosols: methodology and application. *Atmospheric Chemistry and Physics.* **10**(15), pp.7017-7039.

Liss, P.S. and Merlivat, L. 1986. Air-Sea Gas Exchange Rates: Introduction and Synthesis. In: Buat-Ménard, P. ed. *The Role of Air-Sea Exchange in Geochemical Cycling.* Dordrecht: Springer Netherlands, pp.113-127.

Mann, G.W., Carslaw, K.S., Ridley, D.A., Spracklen, D.V., Pringle, K.J., Merikanto, J., Korhonen, H., Schwarz, J.P., Lee, L.A., Manktelow, P.T., Woodhouse, M.T., Schmidt, A., Breider, T.J., Emmerson, K.M., Reddington, C.L., Chipperfield, M.P. and Pickering, S.J. 2012. Intercomparison of modal and sectional aerosol microphysics representations within the same 3-D global chemical transport model. *Atmospheric Chemistry and Physics.* **12**(10), pp.4449-4476.

Mann, G.W., Carslaw, K.S., Spracklen, D.V., Ridley, D.A., Manktelow, P.T., Chipperfield, M.P., Pickering, S.J. and Johnson, C.E. 2010. Description and evaluation of GLOMAP-mode: a modal global aerosol microphysics model for the UKCA composition-climate model. *Geoscientific Model Development.* **3**(2), pp.519-551.

Mann, G.W., Dhomse, S., Deshler, T., Timmreck, C., Schmidt, A., Neely, R. and Thomason, L. 2015. Evolving particle size is the key to improved volcanic forcings. *Past Global Changes Magazine.* **23**(2), pp.52-53.

Morgenstern, O., Braesicke, P., O'Connor, F.M., Bushell, A.C., Johnson, C.E., Osprey, S.M. and Pyle, J.A. 2009. Evaluation of the new UKCA climate-composition model - Part 1: The stratosphere. *Geoscientific Model Development.* **2**(1), pp.43-57.

Neu, J.L., Prather, M.J. and Penner, J.E. 2007. Global atmospheric chemistry: Integrating over fractional cloud cover. *Journal of Geophysical Research: Atmospheres.* **112**(D11), D11306.

Niemeier, U., Timmreck, C., Graf, H.F., Kinne, S., Rast, S. and Self, S. 2009. Initial fate of fine ash and sulfur from large volcanic eruptions. *Atmospheric Chemistry and Physics.* **9**(22), pp.9043-9057.

O'Connor, F.M., Johnson, C.E., Morgenstern, O., Abraham, N.L., Braesicke, P., Dalvi, M., Folberth, G.A., Sanderson, M.G., Telford, P.J., Voulgarakis, A., Young, P.J., Zeng, G., Collins, W.J. and Pyle, J.A. 2014. Evaluation of the new UKCA climate-composition model - Part 2: The Troposphere. *Geoscientific Model Development.* **7**(1), pp.41-91.

Osprey, S.M., Gray, L.J., Hardiman, S.C., Butchart, N. and Hinton, T.J. 2013. Stratospheric Variability in Twentieth-Century CMIP5 Simulations of the Met Office Climate Model: High Top versus Low Top. *Journal of Climate.* **26**(5), pp.1595-1606.

Regayre, L.A., Pringle, K.J., Booth, B.B.B., Lee, L.A., Mann, G.W., Browse, J., Woodhouse, M.T., Rap, A., Reddington, C.L. and Carslaw, K.S. 2014. Uncertainty in the magnitude of aerosol-cloud radiative forcing over recent decades. *Geophysical Research Letters.* **41**(24), pp.9040-9049.

Reynolds, R.W., Smith, T.M., Liu, C., Chelton, D.B., Casey, K.S. and Schlax, M.G. 2007. Daily high-resolution-blended analyses for sea surface temperature. *Journal of Climate.* **20**(22), pp.5473-5496.

Sander, S., Friedl, R., Golden, D., Kurylo, M., Huie, R., Orkin, V., Moortgat, G., Wine, P., Ravishankara, A., Kolb, C., Molina, M., Finlayson-Pitts, B., Huie, R., Orkin, V.L. and Keller-Rudek, H. 2006. Chemical kinetics and photochemical data for use in atmospheric studies, NASA Panel for Data Evaluation, Evaluation number 15, JPL Publication 06-2. California Insitute of Technology, Pasadena, California: *Jet Propulsion Laboratory*. [Online].

Scaife, A.A., Butchart, N., Warner, C.D. and Swinbank, R. 2002. Impact of a spectral gravity wave parameterization on the stratosphere in the met office unified model. *Journal of the Atmospheric Sciences.* **59**(9), pp.1473-1489.

Sheng, J.X., Weisenstein, D.K., Luo, B.P., Rozanov, E., Stenke, A., Anet, J., Bingemer, H. and Peter, T. 2015. Global atmospheric sulfur budget under volcanically quiescent conditions: Aerosol-chemistry-climate model predictions and validation. *Journal of Geophysical Research-Atmospheres.* **120**(1), pp.256-276.

Slinn, W.G.N. 1982. Predictions for particle deposition to vegetative canopies. *Atmospheric Environment (1967).* **16**(7), pp.1785-1794.

Slinn, W.G.N. 1984. Precipitation Scavenging. In: Randerson, D. ed. *Atmospheric Science and Power Production.* Springfield, VA: US Department of Energy, pp.466–532.

Spracklen, D.V., Pringle, K.J., Carslaw, K.S., Chipperfield, M.P. and Mann, G.W. 2005. A global off-line model of size-resolved aerosol microphysics: I. Model development and prediction of aerosol properties. *Atmospheric Chemistry and Physics.* **5**, pp.2227-2252.

Telford, P.J., Abraham, N.L., Archibald, A.T., Braesicke, P., Dalvi, M., Morgenstern, O., O'Connor, F.M., Richards, N.A.D. and Pyle, J.A. 2013. Implementation of the Fast-JX Photolysis scheme (v6.4) into the UKCA component of the MetUM chemistry-climate model (v7.3). *Geoscientific Model Development.* **6**(1), pp.161-177.

Thomason, L.W., Burton, S.P., Luo, B.P. and Peter, T. 2008. SAGE II measurements of stratospheric aerosol properties at non-volcanic levels. *Atmospheric Chemistry and Physics.* **8**(4), pp.983-995.

Thomason, L.W., Ernest, N., Millan, L., Rieger, L., Bourassa, A., Vernier, J.P., Manney, G., Luo, B.P., Arfeuille, F. and Peter, T. 2018. A global space-based stratospheric aerosol climatology: 1979-2016. *Earth System Science Data.* **10**(1), pp.469-492.

Vehkämaki, H., Kulmala, M., Napari, I., Lehtinen, K.E.J., Timmreck, C., Noppel, M. and Laaksonen, A. 2002. An improved parameterization for sulfuric acid-water nucleation rates for tropospheric and stratospheric conditions. *Journal of Geophysical Research-Atmospheres.* **107**(D22), 4622.

Walters, D.N., Williams, K.D., Boutle, I.A., Bushell, A.C., Edwards, J.M., Field, P.R., Lock, A.P., Morcrette, C.J., Stratton, R.A., Wilkinson, J.M., Willett, M.R., Bellouin, N., Bodas-Salcedo, A., Brooks, M.E., Copsey, D., Earnshaw, P.D., Hardiman, S.C., Harris, C.M., Levine, R.C., MacLachlan, C., Manners, J.C., Martin, G.M., Milton, S.F., Palmer, M.D., Roberts, M.J., Rodriguez, J.M., Tennant, W.J. and Vidale, P.L. 2014. The Met Office Unified Model Global Atmosphere 4.0 and JULES Global Land 4.0 configurations. *Geoscientific Model Development.* **7**(1), pp.361-386.

Webster, S., Brown, A.R., Cameron, D.R. and Jones, C.P. 2003. Improvements to the representation of orography in the Met Office Unified Model. *Quarterly Journal of the Royal Meteorological Society.* **129**(591), pp.1989-2010.

Weisenstein, D.K., Yue, G.K., Ko, M.K.W., Sze, N.D., Rodriguez, J.M. and Scott, C.J. 1997. A two-dimensional model of sulfur species and aerosols. *Journal of Geophysical Research-Atmospheres.* **102**(11D), pp.13019-13035.

Wesely, M.L. 1989. Parameterization of surface resistances to gaseous dry deposition in regional-scale numerical models. *Atmospheric Environment (1967).* **23**(6), pp.1293-1304.

Zhang, L., Gong, S., Padro, J. and Barrie, L. 2001. A size-segregated particle dry deposition scheme for an atmospheric aerosol module. *Atmospheric Environment.* **35**(3), pp.549-560.

Appendix B Supplement to Chapter 2

Table B.1: Ice cores used for volcanic sulfate deposition fluxes after the 1815 eruption of Mt. Tambora and their metadata. Antarctica ice core details taken from Table S1, Sigl et al. (2014).

Antarctica ice cores				Greenland ice cores			
Ice core	**Lat**	**Lon**	**Reference**	**Ice core**	**Lat**	**Lon**	**Reference**
WDC06A	-79.47	-112.09	*Sigl et al. (2013)*	B20	79	-36.5	*Bigler et al. (2002), Gao et al. (2006)*
WDC05Q	-79.47	-112.08	*Sigl et al. (2013)*	GISP2	72.6	-38.5	*Gao et al. (2006), Zielinski et al. (1994)*
SP04	-89.95	17.67	*Budner & Cole-Dai, (2003)*	20D	65	-45	*Gao et al. (2006), Mayewski et al. (1990)*
SP01	-89.95	17.67	*Ferris et al. (2011)*	NGRIP	75.1	-42.3	*Plummer et al. (2012)*
DML05	-75.00	0.02	*Traufetter et al. (2004)*	NEEM-2011-S1	77.45	-51.06	*Sigl et al. (2013)*
DML07	-75.58	3.43	*Traufetter et al. (2004)*	Humboldt	78.53	-56.83	*Sigl et al. (2013)*
B40	-75.00	0.06	*Sigl et al. (2014)*	Site T	72.58	-38.45	*Mosley-Thompson et al. (2003)*
NUS08-4	-82.82	18.90	*Sigl et al. (2014)*	GITS	77.14	-61.10	*Mosley-Thompson et al. (2003)*
NUS08-5	-82.63	17.87	*Sigl et al. (2014)*	D2	71.75	-46.33	*Mosley-Thompson et al. (2003)*
NUS07-2	-76.07	22.47	*Sigl et al. (2014)*	D3	69.8	-44.0	*Mosley-Thompson et al. (2003)*
NUS07-5	-78.65	35.63	*Sigl et al. (2014)*	Raven	65.9	-46.3	*Mosley-Thompson et al. (2003)*
NUS07-7	-82.07	54.88	*Sigl et al. (2014)*	Dye 3	65.18	-43.83	*Larsen et al. (2008)*
EDC96	-75.10	123.35	*Castellano et al. (2005)*	GRIP	72.58	-37.64	*Larsen et al. (2008)*
DFS10	-77.40	39.62	*Sigl et al. (2014)*	SU07	72.5	-38.5	*Cole-Dai et al. (2009)*
DF01	-77.37	39.70	*Motizuki et al. (2014)*	D4	71.4	-43.9	*McConnell et al. (2007)*
W10k	-66.75	112.83	*Sigl et al. (2014)*				
DIV2010	-76.77	-101.74	*Sigl et al. (2014)*				
NUS08-7	-74.88	1.60	*Sigl et al. (2014)*				
NUS07-1	-73.72	7.98	*Sigl et al. (2014)*				
TalosDome	-72.48	159.06	*Stenni et al. (2002)*				
Taylor Dome	-77.81	158.72	*Mayewski et al. (1996)*				
DomeA	-80.37	77.22	*Jiang et al. (2012)*				
DSS	-66.77	112.80	*Plummer et al. (2012)*				
Siple Station	-75.91	-83.91	*Cole-Dai et al. (1997)*				
Dyer	-70.66	-64.87	*Cole-Dai et al. (1997)*				
PlatRemote	-84.00	43.00	*Cole-Dai et al. (2000)*				

Table B.2: Ice cores used for preindustrial background sulfate deposition fluxes (1850–1860 mean) taken from Lamarque et al. (2013).

Antarctic ice cores			Arctic ice cores		
Ice core	**Lat**	**Lon**	**Ice core**	**Lat**	**Lon**
W10	-66.73	112.83	ACT11d	66.48	-46.31
DIV	-76.77	-101.74	D4	71.4	-43.9
WD	-79.47	-112.07	Zoe	72.6	-38.3
NUS08-7	-74.88	1.60	NEEMS3	77.45	-51.06
NUS08-5	-82.63	17.87	Tunu	78.02	-33.99
NUS07-7	-82.07	54.88	McCall	69.3	-143.8
NUS07-5	-78.65	35.63	Akademii Nauk	80.52	94.82
NUS07-2	-76.07	22.47	Flade Isblink	81.58	-15.7
NUS07-1	-73.72	7.98			

Table B.3: Mean polar (60°–90°) cumulative deposited sulfate (kg SO_4 km^{-2}) and revised BTD factors ($\times 10^9$ km^2) calculated from mean polar deposited sulfate and hemispheric peak atmospheric sulfate burden as opposed to ice sheet deposited sulfate (ensemble mean).

Model	**Arctic deposition [kg SO_4 km^{-2}]**	**NH_BTD [$\times 10^9$ km^2]**	**Antarctic deposition [kg SO_4 km^{-2}]**	**SH_BTD [$\times 10^9$ km^2]**
CESM1(WACCM)	125	0.27	100	0.58
MAECHAM5-HAM	175	0.21	287	0.17
SOCOL-AER	131	0.25	168	0.33
UM-UKCA	77	0.38	53	1.07

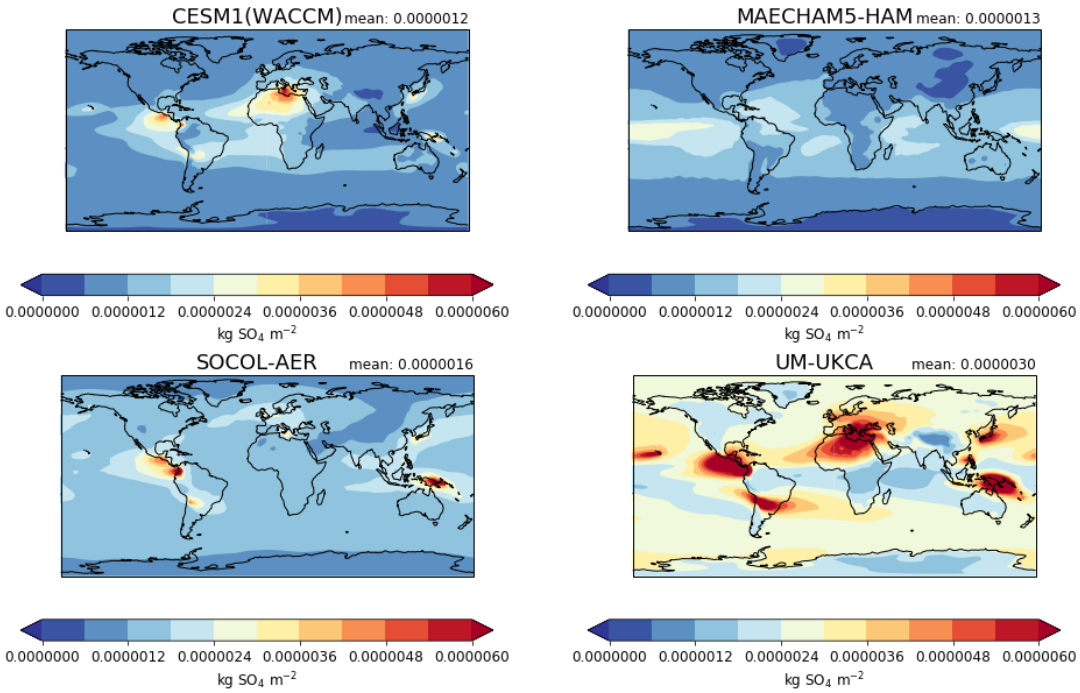

Figure B.1: Preindustrial background (no Tambora) global atmospheric sulfate burdens in the control simulations (kg SO_4 m^{-2}).The value shown in the top right-hand corner of each plot refers to the global mean sulfate burden. Background values are averages of the monthly mean model output from 5 control simulations each with 48 months of data for UM-UKCA, 3 controls each with 60 months of data for CESM1(WACCM), and 1 control with 60 months of data for MAECHAM5-HAM and SOCOL-AER.

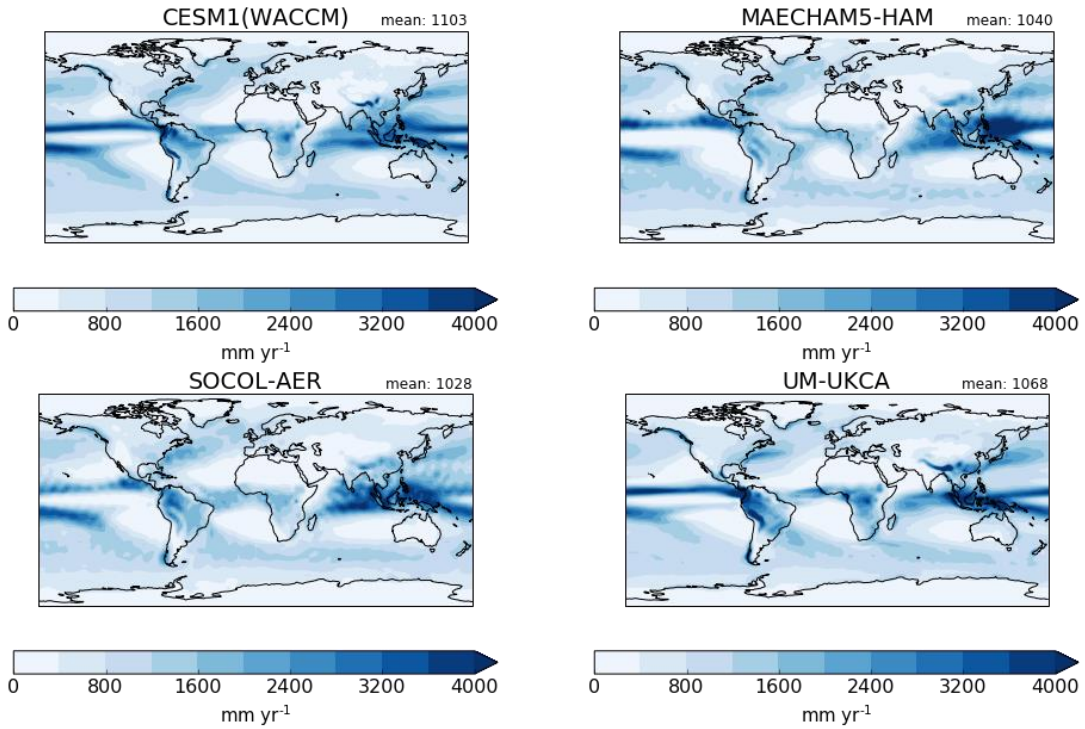

Figure B.2: Preindustrial background global precipitation in the control simulations (mm yr^{-1}). SOCOL-AER is included here for reference but deposition in SOCOL-AER is not connected to the precipitation. The value shown in the top right-hand corner of each plot refers to the global mean precipitation. Background values are averages of the monthly mean model output from 5 control simulations each with 48 months of data for UM-UKCA, 3 controls each with 60 months of data for CESM1(WACCM), and 1 control with 60 months of data for MAECHAM5-HAM and SOCOL-AER.

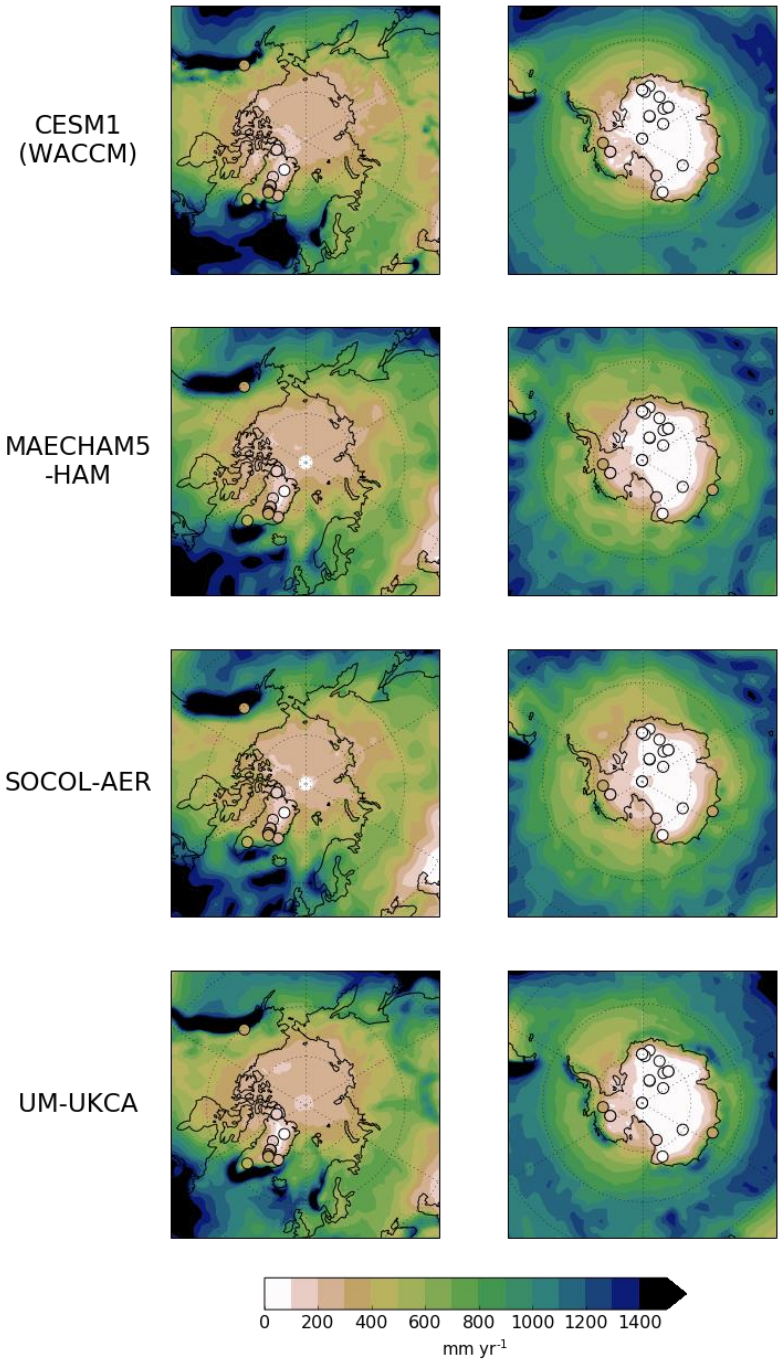

Figure B.3: Preindustrial background polar precipitation in the control simulations (mm yr^{-1}) (shading) and ice core accumulation (mm liquid water equivalent yr^{-1}) in ice cores (filled circles) (Sigl et al., 2014). Antarctic ice core accumulation rates are an average of annual ice core accumulation from 1850–1860 taken from Sigl et al. (2014). Greenland ice core accumulation rates are taken from Gao et al. (2006) (their Table 1). SOCOL-AER is included here for reference but deposition in SOCOL-AER is not connected to the precipitation. Background values are averages of the monthly mean model output from 5 control simulations each with 48 months of data for UM-UKCA, 3 controls each with 60 months of data for CESM1(WACCM), and 1 control with 60 months of data for MAECHAM5-HAM and SOCOL-AER.

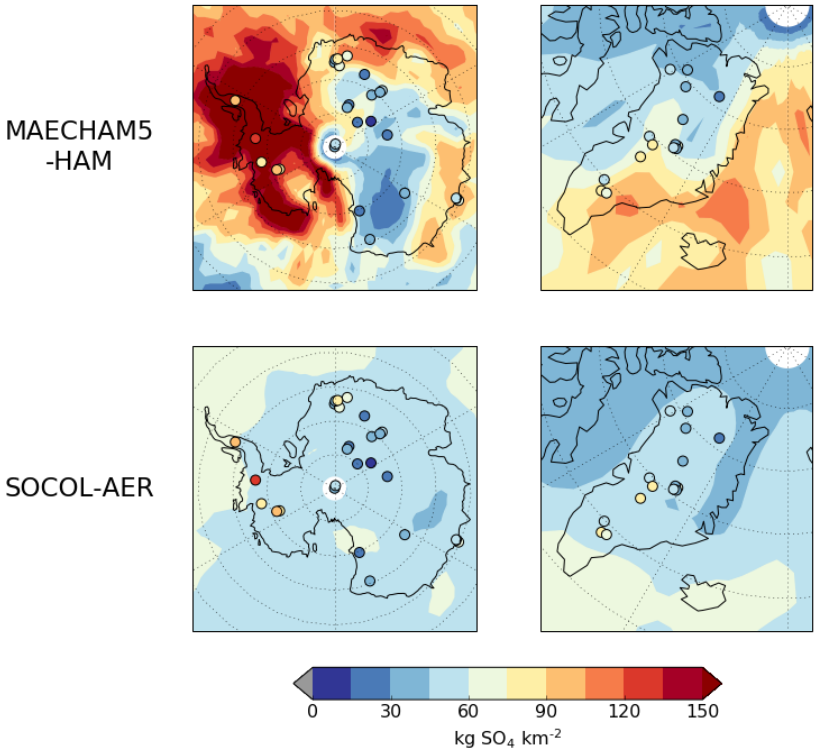

Figure B.4: Cumulative deposited sulfate (kg SO_4 km^{-2}) for MAECHAM5-HAM and SOCOL-AER (ensemble mean). Model results have been reduced by a factor of 3 (for MAECHAM5-HAM the slope of the regression line between simulated deposited sulfate and ice core records in Antarctica was 3.7 and 1.7 in Greenland. SOCOL-AER is reduced by the same factor for comparison). MAECHAM5-HAM is able to simulate the spatial pattern of ice sheet deposited sulfate when compared to ice cores (circles), but the magnitude is too large.

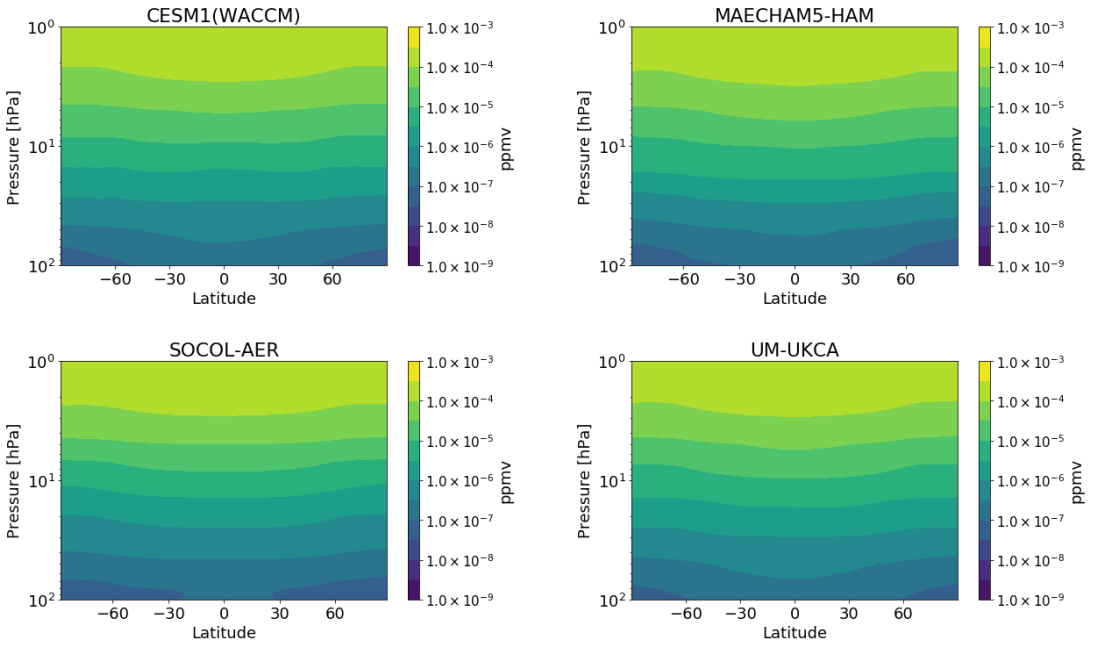

Figure B.5: Preindustrial background zonal mean stratospheric OH in the control simulations (ppmv). Background values are averages of the monthly mean model output from 5 control simulations each with 48 months of data for UM-UKCA, 3 controls each with 60 months of data for CESM1(WACCM), and 1 control with 60 months of data for SOCOL-AER. In MAECHAM5-HAM the OH is prescribed and plotted here is the 12-month average.

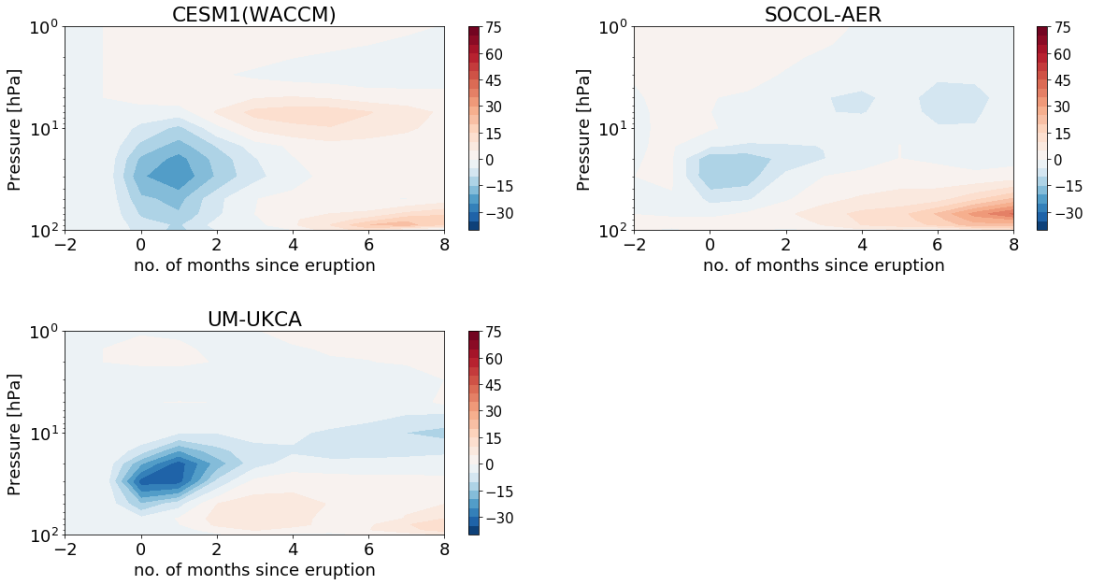

Figure B.6: Percentage change in tropical (15°S–15°N) OH in the first 8 months after the eruption (ensemble mean) for each model that includes interactive OH chemistry.

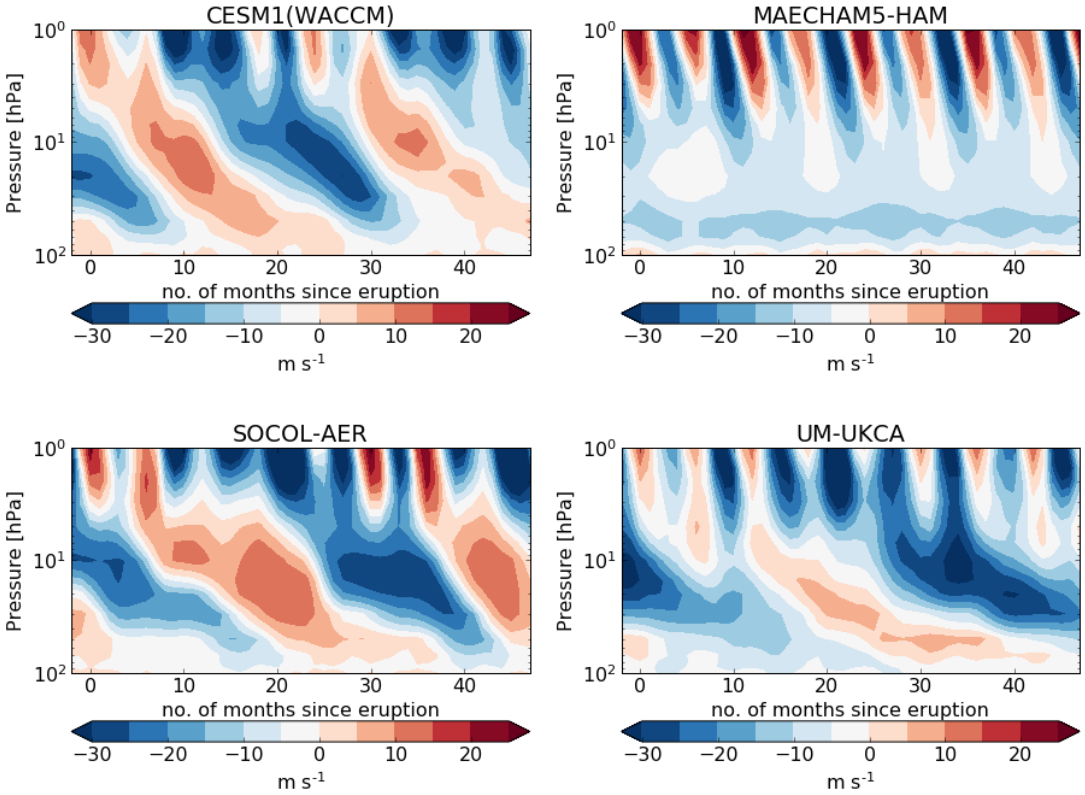

Figure B.7: Tropical mean (15°S–15°N) zonal wind for the volcanic simulations in each model (ensemble mean). Tropical winds in UM-UKCA, SOCOL-AER and CESM1(WACCM) oscillate, exhibiting characteristics of the QBO, with downward propagating easterly and westerly winds, but length of phase differs. QBO easterly phase is longer in UM-UKCA; ~2.5 years compared to ~1.5 years in CESM1(WACCM) and SOCOL-AER. MAECHAM5-HAM does not include representation of the QBO and winds remain easterly in the lower stratosphere throughout the simulations.

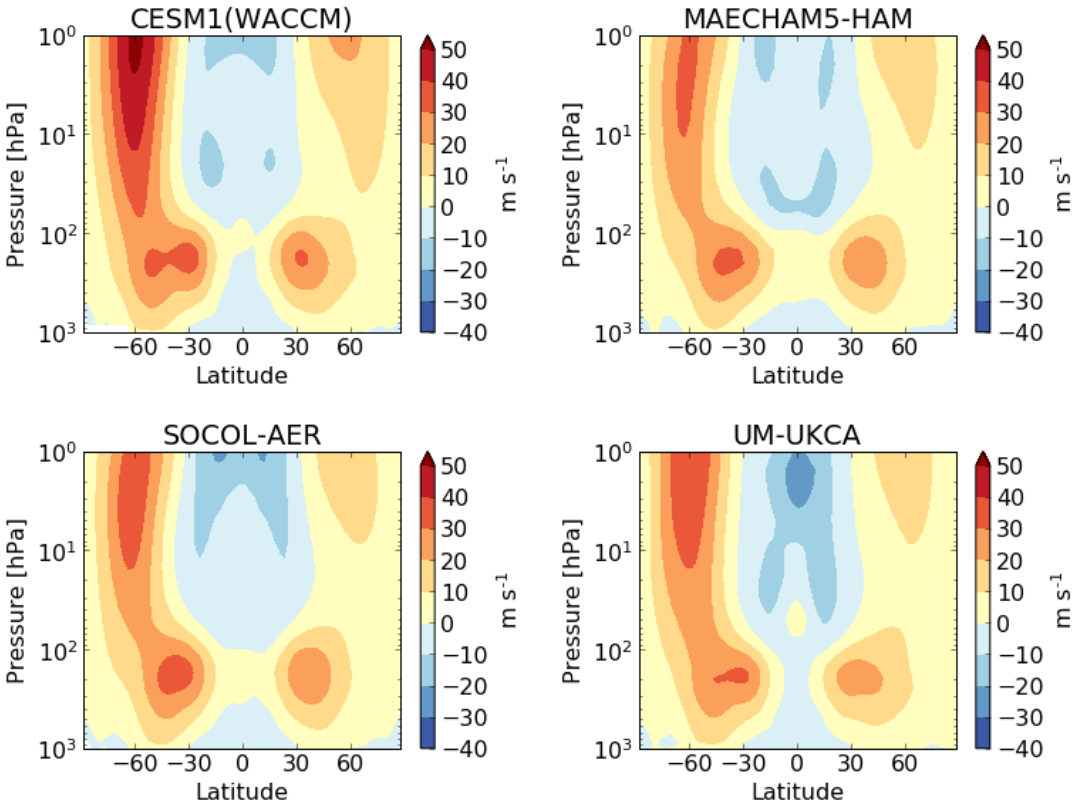

Figure B.8: Preindustrial background zonal mean zonal wind in the control simulations (m s^{-1}). Background values are averages of the monthly mean model output from 5 control simulations each with 48 months of data for UM-UKCA, 3 controls each with 60 months of data for CESM1(WACCM), and 1 control with 60 months of data for MAECHAM5-HAM and SOCOL-AER. Zonal wind is output on 36 pressure levels in UM-UKCA, 33 pressure levels in MAECHAM5-HAM and 32 pressure levels in SOCOL-AER. Zonal wind in CESM1(WACCM) is output on an atmosphere hybrid sigma-pressure coordinate and has been interpolated to the pressure levels used in UM-UKCA.

References

Bigler, M., Wagenbach, D., Fischer, H., Kipfstuhl, J., Millar, H., Sommer, S. and Stauffer, B. 2002. Sulphate record from a northeast Greenland ice core over the last 1200 years based on continuous flow analysis. *Annals of Glaciology.* **35**, pp.250-256.

Budner, D. and Cole-Dai, J. 2003. The number and magnitude of large explosive volcanic eruptions between 904 and 1865 A.D.: Quantifying evidence from a new south pole ice core. In: Robock, A. and Oppenheimer, C. eds. *Volcanism and the Earth's Atmosphere.* Washington, D.C., USA: AGU, pp.165-176.

Castellano, E., Becagli, S., Hansson, M., Hutterli, M., Petit, J.R., Rampino, M.R., Severi, M., Steffensen, J.P., Traversi, R. and Udisti, R. 2005. Holocene volcanic history as recorded in the sulfate stratigraphy of the European Project for Ice Coring in Antarctica Dome C (EDC96) ice core. *Journal of Geophysical Research-Atmospheres.* **110**(D6), D06114.

Cole-Dai, J., Ferris, D., Lanciki, A., Savarino, J., Baroni, M. and Thiemens, M.H. 2009. Cold decade (AD 1810-1819) caused by Tambora (1815) and another (1809) stratospheric volcanic eruption. *Geophysical Research Letters.* **36**, L22703.

Cole-Dai, J.H., Mosley-Thompson, E., Wight, S.P. and Thompson, L.G. 2000. A 4100-year record of explosive volcanism from an East Antarctica ice core. *Journal of Geophysical Research-Atmospheres.* **105**(D19), pp.24431-24441.

Cole-Dai, J.H., MosleyThompson, E. and Thompson, L.G. 1997. Annually resolved southern hemisphere volcanic history from two Antarctic ice cores. *Journal of Geophysical Research-Atmospheres.* **102**(D14), pp.16761-16771.

Ferris, D.G., Cole-Dai, J., Reyes, A.R. and Budner, D.M. 2011. South Pole ice core record of explosive volcanic eruptions in the first and second millennia A.D. and evidence of a large eruption in the tropics around 535 A.D. *Journal of Geophysical Research: Atmospheres.* **116**(D17), D17308.

Gao, C., Robock, A., Self, S., Witter Jeffrey, B., Steffenson, J.P., Clausen Henrik, B., Siggaard-Andersen, M.-L., Johnsen, S., Mayewski Paul, A. and Ammann, C. 2006. The 1452 or 1453 A.D. Kuwae eruption signal derived from multiple ice core records: Greatest volcanic sulfate event of the past 700 years. *Journal of Geophysical Research: Atmospheres.* **111**(D12), D12107.

Jiang, S., Cole-Dai, J., Li, Y.S., Ferris, D.G., Ma, H.M., An, C.L., Shi, G.T. and Sun, B. 2012. A detailed 2840 year record of explosive volcanism in a shallow ice core from Dome A, East Antarctica. *Journal of Glaciology.* **58**(207), pp.65-75.

Lamarque, J.F., Dentener, F., McConnell, J., Ro, C.U., Shaw, M., Vet, R., Bergmann, D., Cameron-Smith, P., Dalsoren, S., Doherty, R., Faluvegi, G., Ghan, S.J., Josse, B., Lee, Y.H., MacKenzie, I.A., Plummer, D., Shindell, D.T., Skeie, R.B., Stevenson, D.S., Strode, S., Zeng, G., Curran, M., Dahl-Jensen, D., Das, S., Fritzsche, D. and Nolan, M. 2013. Multi-model mean nitrogen and sulfur deposition from the Atmospheric Chemistry and Climate Model Intercomparison Project (ACCMIP): evaluation of historical and projected future changes. *Atmos. Chem. Phys.* **13**(16), pp.7997-8018.

Larsen, L.B., Vinther, B.M., Briffa, K.R., Melvin, T.M., Clausen, H.B., Jones, P.D., Siggaard-Andersen, M.L., Hammer, C.U., Eronen, M., Grudd, H., Gunnarson, B.E., Hantemirov, R.M., Naurzbaev, M.M. and Nicolussi, K. 2008. New ice

core evidence for a volcanic cause of the A.D. 536 dust veil. *Geophysical Research Letters.* **35**(4), L04708.

Mayewski, P.A., Lyons, W.B., Spencer, M.J., Twickler, M.S., Buck, C.F. and Whitlow, S. 1990. An ice core record of atmospheric response to anthropogenic sulfate and nitrate. *Nature.* **346**(6284), pp.554-556.

Mayewski, P.A., Twickler, M.S., Whitlow, S.I., Meeker, L.D., Yang, Q., Thomas, J., Kreutz, K., Grootes, P.M., Morse, D.L., Steig, E.J., Waddington, E.D., Saltzman, E.S., Whung, P.Y. and Taylor, K.C. 1996. Climate change during the last deglaciation in Antarctica. *Science.* **272**(5268), pp.1636-1638.

McConnell, J.R., Edwards, R., Kok, G.L., Flanner, M.G., Zender, C.S., Saltzman, E.S., Banta, J.R., Pasteris, D.R., Carter, M.M. and Kahl, J.D.W. 2007. 20th-century industrial black carbon emissions altered arctic climate forcing. *Science.* **317**(5843), pp.1381-1384.

Mosley-Thompson, E., Mashiotta, T.A. and Thompson, L.G. 2003. High resolution ice core records of late Holocene volcanism: Current and future contributions from the Greenland PARCA cores. In: Robock, A. and Oppenheimer, C. eds. *Volcanism and the Earth's Atmosphere.* Washington, D. C, USA: AGU, pp.153-164.

Motizuki, Y., Nakai, Y., Takahashi, K., Igarashi, M., Motoyama, H. and Suzuki, K. 2014. Dating of a Dome Fuji (Antarctica) shallow ice core by volcanic signal synchronization with B32 and EDML1 chronologies. *The Cryosphere Discussions.* **8**, pp.769-804.

Plummer, C.T., Curran, M.A.J., van Ommen, T.D., Rasmussen, S.O., Moy, A.D., Vance, T.R., Clausen, H.B., Vinther, B.M. and Mayewski, P.A. 2012. An independently dated 2000-yr volcanic record from Law Dome, East Antarctica, including a new perspective on the dating of the 1450s CE eruption of Kuwae, Vanuatu. *Climate of the Past.* **8**(6), pp.1929-1940.

Sigl, M., McConnell, J.R., Layman, L., Maselli, O., McGwire, K., Pasteris, D., Dahl-Jensen, D., Steffensen, J.P., Vinther, B., Edwards, R., Mulvaney, R. and Kipfstuhl, S. 2013. A new bipolar ice core record of volcanism from WAIS Divide and NEEM and implications for climate forcing of the last 2000 years. *Journal of Geophysical Research-Atmospheres.* **118**(3), pp.1151-1169.

Sigl, M., McConnell, J.R., Toohey, M., Curran, M., Das, S.B., Edwards, R., Isaksson, E., Kawamura, K., Kipfstuhl, S., Kruger, K., Layman, L., Maselli, O.J., Motizuki, Y., Motoyama, H., Pasteris, D.R. and Severi, M. 2014. Insights from Antarctica on volcanic forcing during the Common Era. *Nature Climate Change.* **4**(8), pp.693-697.

Stenni, B., Proposito, M., Gragnani, R., Flora, O., Jouzel, J., Falourd, S. and Frezzotti, M. 2002. Eight centuries of volcanic signal and climate change at Talos Dome (East Antarctica). *Journal of Geophysical Research-Atmospheres.* **107**(D9), 4076.

Traufetter, F., Oerter, H., Fischer, H., Weller, R. and Miller, H. 2004. Spatio-temporal variability in volcanic sulphate deposition over the past 2 kyr in snow pits and firn cores from Amundsenisen, Antarctica. *Journal of Glaciology.* **50**(168), pp.137-146.

Zielinski, G.A., Mayewski, P.A., Meeker, L.D., Whitlow, S., Twickler, M.S., Morrison, M., Meese, D.A., Gow, A.J. and Alley, R.B. 1994. Record of volcanism since 7000 BC from the GISP2 Greenland ice core and implications for the volcano-climate system. *Science.* **264**(5161), pp.948-952.

Appendix C Supplement to Chapter 3

We include an additional Figure complementary to Figure 3.3 in which we show the decomposition of the net radiative forcing efficiency into its shortwave and longwave components. A table of the model output values for each of the simulated eruptions is also included. We describe the online tool where users can explore our results in more detail.

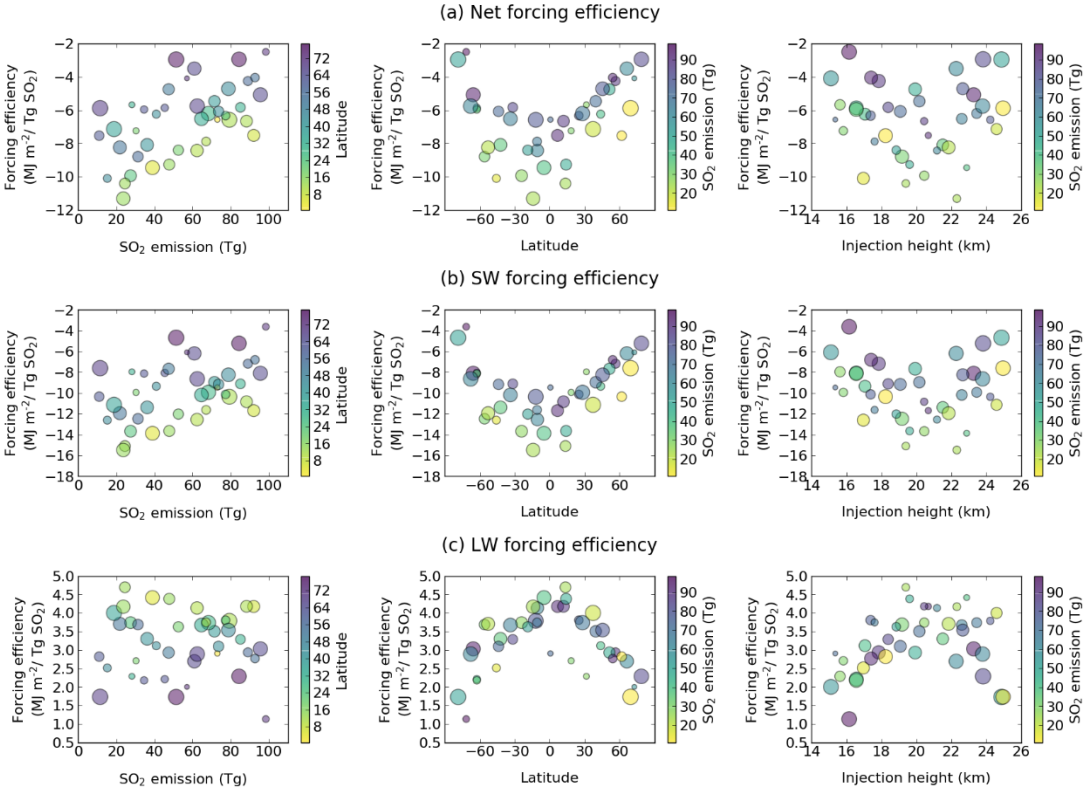

Figure C.1: Net, shortwave (SW) and longwave (LW) radiative forcing efficiency (time-integrated forcing divided by SO_2 emission) versus the eruption source parameters for all 41 simulations (training and validation). Each plotted point represents the output of one model simulation. For each output quantity (panels a - c), we show the output value vs. SO_2 emission (left), latitude (middle) and injection height (right). For the left hand plots the colour of the points indicates the latitude of the eruption in each simulation and the size indicates the injection height (the larger the point, the higher the injection height). For the plots in the middle, the colour represents the mass of SO_2 emitted and the size indicates the injection height. On the right, the colour indicates the mass of SO_2 emitted and the size represents the latitude of the eruption (smaller for low latitudes, larger for high latitudes).

Table C.1: Eruption source parameter values and model output values for the 41 simulations. Simulations 1-30 are the training runs. Simulations 31-41 are the validation runs. Injection height is the bottom of the 3-km plume.

Simulation	SO_2 emission (Tg)	Latitude (°N)	Injection height (km)	Average global sulfate e-folding decay time (months)	Integrated global mean sAOD at 550 nm (months)	Integrated global mean net radiative forcing (MJ m^{-2})
1	36.2	-42.2	21.5	9.1	5.9	-292.6
2	62.4	-10.5	21.2	9.4	10.2	-525.2
3	27.5	-24.1	20.5	10.4	5.7	-273.1
4	41.0	43.8	17.1	8.8	5.7	-255.5
5	79.4	-11.9	24.2	8.5	10.3	-521.8
6	31.4	-56.0	19.2	9.5	5.5	-275.7
7	77.4	25.1	17.4	9.2	10.5	-489.4
8	71.5	39.6	20.2	8.2	9.1	-390.5
9	61.0	66.3	22.3	6.5	5.5	-213.1
10	85.2	-31.7	18.4	7.5	9.7	-496.3
11	68.4	28.2	23.5	8.3	8.2	-423.5
12	45.4	-62.6	16.6	7.8	5.2	-266.2
13	39.0	-4.9	22.9	10.5	7.4	-368.5
14	24.5	13.6	19.4	11.8	5.2	-255.0
15	30.3	18.5	15.8	10	4.1	-219.6
16	64.7	-33.7	22.6	8.5	8.8	-421.4
17	89.1	56.6	17.8	7.8	9.7	-378.0
18	73.0	0.7	15.4	10.3	9.0	-479.4
19	47.5	51.4	19.9	7.5	5.6	-225.2
20	95.7	-65.7	23.3	7.1	10.3	-485.1
21	21.9	-52.9	21.8	9.7	3.9	-180.0
22	84.4	78.8	23.8	5.9	6.6	-248.0
23	52.6	-18.8	18.9	9.6	9.2	-441.8
24	11.0	61.9	18.2	7.2	1.7	-82.9
25	98.5	-71.7	16.2	3.7	4.9	-245.5
26	57.1	72.7	15.1	7.2	5.8	-233.1
27	51.4	-78.6	24.9	4.9	3.7	-151.7
28	18.8	37.2	24.6	9.5	2.7	-134.0
29	15.3	-45.8	17.0	9.8	2.7	-154.1
30	92.1	6.8	20.7	8.5	13.5	-692.2
31	67.2	-10.8	17.6	9.2	10.5	-529.1
32	88.3	11.9	20.4	8.1	11.7	-588.1
33	47.8	14.1	19.6	9.7	8.7	-442.9
34	34.6	-62.6	16.6	7.5	4.1	-205.8
35	62.5	-67.9	23.8	7.7	7.5	-359.4
36	92.8	54.2	17.4	7.8	9.8	-374.8
37	78.8	45.5	22.7	7.1	8.3	-371.2
38	23.7	-14.2	22.3	11.5	5.2	-267.7
39	28.2	31.6	15.6	8.7	3.6	-159.9
40	11.5	69.5	25.0	6.5	1.4	-67.5
41	73.7	-43.9	19.1	7.8	8.8	-447.3

Online tool

We provide an online tool for exploration of the three emulators built in this study available at:

http://www.see.leeds.ac.uk/see-research/icas/volcanic_forcing_online_tool/

The online tool allows the user to choose an emulator (e.g. time-integrated net radiative forcing) and display response surfaces in either 3D (3D scatter) or 2D (contour). The 3D scatter plot can be rotated and moved. Sliders are provided to choose any fixed value for the 2D contours as in Figures 3.5-3.7. Hovering over the surfaces displays information on the data point. The emulators can also be constrained by choosing a range of model output values using sliders. To display the constrained parameter space in 3D shown in Figure 3.10 (Section 3.3.3.2) select Plot type 3D scatter, Model output sAOD and move the slider at the bottom of the plot to 10.

The data provided is not sampled as extensively as in the paper to reduce the size of the webpage.

We are very grateful to Richard Rigby for his help with creating the tool. The online tool was created using plotly (Plotly Technologies Inc. Collaborative data science. Montréal, QC, 2015. https://plot.ly.)

Appendix D Supplement to Chapter 4

We include supplementary figures of the experimental design (Figure D.1), emulator validation (Figures D.2-D.3), total sulfate deposition in each UM-UKCA simulation (Figure D.4) and ice sheet deposition time series for two example eruption-realisations (Figure D.5). Figure D.6 shows the seasonal differences in the emulated deposition response surfaces and Figure D.7 shows the emulated radiative forcing response surfaces for January and July eruptions. Figures D.8 and D.9 show the constrained parameter spaces for each of the top 10 bipolar deposition signals in Sigl et al. (2015), for January and July eruptions, respectively. Table D.1 includes the values of each model output for each of the 82 model simulations.

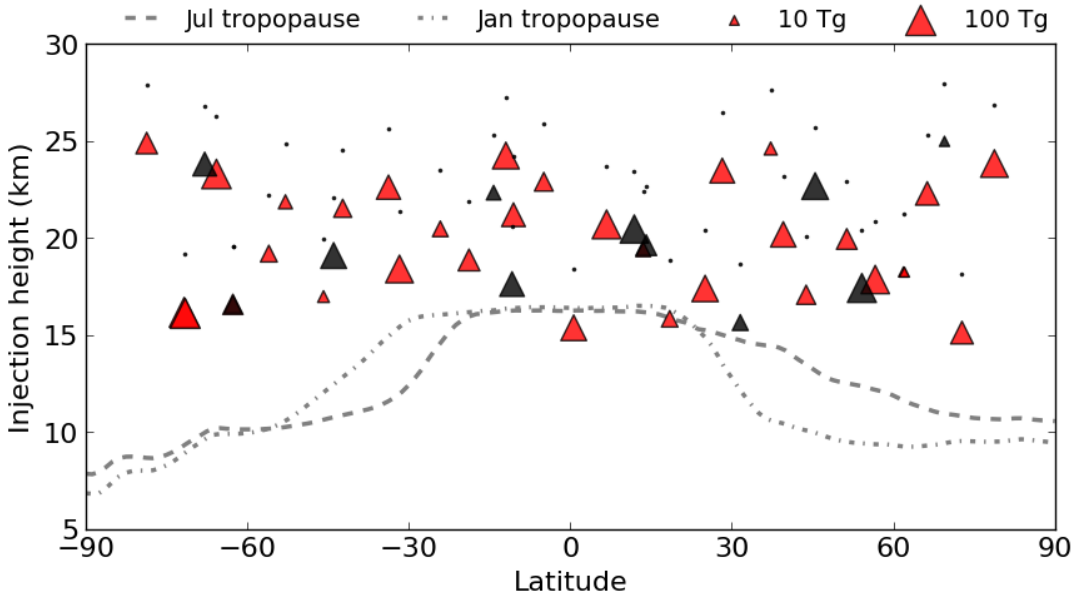

Figure D.1: Volcanic eruptions simulated. Each triangle represents two model simulations that were conducted using UM-UKCA (one in January and one in July). The location of the triangle indicates the latitude and injection height of the SO_2 emission for each eruption. The injection height indicates the bottom of the emitted plume; emissions are distributed linearly between this value and 3 km higher, which is shown by the dots above each triangle. The size of the triangle represents the mass of SO_2 emitted. The simulations span SO_2 emissions between 10 Tg and 100 Tg, latitudes between 80°S and 80°N and injection heights between 15 km and 25 km. Red triangles are training runs, which are the simulations used to build the statistical emulators. Black triangles are simulations that were used to validate the statistical emulators after they were built. There are two simulations (one training run and one validation run) at ~63°S and ~17 km which have SO_2 emissions of 35 Tg and 45 Tg and are not easily distinguished by the marker size scale. The grey lines show the simulated monthly mean zonal mean January (Jan) and July (Jul) tropopause heights.

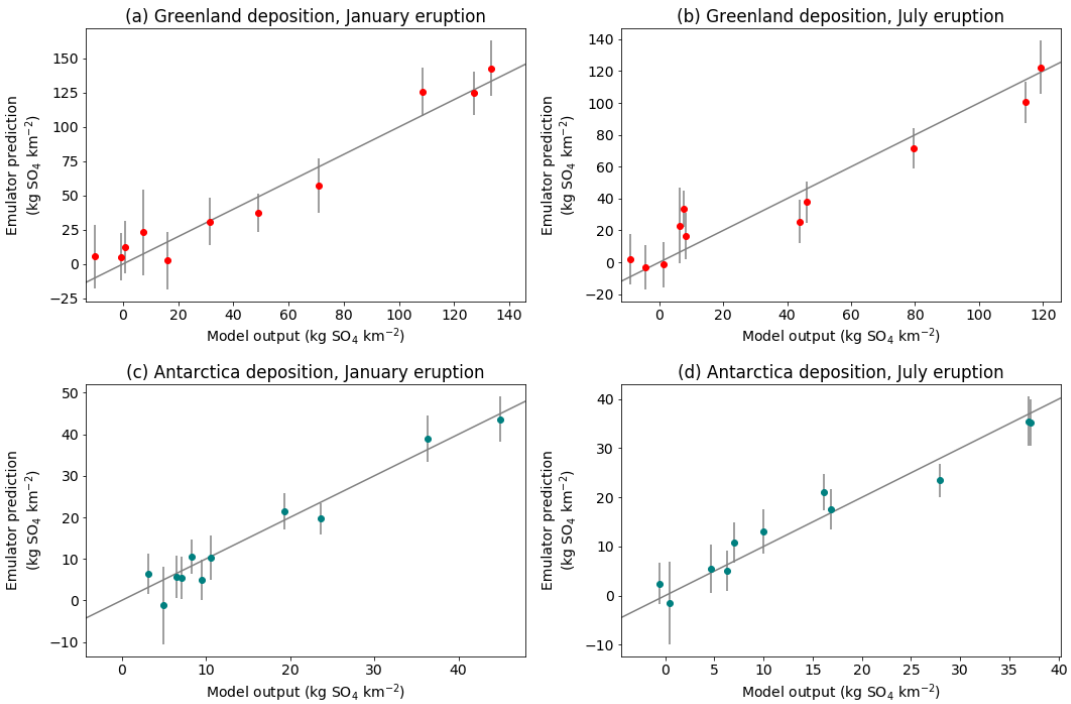

Figure D.2: Validation of each deposition emulator. For each variable (a-d), the value of the model output for the 11 validation runs is plotted against that predicted by the emulator (red for Greenland deposition and teal for Antarctica deposition). The vertical lines are 95% confidence bounds on the emulator mean predictions. The solid grey line marks the 1:1 line.

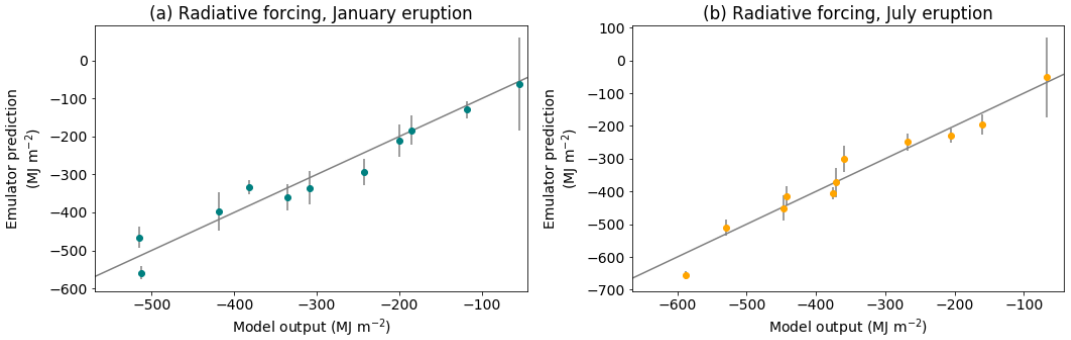

Figure D.3: Validation of the time-integrated global mean radiative forcing emulators for eruptions in January (a) and eruptions in July (b). The value of the model output for the 11 validation runs is plotted against that predicted by the emulator. The vertical lines are 95% confidence bounds on the emulator predictions. The solid grey line marks the 1:1 line.

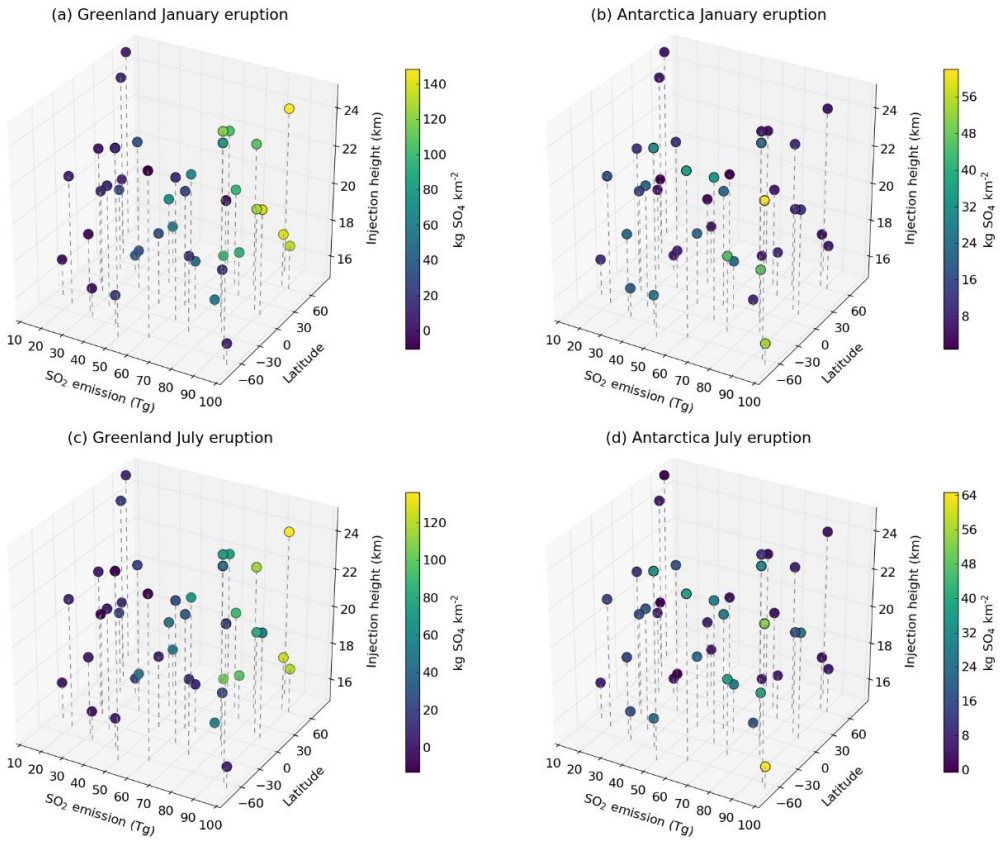

Figure D.4: Time-integrated anomalous deposited sulfate (colours) on each ice sheet simulated in UM-UKCA against the eruption source parameters. Panels (a) and (b) show the deposition to Greenland and Antarctica for January eruptions. Panels (c) and (d) show the deposition to Greenland and Antarctica for July eruptions. Each scatter point shows the time-integrated deposition for one simulation. The vertical dashed lines join each scatter point to the x-y plane for visualization.

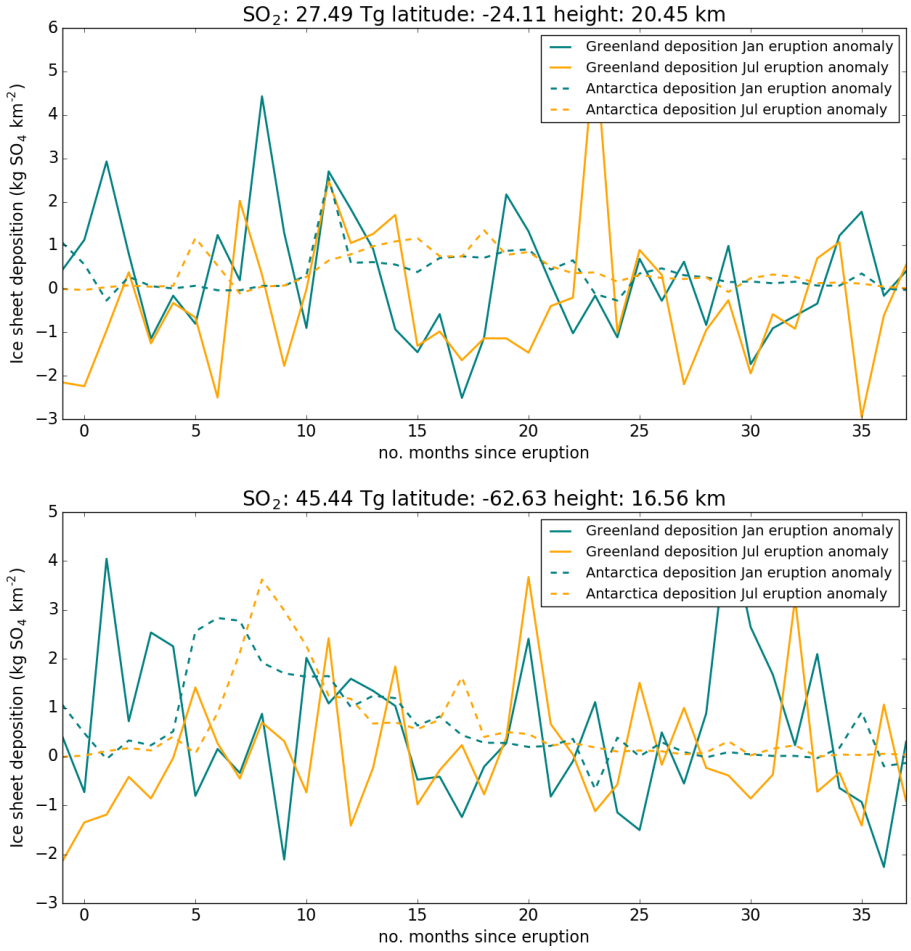

Figure D.5: Anomalous sulfate deposited on Greenland (solid) and Antarctica (dashed) for two example eruption-realisations (top and bottom) on 1 January (teal) and 1 July (orange). For the eruption at 24°S (top), total (time-integrated) anomalous deposited sulfate on Greenland following the July eruption is -13 kg SO_4 km^{-2}. For the eruption at 63°S (bottom), total anomalous deposited sulfate on Greenland following the January eruption is 21 kg SO_4 km^{-2}.

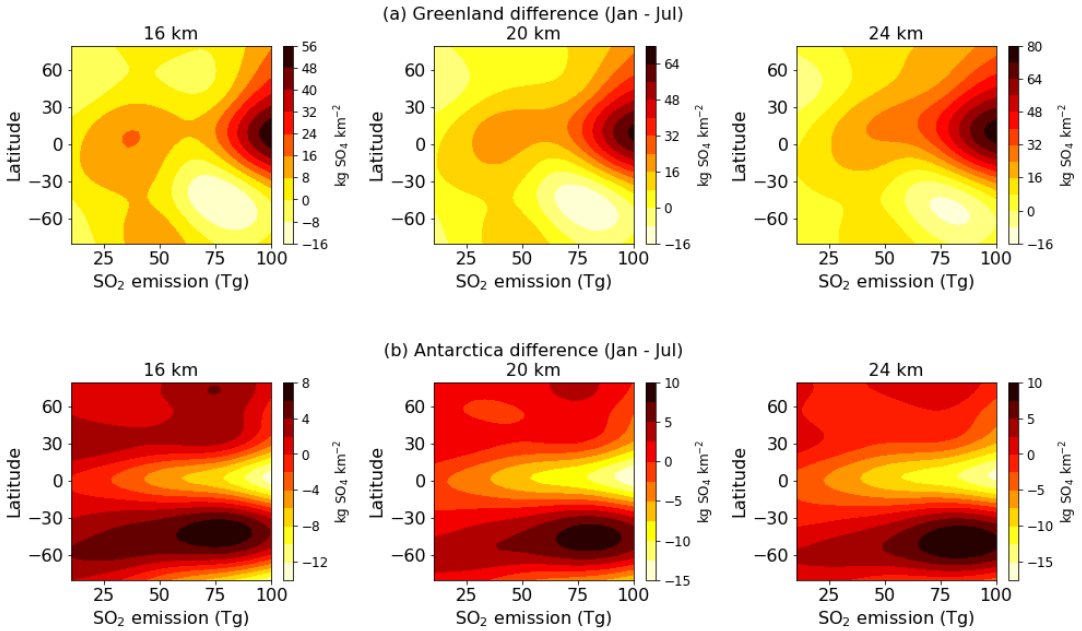

Figure D.6: Seasonal differences in the emulated response surfaces in Figure 4.2 (main text) (January surface – July surface) for Greenland deposition (a) and Antarctica deposition (b).

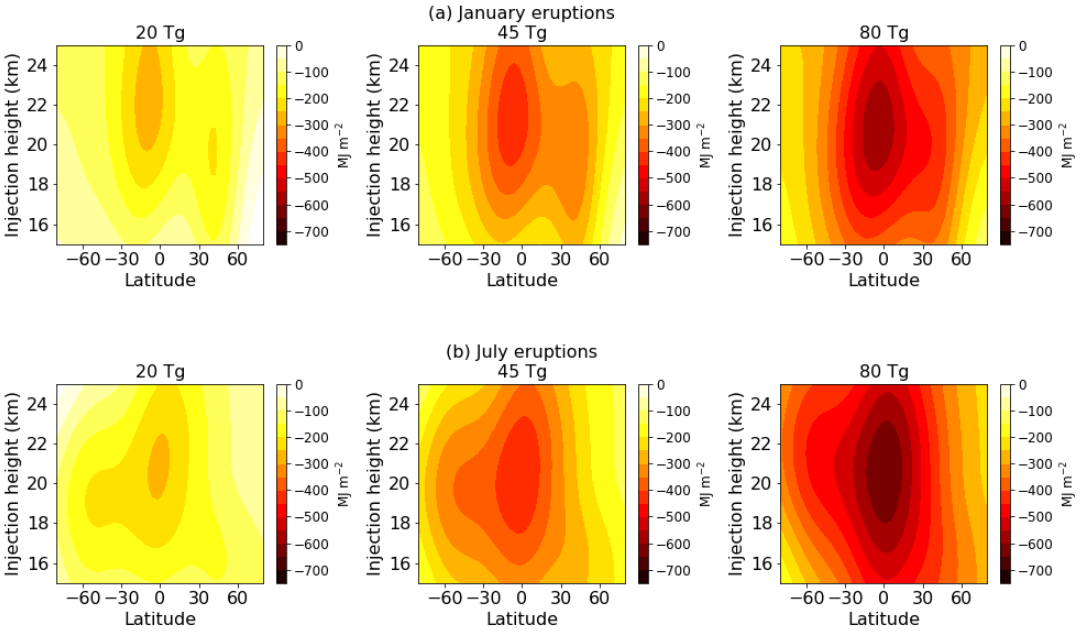

Figure D.7: Emulated response surfaces of the time-integrated global mean net radiative forcing at fixed SO_2 emissions of 20 Tg, 45 Tg and 80 Tg for January eruptions (a) and July eruptions (b) (as in Figure 7 Marshall et al. (under review)). The contour plots show the emulator prediction against latitude and injection height of the emissions for each of these emission magnitudes.

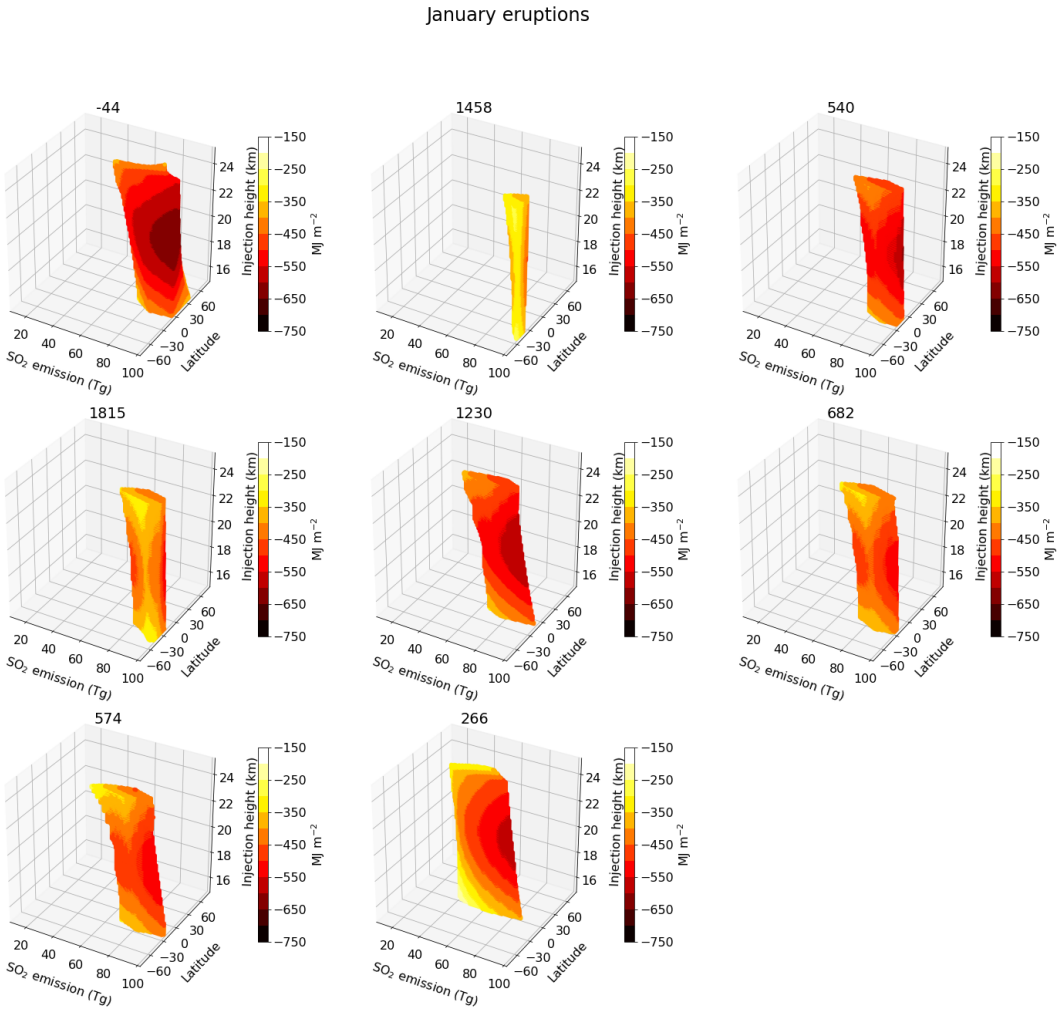

Figure D.8: Constrained parameter space for the top 10 deposition signals from Sigl et al. (2015) if the eruption occurred in January. Each panel shows for one bipolar signal the combinations of SO_2 emission, latitude and injection height that result in Greenland and Antarctica deposition that is consistent with the ice-core-derived sulfate deposition estimates. The constrained space is made up of scatter points of the parameter combinations and the colour of each scatter point shows the emulator mean prediction of the RF for each of these eruptions.

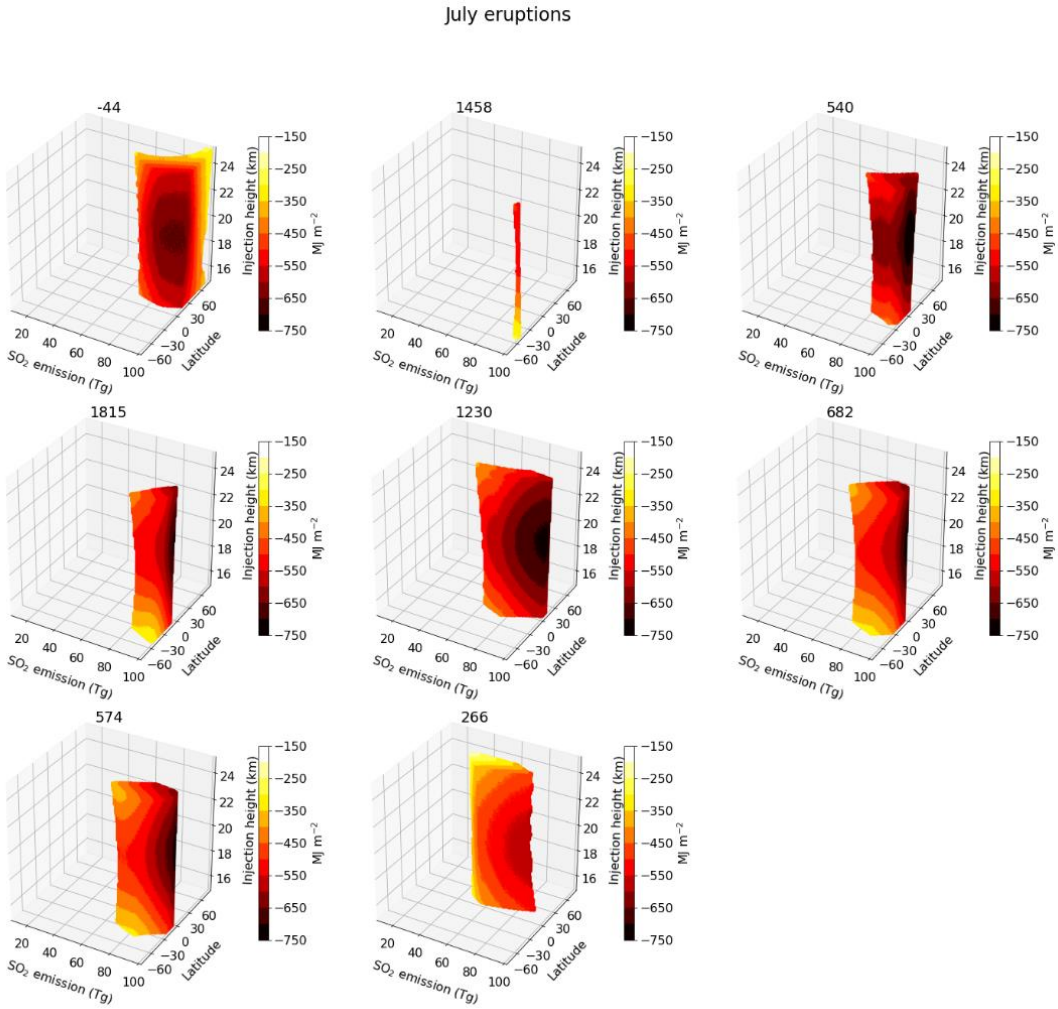

Figure D.9: As Figure D.8 but for July eruptions.

Table D.1: Eruption source parameter values and model output values (time-integrated anomalous deposited sulfate and time-integrated global mean net radiative forcing (RF)) for the 41 January and July eruptions. Simulations 1-30 are the training runs. Simulations 31-41 are the validation runs.

	Eruption source parameters			**Greenland deposition ($kg\ SO_4\ km^{-2}$)**		**Antarctica deposition ($kg\ SO_4\ km^{-2}$)**		**RF ($MJ\ m^{-2}$)**	
	SO_2 emission (Tg)	**Latitude**	**Injection height (km)**	**Jan**	**Jul**	**Jan**	**Jul**	**Jan**	**Jul**
1	36.2	-42.2	21.5	9.1	0.6	21.7	18.8	-220.8	-292.6
2	62.4	-10.5	21.2	26.0	31.7	22.7	27.4	-518.0	-525.2
3	27.5	-24.1	20.5	10.4	-13.3	14.0	15.0	-271.1	-273.1
4	41.0	43.8	17.1	55.8	46.3	5.3	4.3	-298.5	-255.5
5	79.4	-11.9	24.2	76.2	39.8	22.2	29.7	-502.5	-521.8
6	31.4	-56.0	19.2	-2.3	2.1	23.2	14.1	-151.6	-275.7
7	77.4	25.1	17.4	93.9	98.7	9.0	5.0	-417.3	-489.4
8	71.5	39.6	20.2	96.3	90.8	6.3	4.0	-429.6	-390.5
9	61.0	66.3	22.3	102.9	74.4	4.0	1.8	-257.6	-213.1
10	85.2	-31.7	18.4	14.0	21.3	46.6	37.0	-446.1	-496.3
11	68.4	28.2	23.5	119.5	72.2	5.6	10.5	-380.6	-423.5
12	45.4	-62.6	16.6	20.8	0.8	25.3	22.9	-162.2	-266.2
13	39.0	-4.9	22.9	33.4	18.9	10.4	16.7	-390.3	-368.5
14	24.5	13.6	19.4	24.0	14.8	4.2	5.9	-202.2	-255.0
15	30.3	18.5	15.8	39.5	18.6	5.8	3.3	-150.4	-219.6
16	64.7	-33.7	22.6	12.3	25.3	33.2	29.3	-363.2	-421.4
17	89.1	56.6	17.8	141.2	124.8	3.6	2.7	-317.4	-378.0
18	73.0	0.7	15.4	57.4	53.9	8.3	17.1	-362.3	-479.4
19	47.5	51.4	19.9	65.0	67.5	1.3	2.6	-313.9	-225.2
20	95.7	-65.7	23.3	3.2	17.5	62.1	53.3	-271.9	-485.1
21	21.9	-52.9	21.8	8.1	6.6	15.4	13.1	-134.2	-180.0
22	84.4	78.8	23.8	148.4	136.2	4.6	3.6	-277.4	-248.0
23	52.6	-18.8	18.9	31.8	4.1	22.2	23.0	-421.0	-441.8
24	11.0	61.9	18.2	9.2	7.6	0.8	-0.1	-38.7	-82.9
25	98.5	-71.7	16.2	10.1	2.5	54.0	64.7	-227.2	-245.5
26	57.1	72.7	15.1	95.3	104.1	6.0	3.6	-99.2	-233.1
27	51.4	-78.6	24.9	5.5	-10.3	30.6	32.5	-192.5	-151.7
28	18.8	37.2	24.6	9.2	15.0	5.2	4.8	-145.3	-134.0
29	15.3	-45.8	17.0	-2.3	-1.6	10.2	6.9	-79.0	-154.1
30	92.1	6.8	20.7	139.4	54.2	12.5	28.6	-596.6	-692.2
31	67.2	-10.8	17.6	49.0	7.7	23.6	27.9	-515.8	-529.1
32	88.3	11.9	20.4	127.0	79.6	8.3	16.1	-512.3	-588.1
33	47.8	14.1	19.6	71.0	46.1	3.2	7.0	-335.9	-442.9
34	34.6	-62.6	16.6	-0.6	-4.4	19.3	16.8	-117.8	-205.8
35	62.5	-67.9	23.8	-10.3	-8.9	36.3	37.0	-200.3	-359.4
36	92.8	54.2	17.4	133.4	119.2	6.5	4.7	-381.5	-374.8
37	78.8	45.5	22.7	108.7	114.6	9.5	6.3	-419.0	-371.2

38	23.7	-14.2	22.3	0.6	1.2	10.5	10.0	-242.9	-267.7
39	28.2	31.6	15.6	31.5	44.0	7.1	-0.6	-185.0	-159.9
40	11.5	69.5	25.0	7.2	6.2	5.0	0.4	-55.0	-67.5
41	73.7	-43.9	19.1	16.1	8.2	45.0	37.2	-308.8	-447.3

References

Sigl, M., Winstrup, M., McConnell, J.R., Welten, K.C., Plunkett, G., Ludlow, F., Buntgen, U., Caffee, M., Chellman, N., Dahl-Jensen, D., Fischer, H., Kipfstuhl, S., Kostick, C., Maselli, O.J., Mekhaldi, F., Mulvaney, R., Muscheler, R., Pasteris, D.R., Pilcher, J.R., Salzer, M., Schupbach, S., Steffensen, J.P., Vinther, B.M. and Woodruff, T.E. 2015. Timing and climate forcing of volcanic eruptions for the past 2,500 years. *Nature*. **523**(7562), pp.543–549.